UNIVERSITY OF CAPE TOWN

FACULTY OF SCIENCE
DEPARTMENT OF PHYSICS

P H D T H E S I S

to obtain the title of

Doctor of Philosophy

Speciality : High Energy Nuclear and Particle Physics

Presented by

Kgotlaesele Johnson SENOSI

Vector boson production with the ALICE detector

Advisor: Em. Prof. JWA Cleymans
University of Cape Town

Thesis Advisor: Dr. EZ Buthelezi
iThemba Laboratory of Accelerator Based Science

Submitted on 4^{th} of June 2017

Assessment committee:

Dr K Mueller

Department of Physics, Universitaet Zuerich, Switzerland

Dr KO Schweda

GSI - Helmholtzzentrum fur Schwerionenforschung GmbH, University of Heidelberg, Faculty of Physics and Astronomy, Germany

Vector boson production with the ALICE detector

Abstract:

The main objective of this thesis is to study and investigate the production of massive vector bosons (W^+ and W^-). This a priori mentioned production is not sensitive to hot nuclear matter effects because of the weak coupling nature of these vector bosons. Thus, in heavy ion collisions they provide a good reference for the medium-induced effects on other probes. The production mechanism of these vector bosons is highly isospin dependent and thus they are affected by the initial state effects. Initial state effects include isospin, Fermi motion, EMC effect, shadowing and nuclear absorption. Hence their production in lead-lead (Pb-Pb) and proton-lead (p-Pb) collisions can be used to test some of these initial state effects. In this thesis only two of these initial state effects will be considered namely, isospin and shadowing (referring to shadowing and anti-shadowing). In addition, these vector bosons can be used to provide a non-arbitrary reference to the probes affected by the medium.

Traditionally, in heavy ion collisions, hard processes are expected to scale with the number of binary collision thus a precise study of these vector bosons can be used to test the factorisation assumed in models used to determine centrality. This unique property of electroweak (W) bosons makes them essential probes to study the possible inherent bias in centrality determination. In proton-proton (pp) collisions, their production can be used to obtain information on quark parton distribution functions (PDF).

The data used in the analysis was collected by A Large Ion Collider Experiment (ALICE) at the Large Hadron Collider (LHC). The ALICE detector is designed to study ultra-relativistic heavy-ion collisions, in which a hot and dense, strongly-interacting medium is created. The production of W bosons is studied in p–Pb, p-p and Pb-Pb collisions at 5.023, 8 and 5.023 TeV centre-of-mass energies, respectively. The forward muon spectrometer with the pseudorapidity acceptance $-4.0 < \eta < -2.5$ is used. W bosons are studied via the inclusive single muon differential p_{T} spectrum.

Kgotlaesele Johnson Senosi

October 9, 2017

Preface

This thesis was submitted to the Faculty of Science, University of Cape Town, as a partial fulfillment of the requirements to obtain the PhD degree. The work presented was carried out in the years 2014-2017.

Thesis objectives

The objectives of the work reported in this thesis are primarily to study W-boson in heavy ion collisions with the intent to understand the effect of cold nuclear matter effects as well as the scaling of W-boson yield with the average number of binary collisions. This was primarily done in proton-lead collisions although also possible in lead-lead collisions.

Thesis outline

This thesis is divided into four parts. Part I of the thesis provides background and theoretical concepts of high energy particle physics. A synoptic historical overview of physics leading eventually to the birth of high energy particle physics is presented. The focus is geared towards the importance of massive electroweak bosons in high energy particle physics.

In Part II, the first chapter introduces the CERN Large Hadron Collider together with its four main experiments. A Large Ion Collider Experiment (ALICE), used in this study is described in detail expanding more on detectors used in the analysis. In the second chapter, the ALICE Online and Offline data taking is described from systems used in experiment monitoring to offline data management.

Part III has three chapters, the first and second are dedicated to the descriptions of proton-lead and proton-proton analysis strategies and results, respectively. The last and third chapter of this part is dedicated to the outlook study of W-boson in lead-lead collisions and the preliminary results.

In Part IV there are two chapters, the first is dedicated to the results of proton-lead, proton-proton and lead-lead data separated in sections. And the last chapter consists of the summary, conclusions and outlook/recommendations.

Dedicated to my Family

Contents

List of Tables

List of Figures

Part I

Introduction

All men by nature desire knowledge.

Aristotle

1

Concepts and Literature review

In this chapter, the description and concepts of heavy-ion collisions are presented in detail. This will be done mainly focusing on hard probes (particles produced in initial hard collisions) especially massive vector bosons and their role in the study of heavy ion collisions.

Contents

A Brief History

Particle physics originated from theoretical and experimental developments of fundamental physics which span decades going back as far as the 1890s. One of these experimental developments which has a direct relation with particle physics, is the discovery of radioactivity, independently by Becquerel and Curie in 1890s. The electron was the first of elementary particles to be discovered by J.J. Thomson in 1897. In 1899 Ernest Rutherford classified radioactivity according to its ability to penetrate and ionize, the alpha could be stopped by a piece of paper whereas beta could traverse a few millimeters into aluminum. Another kind of radiation called a gamma or photon was postulated by Planck in 1900 to explain blackbody radiation. At the wake of the 19^{th} century, Albert Einstein took Planck's ideas and proposed a quantum of light (the photon) which behaves like a particle. Einstein's other theories explained the particle-wave duality of photons and special relativity. His other well known theory which assumed the equivalence of mass and energy is general relativity. The discovery of radioactivity which suggested that something was happening to the atoms, led to experiments dedicated to studying the atom. In 1911 Rutherford discovered the nucleus by scattering alpha particles on a gold foil which showed that some alpha particles appear to scatter on a hard sphere. The interpretation of the results suggested that the atom has a small dense and positively charged center which was the first evidence of a proton – atoms were not indivisible after all. In 1913 Niels Bohr succeeded in constructing a theory of atomic structure based on quantum ideas. Until the discovery of the neutron in 1932 by Chadwick, Curie and Joliot the atoms were thought of as bound states of protons and electrons with the mass concentrated in the nucleus [Kra87]. Prior to this discovery, in 1931 Paul Dirac combined quantum mechanics and special relativity to describe the electron, and also positively charged electrons emerged from the theory, which was the first account of antimatter. This work started in 1930 by Bothe and Becker who discovered that bombarding beryllium with alpha particles produced a neutral current but they thought this to be a gamma ray. From this picture arose a question of how can protons be held together in such a small space? Which led to the notion of a force stronger than the repulsive Coulomb force. But this strong force cannot surely follow the same radial dependence as the electromagnetic force otherwise atoms will be crushed into each other. In 1935 Yukawa proposed an explanation for this interaction as an exchange of a massive particle called a pion. This came to be known as an effective theory after the introduction of Quantum ChromoDynamics (see next section) which is a theory of strong interactions. Another hurdle in understanding the heart of the matter was beta-decay, in this process it was seen that energy conservation was not respected since the energy spectra of the emitted beta was a continuum instead of discrete. This was explained by Pauli introducing a

light particle he called a neutron which was later named neutrino by Fermi. It took two decades and a half for Fermi's hypothesized neutrino to be confirmed by Cowan and Reines in 1956. Another experimental advance in the quest to understand the heart of matter was in the 1960s by experiments at the Stanford Linear Acceleration Center (SLAC) which discovered that protons were composite particles. The results were interpreted by saying that protons are composite particles. The technological advances in the middle of the 20^{th} century made it possible to accelerate particles to higher energies which lead to discoveries of more and more unstable particles. In order to explain these abundance of particles Murray Gell-Mann and George Zweig independently and simultaneously proposed the "Quark Model". In the quark model they postulated that these unstable particles (for example Kaons and Lambdas) were made up of other families of fundamental particles besides the ones which make up protons and neutron. The quark model ran into a hurdle with regards to explaining the existence of composite particles which seemed to violate Pauli's exclusion principle. This problem was solved by Greenberg in 1964 who introduced the idea of colour charge to explain how quarks could coexist inside hadrons, that is, baryons are made up of three quarks and mesons of two quarks. The theory of Quantum ChromoDynamics (chromo - color) has been under development since the 1970s and constitutes an important component of the **Standard Model** of particle physics.

1.1 The Standard model

The standard model is a theoretical framework constructed with the mathematical tools of quantum field theory. It is an $SU(3) \times SU(2) \times U(1)$ gauge field theory aimed at describing interactions of fundamental particles with each other. These fundamental particles shown in Figure 1.1 are classified into three families of fermions (quarks and leptons) and gauge bosons (force mediators). As people interact by words or glances, particles interact by exchanging other particles called force mediators. In the present scope there are four forces in nature namely electromagnetic, weak, strong and gravity. The photon is a middle-man among electrically charged particles, this is known as the electromagnetic interaction whereas the weak interaction is mediated by massive vector bosons $W^{\pm}$ and Z^0. The strong interaction, which is the strongest of the four, occurs among colour-carrying particles mediated by the gluon. The recent addition to the standard model is the Higgs boson, whose existence was postulated by Robert Brout and François Englert and Peter Higgs. Peter Higgs and François Englert received a Nobel Prize in 2013 for this work. This particle, confirmed by recent experiments [CH14, C$^+$13, C$^+$13, A$^+$12b, AA$^+$12], is responsible for giving fundamental particle mass by what is known as the "Higgs Mechanism". In addition to the discovery of the Higgs boson, another triumph of the Standard model was the discovery of the penta-quark bound states [A$^+$15c]. Both of these discoveries were made at the Large Hadron Collider (LHC) [EB08]. In the Standard Model only three of the four

forces except for gravity are described. The first to be understood was electricity and magnetism which was unified by Maxwell into electromagnetism. The next was the unification of electromagnetism and weak interactions into the electroweak force (without which the sun would not shine) by Steven Weinberg, Abdus Salam and Sheldon Lee Glashow in the 20th century. Today, physicist seek to unify this with the strong force, without which the nucleus of an atom would break apart.

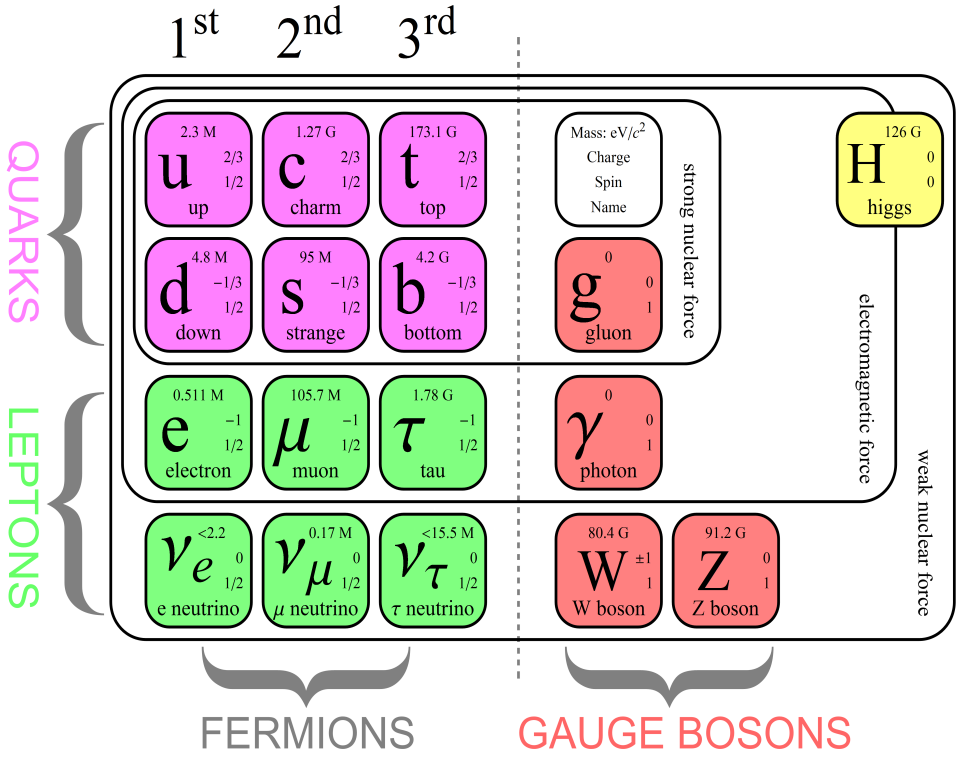

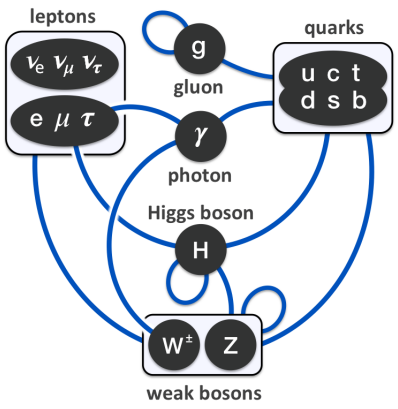

Figure 1.1: Standard model in a nutshell [Ser15].

1.1.1 Quantum ElectroDynamics

The theory of electromagnetism was later quantized by Dirac into what is now known as **Quantum ElectroDynamics** which describes the interaction of charged spin-1/2 particles with the electromagnetic field. Imposing local invariance on the Dirac Langrangian (free fermion Lagrangian)

$$\mathcal{L}_{free} = \bar{\psi}(i\gamma^{\mu}\partial_{\mu} - m)\psi \tag{1.1}$$

the theory demands an addition of a vector potential A_{μ} in order to maintain invariance under $U(1)$ phase transformation. In equation 1.1 ψ and $\bar{\psi}$ are matter fields, m is the mass, ∂_{μ} is a four vector derivative and γ^{μ} are Dirac matrices. This vector potential or the gauge field couples with particles of charge $-e$ in the same way as the photon. Such imply that local invariance (symmetry) leads to a theory of interacting fields which couples through a gauge field, resulting in the following QED Lagrangian.

$$\mathcal{L}_{\text{QED}} = \bar{\psi}(i\gamma^{\mu}\partial_{\mu} - m)\psi + e\bar{\psi}\gamma^{\mu}A_{\mu}\psi - \frac{1}{4}F_{\mu\nu}F^{\mu\nu} \tag{1.2}$$

The first term of the above Lagrangian (equation 1.2) is the same as $\mathcal{L}_{free}$, the second term is the interaction term with e as the interaction strength, and third term is the kinetic term where $F_{\mu\nu}$ and $F^{\mu\nu}$ are field tensors. Gauge invariance prevent the photon from having mass.

1.1.2 Electroweak Theory

This is a unified theory of weak interaction and quantum electrodynamics. Weak interaction is responsible for nuclear processes like β decay and other nuclear reactions. Prior to the experimental discovery that weak interactions violate parity, these interactions were explained under Fermi's formalism in which coupling is among four vectors. This could explain most of the properties of weak interactions but not all. By including the component of an axial-vector in the formalism parity is automatically violated [HM08]. Following the assertion of Lee and Yang in 1956 that weak interactions do not conserve parity led to experiments aimed at proving or disproving this claim. One of the historically significant being the Cobalt 60 experiment by Madame Wu in 1957 which confirmed the parity violation of weak interactions. Thus, the weak interaction vertex instead of having a vectorial structure was to be described by a vector-axial vector structure. Inspired by the idea of Einstein to unify gravity and electromagnetism, Glashow took at task in 1961 to do the same for electromagnetic and weak interactions. He noticed that the only way these two can be described as one is if weak interactions are mediated by massive vector bosons [Gri08] which raised questions since the photon is massless. These two properties of weak interactions were

the main obstacles towards the unification with electromagnetism. A solution was provided by Salam and Weinberg in 1967 [Gri08] using the Yang-Mills field theory and the Higgs Mechanism in a theory based on $SU(2) \times U(1)$ gauge group, where $SU(2)$ is a group generator of weak interaction and $U(1)$ of electromagnetism. Following the same strategy as in QED, that is, imposing local gauge invariance under $SU(2) \times U(1)$ transformation requires an introduction of three isospin vectors $\vec{W}_\mu$ and one scalar B_μ. The first two of the vector currents are charged, related to $W^\pm$, whereas the third component and the scalar are neutral. The two neutral current mix in the Glashow theory, according to

$$\begin{aligned} A_\mu &= B_\mu \cos\theta_{\mathrm{w}} + W^3_\mu \sin\theta_{\mathrm{w}} \\ Z_\mu &= -B_\mu \sin\theta_{\mathrm{w}} + W^3_\mu \cos\theta_{\mathrm{w}} \end{aligned} \tag{1.3}$$

producing a massless A_μ and massive vector Z_μ boson. θ_W is the weak mixing angle or Weinberg angle.

1.1.3 Quantum ChromoDynamics

In 1954 Yang and Mills extended QED, *i.e.* an abelian theory into a non-abelian theory in an attempt to describe the strong interaction. But instead of a $U(1)$ symmetry group they considered an $SU(3)$ symmetry group. The non-abelian nature of this theory implies the self interaction of the gauge field which is the very nature of **Quantum ChromoDynamics**. The force carriers of the strong interaction are called gluons. These gauge fields carry what is known as the colour charge. These force carriers come in three types, and so the $SU(3)$ has 8 group generators. The colour charge is an extra degree of freedom which made it possible to explain the existence of Ω^-, this extra degree allows this state to obey the Pauli exclusion principle and theoretically justifies what was seen in experiments. The QCD Lagrangian is

$$\mathcal{L}_{\mathrm{QCD}} = \sum_q \bar{\psi}^{q,a}(i\gamma^\mu \partial_\mu \delta_{ab} - g_s \gamma^\mu t^C_{ab} \mathcal{A}^C_\mu - m_q \delta_{ab})\psi_{q,b} - \frac{1}{4} F^A_{\mu\nu} F^{A\mu\nu} \tag{1.4}$$

obtained the same way as the QED Lagrangian, this is by using the covariant derivative to eliminate the term which violates invariance when requiring that global invariance holds locally. Where $\psi^{q,a}$ is a quark field spinor with q running over quark flavours and a is the color index; $\mathcal{A}^C_\mu$ is the colour field running over $N_c^2 - 1 = 8$ corresponding to the number of gluons, t^C_{ab} are generators of $SU(3)$, g_s is the QCD coupling constant and $F^A_{\mu\nu}$ is a field tensor. QCD like QED are quantized form of the classical Yang-Mills field theory within which particles are massless. This puzzle was solved by Peter Higgs as well as François Englert and Robert Brout by unifying bosons of the Goldstone theorem with gauge fields which explain the origin of mass by what is known as the 'Higgs Mechanism". Now lets revert our discussion back to the self coupling nature of the gauge bosons of strong force. Since the gluon is self coupling the interaction among colour carrying objects cannot be based on a simple inverse distance potential.

Thus, the interaction potential has two components,

$$V(r) = -\frac{a}{r} + b \cdot r \tag{1.5}$$

the first term is a Coulomb-like potential and the second is a Hooke's law-like potential, which, unlike the Coulomb potential increases with spatial separation. The proportionality constants a and b are obtained by fits to energy levels of quarkonia bound states ($c\bar{c}$ and $b\bar{b}$) to be approximately 0.48 and 0.18 GeV^2 [Gil87]. This property of strong interactions is the main reason free quarks and gluons cannot be seen in nature, this is what is known as **colour confinement**. It is these properties which led to what is known as **asymptotic freedom** which states that at short distances the strong interaction becomes weak.

1.1.3.1 Asymptotic freedom

This phenomenon has an analog to large momentum transfer scattering interactions. The larger the momentum transfer (Q)[1] the smaller the distance probed. The strong coupling, $\alpha_s(Q)$, has an inversely proportional relation with the square of the momentum transfer Q as seen in Figure 1.2. The strong coupling, $\alpha_s(Q)$, sometimes referred to as *running coupling*, pertains to the fact that the coupling is not constant. This is one of the triumphs of QCD. The asymptotic freedom behaviour of strong interactions came from the seemingly unconnected ideas of Giorgio Parisi, Kurt Symanzik and Gerardus t'Hooft in 1972. The connection was later made by David Politzer and by David Gross and Frank Wilczek in 1973 [Ell14]. This is the idea that coupling in QCD is dependent on the scaling Q by

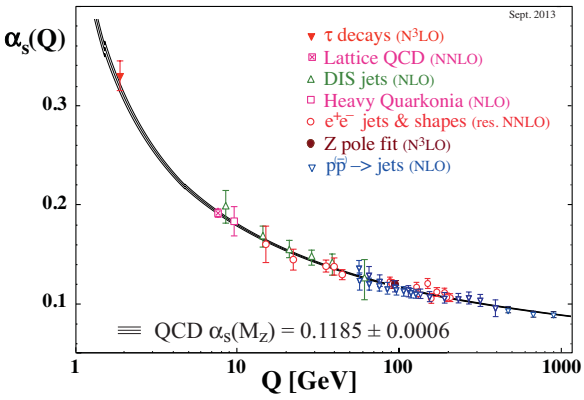

Figure 1.2: Summary of $\alpha_s(Q)$ measurements with the respective order of perturbation shown in brackets. NLO: next-to-leading order, NNLO: next-to-next-leading order, N^3LO: next-to-NNLO and res. NNLO: NNLO matched with resummed leading logs [ea14].

$$\alpha_s(Q) = \frac{12\pi}{(11n_c - 2n_f)\ln(\frac{Q^2}{\Lambda^2})} \tag{1.6}$$

where n_c is the number of colours, n_f is number of quark flavours and Λ is the lowest scaling at which perturbative QCD is applicable [ea14]. In the low energy

[1] Q is the scale at which the hadron structure is probed. This parameter is proportional to the energy transfer involved in hard scattering of the partons.

regime a different approach ought to be taken into account to make predictions; the most successful one being lattice QCD (lQCD), which can also be used to show that the quark interaction potential can be described by Equation 1.5. In lattice QCD the space-time is discretized with quarks at the space points and gluons connecting the lattice space point. Calculations in this case are performed numerically using supercomputers. The other non-perturbative method is the so called "MIT Bag Model" [Joh75]. The two methods can be used to describe the phase transition of hadronic matter to what is known as the **Quark Gluon Plasma**, the latter providing an intuitive view of this transition based on thermodynamic arguments.

1.2 The Quark Gluon Plasma (QGP)

The transition of hadronic matter to this state is attained by increasing the energy (temperature) or baryon chemical density. The QCD phase diagram is depicted in Figure 1.3, showing along the horizontal and vertical axis are the baryon chemical density and temperature (energy density), respectively. Our current knowledge of the evolution of the universe from the Big Bang tells us that the universe went through several phase transitions. The electroweak phase transition occurred earlier followed by the strong phase transition at temperatures approximately 100 GeV and 150 - 180 MeV, respectively. During the electroweak phase transition elementary particles acquired mass whereas during the strong phase transition colour confinement took effect [BBK+13, B+12, Sne06].

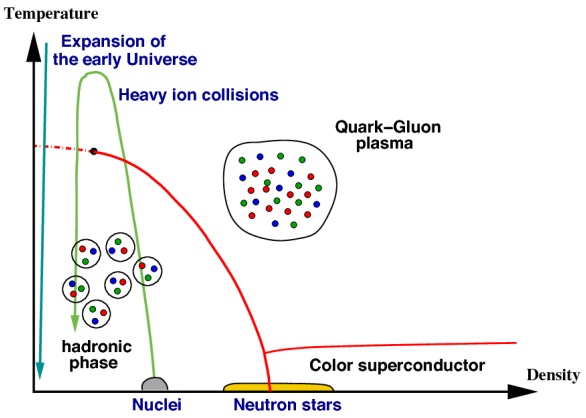

Figure 1.3: QCD phase transition [Ian14, Sat11, Sat10].

Lattice QCD estimate the strong phase transition to occur at temperatures around ∼170 MeV at zero baryon chemical potential as seen in Figure 1.4. This is a temperature above which the so called **chiral symmetry** is restored. Chiral symmetry breaking and restoration as well as confinement and deconfinement are hypothesized to coincide [Fuk08, KL99].

Chiral symmetry is an approximate symmetry of strong interactions in the limit of vanishing quark mass: we know that $m_q \neq 0$, but m_q is far less than the hadron masses so the symmetry holds but it is approximate [Koc95]. Figure 1.4 shows that in the proximity of the critical temperature T_c ∼170 MeV the energy density increases rapidly and is associated with the increasing number of degrees of freedom [Sne06]. In any case the medium formed at unprecedented energy densities ($\varepsilon \gtrsim 1$ GeV/fm^3)

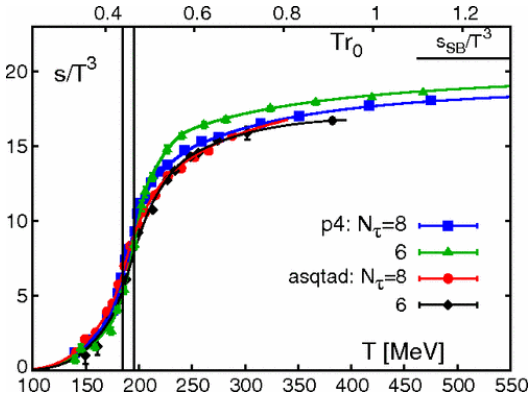

Figure 1.4: Lattice QCD equation of state at zero baryon chemical density [Baz09]. s, T and s_{SB} are entropy, temperature and entropy at the Stefan-Boltzmann limit. The variation of input parameters of lQCD are explained in Ref [Baz09]

does not reach the Boltzmann Limit (s_{SB}/T^3) – which is the limit of a non-interacting gas, which means that the medium formed is strongly interacting. Thus, to probe the properties of the early universe, hadronic matter ought to be studied at high enough energy density ($\varepsilon \gtrsim 1$ GeV/fm^3). This can be attained in the laboratory through relativistic heavy ion collisions.

1.3 Relativistic Heavy Ion Collisions

"One of the most interesting aspects of these collisions is the possibility of forming a phase of deconfined quarks and gluons, a system that is believed to have existed in a few-microseconds old universe. First principle QCD calculations suggest that it is possible to have such a state of matter if the temperatures attained can be of the order of the QCD scale ($\sim$ 200 MeV)" [SKNM13]. The properties of hadronic matter formed in these collisions reaches temperatures of about 170 MeV (10^{12} K) and energy density of between 0.3 - 1.3 GeV/fm^3 (approximately 10^{15} g/cm^3) [Sne06]. This allows to probe deconfinement and confinement of hadronic matter as well as the equation of state of the deconfinement state of matter in the laboratory. Analogous to the universe this state of matter created in heavy-ion collisions expands and cools down [Sne06].

The history of heavy-ion collision experiment

The history of heavy-ion experiments spans many decades. Some of the early experiments were performed at the Bevatron-Bevalac facility at Lawrence Berkley Laboratory in United States of America (USA) [ea76, Lof56] and Synchrophasotron proton synchrotron at Joint Institute of Nuclear Research (JINR) in Dubna Russia [ea80] in the 1970s both of which accelerated nuclei up to 2A GeV. In the late 1970s, came SATURNE, a facility of the French National Laboratory located in Saclay (France)

where heavy-ion collision experiments were conducted at different energies by colliding several nuclei [BRS92]. Another European facility which accelerated heavy-ion up to 2A[2] GeV was the SchwerIonen Synchroton at the Gesellschaft für Forschung SchwerIonen in Germany in 1975 [Kie88]. The Brookhaven National Laboratory in the USA operated the Alternating Gradient Synchroton (AGS) from 1987 to 1995 which accelerated heavy-ions up to 14.2 GeV center-of-mass energy [BL58]. The Super Proton Synchroton at CERN in Geneva provided 19 GeV oxygen and sulphur beams between 1986 and 1991 and then 17 GeV lead beams between 1994 and 2000 to the North Area 49 (NA49) experiment. The SPS also provided heavy ion beams to a host of other NA and West Area (WA) experiments. In the year 2000, the BNL started the operation of the Relativistic Heavy Ion Collider (RHIC) which supplied beams of up to 200 GeV/nucleon center-of-mass energy to experiments like STAR (currently taking data), PHENIX, PHOBOS and BRAHMS. The LHC started colliding lead-lead (Pb-Pb) ions in 2010 at unprecedented $\sqrt{s_{\mathrm{NN}}} =$ 2.76 TeV, the highest center-of-mass energy ever reached by a particle collider at the time. This makes the LHC the first to accelerate heavy-ions at TeV energies. The optimal deliverable energy for lead-lead collisions will reach 5.5 TeV center-of-mass energy. The ALICE detector [A$^+$08b] has been collecting heavy ion data since the beginning.

The above experiments were designed with the purpose of studying matter at extreme energy density and low net-baryon density. It is worth mentioning that there are other future experiments planned which are aimed at studying matter at high baryon chemical and low energy density. These include Nuclotron-based Ion Collider fAcility (NICA) in Dubna [col13] and the Compressed Baryonic Matter (CBM) at GSI/FAIR (Facility for Antiproton Ion Research) [Heu09].

A description of the stages of heavy ion collisions will be discussed in the following subsection.

1.3.1 Dynamical or Space-Time evolution of Heavy-Ion Collisions

Heavy ion collisions evolve in several stages from the initial scattering of partons through deconfinement to their confinement inside hadrons. Figure 1.5 depicts the evolution of heavy-ion collisions from the initial to the freeze out stage. Special relativity dictates that objects moving with speed closer to that of light experience relativistic effects, in this case length contraction is of interest. Hence, these relativistic collisions involve Lorentz contracted heavy ions (Pb, Au, etc.) with the longitudinal profile 100 times smaller than the transverse one. This initial stage of the collision involves heavy ions composed mostly of dense and weakly coupled colour fields (gluons) that carry large transverse momenta. This is what is known as the **Color Glass Condensate** [ADN11], which dominates the wave

[2] A - is the atomic mass

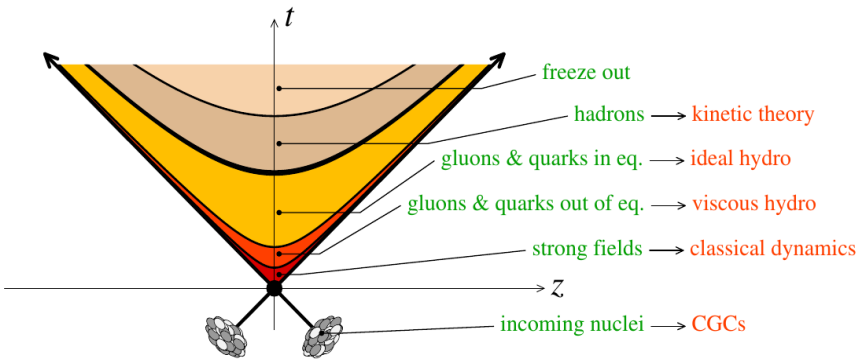

Figure 1.5: Depiction of various stages of the evolution of heavy ion collision in the plane of time (t) and collision axis (z). Proper time $\tau = \sqrt{t^2 - z^2}$ is constant along the hyperbolic lines separating different stages [Ian14].

function of hadrons at ultra-relativistic energies. The increased density of gluons is described by **Balitsky-Fadin-Kuraev-Lipatov (BFKL)** evolution as seen in Figure 1.6 [Lip03]. This is one description of the initial stages of a heavy-ion collisions. The dilute proton structure as seen in Figure 1.6 is described by the **Dokshitzer-Gribov-Lipatov-Altarelli-Parisi (DGLAP)** evolution equation [Lip03]. This can be achieved by fixing the Bjorken-x[3] and increasing the momentum transfer (this is like increasing camera resolution power).

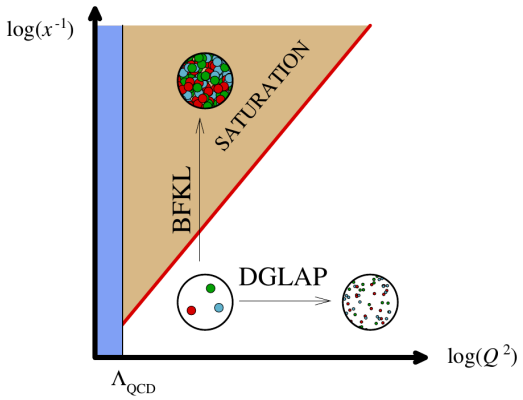

Figure 1.6: Parton evolution in QCD [BNV10].

The next stage happens at $\tau \sim 0$ fm/c when the two heavy ions cross. This is the time during which processes characterised by large momentum transfer ($Q \gtrsim 10$ GeV/c) occur. These interactions are responsible for the production of hard probes, these are particles which are produced from large energy transfers of the order of Q. These include, **electroweak bosons** ($W^{\pm}$ and Z^0), heavy quarks (charm and beauty), jets, direct photons and dilepton pairs. Preceding hard scattering processes are semi-hard processes which occur at time scales of $\tau \sim 0.2$ fm/c involving momentum transfer around the onset of perturbative QCD ($Q \sim 1$ GeV/c). It is at this stage that partons are liberated from the color condensate [ADN11] to form a dense non-equilibrium state of matter. Hadrons seen in the detectors are formed through fragmentation or hadronisation[4] of these initial-state partons (mostly gluons). If these liberated partons interact weakly they will evolve independently to form hadrons which is the phenomenon seen in proton–proton collisions, but the

[3] Bjorken-x - is the fraction of momentum carried by a parton relative to the nucleon.
[4] Hadronisation refer to the mechanism by which quarks and gluons produced in hard processes form hadrons that are observed in the final state.

results of heavy-ion collisions shows collective effects, for example "flow" [Ada07]. These interactions are characteristic of fast thermalisation time ($\tau \sim 1$ fm/c), the partons ought to redistribute their energy within a short time space to compete with fast medium expansion associated with weakly interacting partons. Thus, the formed medium is said to be strongly coupled to account for the fast thermalisation time. If enough energy is redistributed into the collision volume during the thermalisation process the high temperature state of QCD known as QGP is formed. The expansion and cooling of this medium is space-time dependent, that is, equilibrium is only reached locally. Eventually, hadronisation occurs as temperatures reach orders of T_c where the onset of deconfinement is expected. In the time range between 10 and 20 fm/c there exist what is known as a *hot hadron gas*. Above $\tau \sim 20$ fm/c hadrons stop interacting inelastically, that is, the collision length becomes smaller than the interaction rate. This state of the evolution is known as *chemical freeze out* and it occurs at $T_c \simeq 170$ MeV as seen at RHIC [CORW06]. The *kinetic freeze out* occurs at a later stage when the elastic interactions stops and the hadrons fly freely. From recent RHIC beam energy scans and ALICE measurements of T_c are ∼154 MeV and ∼165 MeV [Abe13].

One of the important ingredients in the study of heavy ion collisions is the collision geometry which is used to determine the event activity or **centrality** (explained in the next sub-section).

1.3.2 Collision geometry

Since a nucleus is an extended object, nucleus–nucleus and proton–nucleus collisions can be classified into centrality classes, that is, whether the collision is head–on or the nuclei just graze each other. Collisions can either be peripheral, semi–central or central. This classification is based on the impact parameter (b) or by the number of nucleons participating in the collision or the number of binary collisions. Considering nuclei sizes it might seem inconceivable to estimate these parameters, but there exist theoretical techniques based on the **Glauber Model** which use experimental data. Roy Glauber employed the quantum mechanical scattering theory to composite systems to describe some non-trivial effects seen in the cross sections of proton–nucleus and nucleus–nucleus collisions [MRSS07, Cha14]. The technique's first taste of triumph was in the description of proton scattering on a deutrons and other larger nuclei. Glauber models use experimental inputs, the main one being the nucleon density in the nucleus which is described by a Fermi-type distribution

$$\rho(r) = \rho_0 \cdot \frac{1 + w \cdot (r/R)^2}{1 + \exp(\frac{r-R}{a})} \tag{1.7}$$

with ρ_0 as the charge density, R the nuclear radius and a is the skin depth and w is the eccentricity. The only energy dependent parameter entering these calculations

is the measured nucleus-nucleus inelastic cross section, $\sigma_{NN}^{inelastic}$, which increases with energy. Diffractive and elastic cross sections are generally left out of these calculations [MRSS07]. The main aim of Glauber calculations is to extract the average number of nucleons participating in a collision, N_{part}, and the number of binary collision N_{coll}. These are used to classify collisions according to their centrality. There are two approaches employed in these calculations, **Glauber Monte Carlo** and **Optical Limit Approximation**, which both treat the collision of two nuclei as an interaction of constituent nucleons.

Optical Limit Approximation

This approach is based on the assumption that at relativistic speed the nucleons are traveling in straight trajectories and remain undeflected after the nuclei overlap. This allows to arrive at simple analytic expressions for nucleus–nucleus collision interaction cross section and the number of nucleon collisions in terms of nucleon–nucleon cross section. Figure 1.7 shows the collision geometry in view of Optical Limit Approximation approach. The collision is depicted in to axes, the beam line usually taken as the z-axis and the axis along the impact parameter $\vec{b}$. The probability per unit transverse area for a given nucleon to be in the collision volume is described by the overlap function $\hat{T}_A(\vec{b}) = \int \hat{\rho}_A(\vec{s}, z_A) dz_A$, where $\hat{\rho}_A(\vec{s}, z_A)$ is the probability of finding a nucleon at the point $(\vec{s}, z_A)$. The same holds for nucleus B. The joint probability is given by

$$\hat{T}_{AB}(\vec{b}) = \int \hat{T}_A(\vec{s}) \hat{T}_B(\vec{s} - \vec{b}) d^2 s, \tag{1.8}$$

which is an effective overlap area. The product $\hat{T}_{AB}(\vec{b}) \cdot \sigma_{NN}^{inelastic}$ gives the probability of an interaction. The probability to have n collisions out of possible AB is given by the Binomial distribution

$$\mathcal{P}(n, \vec{b}) = C_n^{AB} [\hat{T}_{AB} \sigma_{NN}^{inelastic}]^n [1 - \hat{T}_{AB} \sigma_{NN}^{inelastic}]^{AB-n} \tag{1.9}$$

where the first term is the total number of combinations of n out of AB, the second term in the probability to have n and the third is the probability to have $AB - n$ misses. Using the mean of a binomial the number of collisions is given by

$$N_{coll}(b) = \sum_{n=1}^{AB} n \mathcal{P}(n, \vec{b}), \tag{1.10}$$

whereas the number of participating nucleons is given by

$$N_{part}(b) = A \sigma_{inelastic}^{B} + B \sigma_{inelastic}^{A} \tag{1.11}$$

This approximation treats the nuclei as constituting continuously distributed nucleons

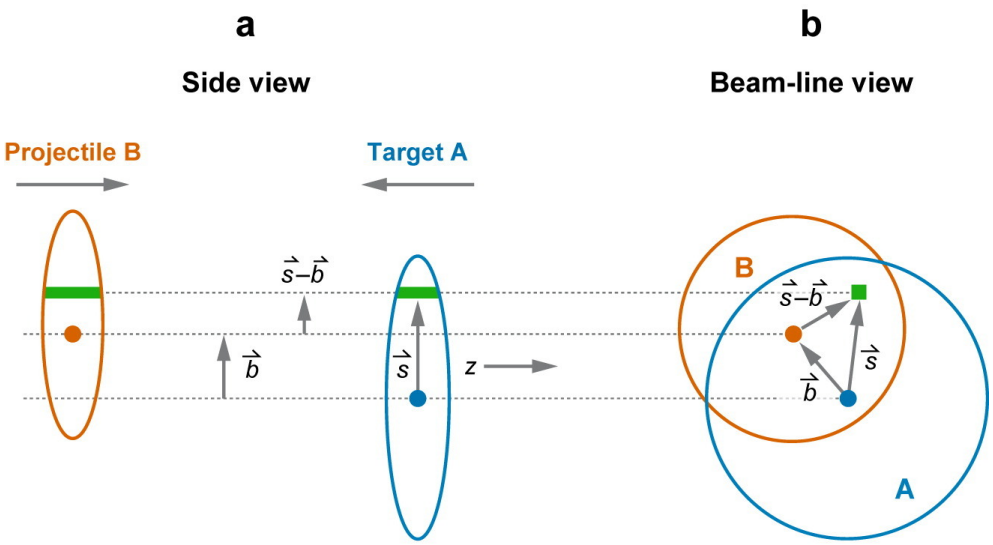

Figure 1.7: Collision geometry in a context of the Optical Glauber approach (Optical Limit Approximation) [MRSS07].

and therefore does not identify the nucleon's spatial position which is the case for the Glauber Monte Carlo approach [MRSS07].

Glauber Monte Carlo

In this approach the nucleus–nucleus collision is treated as a sequence of independent nucleon–nucleon collisions in which the nucleons have straight line trajectories and their inelastic cross sections is independent of previous interactions. In contrast to the Optical Limit approach, a smooth distribution or density of

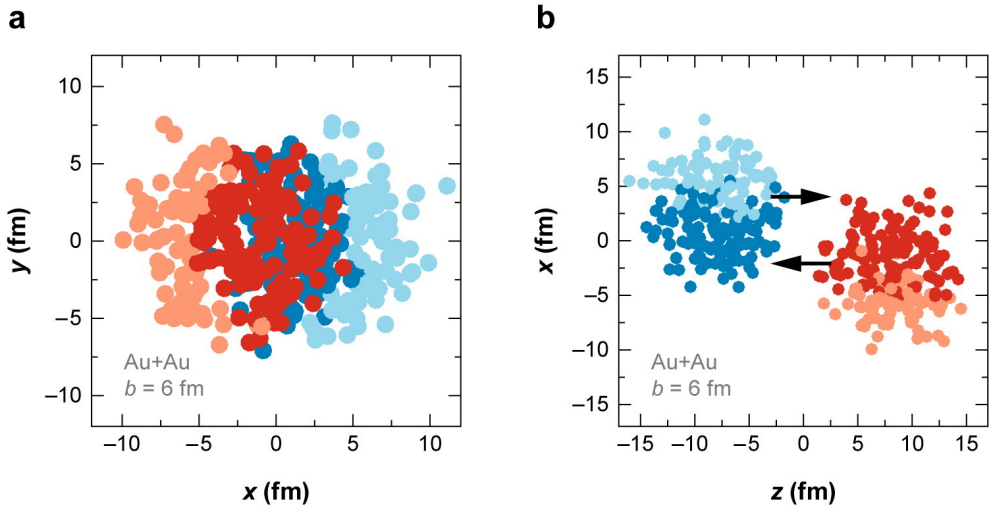

Figure 1.8: Glauber Monte Carlo event [MRSS07]. On the left and right is the event in the $x-y$ and $x-z$ plane.

nucleons is not assumed but rather the nucleons in each nucleus (target and projectile) are arranged in three dimensional spatial coordinates according to their respective nuclear densities. The spatial coordinates vary event by event. Figure 1.8 is an example of such Glauber Monte Carlo event, where the darker colours are nucleons participating in the collision course. Impact parameter b is then drawn randomly from the distribution $d\sigma/db = 2\pi b$. The next step is to test if the collision occurred or not, which is the basis of the Monte Carlo approach. The nucleon–nucleon collision can only take place if

$$d \leq \sqrt{\sigma_{NN}^{inelastic}/\pi}, \tag{1.12}$$

where d is orthonormal to the plane perpendicular to the beam axis. Of course the idea is to relate these beautiful approaches to some experimental observable in order to extract N_{coll} and N_{part}.

1.3.3 Glauber models meet experiments

In experiments N_{coll} and N_{part} are extracted as mean values in classes of event activity. Event activity is determined by measuring the charge particle multiplicity (N_{ch}) per event at both mid ($|\eta| < 1$) and forward (close to the beam line) rapidity. η is an experimental variable which is related to the polar angle (θ) by the equation

$$\eta = -\ln[\tan\frac{\theta}{2}]. \tag{1.13}$$

The definition of centrality classes is based on the premise that the impact parameter b is monotonically dependent on the particle multiplicity seen at mid–rapidity and forward–rapidity. Peripheral events (large b) are characteristic of high and low particle multiplicity at both forward and middle rapidity, respectively. The opposite is expected for the most central events. The classification is done by defining within the same pseudorapidity interval the mean values of N_{coll} and N_{part} in the measured and calculated distribution of dN_{ch}/dN_{event}. Centrality is defined by dividing the dN_{ch}/dN_{event} distribution in percentiles, $0-5\%$ (most central) and $80-100\%$ (most peripheral) as seen in Figure 1.9.
Now that general concepts necessary to study electroweak bosons in heavy-ion collisions have been described, the focus of our attention is turned to our protagonists – electroweak bosons ($W^{\pm}$and Z^0).

1.4 Electroweak bosons

$W^{\pm}$ and Z^0 bosons are massive mediators of the electroweak theory. These particles are one of the successes of the Weinberg-Glashow-Salam model, which predicted their

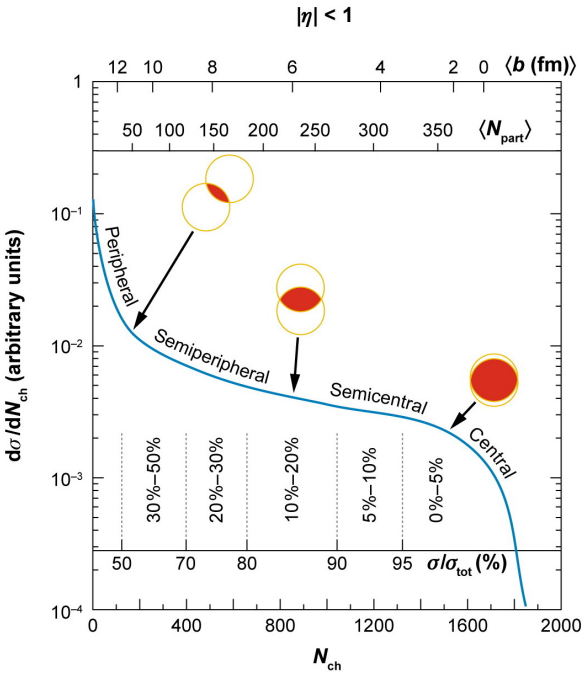

Figure 1.9: An illustrated example of Glauber calculated quantities b and N_{part} correlated with an experimental observable N_{ch} [MRSS07].

existence. The W-boson mass was later measured in 1983 in proton-antiproton ($p\bar{p}$) collisions at the CERN Super Proton Synchroton (SPS) by the UA1 collaboration to be 81^{+5}_{-5} GeV/c^2 [A$^+$83a] and by the UA2 collaboration to be 80^{+10}_{-5} GeV/c^2 [B$^+$83b]. The Z^0 mass was later reported by the two collaboration to be 95.2 ± 2.5 GeV/c^2 [A$^+$83b] and $91.9 \pm 1.3 \pm 1.4$ GeV/c^2 [B$^+$83a] by UA1 and UA2 collaborations, respectively. Subsequently, there was a plethora of measurements of Z^0 boson mass by the Collider Detector at Fermilab (CDF) [Abe89] and MARK II [AAA$^+$89] at the Fermilab Tevatron and Standford Linear Accelerator in electron-positron collisions, respectively. These measurements reduced substantially the systematic uncertainty. The CDF and D0 also reported the measurements of W-boson mass in [Abb98] and [A$^+$01, A$^+$12c]. The precision measurements of W$^+$ and W$^-$ masses were only done later at Large Electron-Positron 2 (LEP2) collider [A$^+$06] and later at the Tevatron [Gro09].
The current global average of masses of these vector bosons together with their respective branching ratio are reported in the Particle Data Group booklet [ea14]. Their masses are:

$$M_{\mathrm{W}} = 80.385 \ \pm \ 0.0150 \ \mathrm{GeV/c^2}$$
$$M_{\mathrm{Z^0}} = 91.187 \ \pm \ 0.0021 \ \mathrm{GeV/c^2}.$$

The masses of these weakly-interacting particles are parameters of the Standard Model hence they have been extensively studied. Their production cross sections are known with precision and thus they are considered as Standard Model benchmarks [CdV09]. Details about the productions and decays are described next.

1.4.1 Production of $W^{\pm}$ and Z^0 bosons

The production of the standard model massive vector bosons is mainly dominated by quark and anti-quark annihilation. $W^{\pm}$ production mixes quark flavours whereas the Z^0 production involves the same flavour of quarks. Figure 1.10 shows their leading order production. The next to leading order (NLO) production processes involve

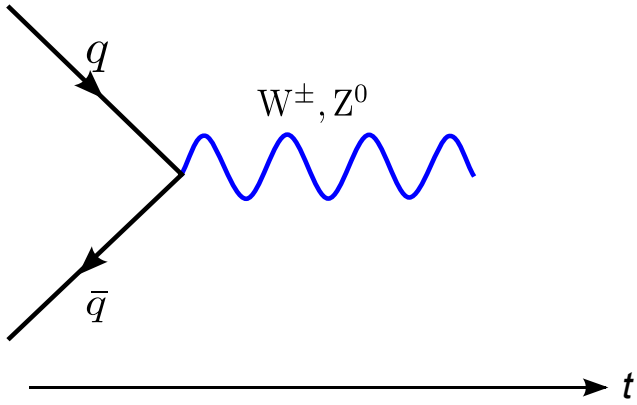

Figure 1.10: Feynman diagram illustration of a leading order (LO) production of $W^{\pm}$ and Z^0. This is, $u\bar{d} \to W^+$, $d\bar{u} \to W^-$ and $u\bar{u}, d\bar{d} \to Z^0$. t represent the time axis.

diagrams with QCD and QED radiation (gluon (g) and photon (γ) respectively) in either the initial state or the final state.

$$qg \to W^{\pm}, Z^0 + q \qquad q\bar{q} \to W^{\pm}, Z^0 + g$$
$$q\gamma \to W^{\pm}, Z^0 + q \qquad q\bar{q} \to W^{\pm}, Z^0 + \gamma$$

The Feynman diagram illustrations of these NLO production processes are depicted in Figure 1.11. The LO production processes dominate the total production cross section of $W^{\pm}$ and Z^0. Figure 1.12 shows the flavour decomposition of their leading order production. In pp collisions at 7 TeV center of mass energy the valence and sea quark annihilation constitute between 80% to 90% of $W^{\pm}$ production and about 40% of Z^0 production [MRST00]. The production cross-section has a dependency on mass and quark generation. It is easier to produce light sea quarks ($\bar{u}$, $\bar{u}$ and $s(\bar{s})$) than the heavier ones (c, b, t, $\bar{c}$, $\bar{d}$ and $\bar{t}$) and the transition probability decreases across quark generations. The transition probability is described by the Cabbibo–Kobayashi–Maskawa matrix. The production cross-section of these vector bosons is sensitive to the quark content of the hadrons. It is this property which makes $W^{\pm}$ and Z^0 good probes to constraint Parton Distribution Functions (PDFs) – $f(x, Q)$. PDFs are probability distributions in terms of the fraction of hadron momentum (x) carried by

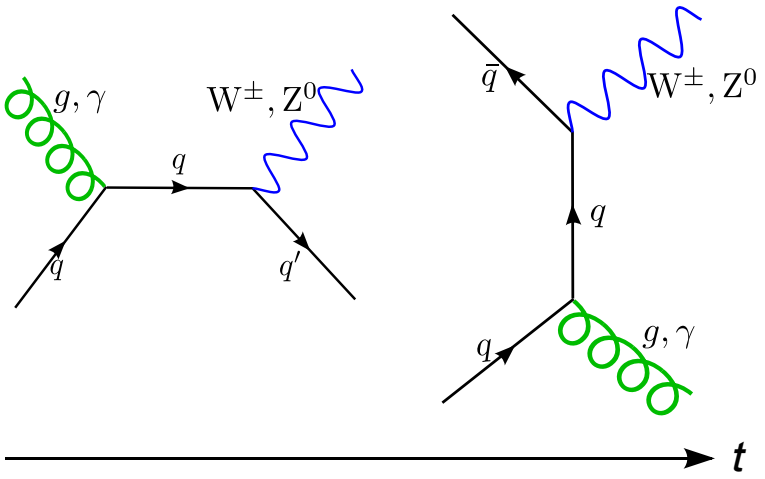

Figure 1.11: Next to leading order (NLO) production processes of $\mathrm{W}^{\pm}$ and Z^0. t is the time axis.

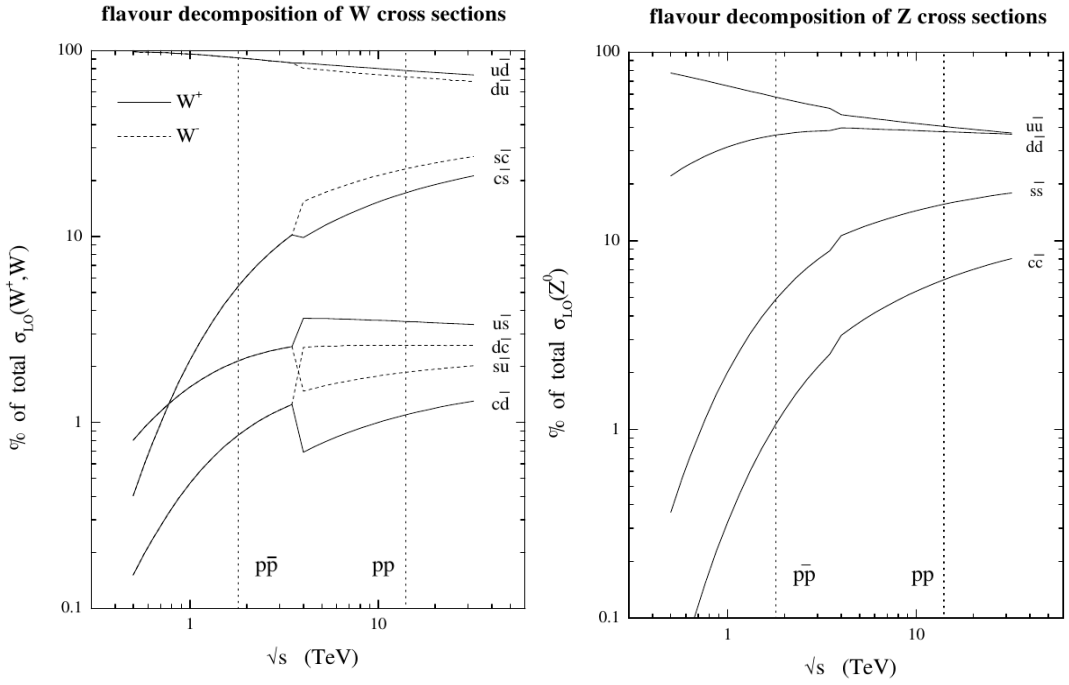

Figure 1.12: Flavour decomposition of the production cross-section of $\mathrm{W}^{\pm}$ and Z^0 at leading order showing different contribution [MRST00].

each parton [ea14] at a certain virtual scale (Q). In order to form a particle of mass M_X the energy transfer must be equal to Q, that is

$$Q \approx \sqrt{x_a \cdot x_b \cdot s} \approx M_X,$$

where x_a and x_b are fractions of momentum of hadron A and B carried by partons a and b respectively, $\sqrt{s}$ is the center of mass energy and M_X is the mass of particle $X = \{\mathrm{W}^{\pm}, \mathrm{Z}^0\}$. A schematic representation of this process is shown in Figure 1.13. Drell and Yan postulated that the cross section of a hard scattering processes can be

divided into a partonic part which is process dependent cross section calculable in pQCD and the global part which is given by PDFs [ea14]. The production cross section

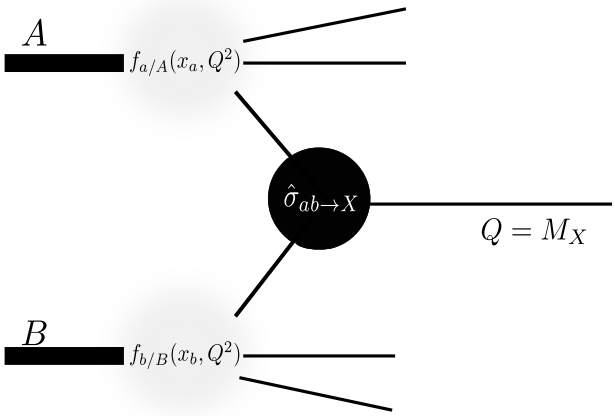

Figure 1.13: Schematic illustration of particle production in hadron collisions. $f_{a/A}(x_a, Q^2)$ and $f_{b/B}(x_b, Q^2)$ are PDFs and $\hat{\sigma}_{ab\to X}$ is the partonic cross section.

of X is thus a convolution of PDFs and the partonic cross section as seen below,

$$\sigma_{AB\to X} = \sum_p \int dx_a dx_b f_{a/A}(x_a, Q^2) f_{b/B}(x_b, Q^2) \hat{\sigma}_{ab\to X} \tag{1.14}$$

where p is an index running over all partons. The perturbative nature of the partonic cross section makes it accessible in different orders of the coupling constant,

$$\hat{\sigma}_{ab\to X} = [\hat{\sigma}_{LO} + \alpha_s(\mu_R^2)\hat{\sigma}_{NLO} + \alpha_s^2(\mu_R^2)\hat{\sigma}_{NNLO} + \cdots]_{ab\to X}, \tag{1.15}$$

where $\alpha_s(\mu_R^2)$ is the strong coupling constant at a certain renormalization scale μ_R.

PDFs contain non-perturbative physics hence they are not accessible in the framework of pQCD and only obtainable from experimental data. There are several collaborations (CTEQ, MSTW [MSTW09], NNPDF [BBC+13], etc.) which provide PDFs by fits to experimental data, ranging from fixed target and deep inelastic scattering experiments, to Drell-Yan and jet productions. These fits are evolved from lower scales (Q_0^2) to higher scales where they are used to make predictions and compared to data. Including more and more data into the fits constraints the PDFs. The differences between these PDFs are in the treatment of uncertainties, heavy quarks and the choice of input data and cuts. A detailed recipe is described in [FW13]. Shown in Figure 1.14 is the kinematic reach of the current input data of the NNPDF2.3 PDFs in the $Q^2 - x$ plane. This PDF includes recent vector boson and jets data from different LHC experiments. Figure 1.15 is evidence of the fact that the structure of the proton is dependent on the virtuality with which it is probed.

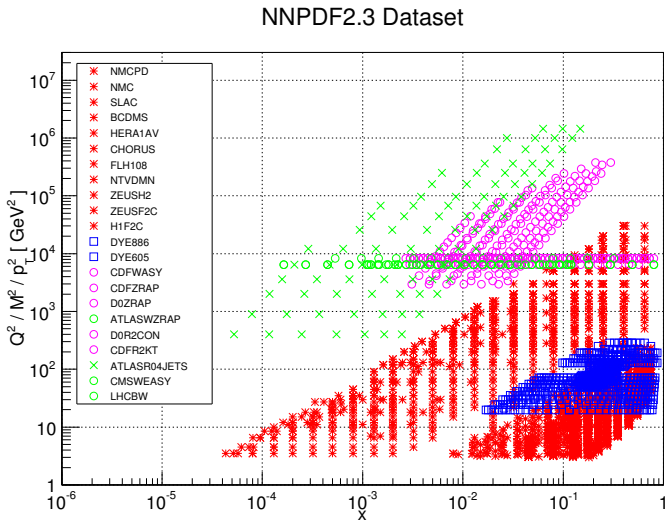

Figure 1.14: The kinematic reach of the experimental input data used for NNPDF2.3 PDF determination. The LHC data from ATLAS, CMS and LHCb collaborations are shown in green [BBC+13].

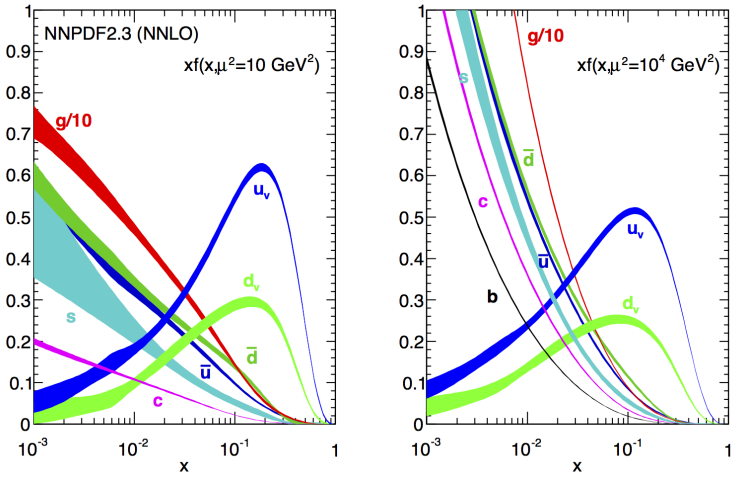

Figure 1.15: NNLO proton PDFs from NNPDF collaboration at different scales $\mu \equiv Q$. The shaded bands represent the one standard deviation around the most probable value. On the y-axis is $x \cdot f(x, \mu)$ [BBC+13].

1.4.2 $W^{\pm}$ and Z^0 bosons in pp collisions

Prior to the LHC and the recent RHIC results [A+11c, dFV10], the production cross sections of the standard model vector bosons were accessible in proton – anti-proton and electron – positron (e^-e^+) collisions. In proton – proton collisions (pp collisions) the dominant partonic production cross section of $W^{\pm}$ and Z^0 bosons is between valence – sea quarks quark scattering unlike in proton – anti-proton collisions ($p\bar{p}$ collisions) where it is amongst valence – valence quark annihilation. The valence – sea quark scattering means that the production involves the annihilation of quarks

with large and small x. The implication, for W and Z bosons is that they will be produced with a longitudinal boost in the quark direction, that is when looking at LO production involving light quarks. The measure of this longitudinal boost is known as rapidity which can also be given by

$$y_{\mathrm{W}^{\pm},\mathrm{Z}^0} = \frac{1}{2}\ln\left(\frac{x_a}{x_b}\right) \tag{1.16}$$

where $x_{a,b}$ is given by:

$$x_{a,b} = \frac{M_{\mathrm{W}^{\pm},Z^0}}{\sqrt{s}} e^{\pm y_{\mathrm{W}^{\pm},Z^0}} \tag{1.17}$$

with the rapidity $y_{\mathrm{W}^{\pm},Z^0}$, mass $M_{\mathrm{W}^{\pm},Z^0}$ of $\mathrm{W}^{\pm}$ and Z^0 and the center of mass energy $\sqrt{s}$. $x_{a,b}$ are fractions of momentum of two colliding protons A and B carried by partons a and b. It follows from this relation that the rapidity distributions of $\mathrm{W}^{\pm}$ and Z^0 bosons are sensitive to the quark and antiquark x–distributions [FW13]. Since the mass of the light quarks (u and d) are approximately equal in comparison to the center of mass energy, the production of the sea quarks ($\bar{u}$ and $\bar{d}$) is approximately the same. Taking into account this assumption and ignoring heavy quarks one arrives at

$$\mathcal{R}_{\mathrm{W}} = \frac{\sigma_{\mathrm{W}^+}}{\sigma_{\mathrm{W}^-}} \approx \frac{u(x_a)\bar{d}(x_b)}{\bar{u}(x_a)d(x_b)} \approx \frac{u(x_a)}{d(x_b)} \tag{1.18}$$

where $\mathcal{R}_{\mathrm{W}}$ is the ratio of W^+ and W^- cross sections (σ_{W^+} and σ_{W^-}) and $u(x_a)$, $\bar{u}(x_a)$, $d(x_a)$ and $\bar{d}(x_b)$ are PDFs of u and d quarks for valence and sea quarks. It follows from Equation 1.17 at large absolute $y_{\mathrm{W}^{\pm},Z^0}$ – where $x_a \sim 1$ and $x_b \ll 1$ corresponds to valence quarks and sea quarks respectively – that the production cross section of $\mathrm{W}^{\pm}$ and Z^0 is sensitive to the quark content of the proton as seen in Equation 1.18. Since valence quarks carry a large fraction of the proton mass, W^+ and W^- bosons are respectively produced with a boost in the direction of the u and d quarks. Thus the leading order production dominates the large rapidity production of $\mathrm{W}^{\pm}$ and Z^0. Figure 1.15 shows that from a large to low fraction of momentum $u(x)$ is larger than $d(x)$ indicating that $\sigma_{\mathrm{W}^+} > \sigma_{\mathrm{W}^-}$ [FW13].

W^+ and W^- bosons are respectively sensitive to the u and d quarks PDFs ($u(x)$, $d(x)$ and their anti-matter partner PDFs), hence the ratio of their production can provide a constraint to these PDFs [RZC+15]. The advantage of using the ratio in Equation 1.18 is that many sources of systematics such as the normalization cancel out [FW13]. The other useful quotient of the W^+ and W^- bosons cross section is the so called "charge asymmetry" computed as a function of rapidity written as:

$$\mathcal{A}(y)_W = \frac{\sigma_{\mathrm{W}^+} - \sigma_{\mathrm{W}^-}}{\sigma_{\mathrm{W}^+} + \sigma_{\mathrm{W}^-}} \approx \frac{u(x) - d(x)}{u(x) + d(x)}. \tag{1.19}$$

Equation 1.19 provides the strongest constraint on the light–flavour PDFs. Recent charge asymmetry measurements ($\mathrm{W}^{\pm} \to \ell^{\pm}\nu$ in proton – proton collisions at 7 TeV,

where $\ell^{\pm}$ stands for leptons, in this case, muons and electrons and ν are neutrinos) by the CMS collaboration [C^{+}12a] are included in NNPDF2.3 PDF, leading to sizable reductions in uncertainties [FW13]. This ratio is directly related to the difference in the u and d PDFs at large rapidity where $\sigma_{\mathrm{W}^+} > \sigma_{\mathrm{W}^-}$ as previously mentioned. Since one cannot measure $\mathrm{W}^{\pm}$ bosons directly one can only access them through their leptonic decay channel, so $\mathcal{A}(y)_W$ is, in actuality $\mathcal{A}(y)_{W\to\ell^{\pm}}$.

The electron – proton data from HERA constrain the low $x \sim 10^{-5}$ [Mar08] whereas precise measurements of vector bosons at the LHC in proton – proton collisions at 7 TeV center of mass provide an understanding of the PDFs in the kinematic region of $10^{-3} \lesssim x \lesssim 10^{-1}$.

In addition to the ratio of W^+ to W^- and $\mathcal{A}(y)_{W\to\ell^{\pm}}$ there is another quantity $\mathcal{R}_{\mathrm{W}^{\pm}/\mathrm{Z}^0}$ given by

$$\mathcal{R}_{\mathrm{W}^{\pm}/\mathrm{Z}^0} = \frac{\sigma_{\mathrm{W}^{\pm}}}{\sigma_{\mathrm{Z}^0}} \approx \frac{u(x)+d(x)}{0.29u(x)+0.37d(x)}. \tag{1.20}$$

The role of this ratio is discussed in [FW13, MRST00] which shows that the production of $\mathrm{W}^{\pm}$ and Z^0 are highly correlated.

1.4.3 $\mathrm{W}^{\pm}$ and Z^0 bosons in heavy-ion collisions

The predictions of the production cross sections of hard probes at different centre-of-mass energy available at RHIC and the LHC are shown in Figure 1.16. Since vector bosons and their leptonic final states interact weakly their production is expected not to be modified by the strongly-interacting medium formed in heavy ion collisions. It is this property which makes them excellent reference probes for medium–induced effects on particles like heavy quarks, J/ψ (and its family) and Υ (and its family), which are quantum mechanical bound states of heavy quarks whose interactions can be treated perturbatively and their wave functions are obtainable from Schrodinger's equation. If these bound states end up inside high-energy density conditions there is a statistical chance that some of them will melt or regenerate [A^{+}17b]. Since at the LHC heavy quarks are produced abundantly statistical recombination outweighs the suppression of their production. The disadvantage of using vector bosons as references is the mass difference between Υ ($M_{\Upsilon} = 9.46$ GeV/c^2) and the mass of the vector bosons and also the difference in the production mechanism [Vog01]. Nevertheless, vector bosons provide valuable probes to study cold nuclear matter (CNM) effects, the most dominant of which is the modification of quark distributions inside the nucleus at high Q. The modification of PDFs is often referred to as shadowing for partons with small momentum fraction ($x \lesssim 10^{-2}$) and anti-shadowing for partons with momentum fraction in the $5\times10^{-2} \lesssim x \lesssim 10^{-1}$ range (see Figure 1.17). In addition to modification of quark distributions there are other cold nuclear matter (CNM) effects, namely – isospin, shadowing, EMC and Fermi motion. The parametrization of cold nuclear

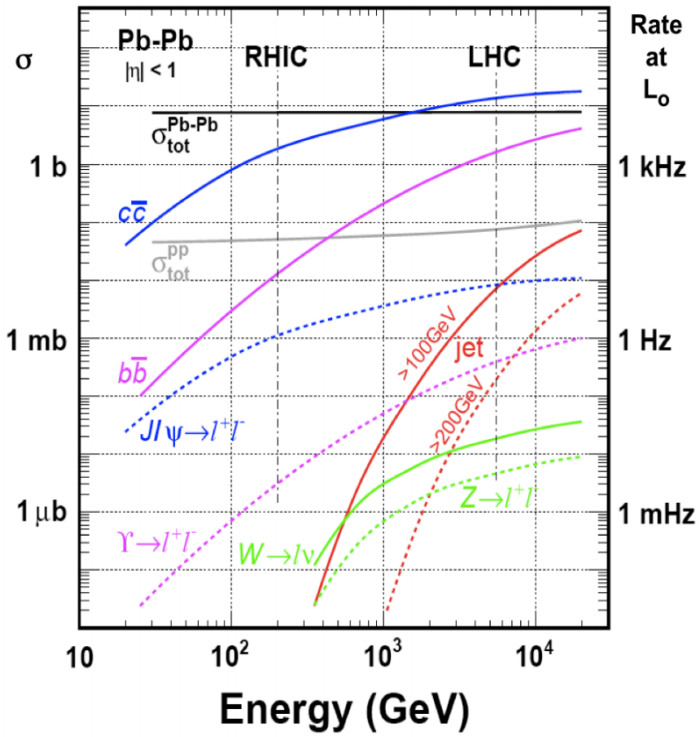

Figure 1.16: The predictions of the cross sections of hard probes at different centre-of-mass energies [Har15].

matter effects can be done phenomenologically by replacing the PDFs in perturbative QCD calculations with nuclear PDFs (nPDFs). Thus the modified PDFs (nPDFs) can be written as

$$f^A(x,Q^2) = \frac{Z}{A} f^{p,A}(x,Q^2) + \frac{N}{A} f^{n,A}(x,Q^2) \tag{1.21}$$

where Z and N are proton and neutron number, respectively, and A is the mass number; $f^{p,A}(x,Q^2)$ and $f^{n,A}(x,Q^2)$ are bound proton and neutron PDFs respectively [RZC+15] and $f^{n,A}(x,Q^2)$ is obtained from the proton PDF measurements by assuming flavor symmetry, this is

$$d^{n,A}(x) = u^{p,A}(x), \quad u^{n,A}(x) = d^{p,A}(x)$$

whereas for sea quarks they are the same. In parametrizations of nPDFs like DSSZ [dFSZS12] and EPS09 [EPS09] these assumptions enter their computation and thus the modifications are defined with the factor

$$R_f(x,Q^2) = \frac{f^{p,A}(x,Q^2)}{f^p(x,Q^2)} \tag{1.22}$$

where $f^p(x,Q^2)$ is the free proton PDF.

The lack of available experimental data leads to less precise knowledge of parton distributions in nuclei compared to free proton parton densities. The current state-of-the-art nPDFs are called EPS09 [EPS09] and they include data from deep inelastic scattering

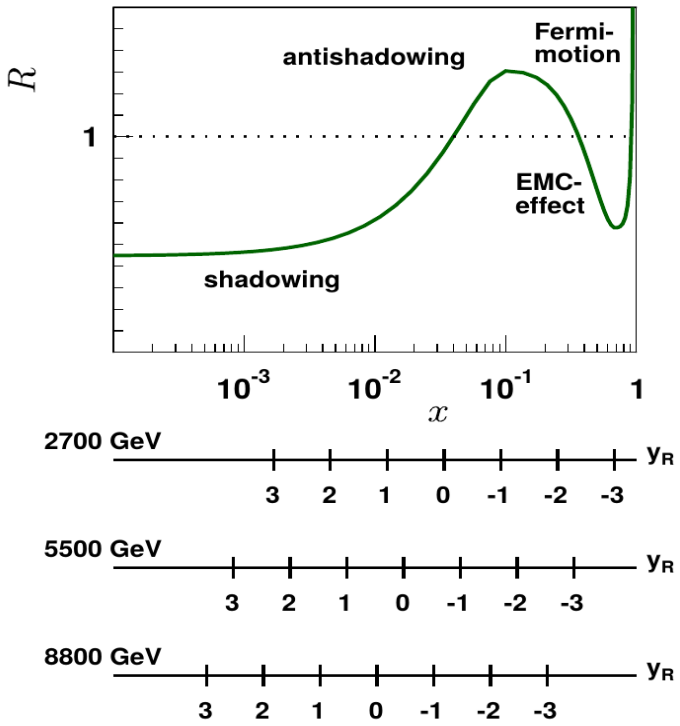

Figure 1.17: The cold nuclear modification factor ($R_f(x, Q^2)$) schematic representation as a function of Bjorken$-x$ showing different regions where CNM effects dominates. The rapidity reach of Z^0 at different LHC energies [PS11] is also shown.

(DIS) on nuclear targets, Drell-Yan dilepton production in proton-nucleus collisions and inclusive pion production in deutron-gold collisions [PS11]. The assumption which enters into this framework, for example, flavour decomposition which treats u and d the same are described in [PS11].

Although vector bosons $W^{\pm}$ and Z^0 are not sensitive to the medium formed in heavy ion collisions they might be affected by CNM effects and thus are sensitive to the initial state effects. The prior mentioned nucleon-structure dependent production mechanisms of these vector bosons make them good probes for CNM effects. The effects of initial state (CNM) on the production of vector bosons are well detailed in [PS11, Vog01, RZC+15]. The predictions of cross section as a function of rapidity are shown in Figure 1.18 with and without nuclear effects [PS11]. According to [PS11], due to the symmetry in Z-boson rapidity spectra without nuclear effects, it is easier to disentangle nuclear effects with Z-boson than with W-boson. The precise measurement of W-boson in heavy-ion collisions can lead to an improved determination of nPDFs and the asymmetries in the individual yields of W^+ and W^- should help with flavour decomposition of u and d quarks due to its isospin-dependent production mechanism. Shadowing refers to the modification or screening of the interaction of quarks inside the nucleus. The modification of the PDFs as described by Equation 1.23 might lead to the suppression or enhancement of the production of the intermediate vector boson

depending on the accessible Bjorken-x. Figure 1.18 shows the modifications of PDFs taking into account in the parametrization also other nuclear effects as described by [EPS09]. Figure 1.18 shows that both W^+ and W^- boson production at backward rapidity (negative rapidity) is enhanced whereas at forward rapidity is reduced although within large uncertainties.

If one considers only the isospin, the parton distribution functions can be described by the following simple relations

$$\begin{aligned} u^A(x) &\approx \frac{Z}{A}u(x) + \frac{N}{A}d(x) \\ d^A(x) &\approx \frac{Z}{A}d(x) + \frac{N}{A}u(x) \end{aligned} \tag{1.23}$$

where Z, N and A are proton, neutron and mass numbers respectively, and $u^A(x)$ and $d^A(x)$ are PDFs inside the nucleus. In order to access the extent of this effect the ratios of the modified PDFs ($u^A(x)$ and $d^A(x)$) to the free nucleon PDFs ($u(x)$ and $d(x)$) are computed in [RZC+15] to be

$$\begin{aligned} \frac{u^A(x)}{u(x)} &\approx \frac{Z-N}{A} + \frac{2N}{A}\frac{1}{1+\mathcal{A}(x)} \\ \frac{d^A(x)}{d(x)} &\approx \frac{Z-N}{A} + \frac{2N}{A}\frac{1}{1-\mathcal{A}(x)}. \end{aligned} \tag{1.24}$$

Figure 1.19 shows the isospin effects factor as a function of the $W^{\pm}$ bosons transverse momentum. Since $W^{\pm}$ and its leptonic decay products are not affected by the medium (hot nuclear matter or QGP) effects this isospin dependency translates to the nuclear modification factor of these vector bosons ($W^{\pm}$) as seen in Figure 1.20. In lead-lead collisions this factor is more enhanced due to the increasing u – d asymmetry [RZC+15]. The nuclear modification factor is defined as

$$R_{pA,AA}(p_{\mathrm{T}}) = \frac{d\sigma^{AA,pA}/dp_{\mathrm{T}}}{\langle N_{coll}\rangle d\sigma^{pp}/dp_{\mathrm{T}}} \tag{1.25}$$

where $d\sigma^{AA,pA}/dp_{\mathrm{T}}$ and $d\sigma^{pp}/dp_{\mathrm{T}}$ are differential cross sections of a vector boson as function of transverse momentum in heavy ion collisions and proton-proton collisions, respectively.

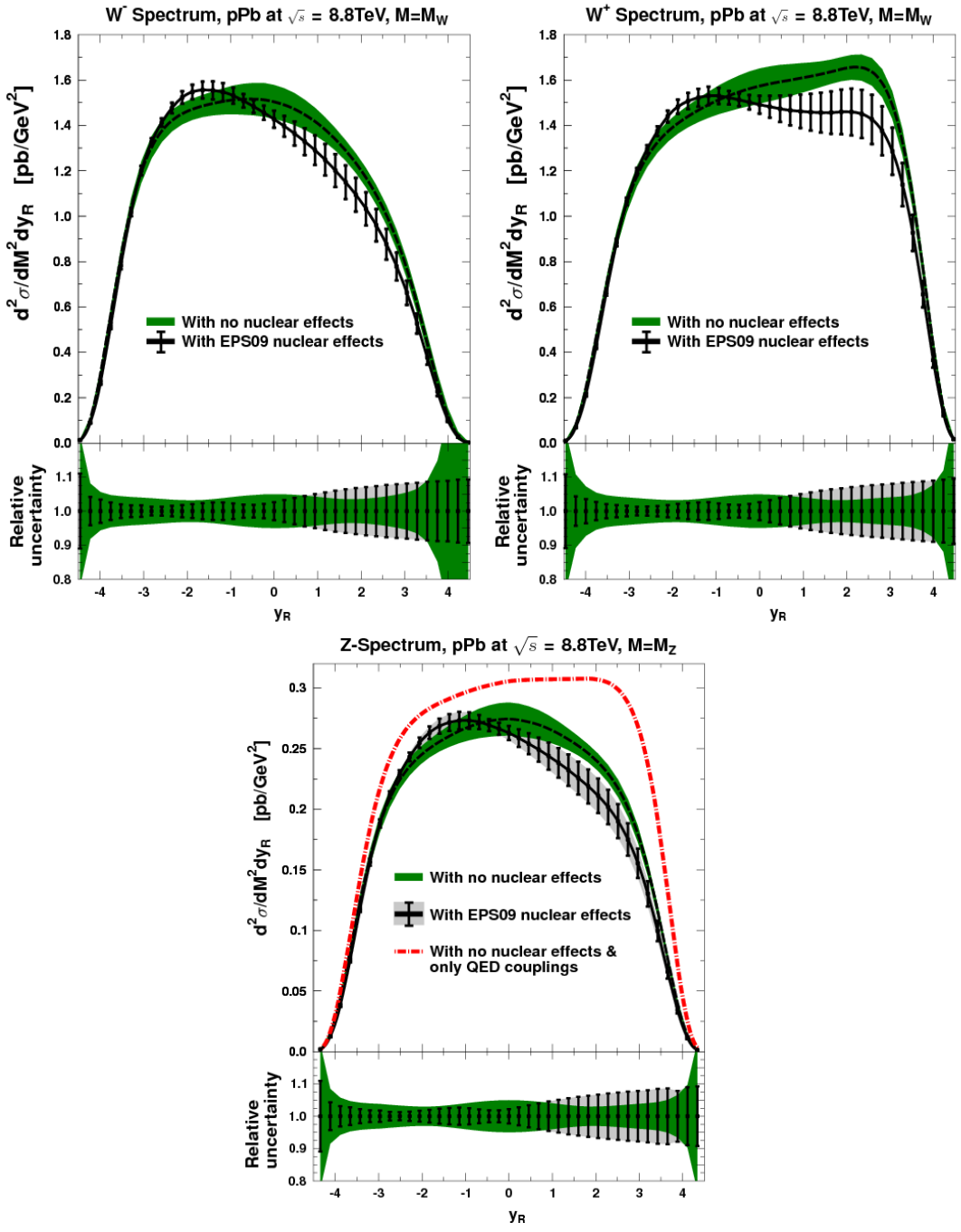

Figure 1.18: Theoretical predictions of cross-sections for $W^{\pm}(Z^0)$-production in pPb collisions at $\sqrt{s} = 8.8$ TeV at the W(Z)-pole, $M^2 = M^2_{W(Z))}$ per unit rapidity. The dashed line represents the central prediction calculated with CTEQ6.6 without applying the nuclear effects, and the green band is the uncertainty range derived from CTE6.6 PDFs. The solid line is the prediction computed by CTEQ6.6 applying the nuclear effects from EPS09. The error bars quantify the uncertainties resulting from the EPS09 uncertainty sets. The lower panels show the relative uncertainties with the same color codes. The red dashed-dotted curve is the prediction with only QED couplings multiplied by 1100 with no nuclear corrections to PDFs [PS11].

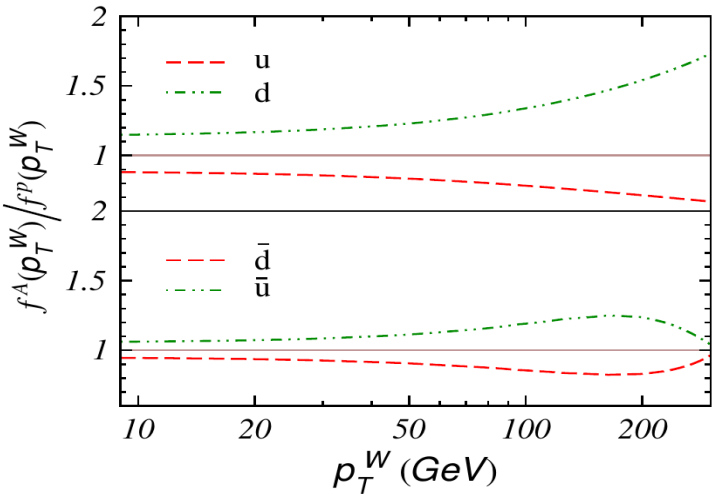

Figure 1.19: The flavor dependent nuclear isospin factor with the factorisation scale at the M_{W}-pole using MSTW NLO PPDFs [RZC+15].

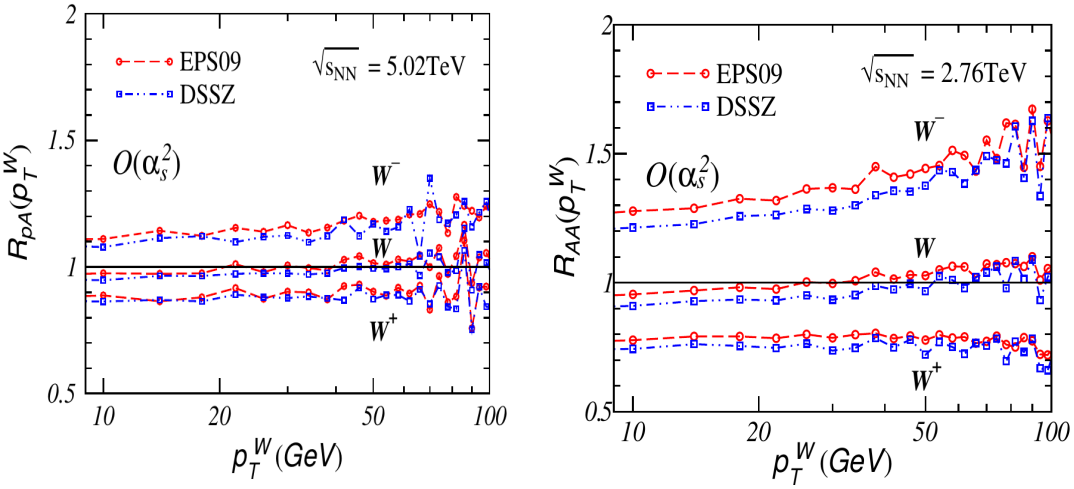

Figure 1.20: $\mathrm{W}^{\pm}$ bosons nuclear modification factor at NLO [RZC+15]. DSSZ [dFSZS12] is another parametrization of nPDFs. $O(\alpha_s^2)$ is the second order expansion of running strong coupling.

Observables

The production cross section is the main observable of any process. This is related to the production rate of a certain process. In this thesis, the production cross sections of vector bosons, $\mathrm{W}^{\pm}$ and Z^0, are determined and then compared with theoretical predictions in order to investigate the claims of shadowing and anti-shadowing [PS11]. Since the cross sections of W^+ and W^- bosons are sensitive to the quark content, they can therefore be used to contrain valence quarks PDFs. This observable however has considerable inherent uncertainties like normalization (and/or) and all other correlated systematics. It is worthwhile to find other observables where these uncertainties cancel out. Furthermore, the charge asymmetry ($\mathcal{A}_{\mathrm{W}}$) provides more sensitivity to the free

proton PDFs than $\mathcal{R}_{\mathrm{W},Z}$, this is attributed to the possible bias which comes from the assumption of flavour blindness assumed in EPS09 used in the calculations in [PS11]. Consequently, $\mathcal{A}_{\mathrm{W}}$ could prove useful in studying free proton PDFs in p–Pb provided the uncertainties are considerably reduced [PS11].

In Refs [V.15, PS11] the forward-to-backward ratio is described as a traditional way of probing the nuclear modifications of PDFs. This asymmetry is defined as,

$$R_{\mathrm{FB}} = \frac{\sigma^{y}_{\mathrm{W}^{\pm}/\mathrm{Z}^{0}}}{\sigma^{-y}_{\mathrm{W}^{\pm}/\mathrm{Z}^{0}}}. \tag{1.26}$$

In the backward $(-y)$ and forward (y) rapidity the cross sections respectively probe the small and large x.

1.4.4 Decays of $\mathrm{W}^{\pm}$ and Z^{0} bosons

Since $\mathrm{W}^{\pm}$ and Z^{0} bosons cannot be accessed directly they are measurable through their decay products. To access a clean sample of these intermediate bosons, weakly interacting final states are used, such as, leptonic final states are shown in Figure 1.21. Since the neutrino cannot be directly reconstructed it makes it difficult to obtain the fully reconstructed information about $\mathrm{W}^{\pm}$. Thus $\mathrm{W}^{\pm}$ bosons are measurable in semi-leptonic decay whereas Z^{0} is accessible through di-leptonic decays. The transverse momentum distribution of $\mathrm{W}^{\pm}$ bosons in the leptonic decay channel is a Jacobean peak at $p_{\mathrm{T}} \sim M_{W^{\pm}}/2$ and the invariant mass[5] of the two leptons from Z^{0} bosons forms a peak around $p_{\mathrm{T}} \sim M_{Z^{0}}$. In addition to the asymmetry between W^{+} and W^{-} from

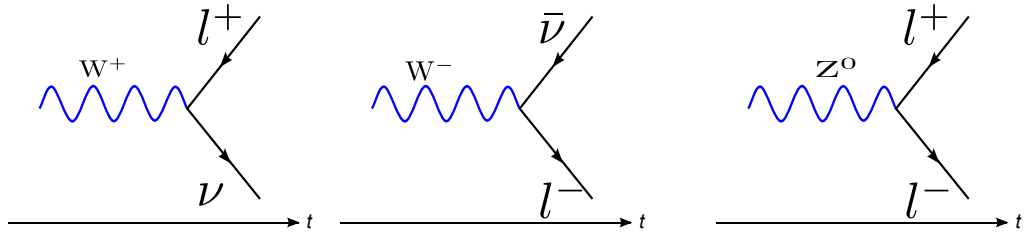

Figure 1.21: Decay of $\mathrm{W}^{\pm}$ and Z^{0}, where l^{-} and l^{+} are leptons whereas $\bar{\nu}$ and ν are neutrinos. t is the time axis.

the isospin effect an additional asymmetry is introduced due to the $V-A$ structure of the their coupling to leptons. $V-A$ refers to the vector – axial vector coupling of $\mathrm{W}^{\pm}$ to leptons which leads to an additional asymmetry. Figure 1.22 shows the schematic of the angular configurations of the W^{+} and W^{-} decay. W^{+} prefers to emit leptons in the opposite direction to the leading quark (valence quark), whereas W^{-} prefers to emit

[5] Invariant mass is a property of a particle which remains unchanged despite the frame of reference. It is defined as $m_{Z^{0}} = \sqrt{(E_{l^{+}} + E_{l^{-}})^{2} - (\mathbf{p}_{l^{+}} + \mathbf{p}_{l^{-}})^{2}}$, where $E_{l^{+}l^{-}}$ and $\mathbf{p}_{l^{+}l^{-}}$ are the energies and three momentums of the leptons

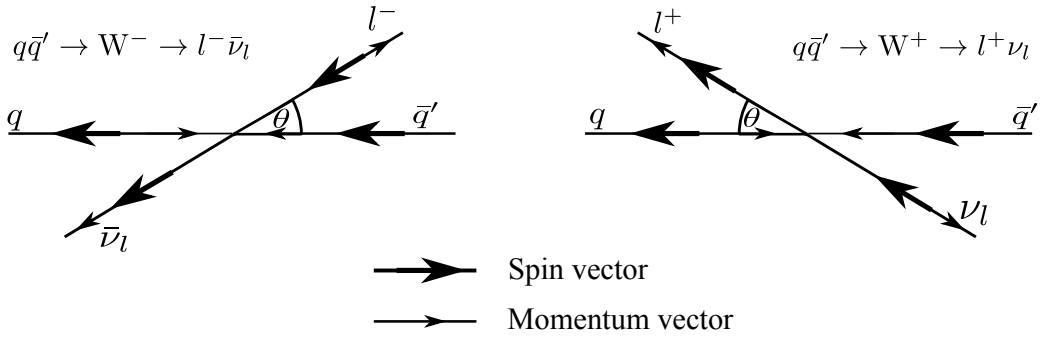

Figure 1.22: Diagram showing the preferred direction of leptons from $\mathrm{W}^{\pm}$ decay.

leptons in the direction of the leading quark. This makes the $\mathrm{W}^{\pm}$ decay anisotropic. As such, at large $\mathrm{W}^{\pm}$ rapidity, W^- decays to a l^- with large rapidity whereas W^+ decays to a l^+ with smaller rapidity due to the decay preference. It is worth mentioning that the cross section is thus maximum when the direction of the outgoing fermion is the same as the direction of the incoming one. Thus the cross section of W^- is greater than that of W^+ at larger rapidity. Shown in Figure 1.23 is the number of $\mathrm{W}^{\pm}$ as a function of rapidity showing the effect described above [CDV07]. The $\mathrm{W}^{\pm}$ and the lepton rapidity are symmetic around $y = 0$. Furthermore, at mid-rapidity vector bosons are formed by quarks with $x_a \sim x_b$ (quarks with almost the same momentum fraction). The modification of the W-boson production due to nuclear effects can amount to 15% [PS11]. Some of the past measurements of these vector bosons are

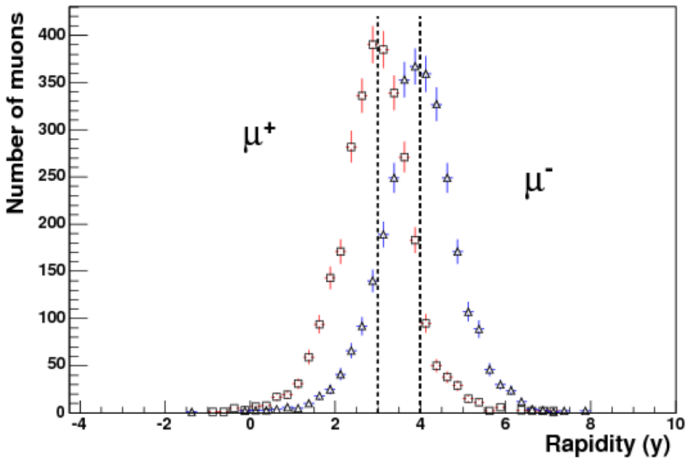

Figure 1.23: Shown here are rapidity distributions of muons from W^+ and W^- boson decays at $y_{\mathrm{W}} \in (3.0, 4.0)$ [CDV07].

summarized in the next subsection.

1.4.5 Overview of previous electroweak bosons measurements

The first measurements of inclusive cross-sections of $W^{\pm}$ were performed by the ATLAS [A+12a, A+11a], CMS [C+11, A+11a] and LHCb [Ae12] collaborations at rapidities $|\eta_e| < 2.47$ (excluding $1.37 < |\eta_e| < 1.52$) and $|\eta_\mu| < 2.4$, $|\eta_e| < 2.47$ (excluding $|\eta_e| < 2.5$) and $|\eta_\mu| < 2.1$, and $2.0 < \eta < 4.5$, respectively. Figure 1.24a shows one of the first measurement of the charge asymmetry as measured by ATLAS in proton-proton collisions at 7 TeV compared with MC@NLO predictions with different PDFs. The uncertainty on data is large enough such that the agreement with all predictions is within 2 sigma. The same goes for the CMS measurement of the same quantity shown in Figure 1.24b. Figure 1.25 shows the summary of all measurements

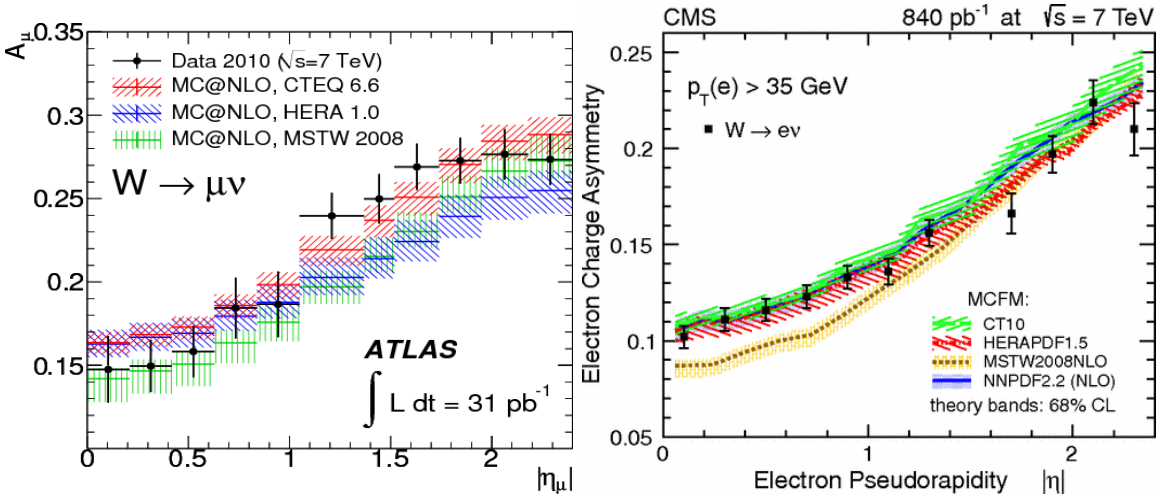

(a) (b)

Figure 1.24: (a) The muon charge asymmetry from W-boson decays in bins of absolute pseudorapidity. The kinematic requirements applied are $p_{\mathrm{T}}^{\mu} > 20$ GeV, $p_{\mathrm{T}}^{\nu} > 25$ GeV and $m_{\mathrm{T}} > 40$ GeV. The data points (shown with error bars including the statistical and systematic uncertainties) are compared to MC@NLO predictions with different PDF sets. The PDF uncertainty bands are obtained by summing quadrature the deviations of each of the PDF error sets [A+11a]. (b) Comparison of the measured electron asymmetry to the predictions of different PDF models for the electron $p_{\mathrm{T}} > 35$ GeV. The error bars include both statistical and systematic uncertainties. The data points are placed in the center of the $|\eta|$ bins. The PDF uncertainty bands are estimated using the PDF reweighting technique and correspond to a 68% confidence level [C+12a].

(W bosons cross section, charge ratios and asymmetry, ratio of the W- to Z-boson cross section) for W and Z bosons in LHCb acceptance. Theoretical predictions are all in agreement with the measurements within uncertainties. The large centre-of-mass and luminosities available at the LHC has made accessible the measurements of W and Z bosons production in proton-nucleus [A+15b, K+16, A+14a, K+15] and nucleus-nucleus [A+15a, A+13a, C+12b, C+15, CKe15, Ce12] collisions. Shown in Figure 1.26 are first measurements of W-boson in PbPb collisions at the LHC by CMS (left) [C+15]

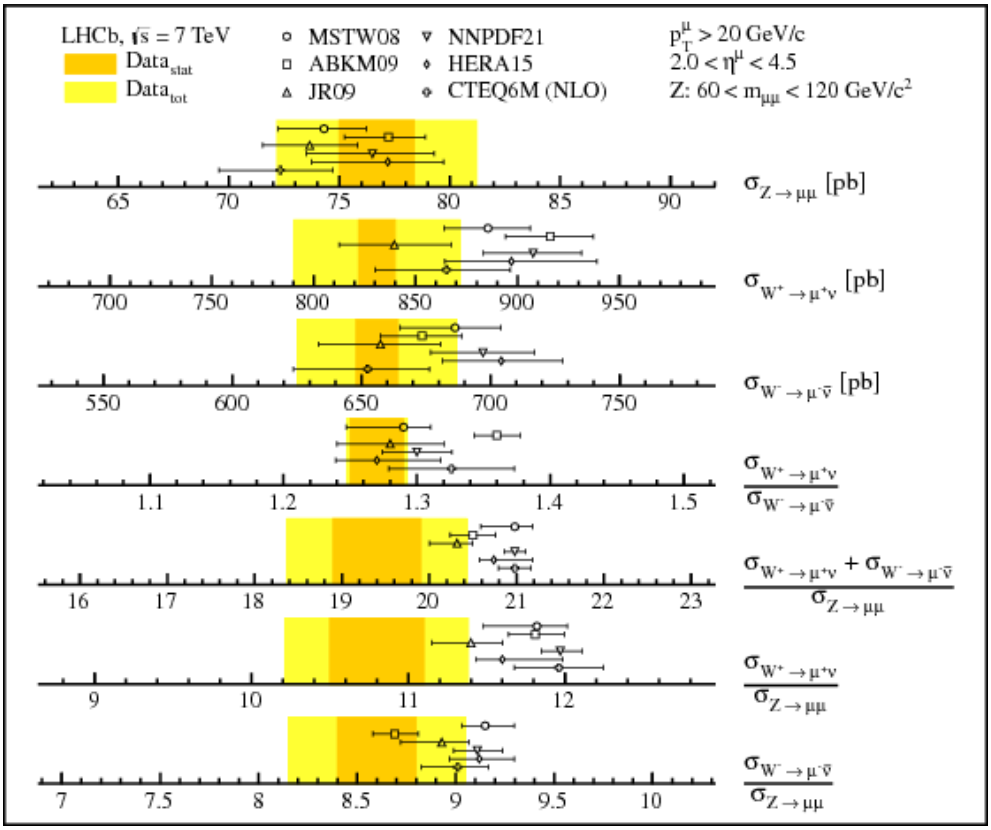

Figure 1.25: Measurements of the Z, W^+ and W^- cross-section and ratios, data are shown as bands which the statistical (dark shaded/orange) and total (light hatched/yellow) errors. The measurements are compared to NNLO and NLO predictions with different PDF sets for the proton, shown as points with error bars. The PDF uncertainty, evaluated at the 68% confidence level, and the theoretical uncertainties are added in quadrature to obtain the uncertainties of the predictions.

and ATLAS (right) [A$^+$15a]. In Figure 1.26 on the left is the centrality dependence of normalised $W \to \mu$ cross sections $(1/T_{AA})(N_W/\Delta\eta)$ in PbPb collisions, for all W candidates (red-filled points) and, separated by charge, W^+ (violet-filled squares) and W^- (green-filled stars). The open symbols at $N_{\text{part}} \approx 120$ represent the MB events. At $N_{\text{part}} = 2$, the corresponding cross sections are displayed for pp collisions divided by $\Delta\eta$, for the same $\sqrt{s}$. For clarity, both W^+ and W^- points are slightly shifted on the horizontal axis. The cross sections are given for the phase space region $|\eta^\mu| < 2.1$ and $p_T > 25$ GeV/c. The error bars represent the statistical, and the horizontal lines the systematic, uncertainties [C$^+$12b]. On the right plot of Figure 1.26 is W-boson production yield per binary collision as a function of the mean number of participants $\langle N_{\text{part}} \rangle$ for W^+, W^-, and $W^\pm$ bosons for combined muon and electron channels. The kinematic requirements are $p_T > 25$ GeV, $p_T^{\text{miss}} > 25$ GeV, $m_T > 40$ GeV, and $|\eta_l| < 2.5$. Statistical errors are shown as black bars, whereas bin–uncorrelated systematic and statistical uncertainties added in quadrature are shown as the filled error box. Bin–correlated uncertainties are shown as the hatched boxes and are offset for clarity. These include uncertainties from $\langle N_{\text{coll}} \rangle$. Also shown is an NLO QCD prediction [A$^+$15a].

The ALICE forward muon spectrometer covers a rapidity interval which allows for

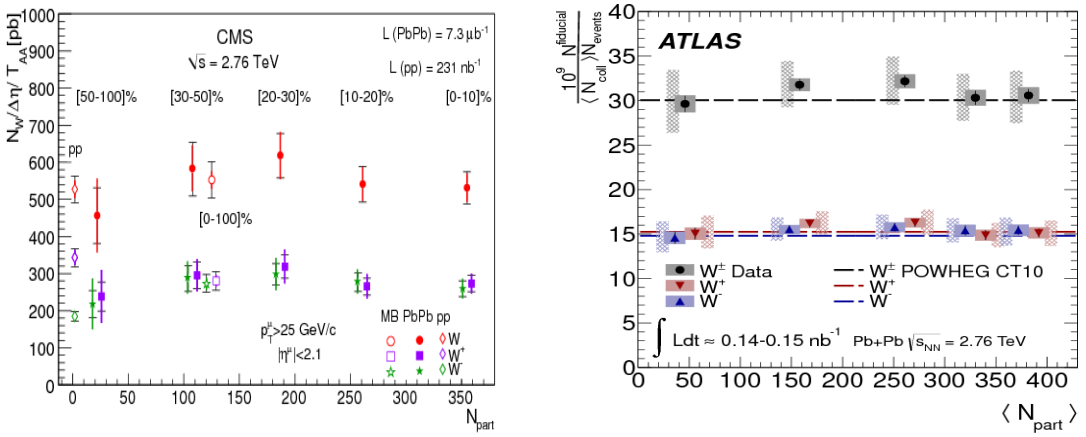

Figure 1.26: On the left and right are measurements of W-boson as function of $\langle N_{\text{part}} \rangle$ as performed by the CMS [C+12b] and ATLAS [A+15a] collaborations, respectively. See text for detailed explanation of the measurements.

complementary measurements to ATLAS and CMS and competitive measurement with the LHCb as shown in Figure 1.27. The advantage of the ALICE measurement is that it provides a measurement of W and Z bosons which covers a new kinematic reach at an order of $Q \sim 100$ GeV/c versus $x \sim 10^{-4}$. This allows to study nPDFs at these kinematic reaches which covers the $10^{-4} < x < 1$ at very high energy transfer Q.

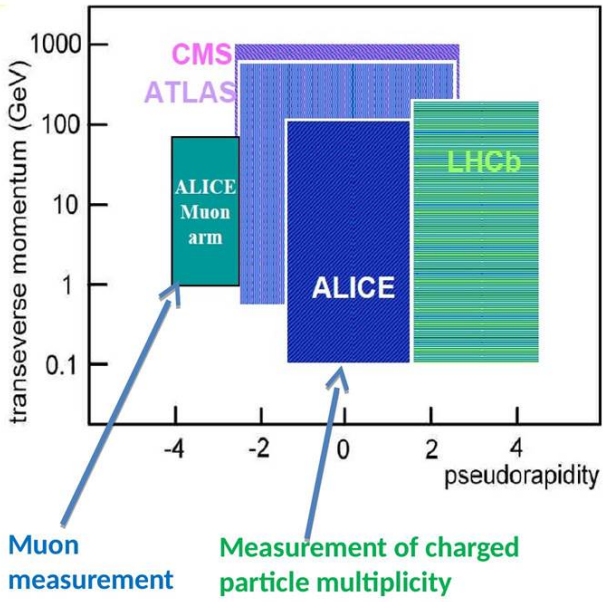

Figure 1.27: The kinematic reaches of different LHC experiments.

Part II

Experimental Methods

"It doesn't matter how beautiful your theory is, it doesn't matter how smart you are. If it doesn't agree with experiment, it's wrong."

Richard P. Feynman

2

Experimental Methodologies

This chapter presents a brief description of the Large Hadron Collider (LHC) accelerator complex with a special emphasis on "A Large Ion Collider Experiment" (ALICE). In the case of ALICE a focus will be on the Foward Muon Spectrometer since the data sample analysed in this work was collected with this particular detector. The ALICE offline and online frameworks are also described.

Contents

2.1 LHC accelerator complex

The historical review of particle physics shows a trend toward performing experiments at higher energies. The current accelerator facility with the highest energy ever reached in the world is the LHC [BCL+04, EB08] at the European Center for Nuclear Research (CERN) located on the Swiss-French border. The LHC is located in a 26.7 km tunnel which previously hosted the Large-Electron-Positron Collider (LEP). The CERN accelerator complex (see Figure 2.1) is a host of several accelerators acting as pre–accelerators for the LHC. The pre–acceleration is done in several stages, which

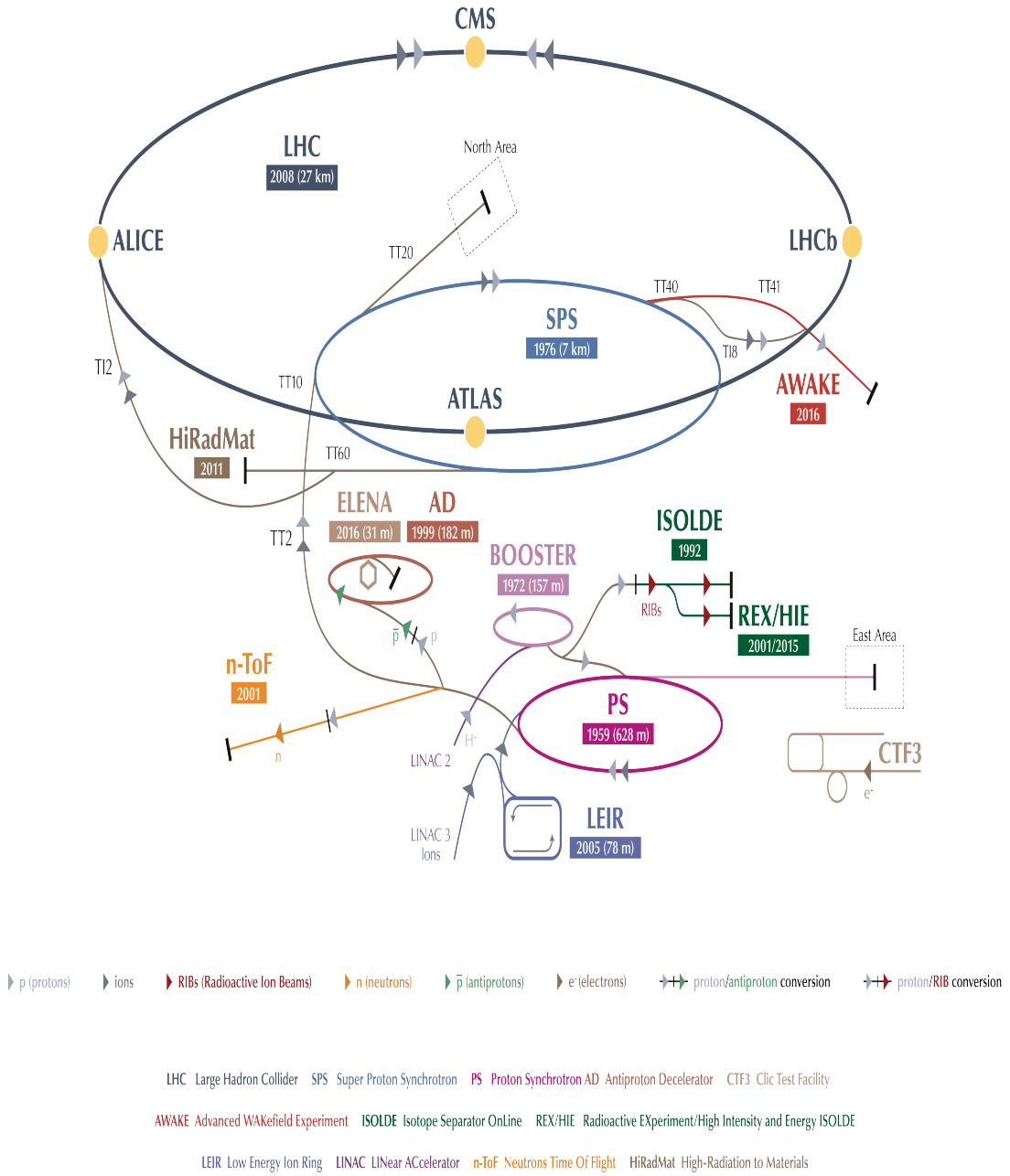

Figure 2.1: CERN accelerator complex [DM16].

is done differently for protons and lead ions. The acceleration of protons start from LINear ACcelerator (LINAC) 2 where protons are accelerated to a maximum energy of 50 MeV before being injected into the BOOSTER where the energy is raised up to 1.4 GeV before they are transferred to the proton synchrotron (PS). In the PS ramps up the energy of the protons to 25 GeV and then they are transferred to the Super Proton Synchrotron (SPS) for a penultimate pre–acceleration to 450 GeV before entering the LHC ring. In 2011 and 2012 the LHC accelerated protons to a maximum of 3500 GeV and 4000 GeV per beam attaining a center-of-mass energy of 7 TeV and 8 TeV, respectively. On the other hand, the acceleration of heavy ions involves more complicated procedures which include stripping of electrons in several stages, and thus the injection starts from a different accelerator known as the Low Energy Ion Ring (LEIR) [Cha04].

In addition to providing unprecedented energies, the LHC has a characteristic design to deliver high luminosities to the four main interaction points, discussed below. **A Large Ion Collider Experiment (ALICE)** is uniquely designed with the extreme conditions of heavy ion collisions in mind. The main physics goal is to study the QCD phase of matter formed at extreme energy densities associated with relativistic heavy collisions. This matter is a "stew" of quarks and gluons which mimics the state of matter that existed a few seconds after the Big Bang. ALICE studies the properties as well as the evolution of the QGP [A$^+$08b, Col95]. In the next section a detailed description of ALICE will be presented, focusing mostly on the Forward Muon Spectrometer.

A Toroidal LHC Apparatus (ATLAS) and **Compact Muon Spectrometer (CMS)** are multiple purpose detectors designed to study standard model physics [A$^+$08a, Col94, C$^+$08, Col97]. These detectors are also used to search for the evidence of physics beyond the standard model which includes tests of theories that postulate the existence of extra dimensions. These are theories concerned with the unification of the fundamental forces of nature.

Large Hadron Collider beauty experiment (LHCb) is dedicated to heavy flavour physics with a primary goal of looking for indirect evidence of new physics in Charge-Parity (CP) violation and rare decays of beauty and charm hadrons. This is mainly because recent heavy flavour results are consistent with Cabibbo-Kobayashi-Maskawa (CKM) mechanism and yet the amount of CP violation cannot account for matter–anitmatter inbalance in the universe [A$^+$08c, Col98].

2.2 A Large Ion Collider Experiment

ALICE is a heavy ion experiment designed with a purpose of studying and characterizing the strongly-interacting matter formed in heavy ion collisions. This characterization is done by studying several observable using final states particles such as electrons, hadrons, photons and muons. ALICE is capable of tracking charged particles in the

wide range of transverse momentum, $0.1 < p_{\mathrm{T}} < 100$ GeV/c and has an excellent ability to handle particle identification in a high multiplicity environment. Although some of the tracking in ALICE is based on drift detectors which are slow, however it is capable of working at at interaction rates of 10 kHz in lead ion collisions.

The ALICE apparatus is an ensemble of seventeen detectors in an overall dimensions of $16 \times 16 \times 16$ m^3 which are categorized as **central barrel detectors**, **forward detectors** and **the forward muon spectrometer**.

The central barrel detectors are placed inside the solenoid magnet previously built for the L3 experiment at LEP. An array of scintillators ALICE Cosmic Rays Detector (ARCODE) are installed outside the magnet. The L3 magnet provides a 0.5 T uniform magnetic field. Starting from the beam pipe going out, there is the Inner Tracking System (ITS), Time Projection Chamber (TPC), Transition Radiation Detector (TRD), Time of Flight (TOF), Electromagnetic Calorimeter (EmCal), PHOton Spectrometer (PHOS), High Momentum Particle Identification Detector (HMPID) and ARCODE [A$^+$08b]. The positioning, acceptance coverage, radius from the beam axis are summarized in Table 2.1 [A$^+$14d].

The ITS is a six layer of high resolution silicon detectors of different technologies. The first layer being the silicon pixel detector (SPD), followed by the silicon drift detector (SDD) and finally the silicon strip detector (SSD). The ITS is design to resolve the primary vertex with resolution better than 100 μm and to find the secondary vertices from decays of long-lived charm and beauty mesons, D (for example, D^+) and B (for example, B^0). The granularity of the ITS allows it to deal with high multiplicity per unit rapidity available in lead collisions. More details about the SPD to follow in Section 2.2.1.

The TPC [A$^+$08b] which is the main tracking detector of the central barrel with a purpose of tracking and identifying particles. The TPC has a good tracking and particle identification of charged particles up to $p_{\mathrm{T}} = 100$ GeV/c with capability of withstanding high multiplicity environment of lead collisions. The cylindrical volume of TPC is filled with 90 m^3 Ne/CO^{2}N$_2$ (85%/9.5%/4.8%) gas mixture. In combination with other central barrel detectors, namely, TOF [A$^+$08b], TRD [A$^+$08b] and the ITS, it is capable of providing particle identification using dE/dx measurement from p_{T} as low as 100 MeV/c to approximately 20 GeV/c. The TRD is a cylindrical volume of multi-wire proportional chambers filled with Xe-CO_2 mixture with fibre or foam radiators at the beginning of each chamber. The TRD uses energy loss and transition radiation to identify and tract charged particles. Furthermore, for momentum greater than 1 GeV/c it useful to enhance the pion rejection capability. TOF [A$^+$08b] is another detector used for particle identification which unlike the previously mentioned ones is based on the Multi-gap Resistive Plate Chamber technology. It is capable of identifying particles in the momentum range from 0.2 to 2.5 GeV/c. Outside the TOF on the upper side (see Figure 2.2) is the EmCal detector which a alternating layers of 1.44 mm lead and 1.46 mm polystyrene scintillator. This detector is used for jet

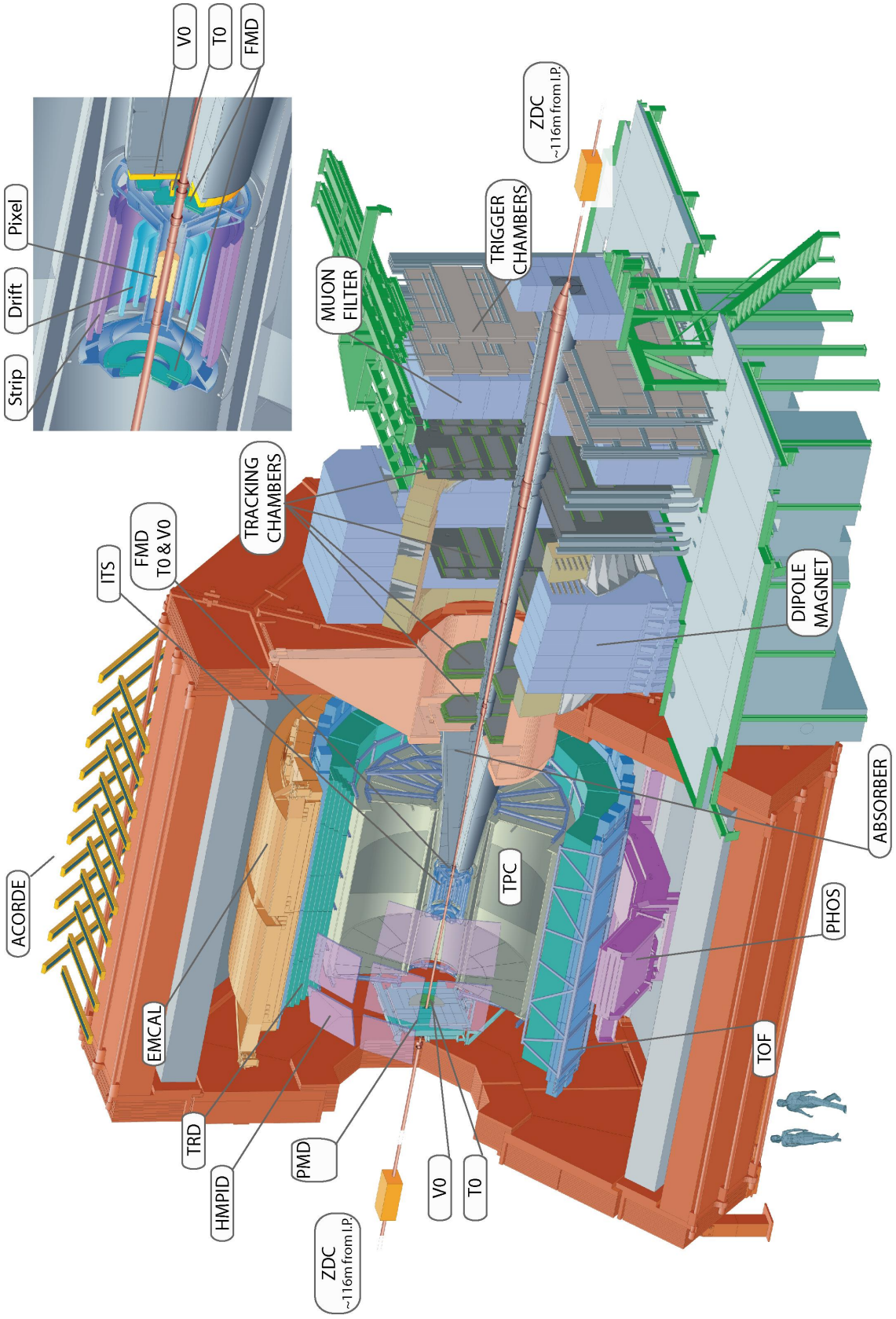

Figure 2.2: ALICE detector layout [A+14d].

studies and also for triggering. On the bottom side is PHOS (see Figure 2.2), a highly granulated lead-tungsten calorimeter with high position and energy resolution. The main physics objectives of this detector is to study the thermal and dynamic properties of the QGP using low p_{T} direct photons and also to study jet-quenching using pions and photon-jet correlations [A$^+$08b]. On top of the L3 magnet is an array of plastics scintillators (ARCODE) used to study cosmic muons in combination with TPC, TRD and TOF. The fast nature of plastic scintillators makes them useful as fast triggers, thus ARCODE is used for L0 (level zero, fast) triggering during commissioning. Cosmic muons triggered by ARCODE are used for alignment, calibration and performance of the ALICE central tracking detectors [A$^+$08b]. The acceptance, position and main purposes of these detectors are summarized in Table 2.1.

Table 2.1: The ALICE central barrel detectors. The coordinate r is measured with respect to ALICE interaction point (IP2). The (*) indicates detectors which are also used for triggering [A$^+$14d].

Detector	Acceptance		Position (r/cm)	Main
	Polar (η)	Azimuthal (ϕ)		Purpose
SPD 1^{st} layer	$\lvert\eta\rvert < 2.0$	full	3.9	tracking,vertex
2^{nd} layer	$\lvert\eta\rvert < 1.4$	full	7.6	tracking,vertex
SDD 1^{st} layer	$\lvert\eta\rvert < 0.9$	full	15.0	tracking,PID
2^{nd} layer	$\lvert\eta\rvert < 0.9$	full	23.9	tracking,PID
SSD 1^{st} layer	$\lvert\eta\rvert < 1.0$	full	38	tracking,PID
2^{nd} layer	$\lvert\eta\rvert < 1.0$	full	43	tracking,PID
TPC	$\lvert\eta\rvert < 0.9$	full	$85 < r < 247$	tracking,PID
TRD*	$\lvert\eta\rvert < 0.8$	full	$290 < r < 368$	PID
TOF*	$\lvert\eta\rvert < 0.9$	full	$370 < r < 399$	PID
PHOS*	$\lvert\eta\rvert < 0.12$	$220° < \phi < 320°$	$460 < r < 478$	photons
EmCal*	$\lvert\eta\rvert < 0.7$	$80° < \phi < 187°$	$430 < r < 455$	photons,jets
HMPID	$\lvert\eta\rvert < 0.6$	$1° < \phi < 59°$	490	PID
ARCODE*	$\lvert\eta\rvert < 1.3$	$30° < \phi < 150°$	850	cosmics

2.2.1 Silicon Pixel Detector

The SPD is the two innermost layers of the ITS, this detector is based on silicon pixels. Being the closest to the interaction point the SPD has the capability to cope with the high track densities (> 50 tracks/cm^2) available in lead collisions. The main purpose of this detector is to provide the vertex information as well as the impact parameters or secondary vertices of weak decays of strange meson and open beauty and charm particles (B and D meson). The SPD is capable of running at frequencies higher than the 100 Hz – accessible to other central detectors – in order to provide

vertex information for the muon events. The radii and acceptance of the two layers are shown in Table 2.1, with the innermost layer 3.9 *cm* from the 800 micron-thick beryllium beam-pipe. The SPD detecting elements are mounted on low-mass carbon fibres to minimize material budget [A+08b]. The computer 3D model (left) and the actual modules (right) of SPD are shown in Figure 2.3. In the p-Pb run of 2013 at

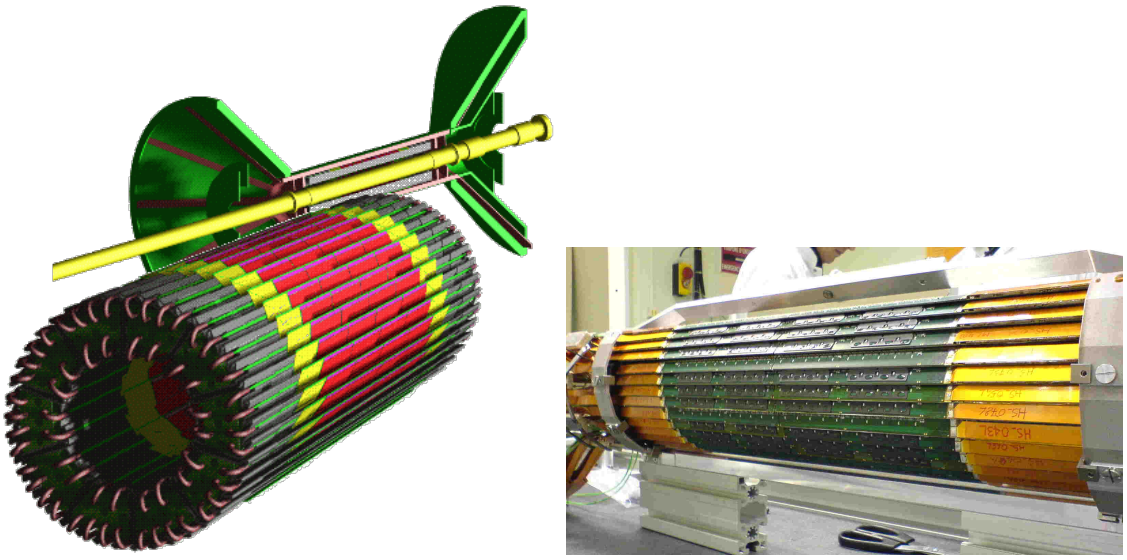

Figure 2.3: Shown here is the 3D model (left) and the physical modules of the Silicon Pixel Detector.

5.023 TeV the SPD was also used to measure event activity using the clusters in the second pixel layer of the SPD. Event activity is a measure of event multiplicity, which is correlated with collision centrality [A+15e].

2.2.2 VZERO and TZERO

The VZERO (V0) detectors are placed on either side of the interaction point at 90 cm and 340 cm covering a rapidity region $2.8 < \eta$ 5.1 and $-3.7 < \eta\ -1.7$. In the negative rapidity also known as the C-side is the V0C which is placed just before the muon absorber whereas V0A covers positive rapidities. These small angle detectors consists of two arrays of segmented plastic scintillators (see Figure 2.4) which are purposed for several functions. In proton-proton and lead-lead collisions they are used to providing minimum-bias (MB) trigger[1] [Ley12] for the central barrel detectors. Since the number of particles produced at midrapidity ($\eta \sim 0$) is monotonously correlated with particles seen by the VZERO at forward rapidities, these detector are also used for centrality determination. The sum of the amplitudes in the V0 arrays is compared with the Negative Binomial Distribution-Glauber (NBD-Glauber) [A+85, MRSS07] fit as seen in

[1]Minimum-bias trigger is an experimentally defined term, referring to the selection of inelastic events with the minimum possible requirements necessary to ensure that an inelastic collision occurred.

Figure 2.6. Putting different cuts on the energy amplitude recorded by these detectors can be used also as centrality triggers (central, semi-central) and also as multiplicity triggers. These require an `AND` mode logic between the arrays. The absence of an `OR` mode MB trigger on the V0C is useful in rejecting the background from false muon triggers. Another important functionality of V0 detectors is the determination of luminosities in *pp* and p-Pb collisions [Col95, A+14c].

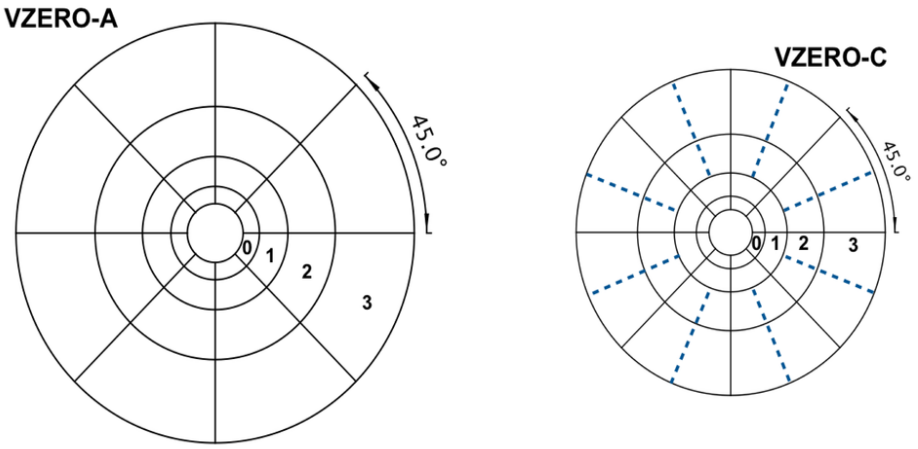

Figure 2.4: Schematic diagram of the VZERO-A and VZERO-C detectors showing the segmentation of the arrays. [A+13b]

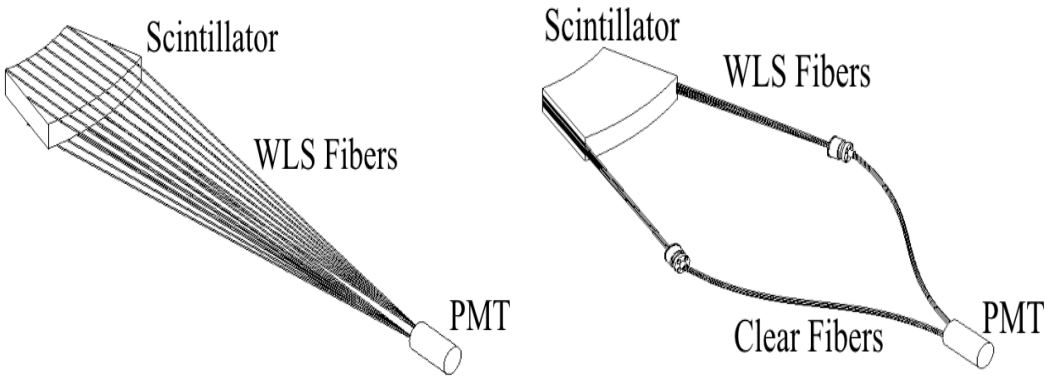

(a) **(b)**

Figure 2.5: The drawings of the cell (segment) design of V0A (left) and V0C (right) for the two inner rings [A+13b].

The two (TZERO) T0 detectors are each an array of 12 Cherenkov counters as seen in Figure 2.7 each with a fine-mesh photomultiplier tube (PMT). These detectors like the V0s are placed on either side at 72.7 cm (T0-C) and 375 cm (T0-A) from the nominal ALICE interaction point. These small angle detectors cover rapidity intervals $-5. \leq \eta \leq -4.5$ and $2.9 \leq \eta \leq 3.3$ [oJ15]. The T0 is one of the fast detectors in ALICE and thus it is used for fast timing, and also provides trigger signal. In order to provide initial time and L0 trigger (wake up signal) a fast detector capable of dealing

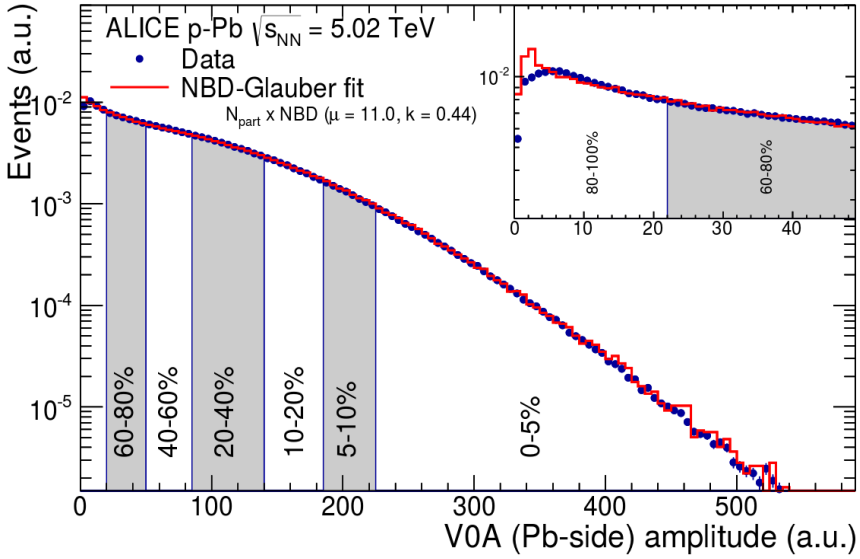

Figure 2.6: Distribution of the sum of amplitudes in the V0A hodoscopes (Pb-going), as well as the NBD-Glauber fit. Centrality classes are indicated by vertical lines. The inset shows a zoom-in on the most peripheral events [A+15e].

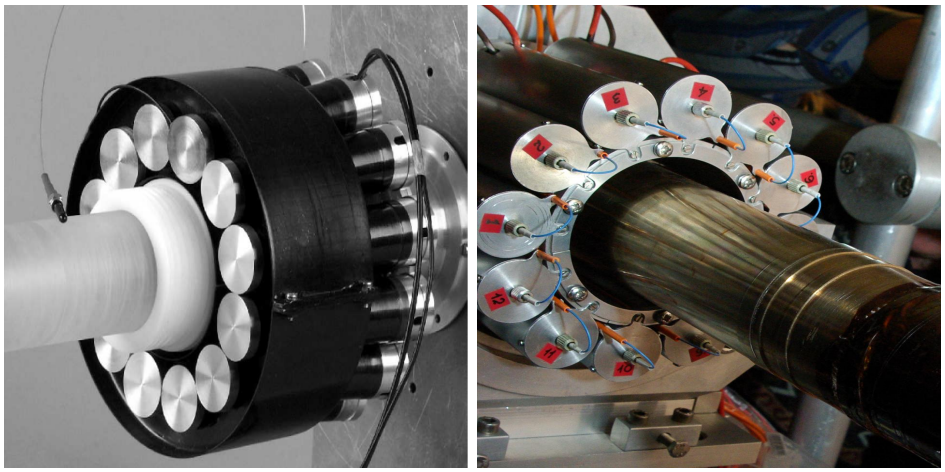

Figure 2.7: The picture showing one arrays of the T0 detectors with 12 Cherenkov counters [oJ15]. On the left is the prototype of T0-C and on the right is the array installed around the beam pipe.

with the optimal running conditions where the bunch[2] separation is 25 ns is required. This is one of the functionalities of T0. Summarized below are the functionalities of T0. The detector is required to:

- supply several signals to the ALICE trigger
- provide a wake-up signal to the TRD prior to L0 trigger
- provide precise start signal to TOF particle identification

[2]A bunch is a beam of a batch of particles squeezed together.

whereas the trigger functionalities includes:

- measuring the approximate vertex position
- providing rough estimation of event multiplicity [Col95, oJ15].

2.2.3 Zero Degree Calorimeter

The ZDC is a set of calorimeters placed in the forward direction at 0° relative to the beam-axis as seen in Figure 2.8, on either sides of the interaction point at ± 116 m (as seen in Figure 2.2). Each is composed of ZN and ZP which are dedicated to measuring neutrons and protons respectively. These detectors are used to measure spectator nucleons - the concept of spectator nucleons is relevant for lead-lead and proton-lead collisions where the collision geometry plays a role. Collision geometry

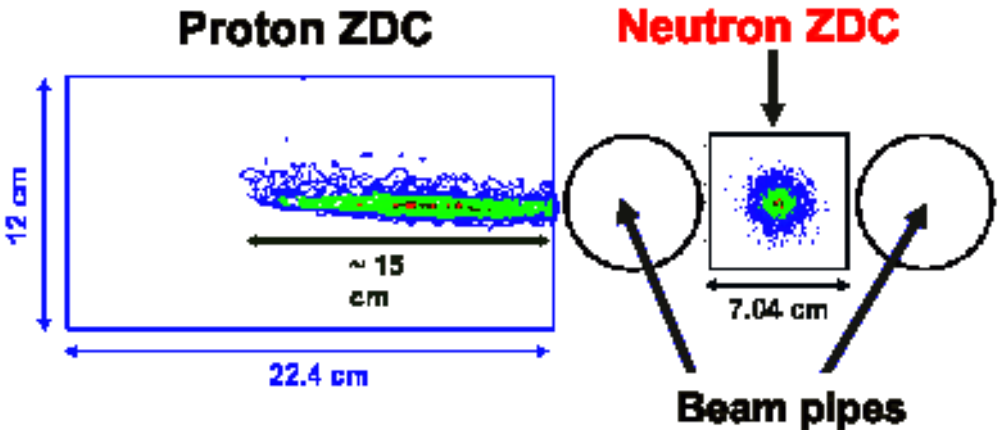

Figure 2.8: Front view of the ZDC set mounted on the adjustable platform in data taking position [Col95].

means that the lead ions can either collide head-on, that is, the distance between their respective centers or impact parameters (b) is approximately zero or they can scrape past each other, that is, the distance between their respective centers is two times the radius. This concept is applicable in proton-lead collisions. The protons which did not participate in the collision will be deflected by the LHC magnet and detected in ZP whereas the neutrons will continue in a straight line to the ZN calorimeter. Centrality is estimated by measuring the amplitude of the energy deposited in the calorimeter by slicing the distribution in energy bins as seen in Figure 2.9. This amplitude is fitted with a model which describes slow nucleon emission called slow nucleon model (SNM) [A^{+}15e].

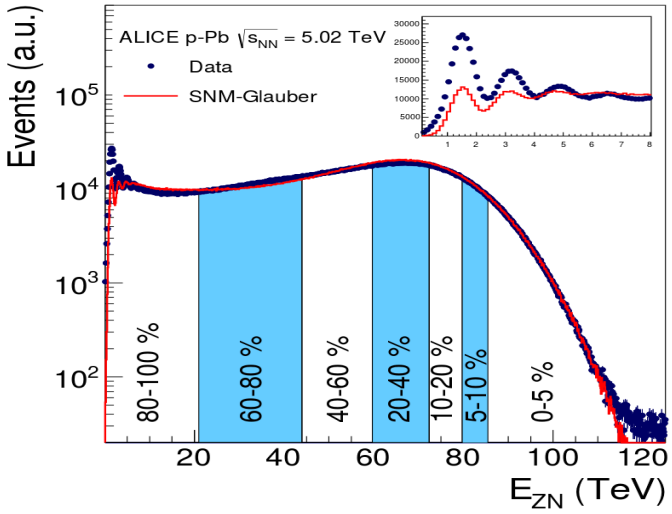

Figure 2.9: Distribution of the neutron energy spectrum measured in the Pb-remnant side ZN calorimeter. The distribution is compared with the corresponding distribution from the SNM-Glauber model [A+15e]. Centrality classes are indicated in the figure. The inset shows a zoom-in on the most peripheral events.

2.2.4 The Forward Muon Spectrometer

Hard probes such as heavy quarkonium states (J/ψ, ψ and the $\Upsilon(1S, 2S, 3S)$) provide important tools to access information about the initial and hot stages of a heavy collision. This is due to their unique production mechanism which is of both soft and hard nature. These particles as well as the Z^0 boson are reconstructed via the di-muon invariant mass. On the other hand, hard probes such as $W^{\pm}$ bosons and open heavy flavours (D and B mesons) are also accessible with the forward muon spectrometer via their single muon decay. Since ALICE is not equipped with a hermetic calorimeter, the missing energy of the neutrino is not measured and thus the $W^{\pm}$ signal is a Jacobean peak on the single muon transverse momentum distribution at half its mass signal as mentioned in subsection 1.4.4. $W^{\pm}$ and Z^0 bosons are mostly sensitive to the initial stages of the heavy ion evolution whereas open heavy flavours are experience the whole evolution.

The muon spectrometer shown in Figure 2.10 covers the polar angle interval of $171° \leq \theta \leq 178°$ which corresponds to the pseudorapidity acceptance $-2.5 < \eta < -4.0$. From the interaction point (IP) the muon spectrometer consists of the front absorber to minimize background from hadrons, five tracking stations (TRK), with the third stations placed inside the dipole magnet, then before the two trigger stations (TRG) is a large iron wall or muon filter which is used to stop muons from secondary decays inside the absorber. Behind the trigger stations is another absorber which is strategically placed to reduce background from beam particles. In order to deal will huge densities of background tracks from hadrons in heavy-ion collisions, a large absorber material

is placed before the tracking chamber to minimize this background. This absorber material also limits lowest accessible p_{T} to 4 GeV/c. The resolution of 100 MeV/c^2 is such that it enables the separation of different states of Υ which also played a role in determining the strength of the dipole magnet required as well as the spatial resolution of the tracking chambers. The high track multiplicities available in the LHC heavy-ion collisions requires high granularity detectors for tracking and triggering, thus the muon spectrometer is equipped with such detectors. These tracking and triggering detectors are made of thin detecting elements to minimize multiple scattering.

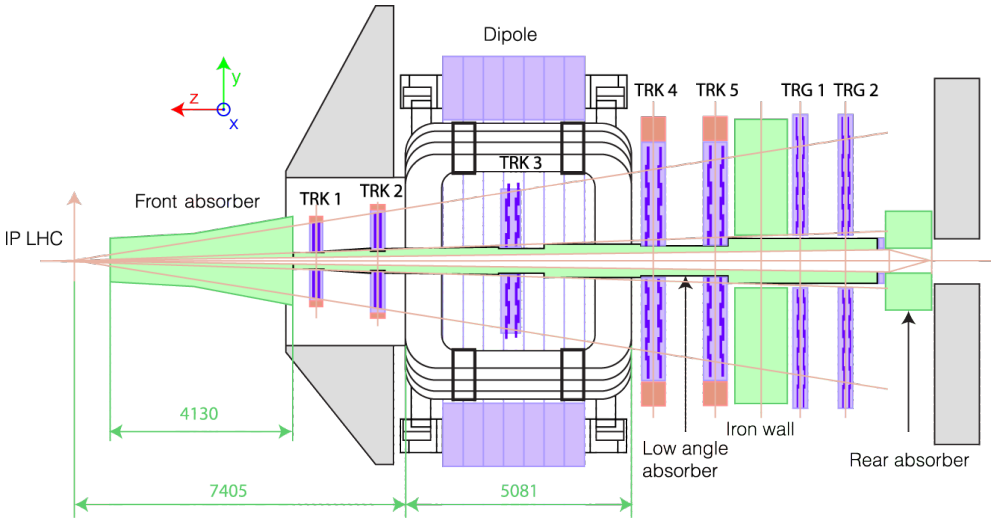

Figure 2.10: Longitudinal profile view of the ALICE muon spectrometer [ALI08a].

The Absorbers and Beam Shield

These were designed with the purpose of reducing background in the forward muon spectrometer acceptance. The beam shield is used to reduce background at large rapidity (along the beam-pipe) from particles which interact with the beam-pipe material and produce tracks in the spectrometer. The beam shield is made up of steel, lead and Tungsten Heavy Alloy ($WNiCu$). It extends from inside the front absorber as shown in Figure 2.10 and 2.11. In Figure 2.10 it is shown by the green pencil-like shape which extends beyond the trigger stations. The front absorber is strategically placed to minimize background from light hadrons (pions and kaons) by taking into account their mean free paths. The front absorber is located 90 cm from the interaction point and this ensures that pions and kaons which did not decay before the absorber are stopped and decay inside the absorber. It is made of concrete, methane (CH_2) and carbon with the length of 4.13 meters capable of reducing the flux of charged particles in spectrometer acceptance by two orders of magnitude. The length of the absorber corresponds to 10 interaction lengths. The layout and composition of the front absorber is depicted in Figure 2.11. While the beam shield and the front absorber shield the tracking stations, an extra protection in the form of the muon filter is used to shield the trigger stations. The combination of the

front absorber and muon filter stops muons with momentum less than 4 GeV/c from reaching the trigger stations.

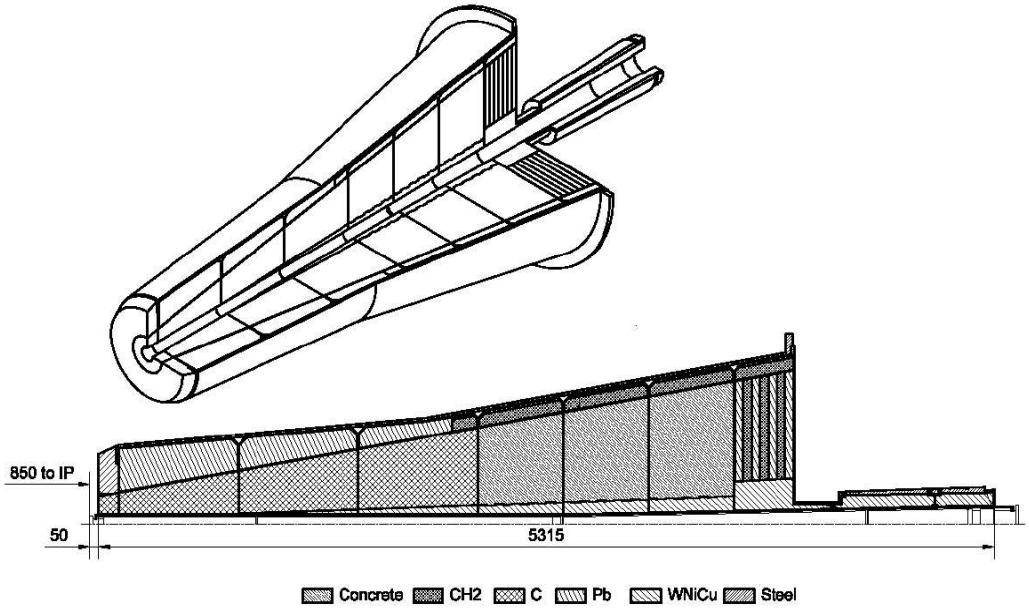

Figure 2.11: Layout of the front absorber.

The muon filter is a 1.2 meters (7.2 interaction lengths) iron wall placed after the tracking stations and before the trigger chambers as seen in the Figure 2.10.

The Dipole Magnet

This water-cooled warm magnet shown in Figure 2.12 encapsulates tracking station three of the muon spectrometer as shown in Figure 2.10. It provides a maximum magnetic field of 0.7 T and an integrated magnetic field of 3 Tm. It has an overall dimensions of $5 \times 7.1 \times 9$ m^3 and a total weight of 890 tons. This dipole magnet provides a uniform magnetic field perpendicular to the beam-axis within the acceptance of $171° < \theta < 178°$. The low magnetic strength of this dipole allows the measurement of muons down to momentum as low as 4 GeV/c. In addition, another feature of this magnet is its polarity which can be reversed within a short time.

Tracking stations

The tracking system is arranged into five stations each of which is made of two tracking chambers. Each chamber has two cathode planes which are both readout to provide two-dimensional hit information. These are bending and non-bending planes. The design of the tracking chambers shown in Figure 2.13 was driven by two main features: to achieve the reconstruction of the Υ invariant mass with a

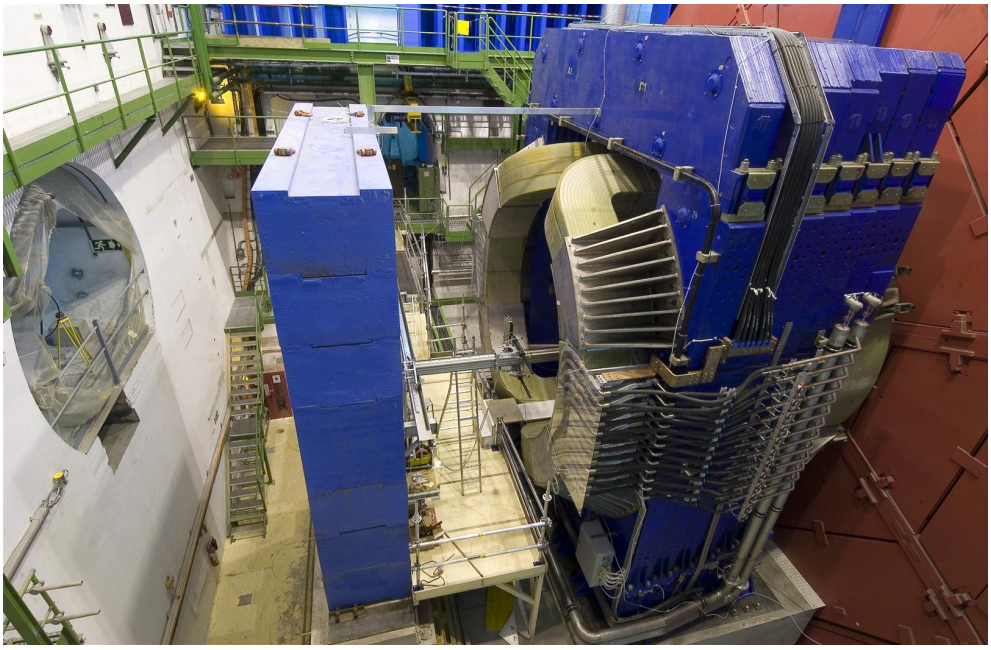

Figure 2.12: ALICE muon dipole magnet [ALI08b].

resolution of 100 MeV/c^2 which requires a spatial resolution of 100 μm and the capability to operate in a hit density of about 5×10^{-2} cm^{-2} expected in central Pb–Pb collisions. Another constraint is the 100 m^2 areal coverage of the tracking

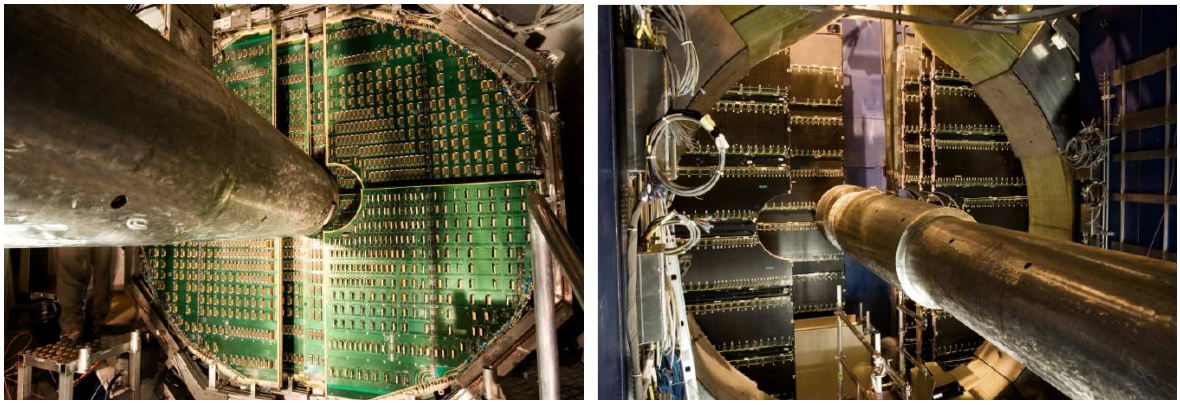

Figure 2.13: Different architecture of muon tracking chambers, on the left is the quadrant structure used for station 1, 2 and 3 and on the right is the slat structure used for station 4 and 5 [ALI08b].

chambers. The Multi-Wire Proportional Chambers with read-out based on cathodes is the technology used to meet these requirements. The two cathode planes which makes up a chamber of each station provides a bi-dimensional information in addition to the position of the chamber from the interaction point in order to have a three dimensional information of the muon track. These cathode planes are segmented in such a way that the occupancy is kept at 5%. Since the hit density decreases with distance from the beam-pipe, the size of the pad increases with the radius from the

beam-pipe. This design optimization allows the use of only one million channels. The schematic of the tracking chamber is shown in Figure 2.14. The multiple scattering of

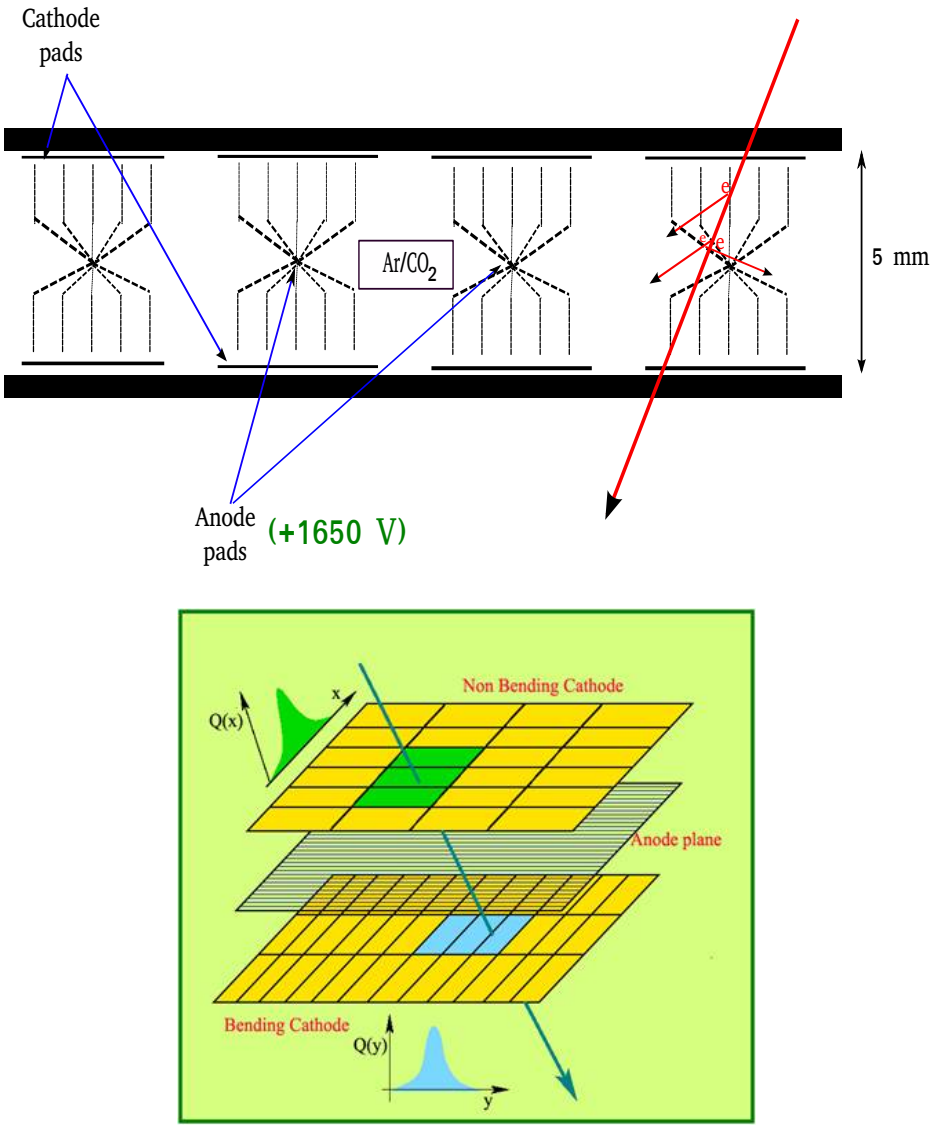

Figure 2.14: Schematic of the cathode plate chambers of the tracking station. The schematic showing the bending and non-bending plane of each chamber is shown in the bottom schematic as taken from [oNP05].

muons in the chambers is reduced by the use of carbon fibres resulting in thickness of 0.03 interaction lengths ($0.03X_0$). The design of the chambers (shown Figure 2.13) have been adapted to meet certain constraints depending on the station and its proximity to the interaction point, although they are all based on the standard MWPC technology. The first two station are based on the quadrant design with readout distributed on the surface [GPP98] whereas the other stations are based on the slat design with readout on the sides of the slats. In order to avoid dead zones, the slats are placed in such way that they overlap.

The readout electronics of the tracking chambers are mounted on the front-end

board called MANU (MAnus NUmèrique). Mounted on the MANUs is a 16-channel chip called MANAS (Multiplexed ANALogic Signal processor) which performs the following functionalities: charge amplification, filtering, shaping, and track and hold. The digitization of the signal is done on board. The channels of four of these chips are fed into a 12-bit ADCs, read out by the Muon Arm Readout Chip (MARC) [Col95]. This MARCs perform a zero suppression and allows communication with the readout. The 1.08 million channels of the tracking chambers are treated by 17 000 MANU cards. The control of the Front-End Electronics (FEE) and concentration of data is performed by the CROCUS (Cluster Read Out Concentrator Unit System) crates, which, during data taking format the data from the chambers, transfer them to the data acquisition system (DAQ[3]) and dispatch the trigger signals. These crates are connected to the MANUs by the Protocol for the ALICE Tracking CHamber (PATCH) buses. Each chamber is readout by two CROCUS crates.

Alignment of the chambers

In order to achieve the 1% resolution at the Υ mass peak needed to achieve separation of the Υ family the chambers have to be properly aligned. In order to align the chambers, with special runs[4] without magnetic field are periodically carried out. Straight tracks from these runs are processed with the Millepede algorithm [Blo06, V. 09a, V. 09b] to determine the positions of the chambers. These initial positioning of the chambers however changes upon switching on the magnetic fields and the electronic power supplies. In addition, they can also be affected by the thermal expansion of the chambers as well as their support structure. These displacements and deformations are measured and recorded during data taking by the Geometry Monitoring System (GMS) [Las98], with a resolution better than 40 μm. The GMS is an array of 460 optical sensors placed on platforms located at each corner of the tracking chambers.

Triggering stations

The two trigger stations (TRG1 and TRG2 as seen in Figure 2.10) are placed one meters apart with the first one 16 metres from the interaction behind the muon filter (iron wall). The muon filter is a 120 cm thick iron wall which corresponds to 7.2 interaction lengths and placed between the tracking and triggering chambers. Each station is made of two planes of 18 large area Resistive Plate Chambers (RPCs). The RPCs are made of low resistivity ($\sim 3 - 9 \times 10^9$ Ωcm) bakelite electrodes separated by 2 mm gap $Ar/C_2H_2F_4/SF_2/i-$ butane (49%/40%/7%/1%) gas mixture. The outside of the bakelite electrodes is painted with graphite, with one side connected to the high-voltage and the other to the ground, whereas the inside is painted with linseed

[3]DAQ is the Data AcQuisition system which will be discussed in the section
[4]Run is a continuous data taking under the same conditions

oil. Figure 2.15 shows the schematic of this design. The signal of muons is picked up inductively on both sides of the detector by means of orthogonal copper strips, in the x (bending plane) and y (non-bending plane) directions. These segmented strips provide the (x, y) coordinates. The read-out strips are connected to front-end discriminators (ADULT), which are adapted to the timing properties of the detector. This signal is discriminated in the FEE without pre-amplification before reaching the shaper. The role of the FEE is to transmit a logical signal to the trigger electronics when a valid analog pulse has been read on the corresponding channel. About 20992 electronics channels are used to readout the signals from the RPCs. The signals of

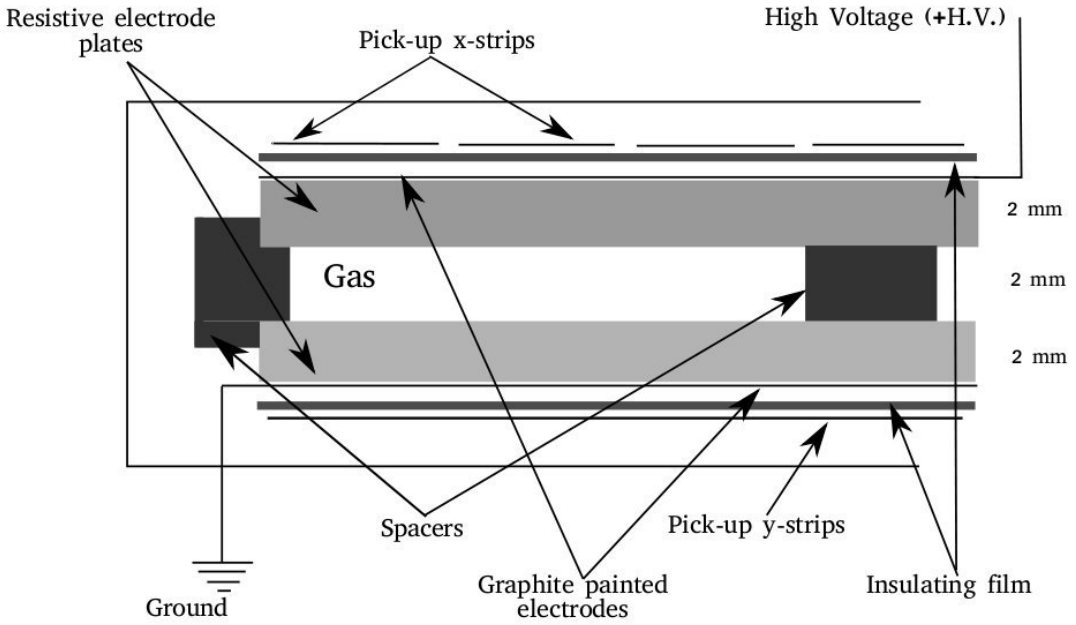

Figure 2.15: Schematic of the Resistive Plate Chambers.

one track coming from the FEE, consists of x and y fired strip patterns of the four detection planes traversed by the track, are sent to the local trigger electronics. In addition, local trigger boards have a function of identifying single tracks with p_{T} above pre-defined cuts. The regional and global trigger boards which collect the information from the local boards in order to select dimuon or single muon events. Analogous to the tracking chambers, the segmentation of the trigger chamber is such that the finer strips are placed closer to the beam-pipe. The spatial resolution attainable with these design is better than 1 cm, the chamber response is fast, the signal rises about 2 ns and the time resolution is 1-2 ns [JRR04].

2.3 ALICE muon trigger decision

The trigger decision as mentioned in the previous section is taken by the RPCs. This p_{T}-based trigger decision can be made within 1.2 μs (L0), where candidate muons can

either be single muons or di- muons. This p_{T} cut is based on the deviation of the muon track relative to the infinite p_{T} track as depicted in Figure 2.16. This deviation in the y-plane or bending plane should be smaller than a certain deviation δy corresponding to a p_{T} threshold. The trigger decision is made in three stages by the:

- local trigger board which uses the information from the surface of the detector to decides whether there is no trigger, a negative or positive muon trigger or zero deviation trigger
- regional trigger board uses the information from the local trigger board to determine whether there is a single muon track candidate or more than one candidate tracks (unlike and like sign candidate)
- global trigger board collects the information from the regional board and use it to provide trigger signals to be sent to the **Central Trigger Processor (CTP)**. These trigger inputs are:
  - All p_{T}
  - MUL: dimuon unlike sign low p_{T}
  - MLL: dimuon like sign low p_{T}
  - MSH: single muon high p_{T}
  - MSL: single muon low p_{T}.

The values of the p_{T} threshold can vary between 0.5 to 4.2 GeV/c. It is worth noting that these p_{T} thresholds are justified to reduce background muons from kaons and pions. The CTP receives information from different detectors and coordinates them to

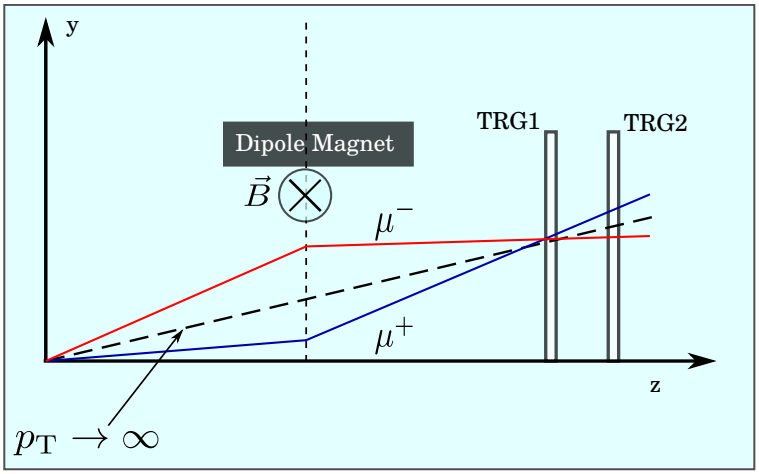

Figure 2.16: Trigger decisions Chambers.

determine whether the event is interesting or not. The decision is taken by considering that for a particular interesting event certain detectors should trigger. Following an accepted trigger, the tracking and triggering chambers are read-out.

2.4 ALICE online

The ALICE online system consists of three components, namely: **Central Trigger Processor (CTP)** or **Trigger (TRG)**, **High Level Trigger (HLT)** and **Data AcQuisition (DAQ)**. In addition, there are two control systems used for the operation of the online system, namely: the **Detector Control System (DCS)** and **Experiment Control System (ECS)**. These two control systems are interfaced to the online system as shown in Figure 2.17. The **ALICE control system** as shown in

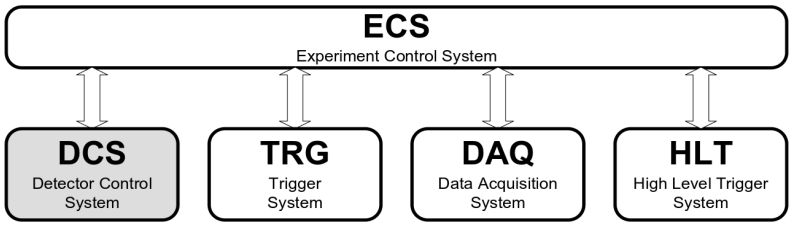

Figure 2.17: ALICE online system interface [FJL+04].

Figure 2.18 is interfaced with the online operations as well as other systems important for the workings of the experiment in general. The DCS is also linked with other components necessary for operations and monitoring of the experiment, e.g: LHC operations, electricity, ventilation, cooling, gas, magnets, safety systems and access controls. The system provides the optimal operational conditions so that the data taken with the experiment is of the highest quality [Col95]. Through the DCS and

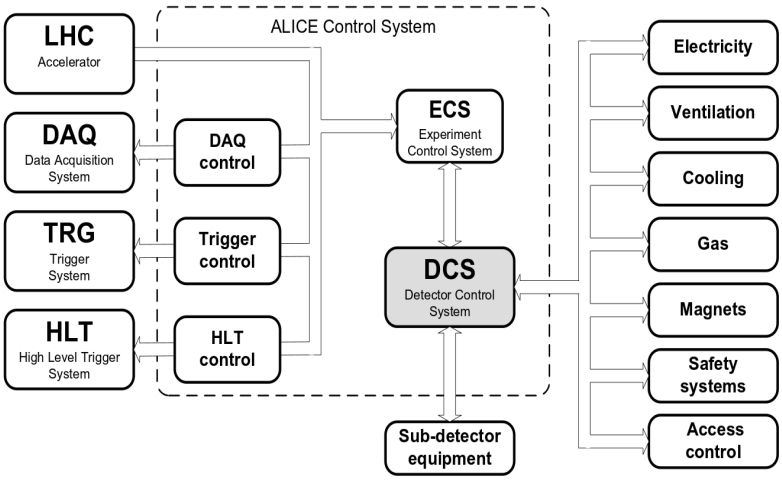

Figure 2.18: ALICE online system interface [FJL+04].

ECS, this system is capable of configuring, monitoring and controlling the equipments of the sub-detectors. The details and operations of these systems are detailed in the following sections.

2.4.1 ALICE trigger (Central Trigger Processor)

The ALICE Central Trigger Processor [Col95, FJL+04] is designed to select events having a variety of different features at rates which can be scaled down to suit physics requirements and the restrictions imposed by the bandwidth of the Data Acquisition (DAQ) system and the High-Level Trigger (HLT), see subsection 2.4.2. The CTP make use of the busy time of the detectors following a valid trigger to perform trigger selections in a way which is optimised for several running modes. Several detectors, each provide a number of logical trigger signals or trigger classes which characterize a specific measurement of that particular detector. In the case of the muon spectrometer, there are five logical trigger signals to be sent to the CTP as mentioned in sub-subsection 2.2.4. The CTP performs logical operations of these trigger inputs combined with those from other detectors to form different physics triggers (MB, central collision, dimuon event, high multiplicity, etc). In addition, the CTP takes care of downscaling, pile-up[5] protection, ready status of different detectors and read-out memories, trigger priority, and finally synchronization with the LHC machine clock cycle, as distributed by the Trigger Timing and Control (TTC) system [Tay02, BMM06]. The CTP is interfaced to the external systems as shown in Figure 2.19. Listed below are functions pertaining to each [Col95, FJL+04]:

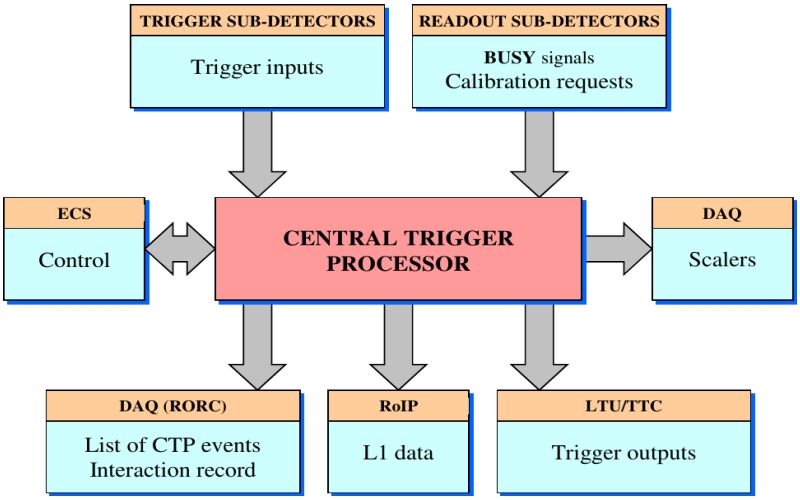

Figure 2.19: CTP in context.

- it includes programmable elements which are capable of aligning *trigger inputs* from sub-detectors which arrive at different times. These has to be trigger inputs from the same bunch crossing
- enables sub-detectors to perform standalone calibration locally

[5]Pile-up is a when multiple collisions occur in a single bunch crossing. In high luminosity colliders there is a non-negligible probability that one single bunch crossing may produce several separate events, known as pile-up events.

- its link to the ECS enables its configuration and running, and additionally the partitioning[6].
- a list of events which are tagged as interesting are sent to the DAQ. In addition, the record of all the bunch crossing in which an interaction occurred is kept.
- sends trigger outputs in the form of trigger pulses and trigger data to the detector, subject to the BUSY status coming from the detector
- performance of the trigger is monitored using scalers, which are read out separately and go to a monitoring computer dedicated to this task.

In ALICE, the trigger inputs are divided into three different levels, L0, L1 and L2, which have different associated latencies or busy time [Col95,FJL+04]. The L0 input or decision comes from detectors which can send the signal within 1.2 μs of the collision, whereas trigger logic decision L1 which can be made within 6.8 μs of the interaction makes up a semi-fast cluster. The L2 decision which comes from the slower cluster is made after 88 μs. The L0 decision is made by inputs from detectors such as the SPD, VZERO, T0 and the muon trigger. Most importantly, with so many sub-detectors and thus several trigger logics or classes, the bandwidth to the DAQ becomes a problem. Hence the CTP is also used to adjust the rate of the triggers in order to reflect the physics needs.

Examples of different triggers are: MB, MSH, etc. The MB trigger is a coincidence of signals from V0A and V0C or T0A and T0C detectors. Muon triggers are a coincidence of the MB and either MSL, MUL, MLL, MSH or all p_{T} as defined in section 2.3. In a case that an interesting event is triggered, a signal is sent to the read-out detectors like muon tracking chambers so that the data can be sent to the DAQ.

2.4.2 Data AcQuisition

The Data AcQuisition system of ALICE is designed to handle high data rates and small event size in *pp* collisions and low interaction rate and large event size (4 GB/s) in Pb–Pb collisions. The design consideration is also driven by the requirement to handle and allocate resources (bandwidth) to different clusters of detectors dedicated to certain physics. The overview of the DAQ architecture is shown in Figure 2.20. Once the CTP has tagged an event as interesting, a trigger signal is dispatched to the front-end read-out (**FERO**) of detectors involved (cluster) through a **Local Trigger Unit (LTU)**. The data from the FEROs and the control commands to, are sent through dedicated **Detector Data Links** (**DDLs**). This data is received by the **DAQ Read-out Card** (**D-RORC**) hosted on detector specific computers

[6]Partitioning refers to the grouping of detectors into clusters. This allows independent operation of groups of sub-detectors depending on physics interest. For example, the muon cluster must contain in addition SPD for vertexing and V0 or T0 for MB.

called **Local Data Concentrators** (**LDCs**) where event fragments are sent to be assembled into sub-events. The sub-events are then sent to a farm of computers called

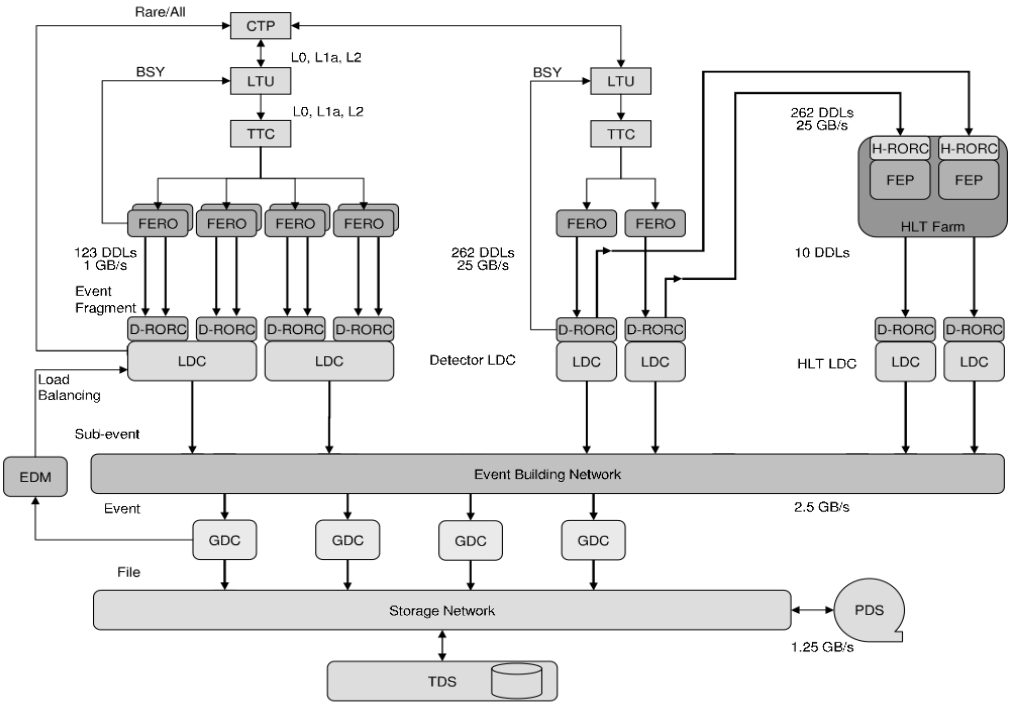

Figure 2.20: DAQ architecture overview.

Global Data Concentrators (**GDCs**) where the whole event is built. This data is subsequently shipped to a **Transient Data Storage** (**TDS**). For each run this data is registered on **ALICE ENvironment** (**AliEn**) also hosted via **MONitoring Agents using a Large Integrated Services Architecture** (**MonALISA**). The **Event Destination Manager** or **EDM** controls where the event is sent TDS or Permanent Data Storage (PDS).

2.4.3 High Level Trigger

In order to meet the high computing demands, the **High Level Trigger** consists of a PC farm of up to 1000 multi-processor computers. These computers receive via DDLs copies of raw data of all ALICE detectors. The processing or raw data is performed by **Front- End Processors** (**FEPs**) hosting the **HLT-Readout Receiver Card** (**H-RORC**). The selected data are transferred to dedicated LDCs. The role of the HLT is to perform an online analysis to select relevant events or sub-events and compress it without losing the physics content in order to meet the available DAQ bandwidth. It required to:

trigger – accept or reject based on detailed online analysis

select – a physics region of interest within the event by performing only a partial readout

compress – use compression algorithms to reduce the event size without losing physics information.

The computation on the HLT farm is performed on nodes running in parallel. Once all the steps of triggering, selecting and compressing are done, the reconstructed events are saved into a data format called **Event Summary Data** (**ESDs**) and subsequently shipped to DAQ.

2.4.4 Detector and Experiment Control System

The role of the **Detector Control System** is to ensure safe and proper operation of the experiment during data taking and commissioning (unlike other online systems). It provides the ability to configure, monitor and remote control of experimental equipments. Since the DCS has to be developed for several sub-detectors, a coherent control system with common features was created to deal with these demands. Some additional design requirements and goals are listed below:

Flexible and scalable,

Centralized, User-friendly and intuitive operation,

Safe and reliable,

and **Remote access**.

The system is designed to **configure and archive** data required for the operation of the experiments. Maintainability is an important feature of the DCS to ensure continuity in case the expertise is no longer available.

The software architecture of the DCS has a tree-like control structure representing the sub-detectors, their sub-systems and devices. The basic building block of this architecture are device units which are equipments of the sub-detectors. These are called device units. Up in the tree hierarchy are control units, which are components of a sub-detector which controls the device units. The behaviour of a control unit can be conveniently modelled with the use of a finite state machine (used also by other online systems). This defines an arbitrary number of states the unit can be in, and the transitions between these states. These transitions can either be triggered by state transitions from one or more of the children (device units) or upon reception of a command (either from the unit's parent or from an operator).

The **Experiment Control System** is a top level control system providing a framework by which a unified view the activity and perform operations on the experiment. In addition, it allows the partitioning of the experiment, enabling parallel non-interacting

operations of the detectors. Finally, the ECS has a role of coordinating other online systems (see Figure 2.17) in order to fulfil a common goal. The centre of the system a database (see Figure 2.21), where all the resources are described. The **Experiment Control Agent** facilitates the manipulation of this database whereas the **Partition Control Agent** allocates resources seen by the online systems. PCA creates a working environment for the Detector Control Agent (DCA), in such a way that only allocated resources are seen by the sub-systems.

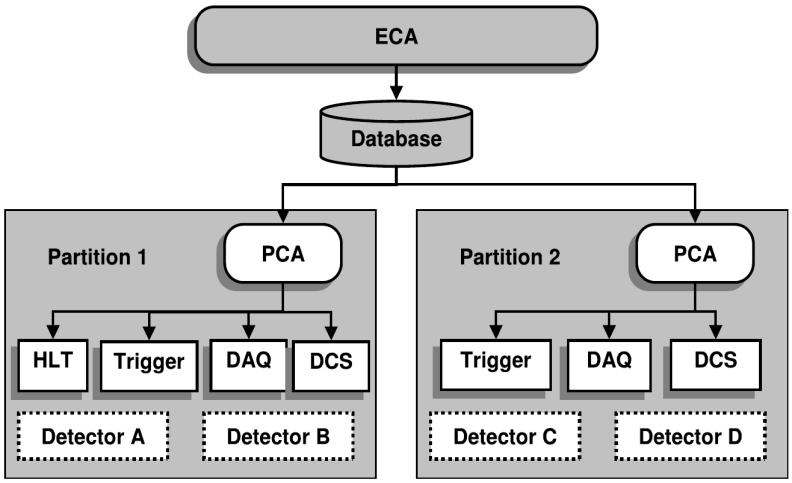

Figure 2.21: ECS architecture overview.

2.5 ALICE offline

The ALICE offline project AliROOT (ALICE ROOT) is a C++ based framework on the ROOT [BR97] platform. The development of this project started in 1998, with the primary role of providing a platform for event generation, detector simulation, event reconstruction, data acquisition, event visualization, online and offline data processing. This framework is distributed across the world-wide computing grid.

2.5.1 Computing grid

The ALICE computing facilities are distributed around the world. The grid Middleware allows the different computing facilities to operate as one computer centre. This distributed computing infrastructure which serves ALICE and other LHC experimental programmes is coordinated by the Worldwide LHC Computing Grid (WLCG) project. South Africa is part of the WLCG via the Center for High Performance Computing (CHPC). Figure 2.22 shows the hierarchical schematic view of the ALICE offline computing in the framework of the tiered MONARC model. The Tier-0 computing centre at CERN has a role of housing the raw data from experiments, this task is

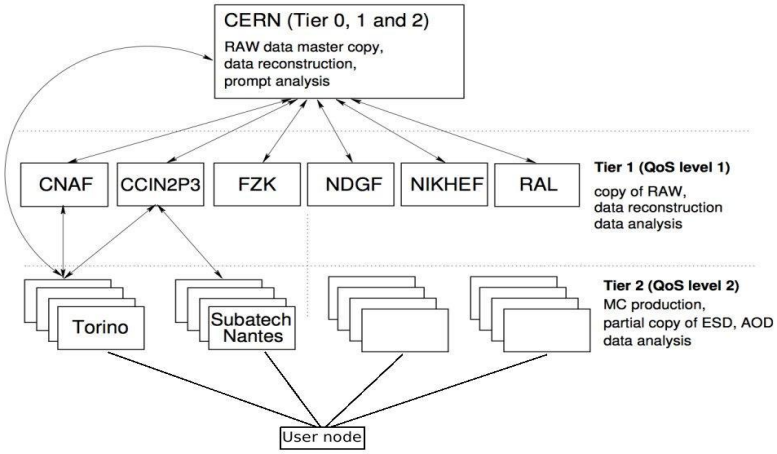

Figure 2.22: Schematic view of the Tier structure with the added user node.

shared with regional computing centres called Tier-1 composed of highly safe storage mediums for a natural backup. These Tier-1 computing centres has in addition a role of processing the raw data, reconstruction and data analysis. The Tier-2's are clustered around Tier-1 and have the main role of end user activities, for example Monte Carlo simulation, data analysis and stores copies of reconstructed data this is, Event Summary Data (ESD) and Analysis Object Data (AOD). The first reconstruction pass to ESDs is shared among Tier-0 and Tier-1. Since during data taking these tasks are to be performed in parallel, there is need to manage resources, monitoring and authentication. LHC experiments provide virtual environment which acts as pathways to the distributed computing facilities, these are known as Virtual Organisations (VO). The services available to the ALICE community (ALICE VO) are outlined in Figure 2.23. Access to these services is offered and controlled by the **Ali**CE **En**vironment (AliEn) framework. This environment provides the user with a homogeneous interface to the WLCG and provide a shield from the complexity of the heterogeneous grid environment. The AliEn workload management system manages a common task queue on each site or computer facility providing Computer Elements to the ALICE VO. This workload manager optimizes the queue, according to availability of resources, quota and CPU time. The **AliEn Site Services** is used for monitoring and publishing the status of the grid. This is done using the **Mon**itoring **A**gents using a **L**arge **I**tegrated **S**ervices **A**rchitecture (**MonALISA**). The progress of analysis and simulation tasks are published on MonALISA, as well as the shuttle[7] status (offline). In addition to the control systems, there is a data quality monitoring system called the Data Quality Monitoring (DQM) which used to validate data before the shuttle. The **Application Programming Interface** (**API**) provides the interface between ROOT and the AliEn services. ALICE ROOT framework coined AliROOT, is a ROOT based platform used for the task of analysing, simulation, calibration and data reconstruction, to name a

[7]Shuttle is the transportation of data from experiment to tape and registered in the file catalogue.

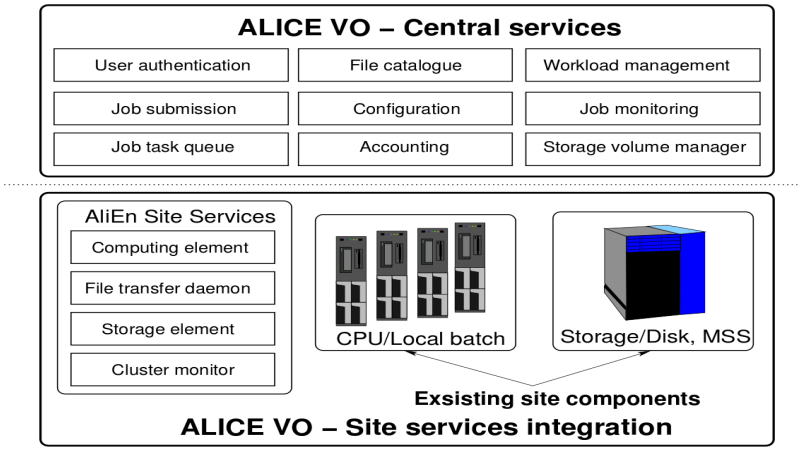

Figure 2.23: Schematic view of the AliEn basic components and deployment principles [Col95].

few. This frame is discussed in the section below.

2.5.2 AliROOT framework

The ALICE offline framework or **AliROOT** schematically shown in Figure 2.24 provides an object-oriented platform for programming as well as an interface with the grid using AliEn. This framework is written in C++ with some background program in FORTRAN (especially, Monte Carlo codes). It provides an environment for software package development for detector simulation, event reconstruction and data acquisition and analysis. The STEER module which is at the centre of the framework has the

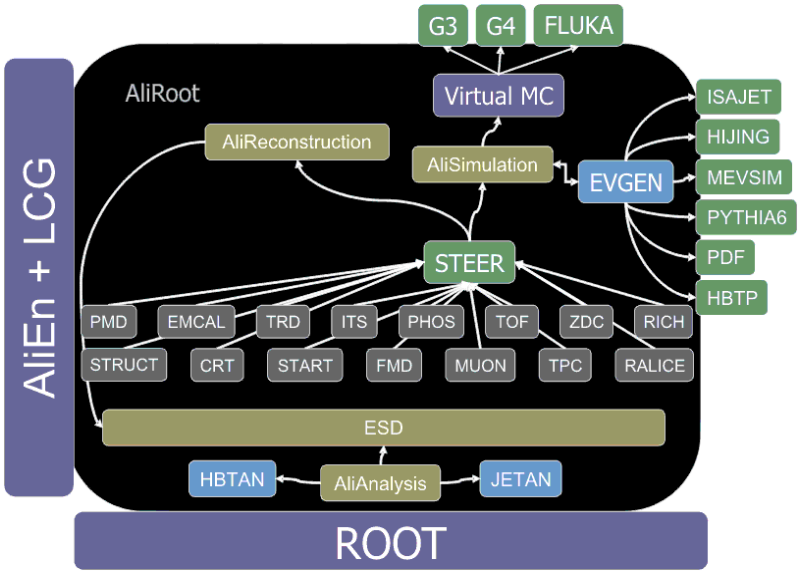

Figure 2.24: ALICE ROOT Framework.

role of providing the run management and interface classes and base classes. As seen

in Figure 2.24 this module coordinates codes from different detectors. The framework provide codes (PYTHIA, HIJING, POWHEG, etc) to simulate hadronic collisions and also for detector response simulations(GEANT3(4) and FLUKA). The reconstruction chain in view of the framework is schematically depicted in Figure 2.25 showing a parallel between **Real Data** and **Monte Carlo** reconstruction. The upper branch

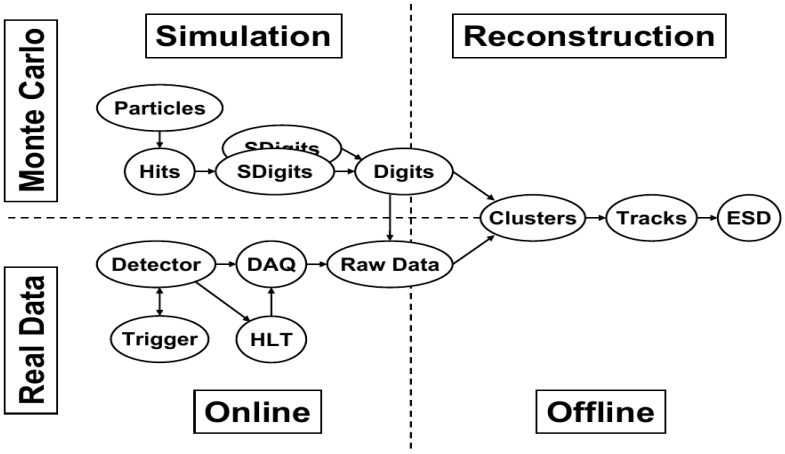

Figure 2.25: ALICE ROOT Reconstruction.

represent the Monte Carlo chain which start from event generators which produce particles. These particles traverse the detectors producing hits. The point where the particle crossed the detector and the amount of energy deposited constitute a hit. In addition, the information the particle which produced the hit is stored therein. In the next step of the reconstruction the information of the parent particle is lost and the spatial resolution is translated into the id of the read-out element (strip, pads, etc) the particle traversed producing digits. The precursor to digits are the summable digits which uses low thresholds this is the noise simulations are not included. The digits are a parallel of raw data. In the lower branch, as mentioned previously the detectors are read-out only when are viable trigger is received. The data is then sent to DAQ or to the HLT to be compressed and subsequently sent to DAQ and then transported to tape as raw data. The reconstruction software takes as input either digits or raw data to produce cluster: this is a set of adjacent digits presumably produced by the same particle. The next step is produce tracks, which contain information about: the curvature and coordinates of the track. This information is stored in the data format called **Event Summary Data (ESD)** which is suitable for physics analysis. There is an additional step which produces the lighter version of ESDs called **Analysis Object Data (AOD)**. AODs contains less or specific information needed for a particular analysis.

Part III

Analysis and Results

"All models are wrong, but some are useful."

George E. P. Box

3

p-Pb collisions

In this chapter the strategy and results of the proton-lead analysis will be discussed.

Contents

3.1 Data taking configuration

The proton-lead collisions program started in September 2012 with a pilot run which lasted a week, whereas the main data taking took place in early 2013. During this period, the proton beam going towards the muon spectrometer defined positive rapidity."The two-in-one magnet design of the LHC imposes the same magnetic rigidity of the beams in the two rings" [A+13d]. The runs utilized in this analysis are from a filling scheme in which 288 bunches collided at the ALICE interaction point (IP2) consisted of 1×10^{10} protons and 6×10^{7} Pb ions. The bunch spacing was set to 200 ns. The energy of proton beam was 4 TeV, whereas, the fully stripped $^{208}Pb^{82+}$ beam had an energy of 82×1.58 TeV. The centre-of-mass energy $\sqrt{s_{\rm NN}} = 5.02$ TeV obtained by equation

$$\sqrt{s_{\rm NN}} = 2\sqrt{s_{pp}} \cdot \sqrt{\frac{Z_1 Z_2}{A_1 A_2}}, \tag{3.1}$$

where s_{pp} is the energy of the proton beam, $A_1 = 1$ and $Z_1 = 1$ represents the atomic number and the mass of the proton, respectively. $A_2 = 208$ and $Z_2 = 82$ represents the atomic number and the mass of lead ion. The asymmetry in energy resulted in a shifted centre-of-mass by 0.465 units of rapidity is obtained by the equation:

$$y = \frac{1}{2}\log(\frac{Z_1 A_2}{Z_2 A_1}) \tag{3.2}$$

The schematic of the ALICE coordinate system is shown in Figure 3.1. The delivered luminosity as a function of time and fills are shown in Figure 3.2. The maximum luminosity attained by ALICE was about 5×10^{27} $cm^{-1}s^{-1}$.

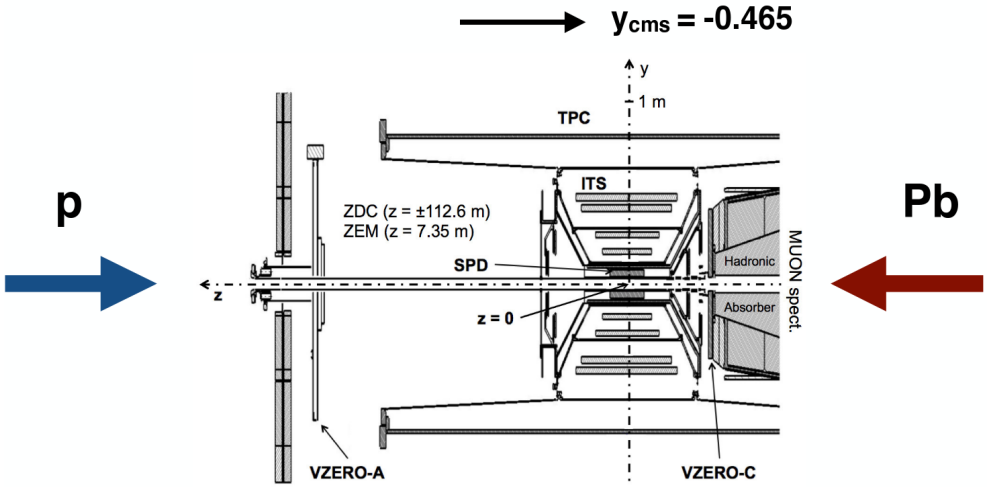

Figure 3.1: Schematic of the ALICE coordinates for the 2013 p–Pb running period [A+13b].

The number of recorded triggers is shown in Figure 3.3 as a function of time.

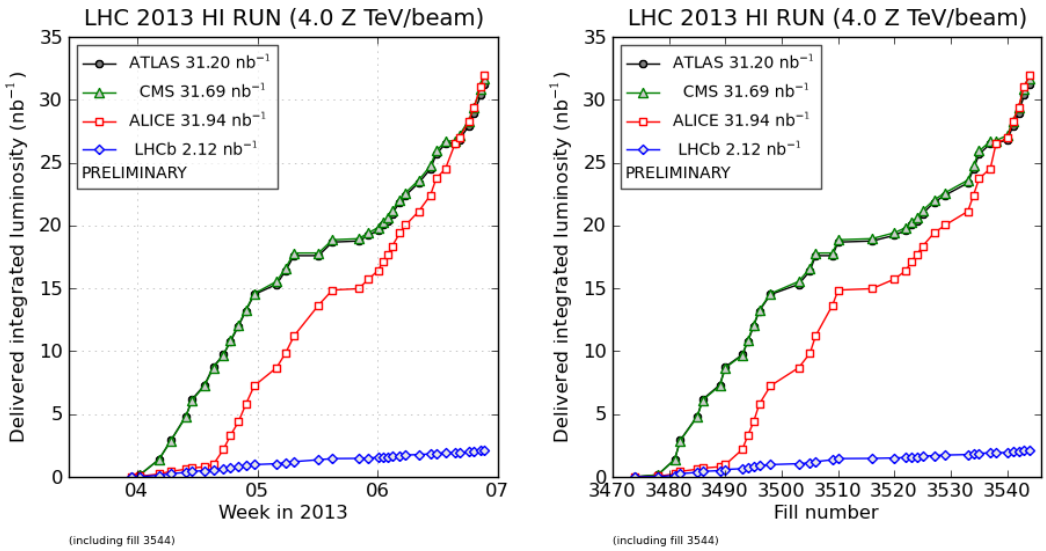

Figure 3.2: Luminosity as a function of time and fill for the proton-lead collisions data taking period [Coo09].

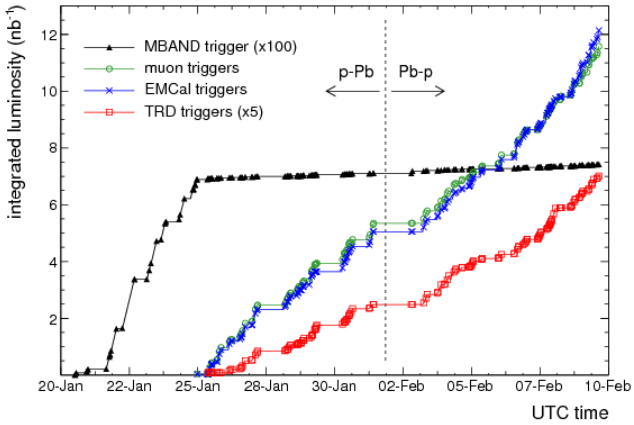

Figure 3.3: Integrated luminosity collected by ALICE with minimum-bias (MB) and rare-triggers [A^{+}14d].

3.2 Data analysis

The data samples analysed consists of Analysis Object Data (AOD) which only contains muon-specific information. The sample is composed of 46 runs from two periods of data taking in which the proton was going towards the forward muon spectrometer. The distinguishing feature of the two periods is the current of the dipole magnet. The periods with negative and positive dipole current are named LHC13d and LHC13e, respectively. Furthermore, there is another sample which consists of 63 runs where the Pb-ion was going towards the forward muon spectrometer. In these runs the dipole magnet was reverted to negative current. The following conversion p-going (LHC13d

and LHC13e) and Pb-going (LHC13f) will be used interchangably. The runs used passed the quality assurance (QA). The QA is a set of criteria used to define the quality of data, these are: the run duration should be at least 10 minutes, the muon tracker and trigger, SPD and V0 or T0 detectors should be in the partition and the global data taking quality flag declared by DQM should be good. The cluster described above should have the trigger partition which includes the muon trigger, SPD and V0 or T0, while the readout partition should include the muon tracker and SPD.

3.2.1 Event selection

There are three offline selection cuts used to refine the event sample, namely, physics selection, good reconstructed vertex and a trigger selection. "The offline event selection is applied with the purpose of selecting hadronic interactions with the highest possible efficiency, while rejecting the machine-induced and physical backgrounds" [A+13c]. The **physics selection** is used to reject machine-induced background caused by the interaction of beam particles with the residual-gas or the mechanical structure of the beam-pipe. As shown in Figure 3.4, these interactions mostly occur outside the interaction region and thus produce an early signal compared to interactions occurring at the nominal IP. These background interactions are rejected by applying a cut on the V0 timing [Kry14].

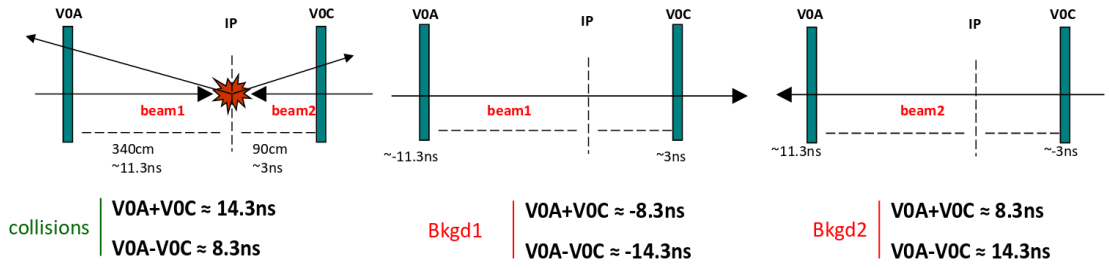

Figure 3.4: Schematic of the V0 timing used for event selection [Kry14].

The ZDC timing is also used to reject beam-induced background [A+13c]. Furthermore, the **primary vertex cut** is used to select events with a good reconstructed vertex using the SPD vertex finding method, which uses the number of vertex contributors or SPD tracklets[1]. Lastly, the analysed data sample contains **MSH-triggered** (as described in sub-section 2.4.1) events. MSH (CMSH7-B-NOPF-MUON [2]) corresponds to muons with a high p_{T} trigger threshold set at ∼4.2 GeV/c. The number events passing different event selections one after another are summarised in Table 3.1.

[1] SPD tracklet is defined as a line segment connecting clusters formed by particles tracks on the first and the second layer of the SPD. In some cases the reconstruction algorithm of the vertex fails or there are no reconstructed space points in the SPD [BDMP09].

[2] CMSH7-B-NOPF-MUON is the name of the triggers used, 7 means that the muon trigger is in coincidence with MB using corresponding to V0, B reflects that main bunches from both side were colliding and NOPF indicates NO Past-Future protection.

	Trigger Selection	Physics Selection	Good Vertex
LHC13d (p-going)	4.60M	4.58M	4.57M
LHC13e (p-going)	5.52M	5.51M	5.50M
LHC13f (Pb-going)	15.67M	15.34M	15.32M

Table 3.1: Summary of the trigger-selected statistics after applying various event cuts: physics selection and primary vertex reconstruction. See text for details

Event characterization: event activity

The following presents a synoptic overview of centrality determination as described in Ref [A$^+$15e]. In heavy-ion collisions (proton-lead or lead-lead collisions), particle production is often studied as a function of event activity or centrality which is somehow related to the impact parameter of the collision as discussed in Chapter 1 in Sub-section 1.3.2. The number of interacting or participating nucleons increases from peripheral to central collisions. This in turn, results in increasing volume, energy and consequently the number of charged particle produced. Centrality determination is thus based on the correlation between impact parameter, the number of participating nucleon and the multiplicity of the collision. In ALICE, centrality is estimated using charge particle multiplicity as measured by forward and central detectors as well as the energy deposited in the zero degree calorimeters place along the beam pipe. In [A$^+$13d, A$^+$15e], the zero degree calorimeter based estimation is said to be unbiased. "The centrality determination is performed by exploiting the rapidity coverage of the various detectors" [A$^+$15e]. The main estimators used for centrality in the following are:

- CL1: which uses the number of clusters in the outer layer of the SPD
- V0A/C: the amplitude measured by the VZERO detector on the A-side and C-side in the Pb-going direction
- ZNA/C: the energy deposited in the neutron calorimeter on the A-side and C-side in the Pb-going direction

The average number of binary collisions determined by the following estimators are shown in Table 3.2 below. Centrality classes have been defined as percentiles of the visible cross-section and allows relating signals from the above detectors to geometrical quantities that can not be directly measured. These quantities or parameters are impact parameters (b), number of binary collisions ($\langle N_{\rm coll}\rangle$), number of participating nucleon ($\langle N_{\rm part}\rangle$) and the nuclear overlap ($\langle T_{\rm AA}\rangle$). The centrality determination is based on the assumption that the signals on these detectors are monotonically related to collision centrality. $\langle N_{\rm coll}\rangle$ is obtained from Negative Binomial-Distribution Glauber-Monte-Carlo fits to the V0A(C) amplitude and the number of clusters in CL1 as seen in Figure 2.6, whereas ZDC-based $\langle N_{\rm coll}\rangle$is obtained by Slow Nucleon Model

	V0A		CL1		V0C		Hybrid ZNA/ZNC	
Multiplicity	$\langle N_{\rm coll}\rangle$	syst	$\langle N_{\rm coll}\rangle$	syst	$\langle N_{\rm coll}\rangle$	syst	$\langle N_{\rm coll}^{\rm mult}\rangle$	syst
2–20%	12.5	10%	12.9	10%	12.5	10%	11.31	3%
20–40%	9.36	9%	9.49	9%	9.39	9%	9.6	2%
40–60%	6.42	7.2%	6.18	7.2%	6.40	7.2%	7.1	4%
60–100%	2.86	6.2%	2.6	6.2%	2.86	6.2%	3.2	3.1%
0–100%	6.87	8%	6.83	8%	6.87	8%	6.9	8%

Table 3.2: Geometric property ($\langle N_{\rm coll}\rangle$) of the p-Pb collisions with different centrality estimators.

(SNM)-Glauber MC fits to the distribution of the energy of deposited in the zero degree calorimeter as shown in Figure 2.9.

3.2.2 Offline muon selection

In the offline physics selection only MSH-triggered events with a good reconstructed primary vertex from the SPD were considered. Furthermore, the data sample was refined at track level by applying the following selection criteria:

- $-4.0 < \eta < -2.5$ fiducial cut is used to remove tracks at the edge of the spectrometer
- θ_{abs}: 171°$< \theta_{abs} <$178°which is the polar angle at the end of the absorber is used to reject muons crossing the high-density region of the front absorber, where the multiple scattering plays an important role
- the p×DCA[3] cut was applied to remove beam-induced background and particles. The DCA of particles produced at the IP follows the Gaussian distribution due to the multiple scatterings in the absorber, whereas the particles coming from elsewhere do not. The tracks with p×DCA greater than $6\sigma_{\rm p\times DCA}$ are rejected. This cut removes completely the contamination which is estimated to be of the order of 7% and 90% in the p-going and Pb-going period, respectively [A$^+$17c].
- finally, the muons are identified by matching the tracks reconstructed in the tracker and the trigger system.

The number of track of muons which passes the track cuts are shown in Table 3.3. Furthermore, these tracks comes from events which passed event cuts.

Figure 3.5 shows the effects of different cuts (selection criteria) on the pseudorapidity and $p_{\rm T}$ distribution. The pseudorapidity and $\theta^{\mu}_{\rm abs}$ selection are essentially falling atop each other. The p×DCA and match-$p_{\rm T}$ are responsible for the drastic change in

[3] p×DCA is the momentum times the **D**istance of **C**losest **A**pproach, which is an extrapolated distance from the IP to the track. p is the momentum of the track.

	LHC13d	LHC13e	LHC13f
η	2.50M	2.92M	7.65M
θ_{abs}	2.49M	2.91M	7.58M
p×DCA	2.48M	2.89M	3.38M
Trigger/tracker matching	1.53M	1.78M	3.38M

Table 3.3: Summary of trigger-selected statistics after applying various selection cuts at event and track level: physics selection, primary vertex reconstruction and track cuts. See text for details

the distributions compared to the distributions with only events selection criteria applied.

3.2.3 Pile-up study

There are two kinds of pile-up: the in-bunch and the out-of-bunch. In the data selection, the muon tracks in the tracking chambers are required to match a track in the muon trigger which has a time resolution of 1-2 ns, thus the reconstructed muon events are not sensitive to pile-up from different bunches (200 ns separation between bunches). The VZERO-A hodoscope has a small timing resolution and the SPD/ZDC has an integration time of 200 ns and therefore a very small contribution from pile-up due to different bunches is expected. Therefore, pile-up events from other bunches (out-of-bunch) are expected to be negligible for detectors used in this analysis. In the following, pile-up will always refer to pile-up from the same bunch crossing. It is known that the number of collisions per bunch crossing follows or can be described by the Poisson distribution [Mre07]. The rate of pile-up can be defined as the ratio of the probability of having more than one collision to having one collision. This can be computed at both hardware and software level and corrected for, accordingly.

Hardware level

The pile-up correction factor $F_{\text{pile-up}}$ at hardware level is defined as:

$$F_{\text{pile-up}} = \mu/(1 - e^{-\mu}) \tag{3.3}$$

with

$$\mu = -\ln\left(1 - \text{purity}_{\text{MB}} \times \frac{\text{L0bRate}_{\text{MB}}}{N_{\text{colliding}} \times f_{\text{LHC}}}\right) \tag{3.4}$$

μ is the mean value of the Poisson distribution which describes the probability to have n collisions when the beams cross each other. $\text{L0bRate}_{\text{MB}}$ is the number of minimum bias events recorded by the L0b counter per data taking time Appendix B in section B.1. $f_{\text{LHC}} = 11245$ Hz is the collision frequency of the LHC. The mean

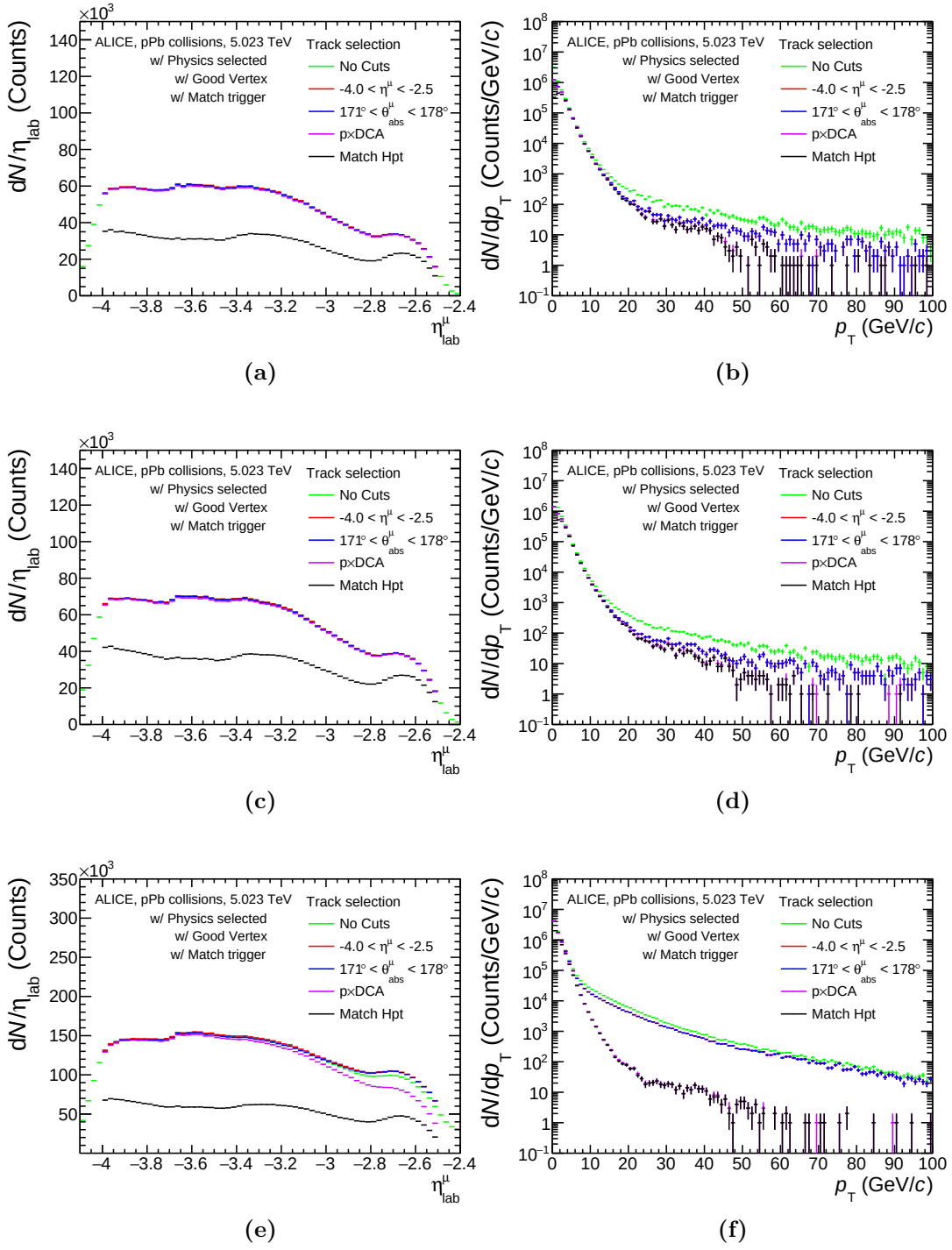

Figure 3.5: The number of events as a function of pseudorapidity (left) and transverse momentum (right) of muons in the Pb-going period showing the effects of different track selection criteria with all event cuts applied.

values of the pile-up correction factors are about 1.02 for both the LHC13de and LHC13f data samples.

Software level

The pile-up events can be flagged using the information of the SPD as is done in this study. This is done by requiring the distance (d) between vertices to be at least 0.6 cm and varying the number of tracks coming from the secondary vertex. However, the event tagging has an efficiency, which may, in principle differ in MB and in muon triggered events. Figure 3.6 shows plots of the pile-up fraction (number of events tagged as pile-up events over the total) as a function of the run numbers. As seen in the plots, the hardware level pile-up rejection is compared with the software level (using SPD) pile-up tagging. In order to estimate the effect of pile-up on the number of events, the number n = 4 option was chosen since it exhibits the highest efficiency ∼0.85 as shown in Figure 3.7.

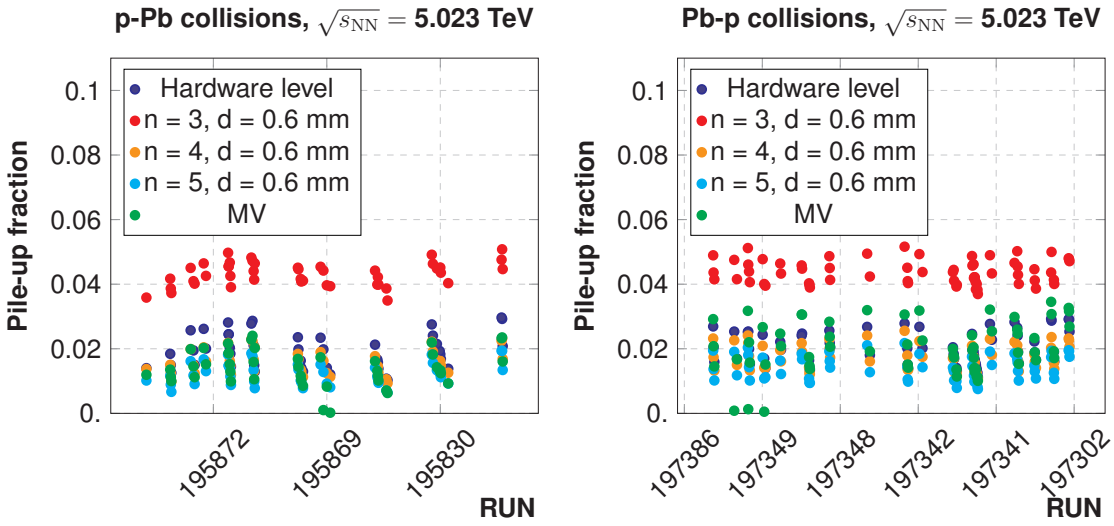

Figure 3.6: Pile-up fractions as a function of run number. Hardware level compared to software level pile up based on SPD.

In Figure 3.8 the fraction of events tagged as pile-up are shown as a function of event activity for three triggers, that is, minimum bias trigger (CINT7 - coincidence of two V0 signals), di-muon (CMUL7 - coincidence of MB and two unlike sign muon trigger) and high p_{T} single muon trigger (CMSH7 - coincidence of MB and a high p_{T} trigger). The trend of pile-up is seen in the plots of Figure 3.9, the MB trigger has lower pile-up than the muon trigger.

The effect of pile-up is mostly dominant in the 0-20% event activity bin, as described in Ref [A$^+$15d]. The bulk of these pile-up events are in the 0-2% bin as seen in Figure 3.9, as a result this event activity bin is discarded. It is worth mentioning that in Figure 3.9 the pile-up fraction is only for the high p_{T} trigger (CMSH7) used in this analysis.

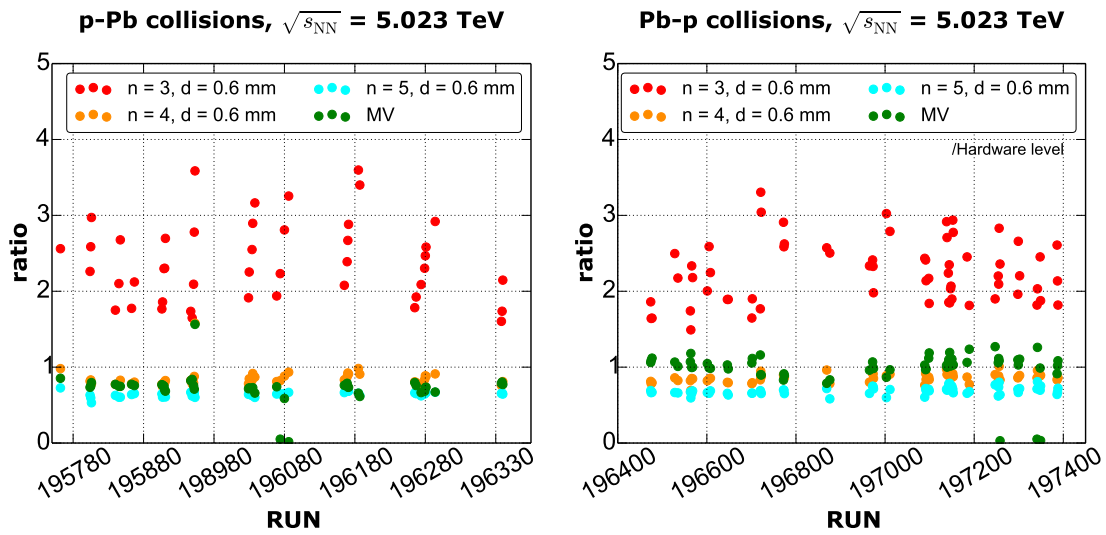

Figure 3.7: The ratio of software to hardware pile-up fraction distribution as a function of run number for the high p_{T} single muon trigger. This is equivalent to the efficiency of the SPD to tag and reject pile-up events.

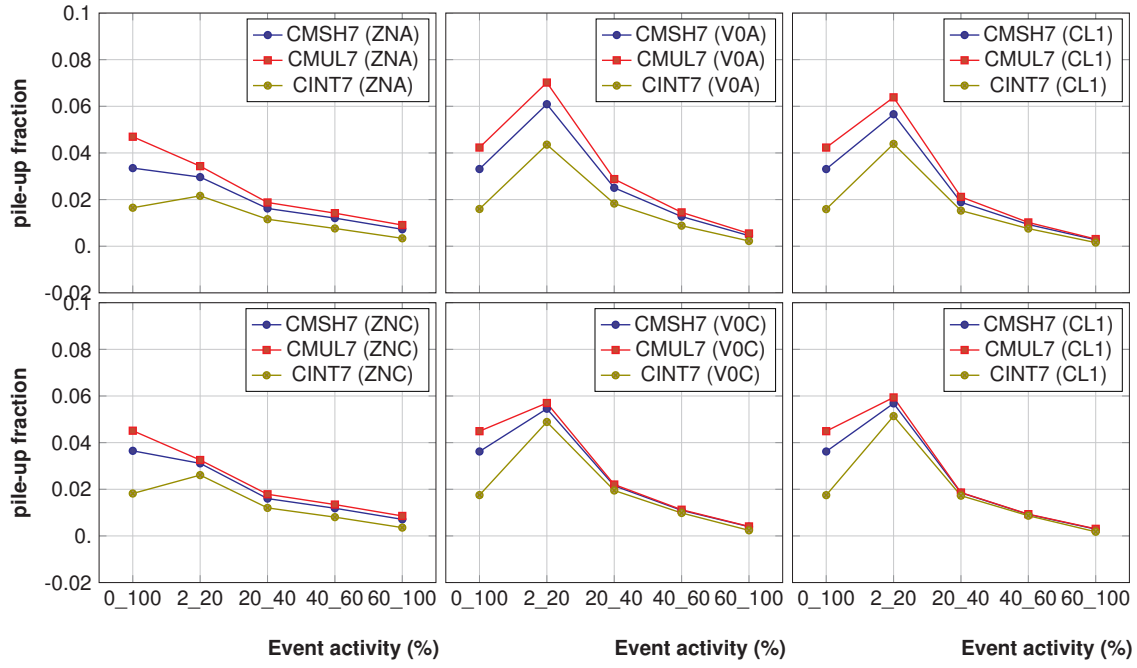

Figure 3.8: Pile-up fractions as a function of event activity for different estimators comparing different triggers (CINT7, CMUL7 and CMSH7). Pile-up events are tagged with the SPD requiring at least 4 tracks to come from a secondary vertex located 0.6 mm away from the primary vertex.

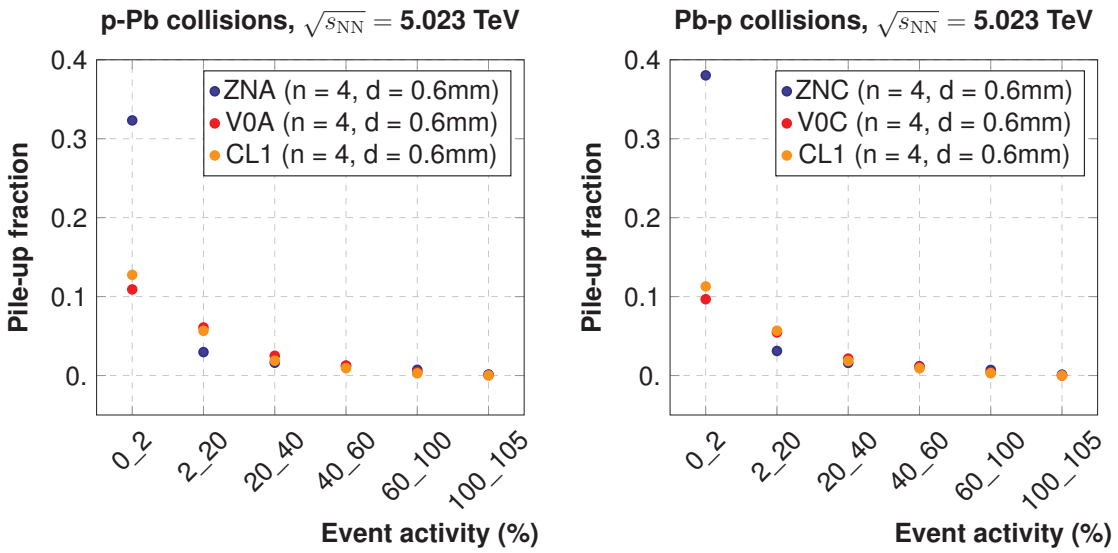

Figure 3.9: Pile-up fraction as a function of event activity for different estimators. Pile-up events are tagged with the SPD requiring at least 4 tracks to come from a secondary vertex located 0.6 mm away from the primary vertex.

3.3 The analysis strategy

The $W^{\pm}$ boson signal is extracted from the single-muon p_T distributions like the ones shown in Figure 3.10 which are composite of light and heavy flavour hadron, W- and Z-bosons decays. The semi-muonic decays of W bosons form a Jacobean peak with a maximum around $p_T \sim M_W/2 \sim 40$ GeV/c^2 as seen in Figure 3.11. Since ALICE is not equipped with a hermetic calorimeter, only the muons with high p_T are measured. The W contribution is thus extracted from the single muon p_T spectrum through a suitable fit to the distributions. As shown in Figure 3.11 there are two main background contribution to the W-boson signal, namely, muons from the decay of heavy-flavour (open charm (D) and beauty (B) meson decay) at low p_T (< 30 GeV/c) and Z-boson contribution at high p_T (> 40 GeV/c).

The signal extraction is thus a combined fit to the single muon p_T spectrum shown in Figure 3.10 with suitable templates:

$$f^{p_T} = N^{\text{raw}}_{\text{bkg}} \cdot f^{p_T}_{\text{bkg}} + N^{\text{raw}}_{\mu \leftarrow W}(f^{p_T}_{\mu \leftarrow W} + R \cdot f^{p_T}_{\mu \leftarrow Z}) \tag{3.5}$$

where, $f^{p_T}_{\text{bkg}}$ is a template of muons from B and D mesons, $f^{p_T}_{\mu \leftarrow W}$ and $f^{p_T}_{\mu \leftarrow Z}$ are $W^{\pm}$ and Z^0/γ^* boson templates, respectively. Parameters $N_{\mu \leftarrow W}$ and N_{bkg} are the number of $W^{\pm}$-boson and heavy-flavour muon candidates. $N_{B,D}$ and $N_{W^{\pm}}$ are free parameters whereas N_{Z^0/γ^*} is fixed to $N_{W^{\pm}}$ by the parameter R, which is the ratio of cross section of Z^0/γ^* to $W^{\pm}$ from POsitive Weight Hardest Emission Generator (POWHEG)

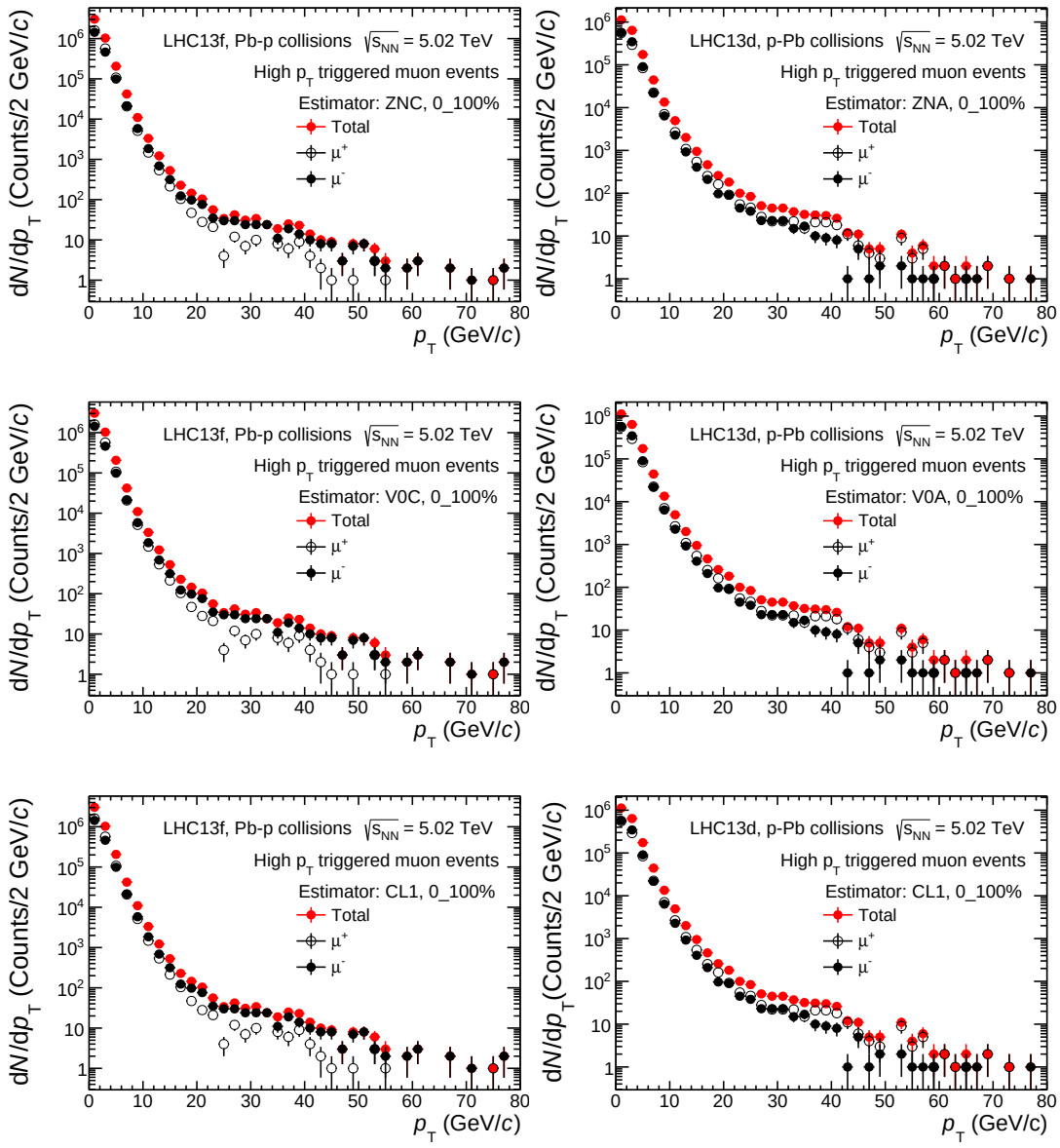

Figure 3.10: The plots show transverse momentum distributions of positive (left column) and negative (right column) muons obtained by selecting different event activity estimators - ZNA (top), V0A (middle) and CL1 (bottom) in the integrated event activity bin (0_100 %) for the p-going period.

theoretical calculations. The main steps are:

- Monte Carlo templates and $A \times \varepsilon$ correction
- Signal extraction
- Normalisation to MB to get the cross-section

Both the signal extraction and the $A \times \varepsilon$ corrections require the determination of

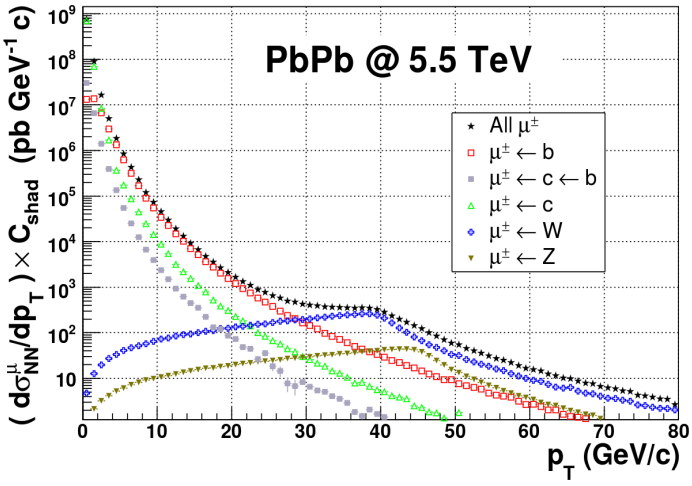

Figure 3.11: The plot showing the contributions to the inclusive single muon transverse momentum spectrum from the PYTHIA MC generator. The inclusive single muon spectrum is shown in black stars [CdV09].

the shape of the p_{T}-distribution of muons from $\mathrm{W}^{\pm}$ boson decays. The background estimations are also based on Monte Carlo simulations which will be described next.

3.3.1 Monte Carlo templates and $A \times \varepsilon$ correction

Monte Carlo methods are popular in physics as tools to estimate the production rate of a certain process and assess detector responses. The former is performed by event generators which are programs (mostly written in the FORTRAN programming language) used to describe the full evolution of the collision. The latter which are used to describe the detector elements composition, spatial position and angular coverage takes the output of event generators as inputs in order to simulate detector responses. Described below are inputs and configurations used to generate templates used for signal extraction.

W and Z templates

The W and Z templates are based on the POWHEG [ANOR08] Next-to-Leading Order (NLO) event generator coupled with PYTHIA6.425 [SMS06] for parton showers. These simulations are performed with CT10 [NLC+08] PDFs. In case of proton-lead collisions, EPS09 [EPS09] parametrization is also used to take into account the nuclear modification of PDFs. The muons from the decay of W and Z bosons are then propagated through the absorption material using GEANT3 [BCG94] to take into account the detector effects. A run-by-run simulation is performed in order to take into account the configuration of the detector in a certain run. These configurations

are saved per run in an Offline Condition DataBase[4] (OCDB).

In order to take into account the isospin dependent nature of W- and Z-boson templates are simulated separately for pp and pn collisions and combined according to Equation 3.6 below:

$$\frac{1}{N_{\mathrm{pPb}}} \cdot \frac{\mathrm{d}N_{\mathrm{pPb}}}{\mathrm{d}p_{\mathrm{T}}} = \frac{Z}{A} \cdot \frac{1}{N_{\mathrm{pp}}} \cdot \frac{\mathrm{d}N_{\mathrm{pp}}}{\mathrm{d}p_{\mathrm{T}}} + \frac{A-Z}{A} \cdot \frac{1}{N_{\mathrm{pn}}} \cdot \frac{\mathrm{d}N_{\mathrm{pn}}}{\mathrm{d}p_{\mathrm{T}}} \tag{3.6}$$

where, $A(=208)$ and $Z(=82)$ represents the mass and the atomic number of a lead ion, and $1/N_{\mathrm{pp}}\mathrm{d}N_{\mathrm{pp}}/\mathrm{d}p_{\mathrm{T}}$ and $1/N_{\mathrm{pn}}\mathrm{d}N_{\mathrm{pn}}/\mathrm{d}p_{\mathrm{T}}$ are the MC templates normalised to the total number of events for pp and pn collisions, respectively. Figure 3.12 shows the Monte Carlo generated shapes for muons from W-boson as a function of transverse momentum for pp and pn collisions.

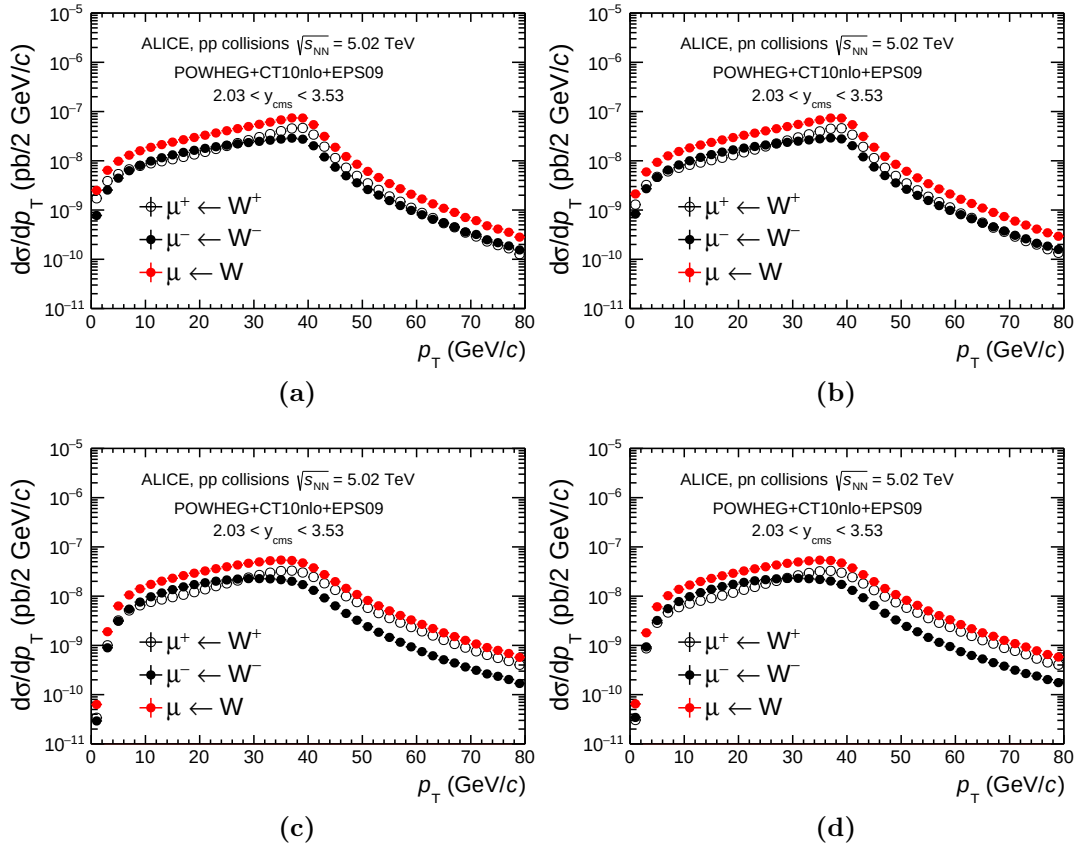

Figure 3.12: Generation level (a) and (b) templates for pp and pn collisions at 5.02 TeV using POWHEG and CT10 with EPS09 PDFs. The reconstruction level templates are shown in (c) and (d). These were reconstructed with alignment 6 (Table 3.4).

In this analysis, the muon templates (W, Z and heavy flavour) are reconstructed with two alignement configurations (in this analysis called aligment 5 and 6) of the muon

[4]Offline Condition DataBase (OCDB) is a catalog of files containing the calibration and alignment data. These are read-only run dependent ROOT objects stored on AliEn.

tracking chambers. Shown in Figure 3.13 are the responses of the detector as a function of muons from the W-boson decay using one of the alignment files from the OCDB. $A \times \varepsilon$ is a quotient of reconstructed and generated transverse momentum distribution under the same kinematic cuts. The difference between the $A \times \varepsilon$ of positive and negative muons as seen in Figure 3.13 (negative dipole polarity) stems from the fact that muons pass opposite side of the chambers which may be differently misaligned. This effect is mirrored in the positive dipole polarity case which sees the negative muons having a similar $A \times \varepsilon$ trend as positive muons in the negative dipole polarity case (see Figure A.3, sub-figure A.3e and A.3f).

As mentioned in section 2.2.4 the alignment of the tracking chamber plays a crucial role in the muon analysis at high p_{T}. This is exhibited in Figure 3.13 in which the $A \times \varepsilon$ is greater than unity for the W^{+} channel, which means that more positive muons are reconstructed at high p_{T} than generated. The position of the chambers is determined before data taking using photogrametry with a precision of about 100 μm using a modified version of the MILLIPEDE [V. 09b] package. This package combines data taken with and without the magnetic field. The residual misalignment of the tracking chamber is taken into account in the simulations using alignment files obtained using MILLIPEDE to compute the acceptance times efficiency. While this method gives an accurate estimate of the relative chamber alignment, it is not sensitive to the global alignment of the whole spectrometer. The bias can be reduced with an iterative approach to create many alignment files, but can not be completely avoided. The residual misalignment results in a shift of the reconstructed momentum of the particle. This shift is expected to affect in opposite directions the positively and negatively charged particles. This bias is estimated by performing reconstruction of the simulation with different alignment files. The templates obtained with an alignment file which tends to reproduce the Upsilon (Υ) resolution seen in data (p-Pb) was used for signal extraction. The comparison of the two alignment files is shown in Figure 3.14, alignment 5 reproduce the Υ mass peak resolution whereas alignment 6 was produced with an intent to degrade this resolution in order to reproduce the one seen in p-Pb collisions data. According to the pp results (see Chapter 4 and Section 4.5) these alignment files underestimate the effect of mis-alignment. In view of this, a data-driven method based on the parametrisation of the measured resolution of the clusters associated to a track was developed to simulate the muon tracker response [Pil14]. The difference between the cluster and the reconstructed track position was parametrized by the Crystal-Ball function [Gai82].

Figure 3.15 shows the effects of the resolution task on the W-boson p_{T} spectra in comparison with the residual alignment files. Furthermore, the effect of the resolution task affects the negatively and positively charged muons in opposite direction as seen in Figure 3.15. The effect of the resolution affects the p_{T} spectra in opposite direction at low and high p_{T} relative to both alignment 5 and 6.

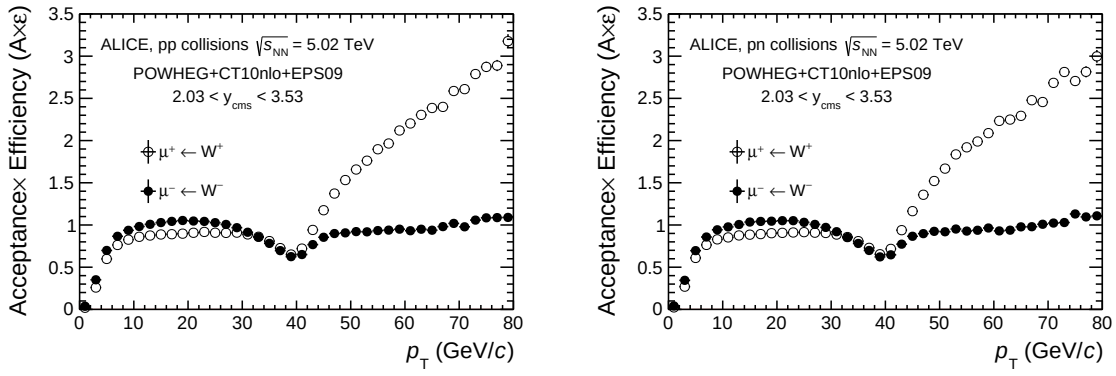

(a) **(b)**

Figure 3.13: $A \times \varepsilon$ as a function of transverse momentum for LHC13d period obtained from pp (left) and pn (right) templates. The plots for LHC13e and LHC13f can be seen in Appendix A.2.

LHC13d ($A \times \varepsilon$)

	μ^+	μ^-
Alignment 5	0.90	0.90
Alignment 6	0.89	0.89
Resolution Task	0.89	0.88

LHC13e ($A \times \varepsilon$)

	μ^-	μ^+
Alignment 5	0.88	0.89
Alignment 6	0.88	0.88
Resolution Task	0.86	0.88

LHC13f ($A \times \varepsilon$)

	μ^-	μ^+
Alignment 5	0.75	0.77
Alignment 6	0.75	0.77
Resolution Task	0.74	0.76

Table 3.4: Acceptance times efficiency for muons from W-boson decay with $p_{\mathrm{T}} > 10$ GeV/c and $-4 < -4 < \eta^{\mu}_{\mathrm{lab}} < -2.5 \ < -2.5$ the three periods. The uncertainty is less than 0.1% error for all the periods.

Heavy flavour decay muons templates

The distribution of muons from heavy flavour decays is described by means of simulations using the FONLL predictions for pp collisions at 5.02 TeV centre-of-mass energy [CFH+12]. This is a combination of three distributions, the decay of $D \to e$, $B \to D \to e$ and $B \to e$. The calculations have been obtained using the CTEQ6.6 [NLC+08] parton distribution functions, without accounting for any nuclear modification of the PDFs. Such modifications, however, are expected to be dominant at low p_{T}, with a negligible contribution in the p_{T} region of interest in this study as shown in the nuclear modification factor of heavy flavour decay muons in [A+17a]. The cross section as a function of p_{T} shown in Figure 3.16 together with the cross section as a function of y of heavy-flavour decay muons are used to obtain

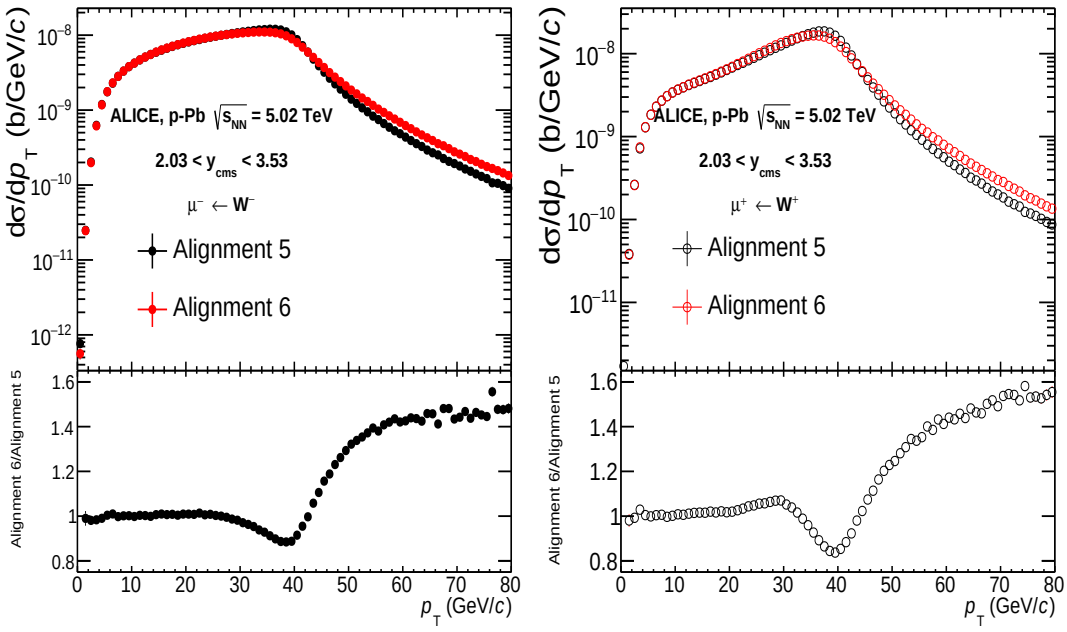

Figure 3.14: The cross section of W-boson decay muons as a function of transverse momentum for positive and negative muons on the top and bottom plots, respectively. Shown here is the comparison of the distribution reconstructed with two residual alignment files.

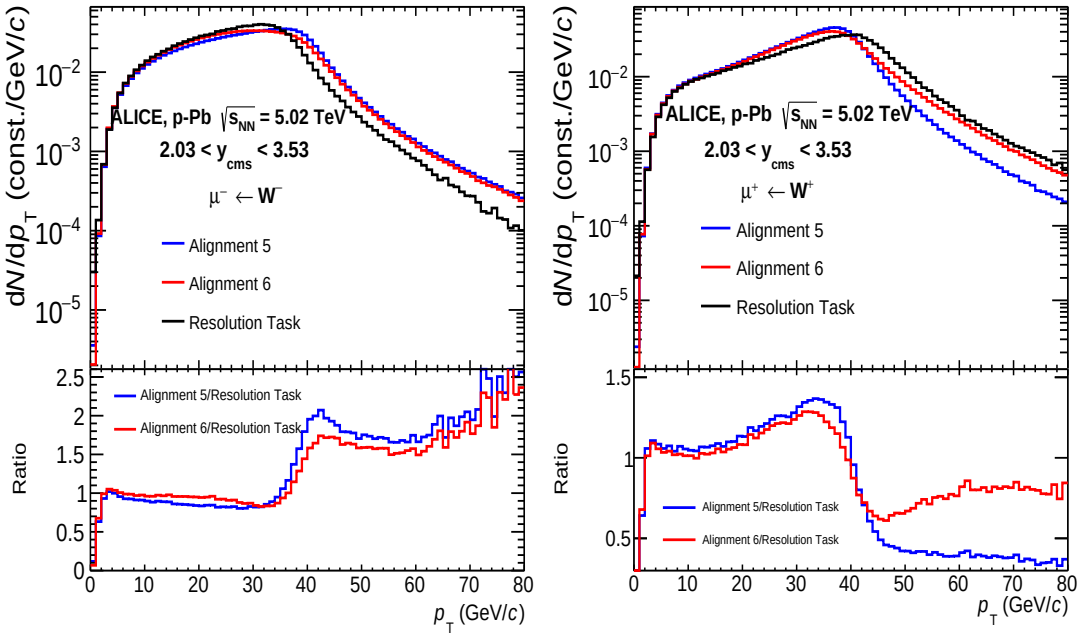

Figure 3.15: The comparison of templates using residual alignments and the data-driven methods. On the top and bottom is the distribution of negatively and positively charged muons, respectively.

the reconstructed distributions. The y distributions are shown in Appendix A.1. In order to take into account the uncertainty associated with FONLL, the shape of the template is changed by considering the minimum and maximum of i) renormalisation and factorization scales[5], ii) quark masses and iii) parton distribution functions. It is worth mentioning that the PDF uncertainty is based on the minimum and maximum of CTEQ6.6 PDF error band. The new shapes are obtained by using the ratio of the distributions varying the scales to the central prediction (default parameters) as weights when analyzing the simulation with the central prediction. The weights are shown in Figure 3.17. The templates obtained with this re-weighting procedure are shown in Figure 3.18

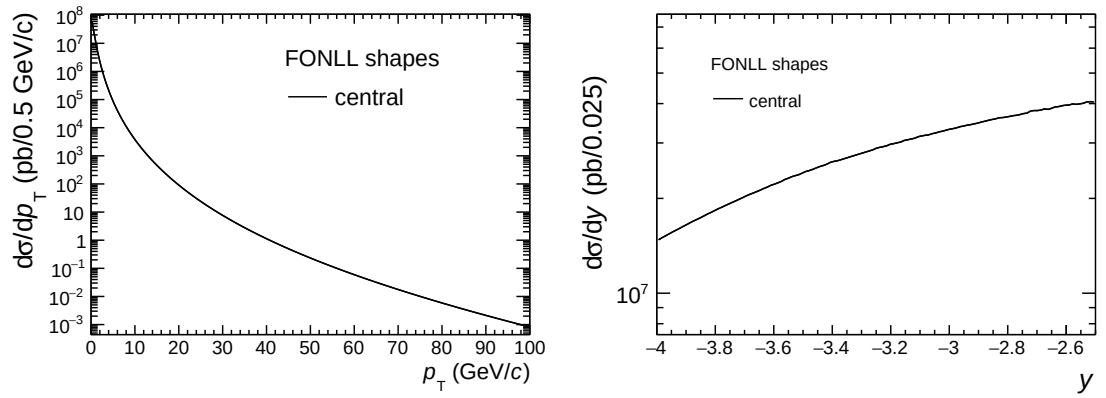

Figure 3.16: The cross section of heavy-flavour muons as a function of transverse momentum (top) and rapidity(bottom). Shown here are the central predictions (with default parameters) of the calculation.

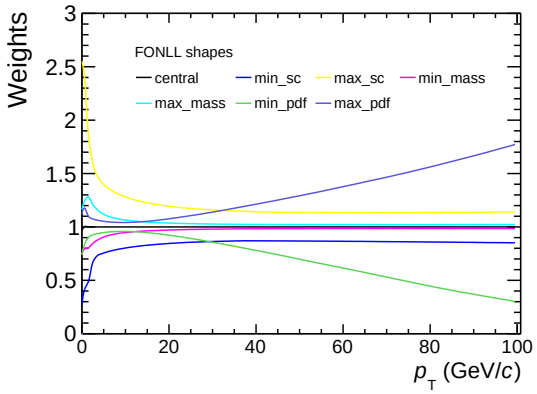

Figure 3.17: The weights (ratio of distributions varying scales, mass and PDFs to the central predictions) of muons from heavy-flavour decays calculated with FONLL by varying factorization scales.

In addition, it is worth mentioning that the iron wall placed before the muon trigger station is effective at rejecting low-p_{T} muons which are mainly produced by the decay of light hadrons and by secondary muons produced in the absorber. The matching of

[5] $\mu_0 = \mu_F = \sqrt{m^2 + p_{\mathrm{T}}^2}$, where m and p_{T} are the mass and the transverse momentum of the heavy quarks (charm and beauty)

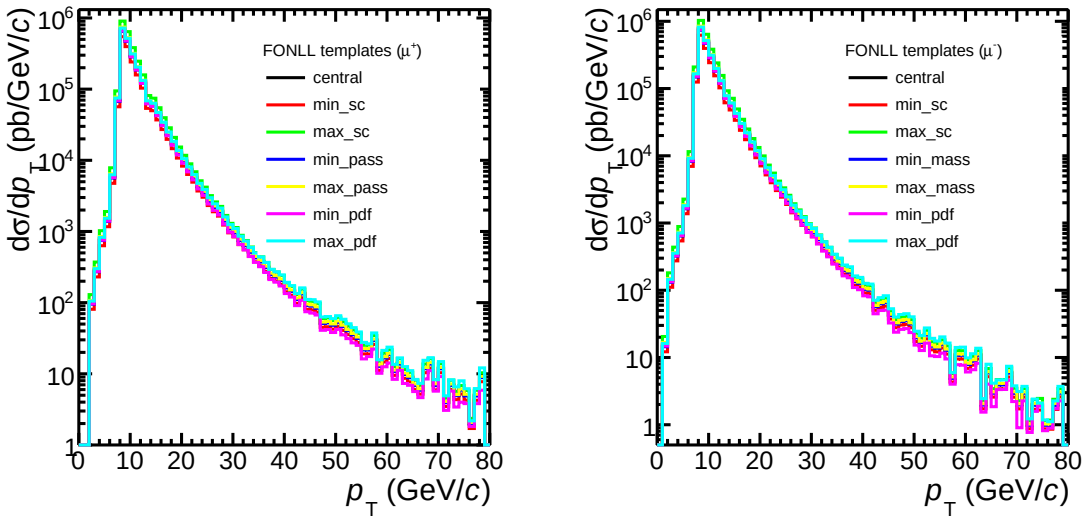

Figure 3.18: The plots on the left and right shows the templates of heavy-flavour decays to negative and positive muons as a function of p_{T} respectively.

the trigger and tracker tracks help to further reject this background. This contribution is steeply falling with p_{T} much more than the heavy-flavour muon contribution. This contribution is about $\sim$2% in the p_{T} region of interest. In the signal extraction procedure, we account for the modifications of the heavy flavour MC templates, and the introduced modifications of the shape are larger than the ones that would arise from the residual contamination of light hadron decays. So the effect of the residual contamination from light-hadron decays is within our systematics.

3.3.2 Signal extraction

In the combined fit to data (Eq. 3.5), the ratio R, which is defined as explained in Section 3.3, is fixed. In order to extract $N_{\mu\leftarrow\mathrm{W}}$, different fits are performed by varying the lower fitting range between $15 \leq p_{\mathrm{T}} \leq 18$ GeV/c with steps of 1 GeV/c and the higher limit is fixed to 50 GeV/c. This is an optimised fit region for the integrated event activity bin which has a lot of statistics. However, as we go differential in event activity bins the decrease in statistics makes the signal extraction a bit tricky. Thus, the lower fit range is moved to $p_{\mathrm{T}} = 10$ GeV/c where the statistics is enough to have control over the fit components, especially the heavy-flavour decay muon background. The upper limit of the lower fit range is set to $p_{\mathrm{T}} = 20$ GeV/c whereas the upper fit range is varied from 50 to 80 GeV/c with steps of 5 GeV/c.

$N_{\mu\leftarrow\mathrm{W}}$ is extracted from the fit trials which pass the criteria below:

- fits must be valid (`TFitResult::IsValid()` has to be `TRUE`)
- fits must converge (`gMinuit->fCstatus` has to be `CONVERGED`)

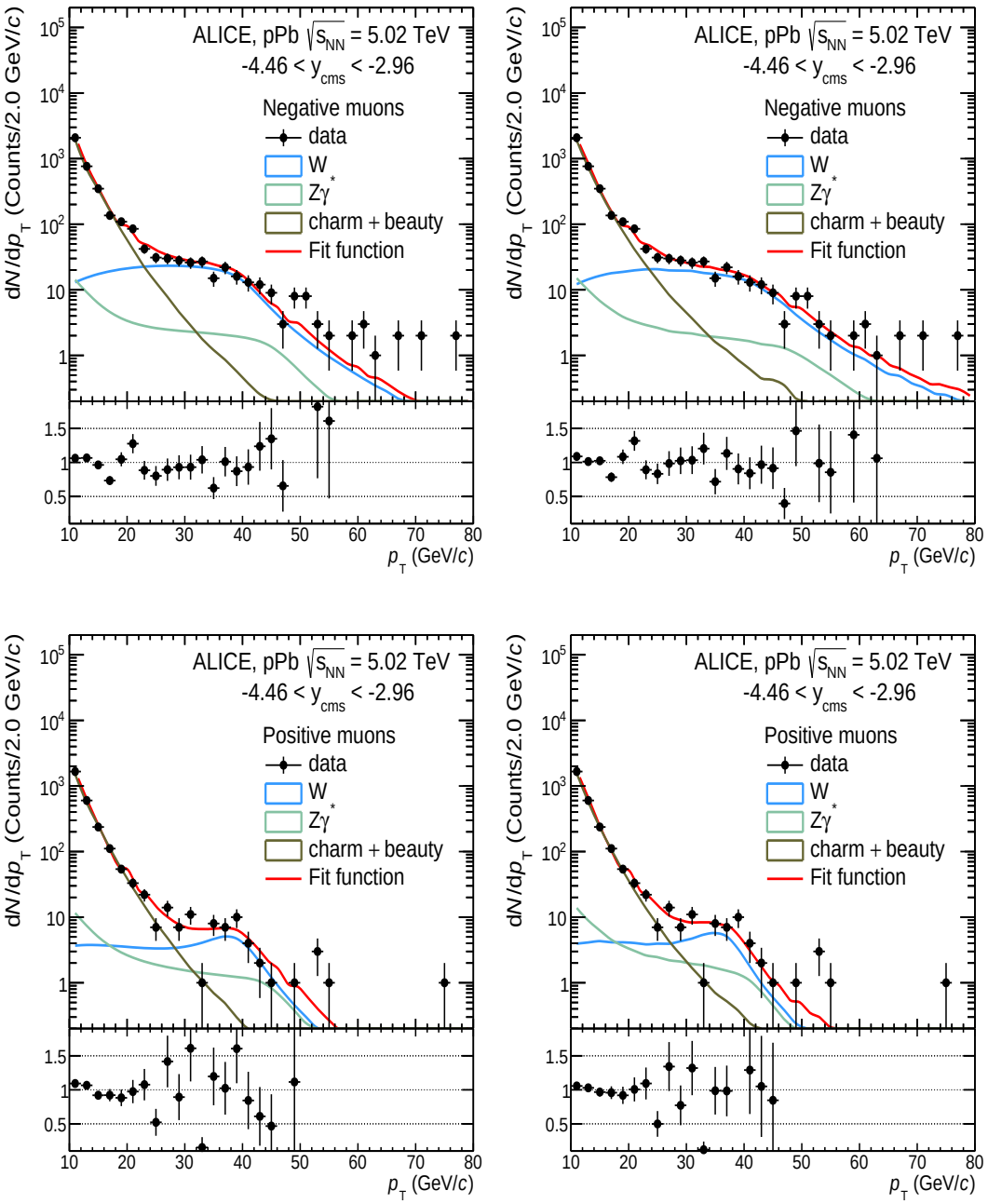

Figure 3.19: Inclusive distribution of negatively (top) and positively (bottom) charged muon candidates measured in the Pb-going data taking periods. On the left and right are plots obtained by fitting with templates from alignment 6 and the resolution task, respectively. The results of the MC template fit for the extraction of the $\mu^+ \leftarrow \mathrm{W}^+$ and $\mu^- \leftarrow \mathrm{W}^-$ signal is shown. In this case, the central value of the FONLL calculations is used for the background description while POWHEG with the CT10 PDF set paired with EPS09NLO is used for W and Z boson production. Bottom panels: ratio of data and the extrapolated fit results in the range $10 < p_{\mathrm{T}} < 80$ GeV/c.

- the covariant matrix is required to be accurate (`TFitResult::CovMatrixStatus()==3`)

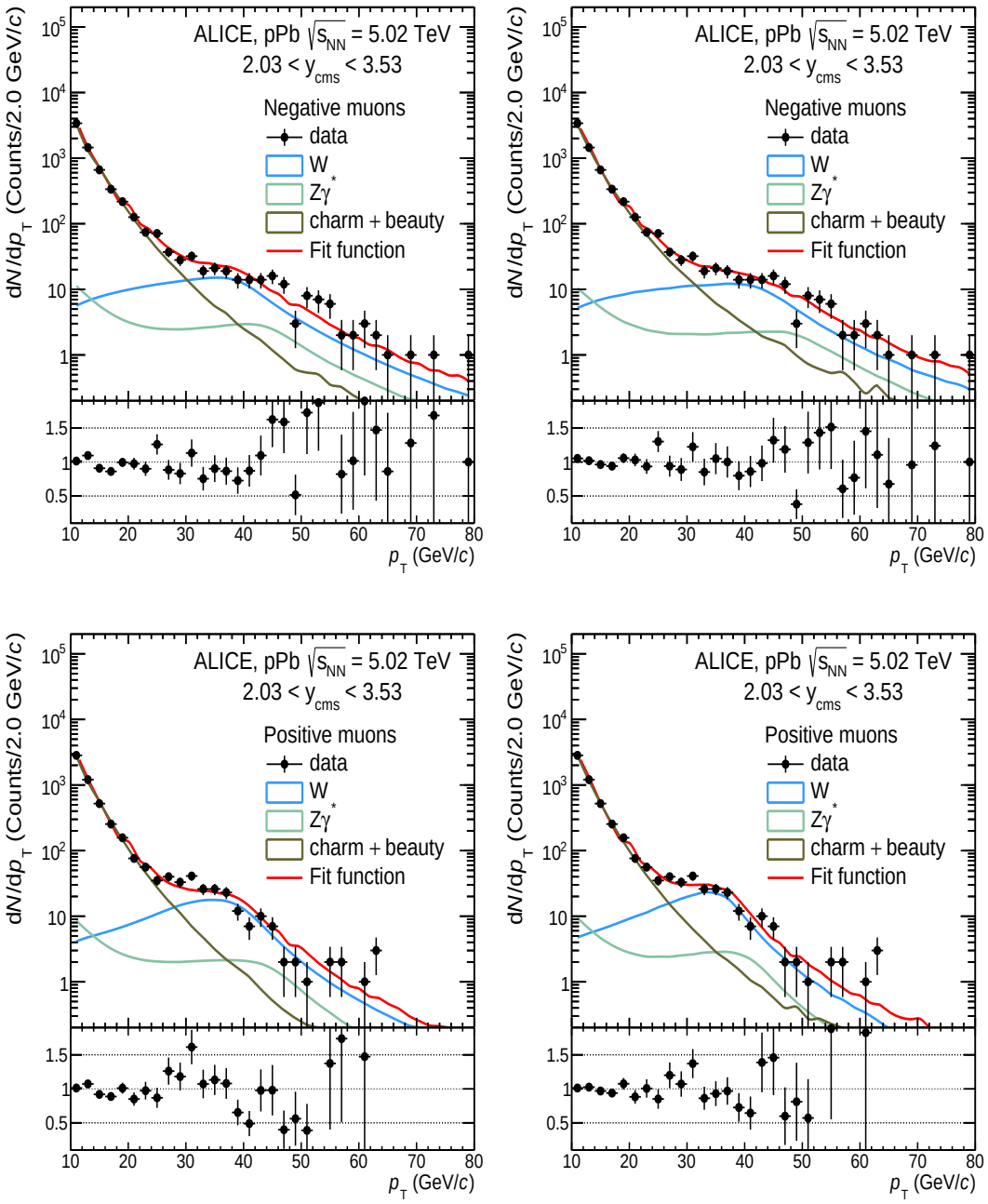

Figure 3.20: Inclusive distribution of negatively (top) and positively (bottom) charged muon candidates measured in the p-going data taking periods. On the left and right are plots obtained by fitting with templates from alignment 6 and the resolution task, respectively. The results of the MC template fit for the extraction of the $\mu^+ \leftarrow \mathrm{W}^+$ and $\mu^- \leftarrow \mathrm{W}^-$ signal is shown. In this case, the central value of the FONLL calculations is used for the background description while POWHEG with the CT10 PDF set paired with EPS09NLO is used for W and Z boson production. Bottom panels: ratio of data and the extrapolated fit results in the range $10 < p_{\mathrm{T}} < 80$ GeV/c.

- fits must have $\chi^2/\mathrm{NDF} < 2$

Since there are empty bins, the log-likelihood method was used in the fit. The difference with respect to the chi-square method, however, was tested to be small, since the fit results are driven by data points with $p_{\mathrm{T}} \lesssim 60$ GeV/c.

The example of the combined fit for the backward rapidity ($-4.46 < y^{\mu}_{\mathrm{CMS}} < -2.96$) in the centrality bin are shown in Figure 3.19 whereas the forward rapidity ($2.03 < y^{\mu}_{\mathrm{CMS}} < 3.53$) plots are shown in Figure 3.20. The fit function describes data at intermediate $p_{\mathrm{T}} < 40$ GeV/c whereas at higher p_{T} statistical fluctuation plays a role. It is worth mentioning that, due to high rapidity reach at backward rapidity, the heavy-flavour decay muon distributions do not play a significant role at high-p_{T} where the signal is abundant. The fraction of Z-boson to heavy-flavour decay muons in Pb-going (p-going) direction is about 0.2 and 0.15 (0.7 and 0.6) for negatively and positively charged muons.

Number of W-boson

The final number of muons from W-boson decays is the weighted average of the tests, defined as:

$$\langle N_{\mu\leftarrow \mathrm{W}} \rangle = \frac{\sum_{i=1}^{n} w_i N_{\mu\leftarrow \mathrm{W,i}}}{\sum_{i=1}^{n} w_i} \tag{3.7}$$

where i runs over the number of n tests performed and $N_{\mu\leftarrow \mathrm{W},i}$ is the number of muons from W-boson decays extracted in each test. i includes the variation of p_{T} fit range, heavy-flavour decay muon shapes (variation of FONLL shapes with uncertainties) and MC template shapes. The weight, w_i, is defined as:

$$w_i = 1 \tag{3.8}$$

The statistical error is given by the average of the error in each measurement:

$$\sigma_{\langle N_{\mu\leftarrow \mathrm{W}} \rangle} = \frac{\sum_{i=1}^{n} (w_i \sigma_{\mu\leftarrow \mathrm{W,i}})}{\sum_{i=1}^{n} w_i} \tag{3.9}$$

Finally, the Root Mean Square (RMS) of the distribution:

$$RMS = \sqrt{\frac{\sum_{i=1}^{n} w_i N^2_{\mu\leftarrow \mathrm{W,i}}}{\sum_{i=1}^{n} w_i} - \langle N_{\mu\leftarrow \mathrm{W}} \rangle^2} \tag{3.10}$$

is the systematic error.

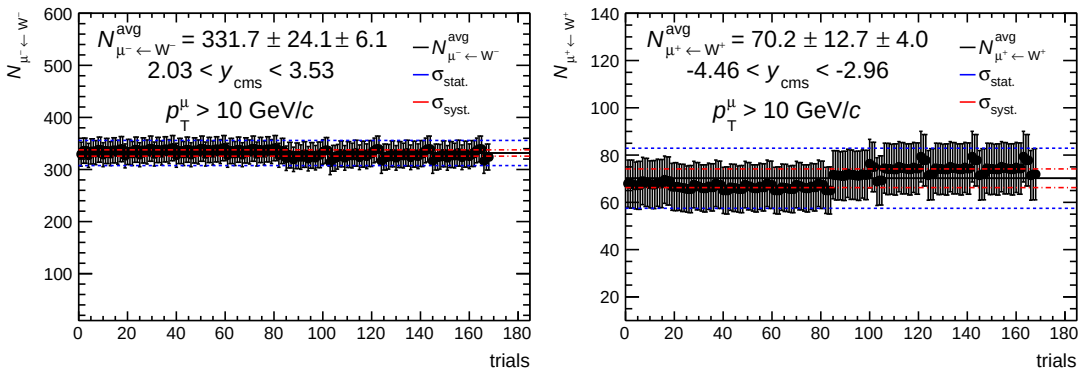

Figure 3.21: N_{W} extracted per trial for Pb-going direction period in the integrated event activity bin for negative (left) and positive (right) muons. $N^{\mathrm{avg}}_{\mu^{\pm}\leftarrow \mathrm{W}^{\pm}}$, $\sigma_{\mathrm{stat.}}$ and $\sigma_{\mathrm{syst.}}$ is the average number of W-boson, statistical uncertainty and systematic uncertainty, respectively. The line in black represents $N^{\mathrm{avg}}_{\mu^{\pm}\leftarrow \mathrm{W}^{\pm}}$, and the bounds of statistical and systematic uncertainties are in blue and red.

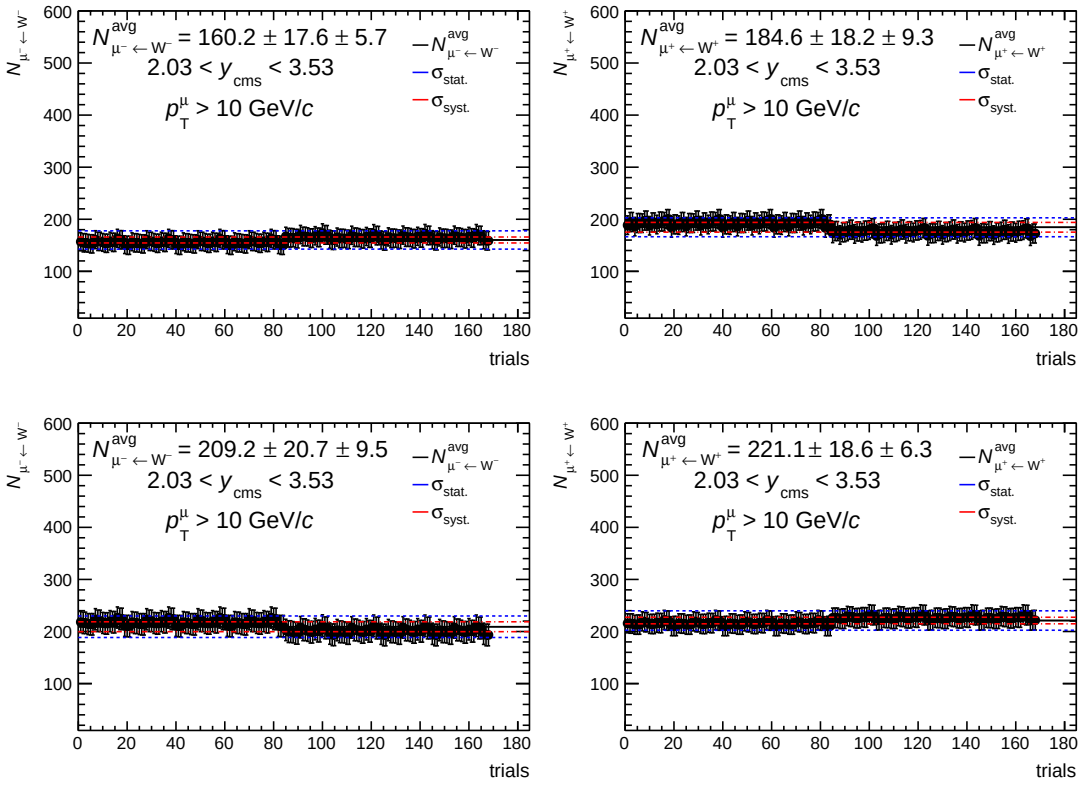

Figure 3.22: N_{W} extracted per trial for p-going (LHC13d in the top two plots and LHC13e in the bottom two plots) direction period in the integrated event activity bin for negative (left) and positive (right) muons. $N^{\mathrm{avg}}_{\mu^{\pm}\leftarrow \mathrm{W}^{\pm}}$, $\sigma_{\mathrm{stat.}}$ and $\sigma_{\mathrm{syst.}}$ is the average number of W-boson, statistical uncertainty and systematic uncertainty, respectively. The line in black represents $N^{\mathrm{avg}}_{\mu^{\pm}\leftarrow \mathrm{W}^{\pm}}$, and the bounds of statistical and systematic uncertainties are in blue and red.

The opposite effect on negative and positive muons is visible in Figures 3.21 and 3.22. The trials which are systematically down or up are from fitting with templates obtained with the resolution task (trials > 80). In Table 4.3 is the number of W-boson extracted as a function of centrality.

Centrality	**LHC13de**		**LHC13f**	
(%)	$N_{\mu^+\leftarrow \mathrm{W}^+}$	$N_{\mu^-\leftarrow \mathrm{W}^-}$	$N_{\mu^+\leftarrow \mathrm{W}^+}$	$N_{\mu^-\leftarrow \mathrm{W}^-}$
0−100	406±26.0±11.3	370±27.1±11.1	70±10.3±4.0	332±24.1±6.1
2−20	103±12.7±4.1	90±13.1±6.2	24±6.1±2.2	84±12.0±4.7
20−40	133±14.00±5.0	107±13.7±5.5	20.±5.2±1.4	99±12.5±5.9
40−60	68±10.4±3.2	73±11.4±3.6	17±4.7±1.1	63±10.0±3.1
60−100	76±11.0±3.8	65±10.6±2.8	8±3.5±0.9	77±11.0±3.0

Table 3.5: Weighted average of the number of W-boson decay muons for different centrality bins for Pb-going and p-going direction. The second and third number are statistical and systematic uncertainty, respectively.

3.3.3 Normalization to minimum-bias (MB)

In experimental physics, particularly in high energy physics where experiments are looking for rare processes in high luminosity environment, a criterion to select interesting events is required. This criterion is known as a "trigger". "Trigger systems are necessary due to real-world limitations in data storage capacity and rates" [VM16]. For example, high transverse momentum muons were selected and used in this analysis. The sample analysed is a fraction of minimum bias events. In order to obtain the MB equivalent of muon triggered events, a suitable normalization factor ($F_{\rm norm}$) which can be obtained with two different methods, is used. The first method which utilizes the trigger outputs and the CTP trigger inputs is termed ‟offline method″. The corresponding normalization factor for MSH triggers are defined as:

$$F_{\rm norm}^{\rm MSH} = \frac{N_{\rm MB} \times F_{\rm pile-up}}{N_{\rm (MB\&\&0MSL)}} \times \frac{N_{\rm MSL}}{N_{\rm (MSL\&\&0MSH)}} \tag{3.11}$$

where $F_{\rm pile-up}$ is the pile-up correction factor for minimum bias events (see later), $N_{\rm MB}$, $N_{\rm MSL}$ and $N_{\rm MSH}$ are the number of MB, MSL and MSH triggers, while 0MSL and 0MSH are the L0 trigger inputs for the single low and high $p_{\rm T}$ triggers, respectively. These results as a function of run number are shown in Figure 3.23, whereas the results as a function of centrality are shown in Figure B.3 of Appendix B.

The second one, termed ‟scaler method″uses the information of L0b (latent zero before any selection) counters which helps in avoiding statistical fluctuations. The corresponding normalization factor is:

$$F_{\rm norm}^{\rm MSH} = \frac{\rm L0b_{MB} \times purity_{MB} \times F_{pile-up}}{\rm L0b_{MSH} \times PS_{MSH}} \tag{3.12}$$

where $\rm L0b_{MB}$ and $\rm L0b_{MSH}$ are the scaler values recorded for minimum bias and muon single high triggers (see Figure B.1 of Appendix B), respectively and $\rm purity_{MB}$ is the fraction of events which satisfy the V0 timing cut. The purity is better than 99% for most of the runs Figure B.2. $PS_{\rm MSH}$ is the fraction of (accepted) MSH trigger events that pass the Physics Selection which is better than 96% for most runs Figure B.2. The values obtained for the normalisation factor ($F_{\rm norm}$) as given in Table 3.6.

	LHC13de		**LHC13f**	
$F_{\rm norm}$	Offline	Scaler	Offline	Scaler
MSH	1021.1	1032.8	794.5	798.3

Table 3.6: Mean values of the normalisation factors for muon single high triggers obtained with the two methods described in the text.

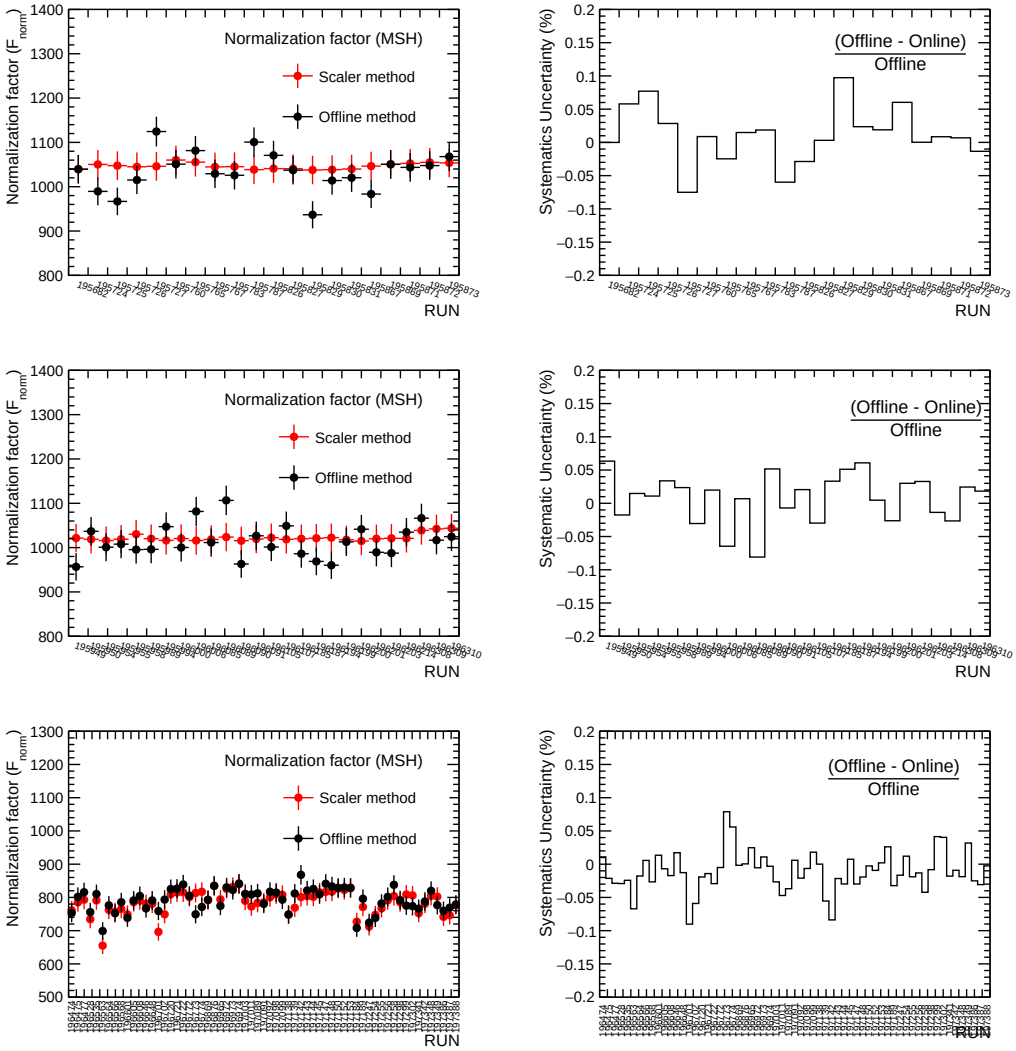

Figure 3.23: Normalization factor (scaler and offline method) as a function of run number for the LHC13d (top), LHC13e (middle) and LHC13f (bottom).

Integrated luminosity

Since the data samples were collected with the muon triggers the integrated luminosities used in the analysis are computed by estimating the number of MB events corresponding to the muon-triggered data samples and then dividing by the MB cross section (σ_{MB}). σ_{MB} for the two periods were measured from Van der Meer (vdM) scans to be 2.12 ± 0.07 b and 2.09 ± 0.07 b for the Pb-going and p-going samples, respectively [A+14c]. These results were obtained using the V0-based method which has a 1% deviation from the T0-based results. This discrepancy is taken into account in the systematic uncertainties. The integrated luminosity $\mathcal{L}_{\mathrm{int}}$ is computed as

$$\mathcal{L}_{\mathrm{int}} = \frac{F_{\mathrm{norm}} \cdot N_{\mathrm{MSH}}}{\sigma_{\mathrm{MB}}}. \tag{3.13}$$

The values of the integrated luminosity are shown in Table 3.7.

	LHC13de	LHC13f
$\mathcal{L}_{\text{int}}$ (nb^{-1})	5.03 ± 0.18	5.81 ± 0.20

Table 3.7: Integrated luminosity for the two data taking periods (Pb-going or LHC13f) and (p-going or LHC13de).

3.4 Systematic uncertainty

Summarized below and shown in Figure 3.25 and Table 3.9 are sources of systematic uncertainty. In Figure 3.25, total is a quadrature sum of all systematic uncertainties as used for the plots in Figure 3.35. In Figure 3.36 the $\langle N_{\text{coll}} \rangle$ systematics associated with each estimator are used.

Tracking and trigger efficiency

The systematic on tracking, trigger and tracker-trigger matching efficiency for the analysed periods have been estimated elsewhere. The results are reported in the paper of the measurement of J/ψ production in p–Pb collisions at $s_{\text{NN}} = 5.02$ TeV [A$^+$14b]. The procedure therein is detailed in Ref. [A$^+$11b]. The uncertainty on the muon tracking efficiency is estimated from the difference between the muon tracking efficiency in MC and that from a data-driven approach based on the redundancy of the tracking stations. It amounts to 2% (3%) for the p-going (Pb-going) period. The uncertainty on trigger efficiency, which is mainly due to the systematic uncertainty in the determination of the efficiency of each trigger chamber from data, amounts to 1%. An additional systematic uncertainty of 0.5% results from the choice of the χ^2 cut in the matching of the tracks reconstructed in the tracker with those in the trigger. In the dimuon analysis, these systematic uncertainties apply to both muons of the pair, which are well separated in phase space and therefore cross different parts of the detector.

Pile-up effect

In section 3.2.3 the two methods used to obtain pile-up were discussed. The efficiency of a pile-up flag is determined by changing the number of contributors and distance from the primary vertex. The flag (n = 4, d = 0.6 cm) provides the highest rejection efficiency (as discussed in section 3.2.3). The fraction of events rejected by the flag is the lowest in the less biased event activity estimator (ZNA and ZNC). The centrality using ZNA (-C) is estimated by measuring the energy deposition while the VZERO-A(-C) and CL1 are based on measuring the hadronic multiplicity. The multiplicity-based

centrality estimators are biased in p-Pb since the range of the multiplicity is of similar magnitude as its fluctuations [A$^+$15e]. Table 3.8 summarizes the fraction of rejected events as a function of event activity using the SPD pile-up rejection. In the centrality integrated cross-section measurement as a function of rapidity, the pile is corrected for and thus this systematic uncertainties is not included.

Centrality	**ZN**		**V0**		**CL1**	
(%)	p-going	Pb-going	p-going	Pb-going	p-going	Pb-going
0−2	0.32	0.380	0.11	0.097	0.13	0.11
2−20	0.03	0.0311	0.061	0.055	0.067	0.06
20−40	0.016	0.016	0.025	0.022	0.02	0.019
40−60	0.012	0.012	0.013	0.011	0.009	0.009
60−100	0.007	0.007	0.0045	0.004	0.003	0.003
0−100	0.034	0.0365	0.033	0.036	0.033	0.036

Table 3.8: The table summarizing the fraction of rejected number of events as a function of event activity.

Alignment

The systematic uncertainty that arises as a result of the alignment of the tracking chambers is assessed as a difference between the misalignment obtained from the data and the data-driven Monte-Carlo described in Section 3.3.1. The difference between these methods is 1% as seen in Table 3.4.

Signal extraction

Since the number of muons from W-boson decays is normally distributed for each signal extraction method (residual alignment and data-driven method), the systematic uncertainty is thus the root mean square. Since we have limited trials in the event-activity integrated bin, the data is sampled according to a Poisson within statistical errors and the same fitting procedure is employed. The distributions of the number of W-boson in p-going (LHC13d) period for the integrated centrality bin are shown in Figure 3.24 compared with theoretical functions from the R statistical package [R C16, DMD15], whereas for p-going (LHC13e) and Pb-going (LHC13f) periods are shown in Figure B.4. As seen in these figures the number of muons from W-boson decay is normally distributed.

Clearly, the trials are normally (Gaussian) distributed and thus the RMS is a suitable systematic uncertainty for the number of W-boson.

Normalization

The systematic uncertainty is the difference between the Scaler and Offline method used to estimate the normalisation factor. The difference between these methods is 1% as seen in Table 3.6. The uncertainty on the MB cross-section is 3% [A$^+$14c], which include the difference between the σ_{MB} estimated with the V0 and T0 detectors.

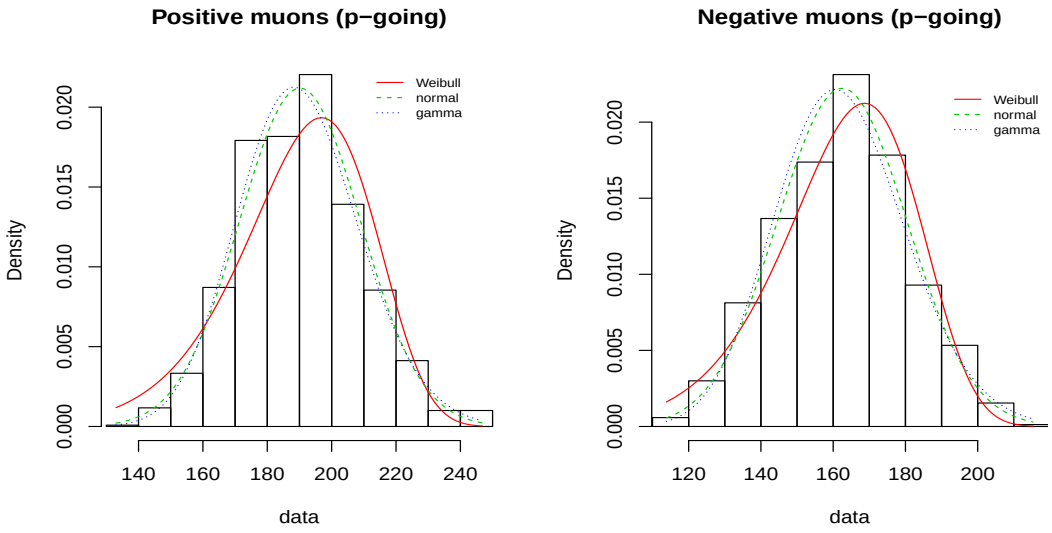

Figure 3.24: The distribution of W-boson in the p-going direction period LHC13d, the colored lines represents different theoretical distributions.

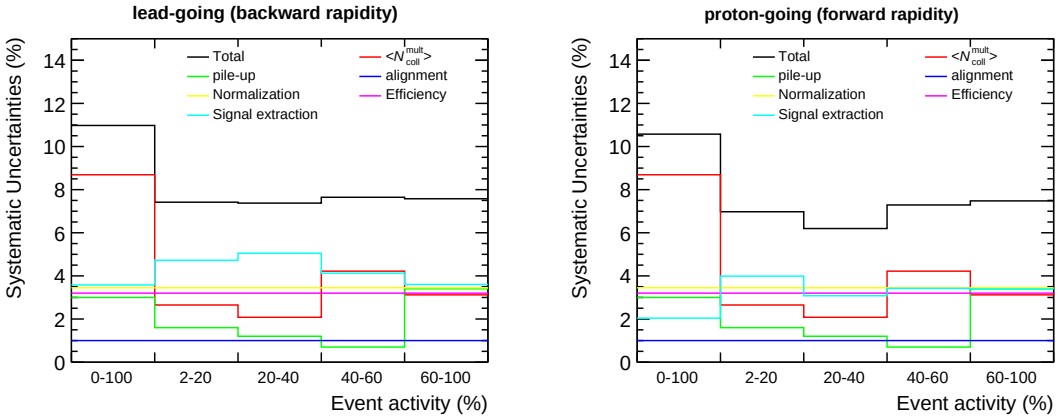

Figure 3.25: Systematic uncertainties as a function of event activity. The $\langle N_{\rm coll}^{\rm mult} \rangle$ uncertainty is the dominant source of systematic. It is worth mentioning that the $\langle N_{\rm coll}^{\rm mult} \rangle$ is the one from ZN-estimator. Total is a quadrature sum of all systematic uncertainties.

Signal extraction	2 – 6%
- vs centrality	5 – 15%
Tracking efficiency	2% (p-going) 3% (Pb-going) (c)
Trigger efficiency	1% (c)
Tracker/trigger matching	0.5% (c)
Alignment	1% (c)
$F_{\rm norm}$	1% (c)
MB cross section	3% (c)
Pile-up	1 - 4 %
$\langle N_{\rm coll}^{\rm mult} \rangle$	2 – 8%

Table 3.9: Summary of systematic uncertainties for W-boson analysis. The uncertainties that are correlated between measurements in different centrality bins are indicated with (c).

3.5 Results

In this section, the results obtained from analysis are described. They include the cross-section, charge ratio and asymmetry, $\langle N_{\rm coll}\rangle$-normalized cross-section ($\sigma^{\langle N_{\rm coll}\rangle}_{\mu\leftarrow \rm W}$) as a function of event activity W-boson to Z-boson ratio as well as the backward to forward ratio. The results for the $\langle N_{\rm coll}\rangle$-normalised cross section include those discussed in the paper [A+15e] which were obtained using a less-biased event activity estimator as well as those obtained using other estimators (CL1 and V0A(-C)).

3.5.1 Cross section

The cross-section of W-boson decay muons is computed as

$$\sigma_{\mu^{\pm}\leftarrow \rm W^{\pm}} = \frac{N_{\mu^{\pm}\leftarrow \rm W^{\pm}}}{A \times \varepsilon_{\mu^{\pm}\leftarrow \rm W^{\pm}} \times \mathcal{L}_{\rm int}} \tag{3.14}$$

where: $N_{\rm W^{\pm}}$, $A\times\varepsilon_{\rm W^{\pm}}$ and $\mathcal{L}_{\rm int}$ is the number of W-boson decay muons, the acceptance times efficiency and the integrated luminosity, respectively. The cross-section of muons from $\rm W^+$ and $\rm W^-$ boson decays with $p_{\rm T} > 10$ GeV/c measured at forward ($2.03 < y_{\rm cms} < 3.53$) and backward ($-4,46 < y_{\rm cms} < -2.96$) rapidities are shown in Figure 3.26 — 3.31. The systematic uncertainty on the cross-section is a quadrature sum given in equation 3.15: signal extraction, tracking, trigger and tracker/trigger efficiency, alignment and normalisation. The systematic uncertainty on pile-up is not included since it is corrected for.

$$\delta = \sqrt{\sigma^2_{\rm sig.\ ext.} + \sigma^2_{\rm track.} + \sigma^2_{\rm trig.} + \sigma^2_{\rm track/trig.} + \sigma^2_{\rm align.} + \sigma^2_{\rm norm.}} \tag{3.15}$$

The cross section results are given in Figures 3.26 — 3.31 the brown and green vertical bands represent the statistical and systematic uncertainties centered at the central value, respectively. The cross sections are summarised in Table 3.10. At backward rapidity the cross-section value of $\mu^+ \leftarrow \rm W^+$ is found to be smaller than that of $\mu^- \leftarrow \rm W^-$ due to isospin effect as well as the parity violation of weak interaction which couples left-handed fermions with right-handed anti-fermions and the helicity conservation of the semi-leptonic decay. This results in an anisotropic emission of fermions, particularly, $\rm W^-$ prefers to emit μ^- in the same direction of its momentum whereas $\rm W^+$ emits μ^+ in the opposite direction to its momentum. This means that μ^+ at backward rapidity ($-4.46 < y_{\rm cms} < -2.96$) comes from $\rm W^+$ at even large absolute rapidities where the cross-section is much smaller. In the forward rapidity ($2.03 < y_{\rm cms} < 3.53$), μ^+ comes from $\rm W^+$ at intermediate rapidity where the cross section is large enough. This effect is visible in Figure 1.23.

$\frac{d\sigma}{dy}$ (nb) [y bin]	$[-4.46 < y_{\rm cms} < -2.96]$	$[2.03 < y_{\rm cms} < 3.53]$
μ^+ (experimental)	10.46±1.89±0.73	62.42±3.73±3.28
pQCD+CT10	12.04±0.68	67.52±2.95
pQCD+CT10+EPS09	11.44±0.69	58.91±4.85
FEWZ+MSTW2008	9.65±0.75	70.77±1.41
FEWZ+MSTW2008+EPS09	9.99±0.75	64.68±1.24
μ^- (experimental)	50.63±3.69±2.23	58.10±3.89±3.18
pQCD+CT10	48.13±2.35	55.51±2.69
pQCD+CT10+EPS09	47.41±2.44	48.71±3.97
FEWZ+MSTW2008	55.01±1.15	56.93±1.07
FEWZ+MSTW2008+EPS09	55.31±1.21	52.30±1.14
$\mu^\pm$ (experimental)	59.84±3.99±2.63	120.15±5.41±5.01
pQCD+CT10	60.17±2.44	123.03±3.99
pQCD+CT10+ EPS09	58.85±2.53	107.63±6.27
FEWZ+MSTW2008	64.67±1.37	127.70±1.77
FEWZ+MSTW2008+EPS09	65.31±1.42	116.98±1.68

Table 3.10: The cross sections of $\mu^- \leftarrow \mathrm{W}^-$ $\mu^+ \leftarrow \mathrm{W}^+$ and $\mu^\pm \leftarrow \mathrm{W}^\pm$ bosons together with the respective theoretical predictions from NLO pQCD and FEWZ with and without shadowing. The first, second and third number of the experimental results represents the central value, statistical uncertainty and systematic systematic uncertainty, respectively. The theoretical uncertainties include factorization and renormalization (scale) which is ±5% and integration errors of about 0.1%.

The measured cross sections are compared with Next-to-Leading Order perturbative Quantum ChromoDynamics (NLO pQCD) [PS11] and Next-to-Next-To-Leding-Order Fully Exclusive W and Z (NNLO FEWZ) [GLPQ11] theoretical predictions with CT10 [NLC$^+$08] and MSTW2008 [MRST00] parton distribution functions with and without nuclear shadowing (EPS09). It is worth mentioning that the free proton PDFs used here are pre-LHC ones, that is, they do not include the LHC data in their global fits. The inclusion of the parametrisation of nuclear modification (EPS09) in the theoretical calculations (NNLO FEWZ, NLO pQCD) results in a slightly lower value of the cross-sections particularly at forward rapidity. This means that the production of W-boson is slightly modified by nuclear effects, although the extent of the modification is smaller than the uncertainty in data, thereby limiting the constraining power of the cross-section. Taking into account only the statistical uncertainty, the measurements and theoretical predictions agrees within $\pm 1.5\sigma$. Theoretical uncertainties include: scale and PDF errors. The factorization and renormalization scale that are of the order of 5%, and the experimental uncertainties (global uncertainties) cancels out in the ratio of the cross sections.

The bottom plots in Figures 3.26 — 3.31 are ratios of the measured and theoretical (with EPS09) cross-section relative to theoretical predictions without parametrisation of nuclear effects (EPS09). The theoretical predictions with and without nuclear

parametrisation are in agreement with the measured cross-section within uncertainty. In order to reduce the uncertainties in both data and theoretical calculations the ratios of the cross-section of muons from W^+ and W^- are computed (see sub-section 3.5.2).

The weak coupling nature and the isospin-dependent production mechanism of W-boson makes it a unique probe for nuclear parton distribution functions (nPDFs). In the small momentum fraction region the production of W-boson is expected to be reduced whereas in the larger momentum fraction range it is expected to be enhanced [PS11] as seen in Figure 1.18.

Shown in Figure 3.32 are the ratios of measured cross-sections by ALICE (this work) and CMS experiment [K$^+$15] to the pQCD calculation with nuclear modification parameterisation. It is worth mentioning as is also outlined in Figure 3.32 that the CMS results shown here are a combination of leptons (e and μ) with p_{T} greater than 25 GeV/c within the pseudorapidity acceptance $|\eta| < 2.4$. The CMS data sample corresponds to an integrated luminosity of 34.6 ± 1.2 nb^{-1}. The leptons in the CMS analysis are isolated to reject heavy flavour and jets backgrounds. Contrary to the work in this thesis, the electroweak processes $W \rightarrow l\nu$ are simulated with PYTHIA6.424. Further details about the CMS analysis can be found in [K$^+$15]. Both measurements are in agreement with the pQCD calculation with nuclear modification parameterisation within uncertainties. The W^- measurement at backward rapidity is more in agreement with theoretical predictions than the measurement reported by the CMS collaboration which reports a slight excess. The W^- measurement in this work rather shows a slight excess at forward rapidity which is in agreement with the CMS point at large positive rapidities.

The ratios of the measurements and the NLO pQCD with EPS09 predictions agrees with the trend exhibited in Figure 1.18 which shows that W^+ and W^- boson production are enhanced at backward rapidity and reduced at forward rapidity. This is because both W^+ and W^- boson measurements agree with NLO pQCD with EPS09 predictions in both rapidity intervals. In any case, a strong conclusion cannot be made due to large uncertainties.

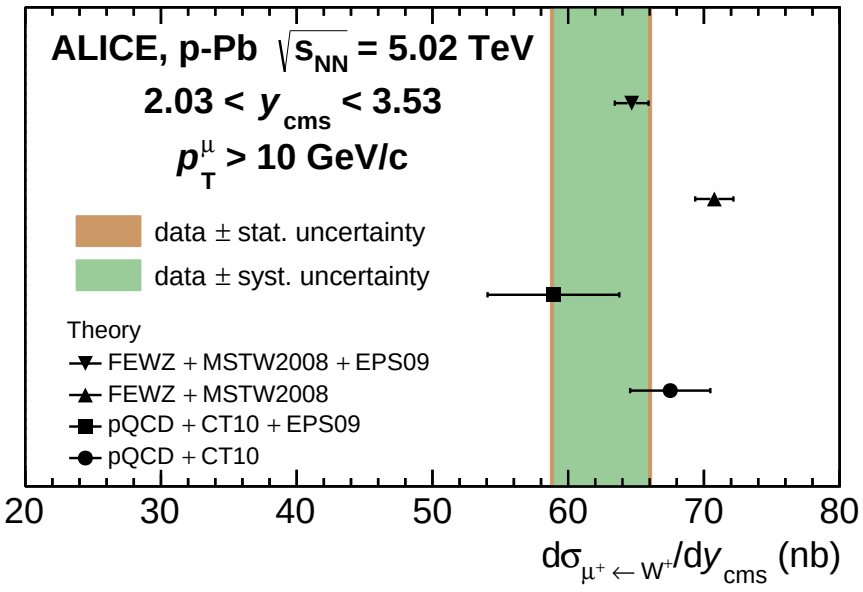

(a)

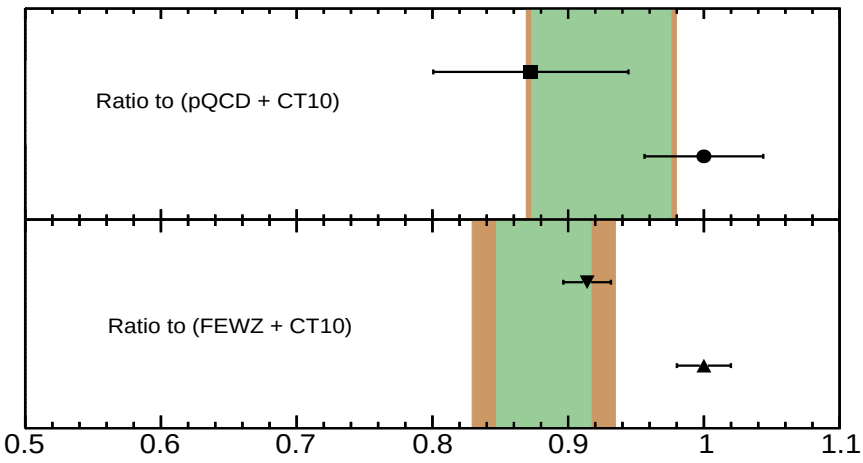

(b)

Figure 3.26: (a) Cross section of $\mu^+ \leftarrow W^+$ at forward rapidity compared to theoretical predictions [PS11, GLPQ11] with and without nPDFs. The brown and green bands represent the statistical and systematic uncertainty, respectively. (b) The top (bottom) panel shows the data and pQCD (FEWZ) calculations divided by the pQCD (FEWZ) calculations without nuclear modification of the PDFs.

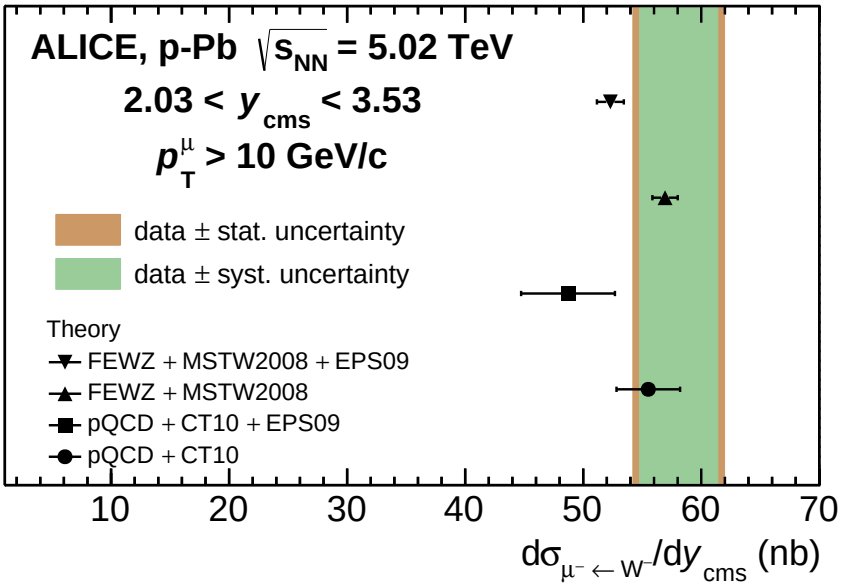

(a)

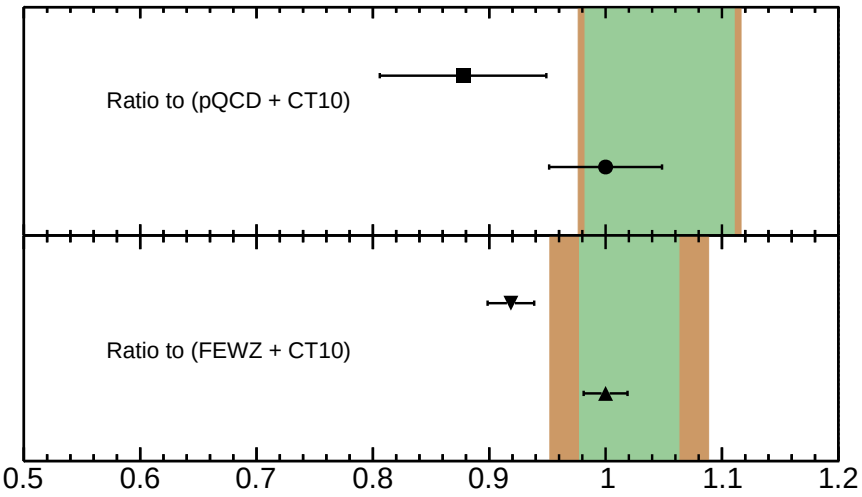

(b)

Figure 3.27: (a) Cross section of $\mu^- \leftarrow W^-$ at forward rapidity compared to theoretical predictions [PS11, GLPQ11] with and without nPDFs. The brown and green bands represent the statistical and systematic uncertainty, respectively. (b) The top (bottom) panel shows the data and pQCD (FEWZ) calculations divided by the pQCD (FEWZ) calculations without nuclear modification of the PDFs.

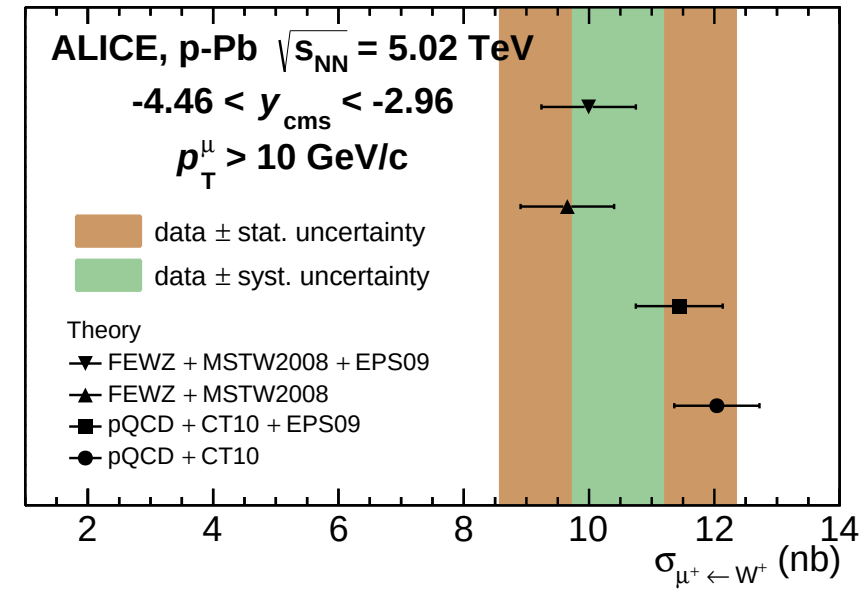

(a)

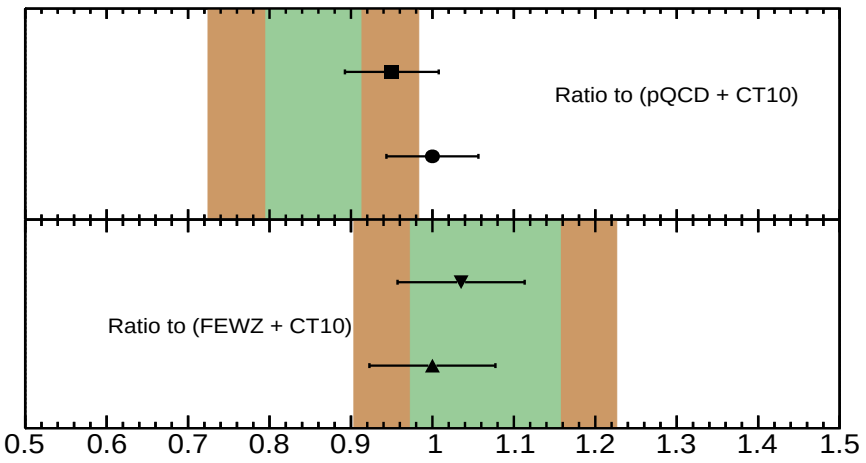

(b)

Figure 3.28: (a) Cross section of $\mu^+ \leftarrow W^+$ at backward rapidity compared to theoretical predictions [PS11, GLPQ11] with and without nPDFs. The brown and green bands represent the statistical and systematic uncertainty, respectively. (b) The top (bottom) panel shows the data and pQCD (FEWZ) calculations divided by the pQCD (FEWZ) calculations without nuclear modification of the PDFs.

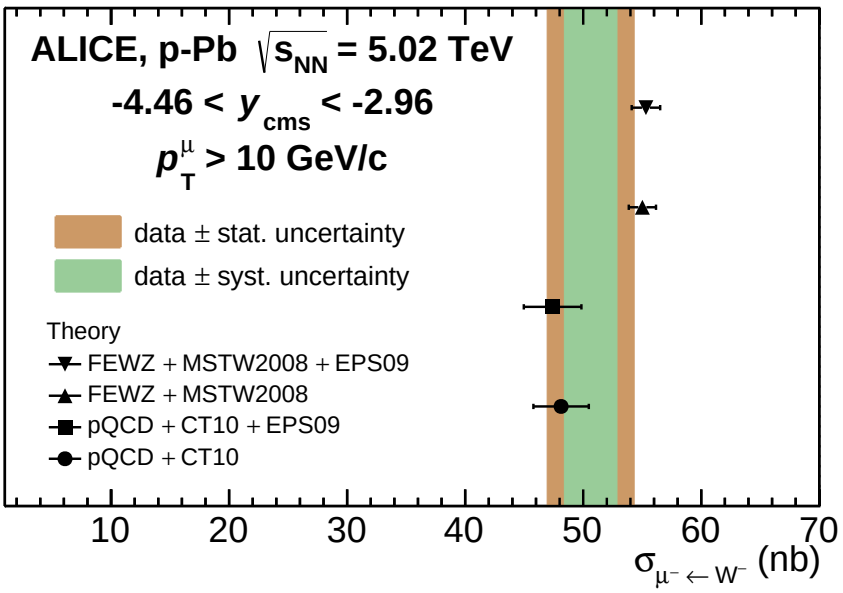

(a)

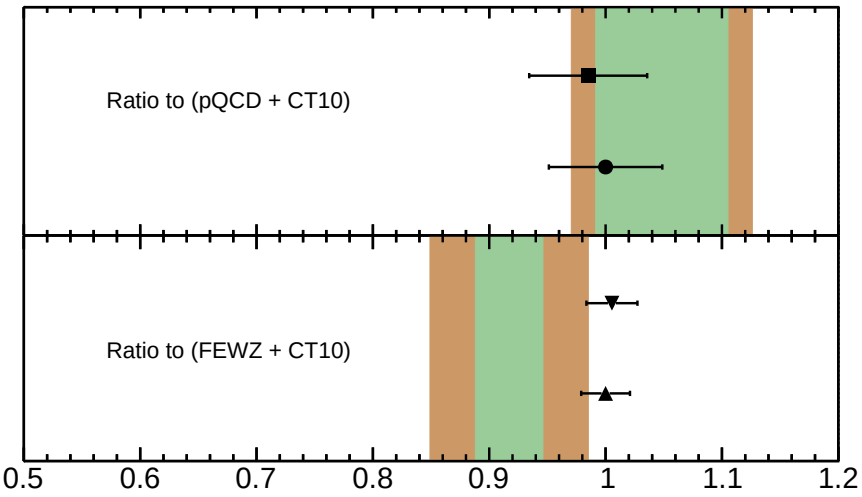

(b)

Figure 3.29: (a) Cross section of $\mu^- \leftarrow \mathrm{W}^-$ at backward rapidity compared to theoretical predictions [PS11, GLPQ11] with and without nPDFs. The brown and green bands represent the statistical and systematic uncertainty, respectively. (b) The top (bottom) panel shows the data and pQCD (FEWZ) calculations divided by the pQCD (FEWZ) calculations without nuclear modification of the PDFs.

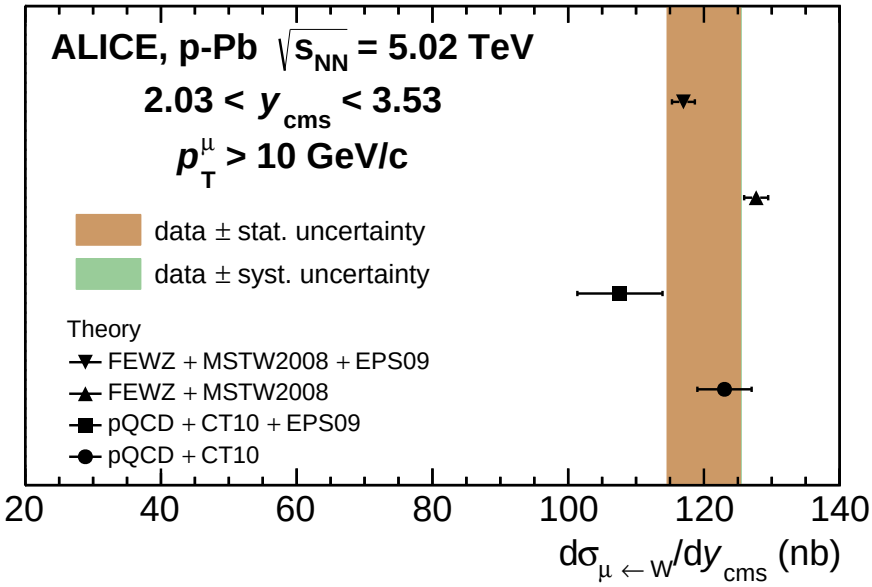

(a)

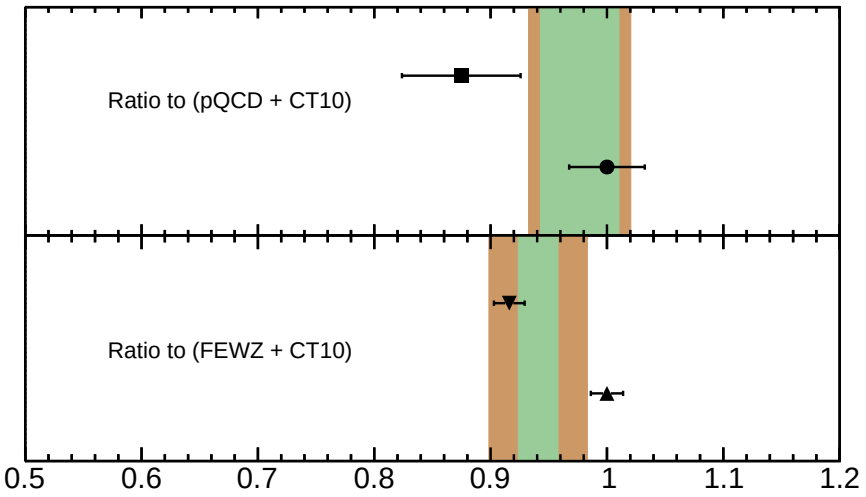

(b)

Figure 3.30: (a) Cross section of $\mu^{\pm} \leftarrow W^{\pm}$ at forward rapidity compared to theoretical predictions [PS11, GLPQ11] with and without nPDFs. The brown and green bands represent the statistical and systematic uncertainty, respectively. (b) The top (bottom) panel shows the data and pQCD (FEWZ) calculations divided by the pQCD (FEWZ) calculations without nuclear modification of the PDFs.

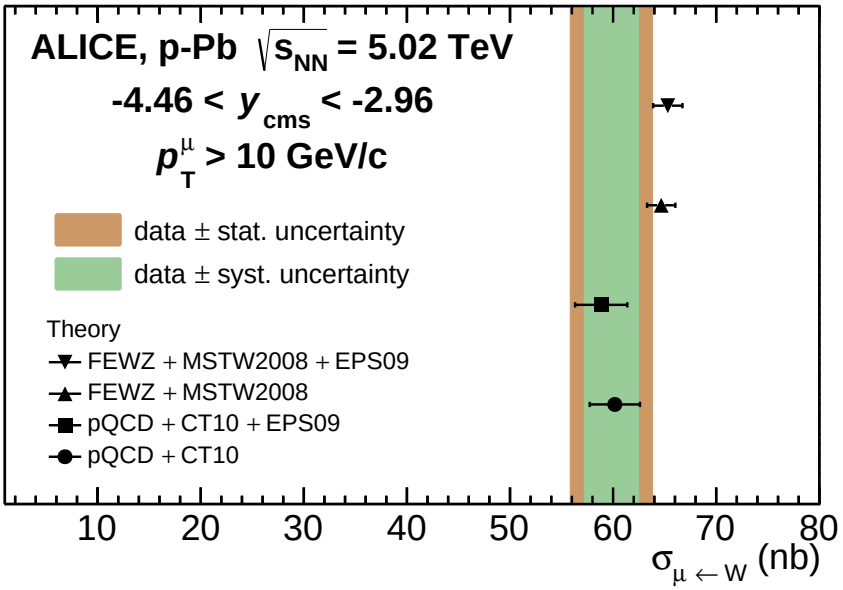

(a)

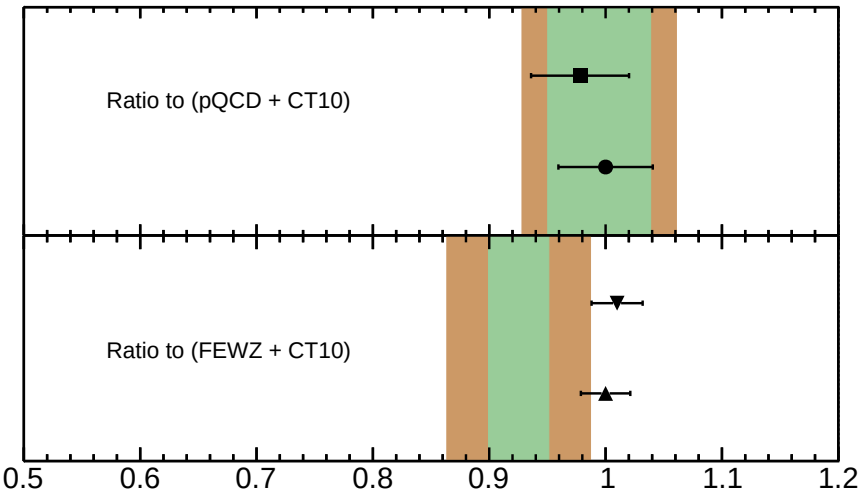

(b)

Figure 3.31: (a) Cross section of $\mu^{\pm} \leftarrow \mathrm{W}^{\pm}$ at backward rapidity compared to theoretical predictions [PS11, GLPQ11] with and without nPDFs. The brown and green bands represent the statistical and systematic uncertainty, respectively. (b) The top (bottom) panel shows the data and pQCD (FEWZ) calculations divided by the pQCD (FEWZ) calculations without nuclear modification of the PDFs.

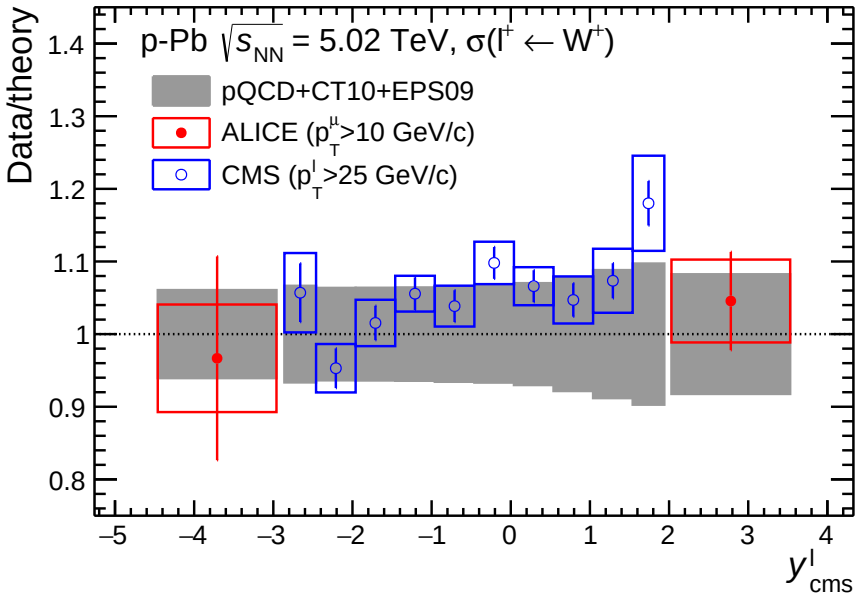

(a)

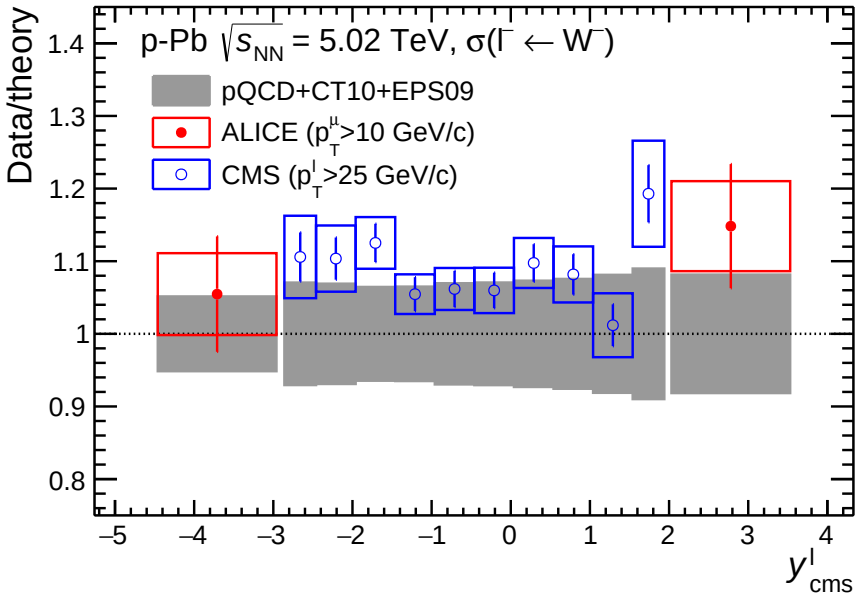

(b)

Figure 3.32: Ratio of data over theoretical calculations for the production cross section of positive (a) and negative (b) muons and leptons from W-boson production measured by the ALICE (this work) and CMS [K$^+$15] experiments, respectively. The pQCD calculations are obtained with CT10 NLO PDF set and with the EPS09NLO parameterisation of the nuclear modifications.

3.5.2 Charge ratio and asymmetry

In order to gain a better sensitivity in the study of the effects of nuclear PDFs compared to the cross-sections, the charge ratio

$$R_{\mathrm{W}} = \frac{N_{\mathrm{W}^+}}{N_{\mathrm{W}^-}} \tag{3.16}$$

and asymmetry

$$\mathcal{A}_{\mathrm{W}} = \frac{N_{\mu^+\leftarrow\mathrm{W}^+} - N_{\mu^-\leftarrow\mathrm{W}^-}}{N_{\mu^+\leftarrow\mathrm{W}^+} + N_{\mu^-\leftarrow\mathrm{W}^-}} \tag{3.17}$$

are computed, where $N_{\mu^+\leftarrow\mathrm{W}^+}$ and $N_{\mu^-\leftarrow\mathrm{W}^-}$ are $A \times \varepsilon$-corrected yields of muons from W^+ and W^- decays, respectively. The experimental measurements and theoretical calculations are summarised in Table 3.11 and plotted together in Figure 3.33.

Asymmetries [y bin]	$[-4.46 < y_{\mathrm{cms}} < -2.96]$	$[2.03 < y_{\mathrm{cms}} < 3.53]$
R_{W} (experimental)	0.21±0.036±0.012	1.10±0.16±0.094
pQCD+CT10	0.025±0.013	1.22±0.051
pQCD+CT10+EPS09	0.24±0.0.014	1.21±0.051
FEWZ+MSTW2008	0.18±0.006	1.24±0.034
FEWZ+MSTW2008+EPS09	0.18±0.014	1.23±0.036
$\mathcal{A}_{\mathrm{W}}$ (experimental)	-0.65±0.081±0.016	0.085±0.091±0.031
pQCD+CT10	-0.60±0.017	0.098±0.021
pQCD+CT10+EPS09	-0.61±0.019	0.095±0.021
FEWZ+MSTW2008	-0.69±0.017	0.094±0.014
FEWZ+MSTW2008+EPS09	-0.70±0.020	0.088±0.026

Table 3.11: The measured and theoretical W-boson charge ratio and asymmetry at forward and backward rapidity. The NLO pQCD calculations have been provided by the authors of Ref [PS11].

In these quotients, most of the theoretical and correlated experimental uncertainties cancel out. The measured charge ratio (R_{W}) and asymmetry ($\mathcal{A}_{\mathrm{W}}$) are compared with the same theoretical predictions used for the cross-section. The charge ratio (R_{W}) is a sensitive probe of the u/d ratio [FW13] and thus can be used to constrain PDFs. According to [PS11], $\mathcal{A}_{\mathrm{W}}$ is much more sensitive to the free proton PDFs than to their nuclear modifications. The uncertainties on the measurements, statistical and systematic, does not allow for a stronger conclusion. Perhaps with an increase in energy and luminosity a better precision can be achieved.

3.5.3 Forward-to-backward ratio

A traditional way to probe nPDFs is to compare the forward and backward yields or cross sections, which are sensitive to the nPDFs at small and large x, respectively. In

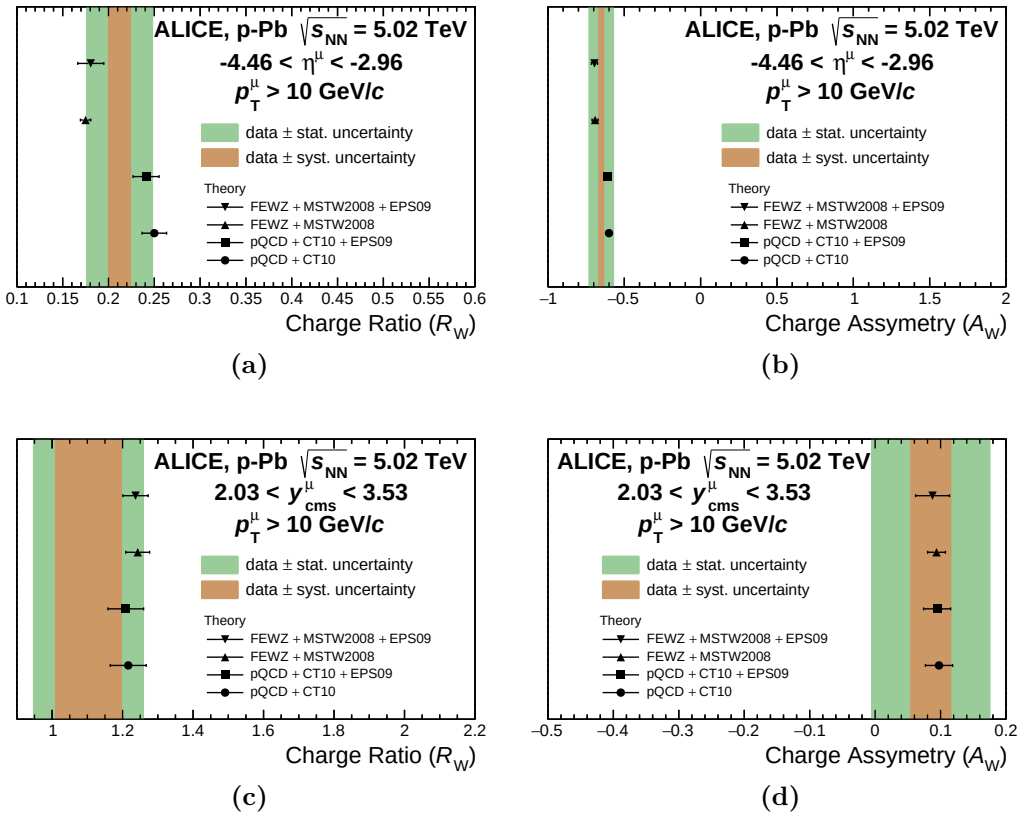

Figure 3.33: The charge ratio and asymmetry of muons from W-boson production are compared to theoretical predictions at backward rapidity (a) and (b), and at forward rapidity (c) and (d), respectively. The yellow and green bands represent the statistical and systematic uncertainties, respectively.

this analysis the comparison is between the yields of W-boson at forward and backward rapidity. This is achieved by using the forward-to-backward ratio, $R_{\rm FB}$ defined as:

$$R_{\rm FB} = \frac{d\sigma_{\mu^{\pm}\leftarrow {\rm W}^{\pm}}/dy(+y_{\rm cms})}{d\sigma_{\mu^{\pm}\leftarrow {\rm W}^{\pm}}/dy(-y_{\rm cms})}. \tag{3.18}$$

This observable has an advantage since it does not rely on knowledge of the yields of W-bosons in *pp* collisions and also, experimental and theoretical uncertainties partially cancel in the ratio. The asymmetry of W-boson production between the p-going (forward rapidity) and Pb-going (backward rapidity) directions is quantified by the $R_{\rm FB}$. In order to compute this ratio the $p_{\rm T}$ distribution is extracted in the common rapidity range ($2.03 < |y_{\rm cms}| < 2.96$), which is the overlap region between $2.03 < y_{\rm cms} < 3.53$ and $-2.96 < y_{\rm cms} < -4.46$. The resultant rapidity range covers only about 0.9 units of rapidity compared to 1.5 units of rapidity for the full acceptance of the forward muon spectrometer. This leads to the reduction of statistics; therefore the same strategy used to extract the signal in differential centrality bins is employed (see sub-section 3.3.2). The signal extraction is performed separately for muons from

W^+ and W^-, then summed to increase the statistics. In this ratio, the uncertainties from normalisation, alignment, trigger efficiency and tracker/trigger matching cancel out partially. This additional asymmetry is shown in Figure 3.34 and the values are shown in Table 3.12.

	Experimental	pQCD+CT10	pQCD+CT10+EPS09
R_{FB}	2.18±0.29±0.13	2.04±0.032	1.83±0.14

Table 3.12: Forward-to-backward ratio of $\mu \leftarrow$ W compared to pQCD theoretical calculations coupled CT10 [NLC+08] PDFs with and without EPS09 [EPS09] as provided by the authors of Ref [PS11].

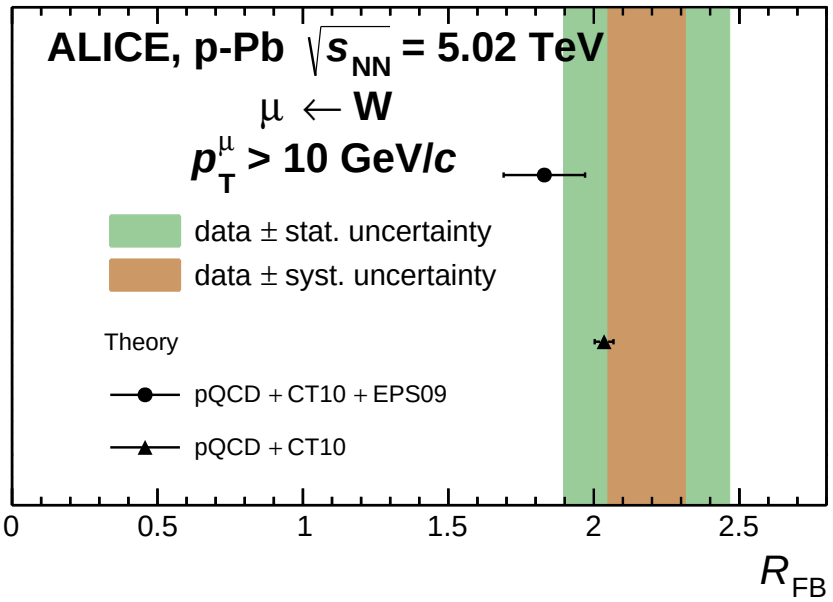

Figure 3.34: Forward-to-backward ratio of $\mu \leftarrow$ W compared to pQCD theoretical calculations coupled CT10 [NLC+08] PDFs with and without EPS09 [EPS09].

The measurement and theoretical predictions with and without nPDFs are in agreement within uncertainties. Although the difference between the central value of the NLO pQCD with and without nPDF is larger (2.09) than their respective uncertainties, the quadrature sum of statistical and systematic uncertainties (0.29) in the measurement is greater than this difference. Thus, the nPDFs cannot be constrained with this current precision.

3.5.4 $\langle N_{\mathrm{coll}} \rangle$-normalized yield

The production of muons from W-boson decays is also studied as a function of event activity (multiplicity) in both rapidity intervals. In order to gain statistics for this observable the number of μ^+ and μ^- are extracted separately and then summed. The

resulting cross sections, normalized to the average number of binary collisions [A+15e], are shown in Figure 3.35 for backward and forward rapidity. The vertical line and open boxes represent statistical and systematic uncertainties. Only uncorrelated systematics uncertainties (uncertainty on $\langle N_{\rm coll}\rangle$, pile-up and signal extraction) are included in the open boxes. The global uncertainty which includes: tracking, trigger and tracker/trigger matching efficiency, alignment and normalization (Normalisation factor and MB cross-section) is shown on the plot. The $\langle N_{\rm coll}\rangle$ uncertainty is the dominant systematic. The dashed line is used to guide the eye along the integrated value.

The $\langle N_{\rm coll}\rangle$-normalised cross sections in differential event activity show a flat trend and are all less than one sigma from the dashed line, taking into account either the statistical or systematic uncertainty. This are shown in Table 3.13. The production cross section is expected to scale with the number of binary collisions for all centrality classes, provided that the centrality determination is not biased. Thus, within uncertainties, the $\langle N_{\rm coll}\rangle$-normalised cross section is found to be compatible with geometric expectation [A+17c], assuming an unbiased centrality determination.

$\frac{\sigma_{\mu\leftarrow \rm W}}{\langle N_{\rm coll}\rangle}$ (nb) [Estimators]	ZNA	V0A	CL1
0-100%	25.27±1.47±2.44	25.38±1.47±2.29	25.38±1.48±2.29
2-20%	21.29±2.37±1.16	21.52±2.19±2.58	22.39±2.26±2.67
20-40%	28.06±2.60±1.10	25.52±2.59±2.50	26.59±2.63±2.57
40-60%	22.35±2.80±1.21	27.84±3.21±2.22	29.11±3.30±2.32
60-100%	24.68±3.02±1.11	29.27±3.43±2.07	23.08±3.07±1.57
$\frac{\sigma_{\mu\leftarrow \rm W}}{\langle N_{\rm coll}\rangle}$ (nb) [Estimators]	ZNC	V0C	CL1
0-100%	13.23±0.86±1.26	13.29±0.87±1.18	13.29±0.87±1.18
2-20%	12.03±1.46±0.65	14.82±1.56±1.76	15.45±1.54±1.87
20-40%	14.13±1.52±0.65	13.25±1.70±1.02	13.29±1.50±1.30
40-60%	12.76±1.66±0.68	9.44±1.45±0.66	9.64±1.61±0.75
60-100%	15.14±1.95±0.63	13.23±0.86±1.26	11.28±1.58±0.83

Table 3.13: $\langle N_{\rm coll}\rangle$-normalized cross sections of $\mu^{\pm}$ from $W^{\pm}$ as a function of centrality at backward (bottom) and forward (top) rapidity for different centrality estimators. The vertical bars and open boxes represent statistical and systematic uncertainties, respectively. The correlated global uncertainties include the MB cross section, normalisation, $A\times\varepsilon$ corrections and tracking and trigger systematics. $\langle N_{\rm coll}^{\rm mult}\rangle$ is referred to here as $\langle N_{\rm coll}\rangle$ for simplicity.

In Figure 3.36, the signal extraction was performed on data where the event activity is determined using other estimators, namely: V0A (C) and CL1, and compared with the unbiased ZN-based estimators. These are described in detail in [A+15e]. Shown in Figures 3.36a and 3.36b are $\langle N_{\rm coll}\rangle$-normalised cross-section for the three estimators at backward ($-2.96 < y_{\rm cms} < -4.46$) and forward ($2.03 < |y_{\rm cms}| < 2.96$) rapidities. The $\langle N_{\rm coll}\rangle$ systematic uncertainties from multiplicity-based estimators

(V0A (C) and CL1) are the largest. The $\langle N_{\mathrm{coll}} \rangle$-normalised cross-section for ZNC estimator exhibit a more flat trend than the other estimators at backward rapidity ($-2.96 < y_{\mathrm{cms}} < -4.46$), whereas at forward rapidity ($2.03 < |y_{\mathrm{cms}}| < 2.96$) they are all consistent with flatness. It is worth mentioning that these estimators select different events and thus the statistical uncertainty within a bin are uncorrelated.

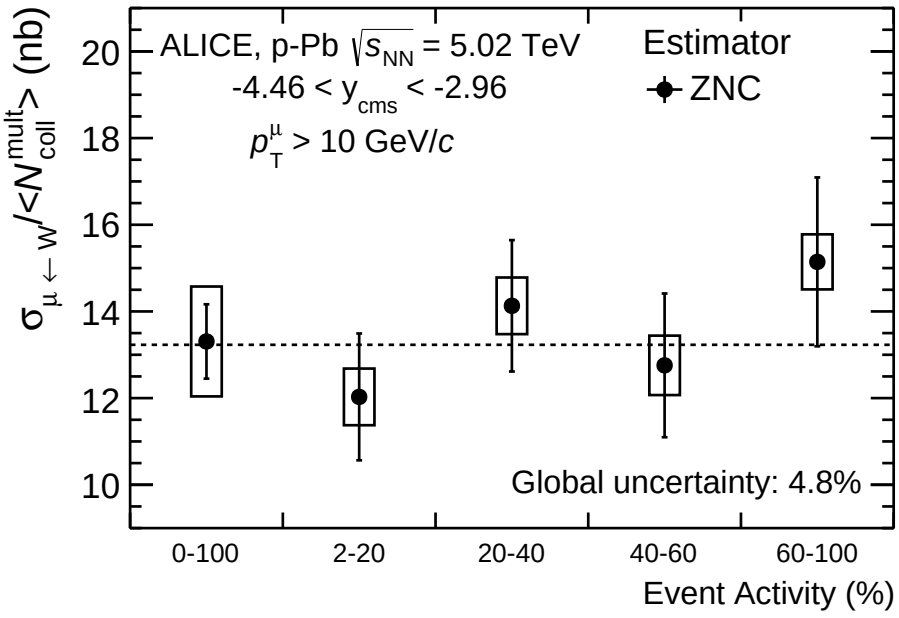

(a)

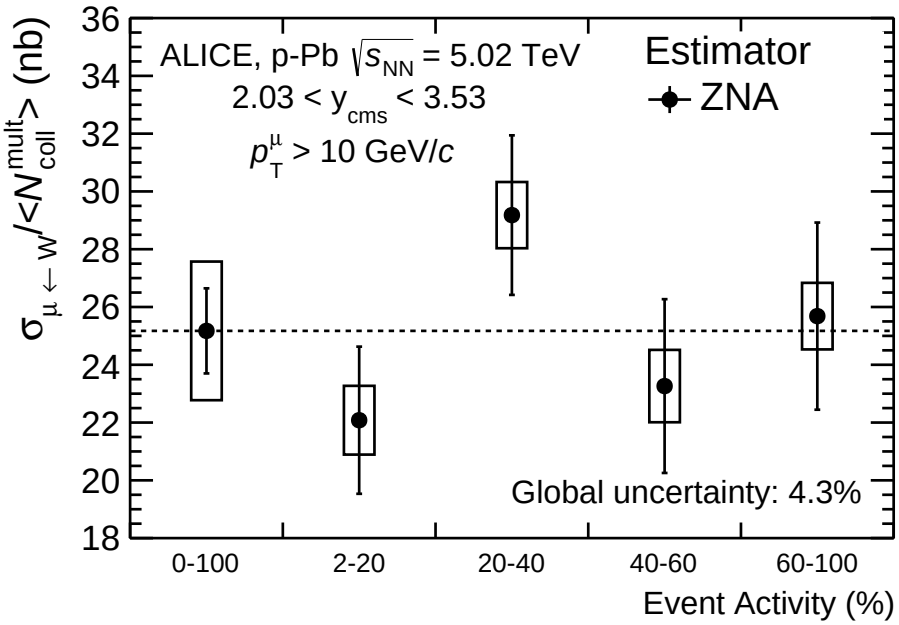

(b)

Figure 3.35: $\langle N_{\rm coll}\rangle$-normalized cross sections of $\mu^{\pm}$ from $\rm W^{\pm}$ as a function of centrality at backward (a) and forward (b) rapidity using the less-biased zero degree detector estimators, ZNA and ZNC. The vertical bars and open boxes represent statistical and systematic uncertainties, respectively. The correlated global uncertainties include the MB cross section, normalisation, $A \times \varepsilon$ corrections and tracking and trigger systematics.

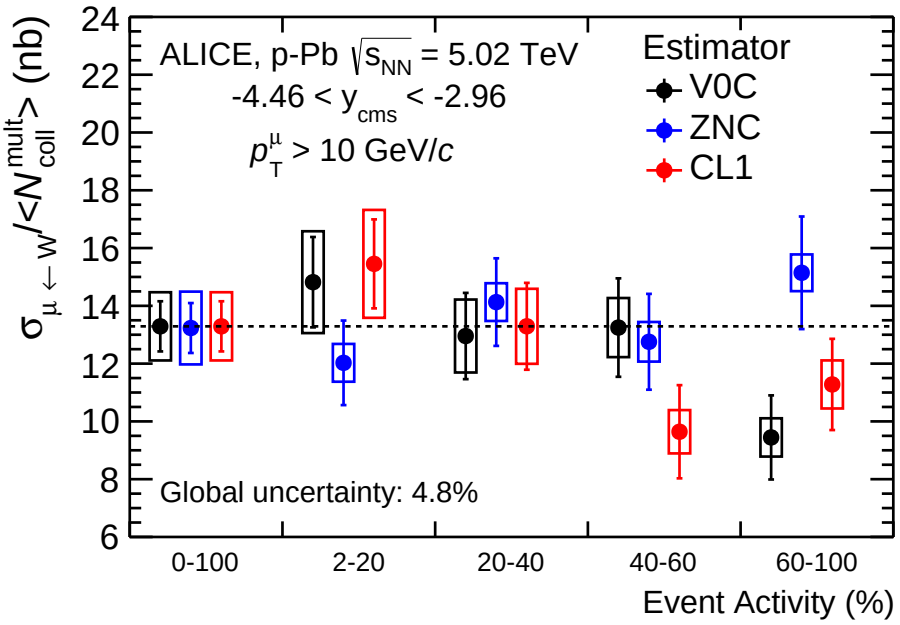

(a)

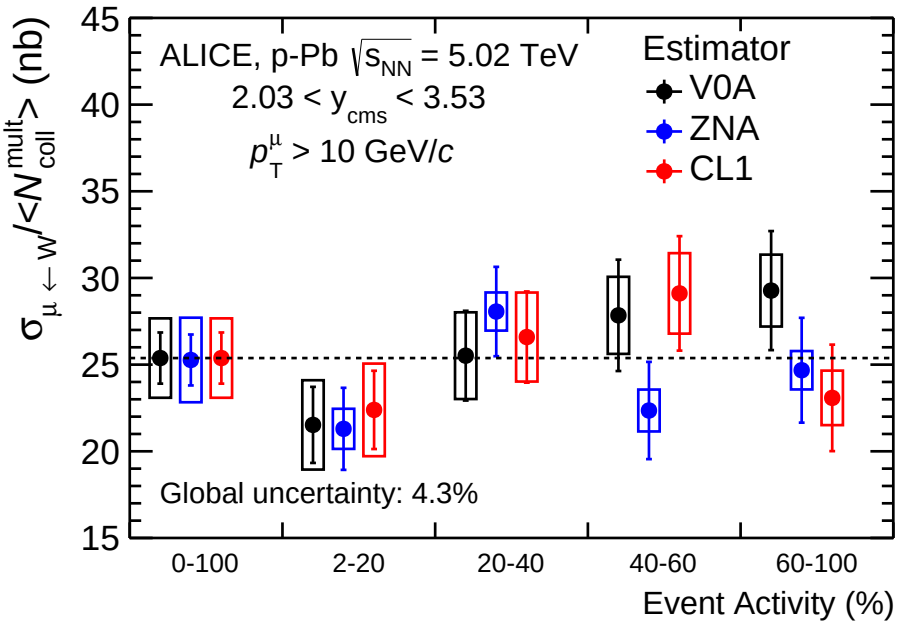

(b)

Figure 3.36: $\langle N_{\mathrm{coll}}\rangle$-normalized cross section of $\mu^{\pm}$ from $\mathrm{W}^{\pm}$ as a function of centrality at backward (a) and forward (b) rapidity. The vertical bars and open boxes represent statistical and systematic uncertainty, respectively. In contrast to Figure 3.35a and 3.35b, here the $\langle N_{\mathrm{coll}}\rangle$-normalized cross sections using different estimators are used. The black, blue and red points represent V0A(C), ZNA(C) and CL1, respectively. The correlated global uncertainties include the MB cross section, normalisation, $A \times \varepsilon$ corrections and tracking and trigger systematics.

"All models are wrong, but some are useful."

George E. P. Box

4

pp collisions

In this chapter the analysis strategy will be described in detail as a prologue for the Chapter presenting the results.

Contents

4.1 Data taking configuration

The proton-proton collisions data taking campaign at 8 TeV center-of-mass energy at the LHC took place in 2012. In that period a maximum of 1380 bunches of 1.6×10^{11} protons with 50 ns spacing were injected into the LHC rings per fill. Each proton beam was then accelerated to a nominal energy of 4 TeV. Given the requirement of a reduced luminosity at the ALICE IP in high luminosity pp collisions periods, the following scenario was adopted:

1. the LHC collided the main proton bunch from one beam with a satellite bunch from another beam as seen in Figure 4.1 below and explained in detail in [JAB+12]. The intensity of the satellite beam corresponded to 0.1% of the main bunch. This resulted in ≤2500 colliding bunches (main-satellite) [A+14d].

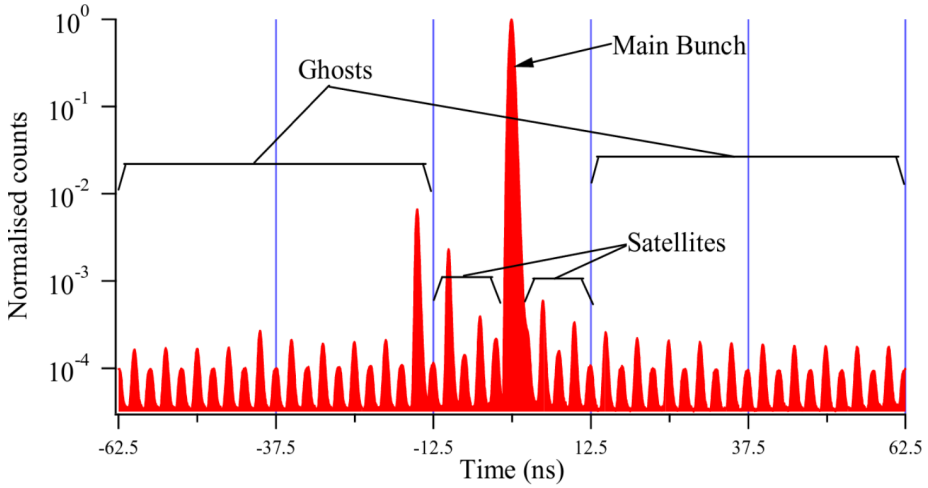

Figure 4.1: An example of a Longitudinal Density Profile showing the definition of ghosts and satellites. The longitudinal profile is in logarithmic scale.

2. the β^*[1] parameter was kept at 3m

$$\beta^* = \pi\sigma^2/4\varepsilon,$$

where σ is the cross-sectional area of the beam and emittance (ε) is the property of a beam which characterises its size or rather the particle beam spread in phase-space.

The two plots in Figure 4.2 show the delivered luminosity as a function of time (left) and fill (right). In this period ALICE recorded data at a luminosity of $5{\times}10^{30}$ cm^{-2}s^{-1} with collisions between enhanced satellite bunches and the main bunches [Cor15].

[1] β^* is the distance from the focus point that the beam width is twice as wide as the size at the focus point.

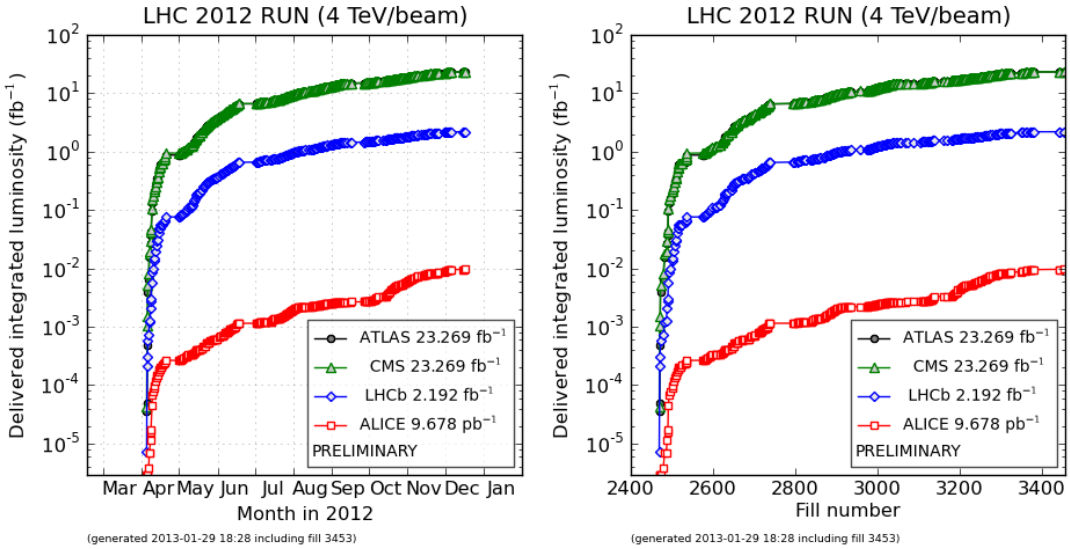

Figure 4.2: Luminosity as a function of time and fill in proton-proton collisions [Coo09].

The number of interactions per bunch-satellite crossing was about 0.01 on average with a corresponding pile-up probability of about 0.5%, reaching a maximum of $\sim$ 1% [A$^+$16b].

4.2 Data analysis

The analysis is based on an AOD data sample from 131 quality-assured runs with MSH (as described in sub-section 2.4.1) triggered events. The integrated luminosity for the runs analysed is about 583 nb. The data sample was further refined by applying the selection criteria described below.

4.2.1 Offline event and track selection

There are three offline event selection criteria used to refine the event sample. These include physics selection, good reconstructed vertex and a trigger selection. "The purpose is to select hadronic interactions with the highest possible efficiency, while rejecting the machine-induced and physical backgrounds" [A$^+$13c]. These were detailed in Chapter 3. In order to further refine the sample, several cuts are applied at track level (detailed in 3.2.2). The number of tracks after different cuts are shown in Table 4.1. In Figure 4.3 are plots showing the distributions of η (left) and p_{T} (right) after applying different track cuts. In green are the distributions obtained after applying only the event cuts, namely, physics selection, good vertex and trigger requirements. The difference between the distributions after applying the two geometrical cuts (requirements) is

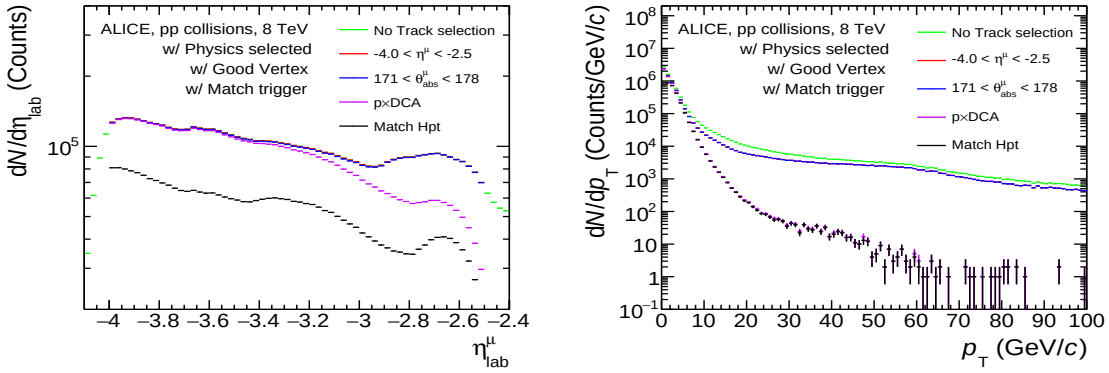

Figure 4.3: Eta (left) and p_{T} (right) distribution of muons showing the effects of different tracks with all event cuts applied.

minimal and as a result the plots lie on top of each other. The p×DCA and the matching of tracker and trigger tracks are applied to clean up the sample. The single muon high p_{T} distributions used for signal extraction are shown in Figure 4.4 (right) together with the pseudorapidity distribution of the tracks (left). In this figure, the distribution of positively and negatively charged muons are shown together with charge independent distribution (Total). These distributions in Figure 4.4 are obtained after applying all offline event and track selection criteria.

	N_{tracks}
Event Cuts	7.18M
η	6.16M
θ_{abs}	6.12M
p×DCA	5.44M
Trigger/tracker matching	3.22M

Table 4.1: Summary of statistics (tracks) after applying various selections at event and track level: physics selection, primary vertex reconstruction and track cuts. See text for details

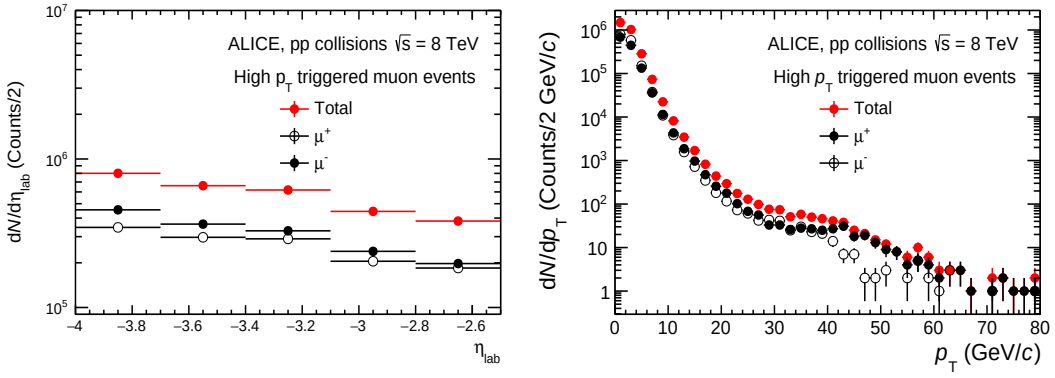

Figure 4.4: On the left and right is the pseudorapidity and p_{T} distributions of negatively and positively charged muons together with charge independent distribution (Total). These distribution are obtained after applying all offline event and track selection criteria.

4.3 Strategy

The analysis strategy employed is similar to the proton-lead case. The template generation is described in the following sections.

4.3.1 Monte Carlo templates and efficiency correction

W and Z templates

Similar to the p-Pb analysis, W- and Z-boson templates are based on the POWHEG [ANOR08] NLO event generator with NLO CT10 PDFs [NLC+08]. These simulations are also used to compute the $A \times \varepsilon$. Figure 4.5 shows the differential cross sections obtained from simulation as well as the $A \times \varepsilon$ plot computed from the POWHEG with NLO CT10 PDF which is a ratio of reconstructed to generated p_{T} spectra. Table 4.2 summarizes the values of $A \times \varepsilon$ computed as fraction of the number of reconstructed to generated tracks with transverse momentum greater than 10 GeV/c.

$A \times \varepsilon$

	μ^+	μ^-
Residual Alignment	0.7764	0.7803
Resolution Task	0.7654	0.7740

Table 4.2: $A \times \varepsilon$ for muons from W-boson decay with $p_{\mathrm{T}} > 10$ GeV/c and $-4 < \eta^{\mu}_{\mathrm{lab}} < -2.5$. Residual alignment means that the $A \times \varepsilon$ is based on alignment from data whereas Resolution Task is based on the data-driven method (discussed in Chapter 4).

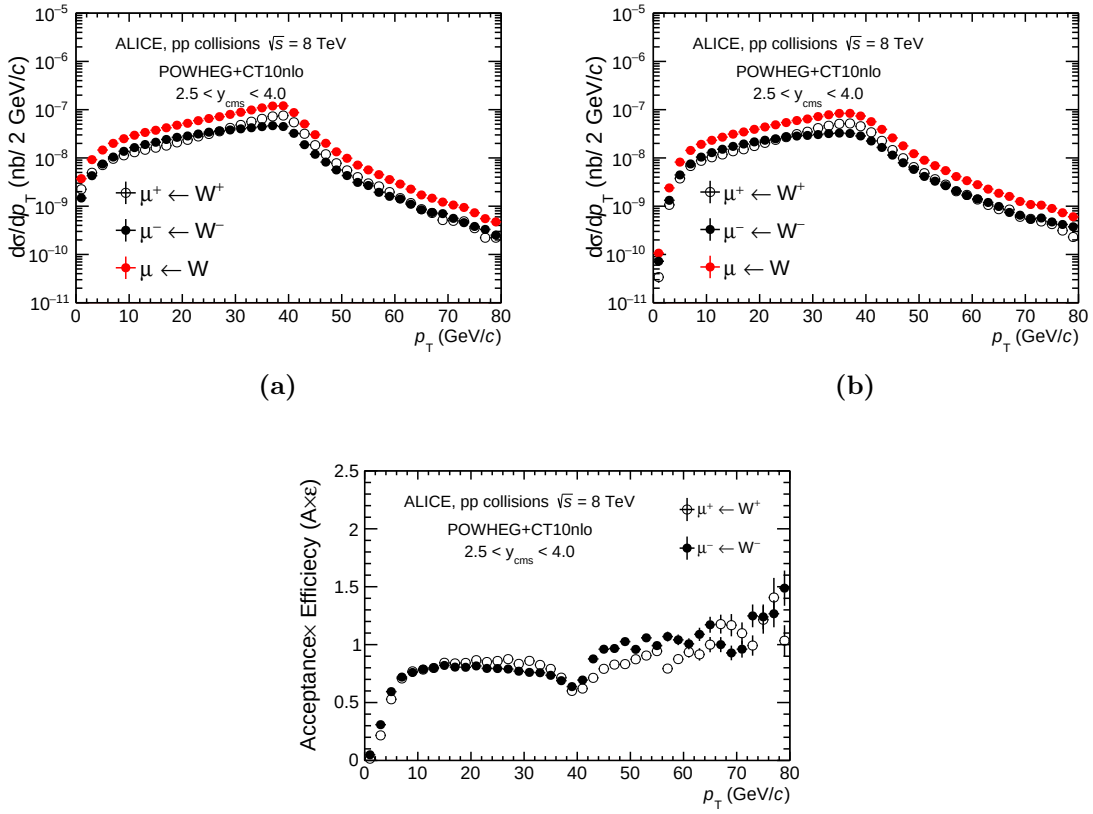

Figure 4.5: In the top left plot (a) are generation level template as obtained from POWHEG with CT10 PDF simulation using PYTHIA for event showering, whereas in (b) are reconstructed templates. The bottom plot shows the $A \times \varepsilon$ of negative and positive muons.

Heavy flavour muon templates

The heavy flavour decay muon templates are based on FONLL central prediction (described in Chapter 3), the distributions (p_{T} and η) are shown in Figure 4.6. The shapes (combination of $D \to e$, $B \to D \to e$ and $B \to e$) in Figure 4.6 are used to produce the templates in Figure 4.7 which are in turn used in the fit. The uncertainty on FONLL was taken into account by using the minimum and maximum

i) of the renormalisation and factorization scales,

ii) quark masses

iii) parton distribution functions (PDFs).

The systematic uncertainty on FONLL is taken into account by reweighting the simulation based on the central prediction by distribution (different uncertainty plots) in Figure 4.8. The resulting distributions with these weights applied are shown in Figure 4.9.

In the end a total of 7 shapes are used based on the above procedure which is also detailed Chapter 3. The variation of the heavy flavour decay muon background contributions is large enough to encompass any contribution from the residual light hadrons decay muons.

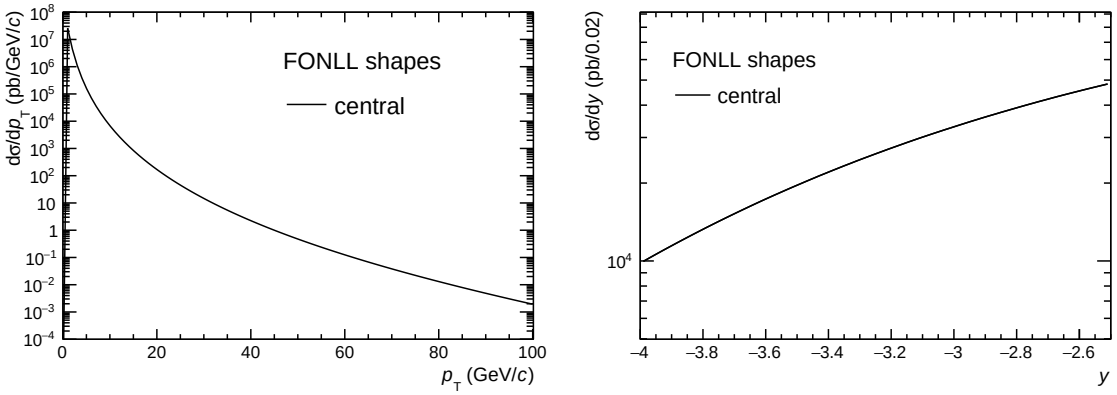

Figure 4.6: The cross section of heavy-flavour muons as a function of transverse momentum (top) and rapidity obtained from FONLL calculations [CFH+12]. Shown here is central prediction (default parameters) of the calculation.

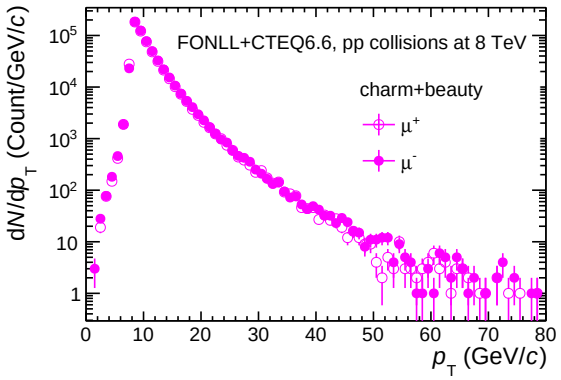

Figure 4.7: The reconstructed p_{T}-distribution of heavy flavour decay muon as a function. The filled and open circles are distributions for negative and positive muons.

The validity of the simulations were tested by plotting together the acceptance times efficiency of the three components as a function of generated p_{T}. Figure 4.10 shows that the distribution reaches 50% efficiency around 4.2 GeV/c and level around the same value ($\sim$ 78%) for the 3 templates which is the efficiency of the spectrometer in this period.

4.3.2 Signal extraction

The signal extraction procedure and the fit criterion are similar to the one used in proton-lead case. The main background contributions come from heavy flavour

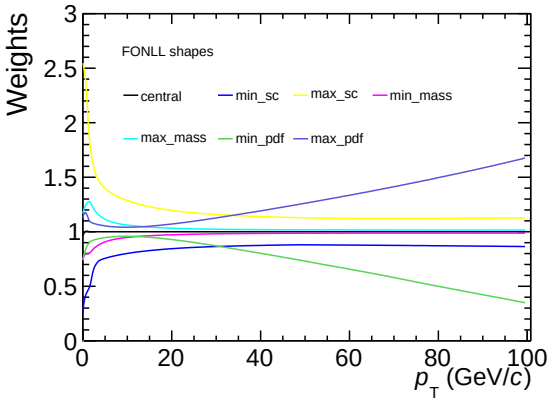

Figure 4.8: The weights (ratio of distributions varying scales to the central predictions) of muons from heavy-flavour decays calculated with FONLL by varying factorization scales.

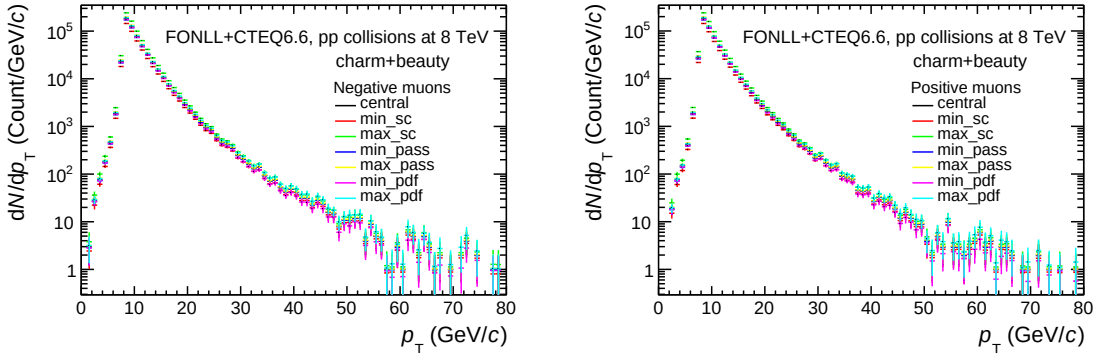

Figure 4.9: The plots on the left and right shows the templates of heavy-flavour negative and positive muons as a function of p_{T} respectively.

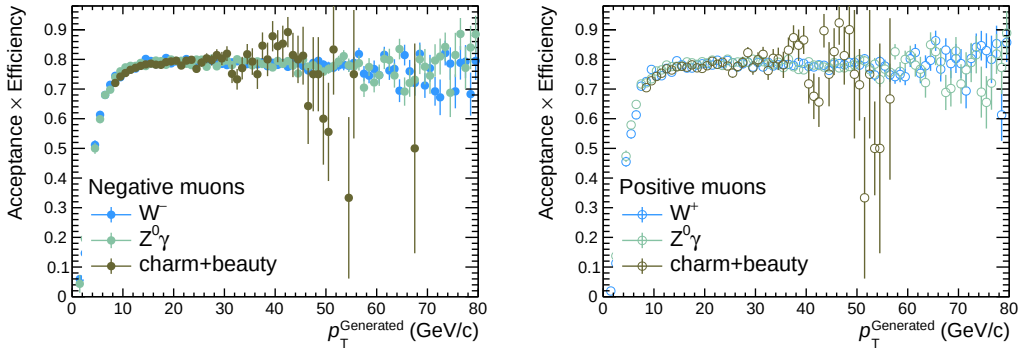

Figure 4.10: The acceptance times efficiency of muons from heavy-flavour decays, W-boson and Z-boson as a function of generated transverse momentum.

and Z-boson decay muons at lower and high p_{T}, respectively. The number of W bosons is extracted $A \times \varepsilon$ correction through a fit based on MC templates of the three contributions. The fit function (Fit function) is a combination of heavy flavour (charm + beauty), W- and Z-boson ($Z\gamma$) decay muon templates as described in Chapter 4. The difference comes from the fit range: the lower limit is set $p_{\mathrm{T}} \in (15, 18]$ GeV/c

whereas the upper limit is fixed at 60 GeV/c. The example of the combined fits to the inclusive single muon p_{T} distributions are shown in Figure 4.11.

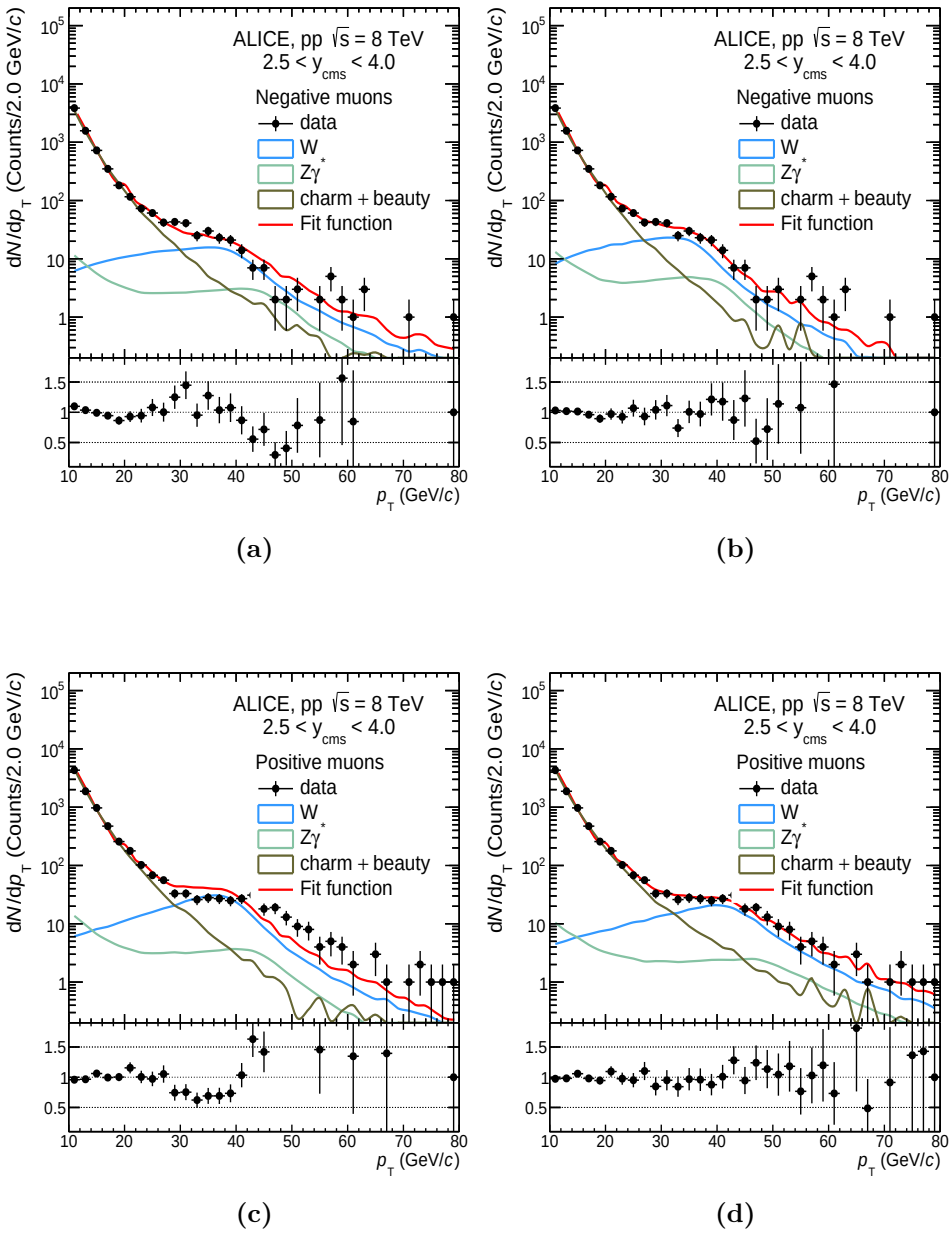

Figure 4.11: Inclusive p_{T}-distribution of negatively (top) and positively (bottom) charged muon candidates, fitted with MC templates obtained with the residual alignment (left) and resolution task (right). The results of the MC template fit for the extraction of $\mu^{+} \leftarrow \mathrm{W}^{+}$ and $\mu^{-} \leftarrow \mathrm{W}^{-}$ signals are shown. In this case, the central prediction (default parameters) of the FONLL calculation is used for the background description of heavy flavour decay muons while POWHEG [ANOR08] with CT10 [NLC^{+}08] PDF set is used for W- and Z-boson production. The left and right plots are fits based on templates obtain with default (residual) alignment and data-driven method, respectively. The bottom panels in each plot show the ratio of data to the extrapolated fit results in the range $10 < p_{\mathrm{T}} < 80$ GeV/c.

The tracker, trigger and trigger-track matching uncertainties obtained from the J/ψ study in proton-proton collisions [A+16b] are added in quadrature to the statistical uncertainty in each bin of the inclusive p_{T} distribution. The tracker, trigger and trigger-track matching uncertainties are 3.5%, 1% and 0.5%, respectively. The uncertainties are included in the signal extraction uncertainty. The number of W bosons ($N_{\mu^{\pm}\leftarrow \mathrm{W}^{\pm}}$) is extracted per trials by varying the p_{T} range, FONLL shape and alignment (MC and data-driven template). $N_{\mu^{\pm}\leftarrow \mathrm{W}^{\pm}}$ is a weighted average of the number of W bosons extracted per trials. The statistical and systematic uncertainties are computed in the same way as the case of proton-lead analysis. The final numbers are shown in Table 4.3. The trend of the trials as seen in Figure 4.12 follow the same trend as the p-going

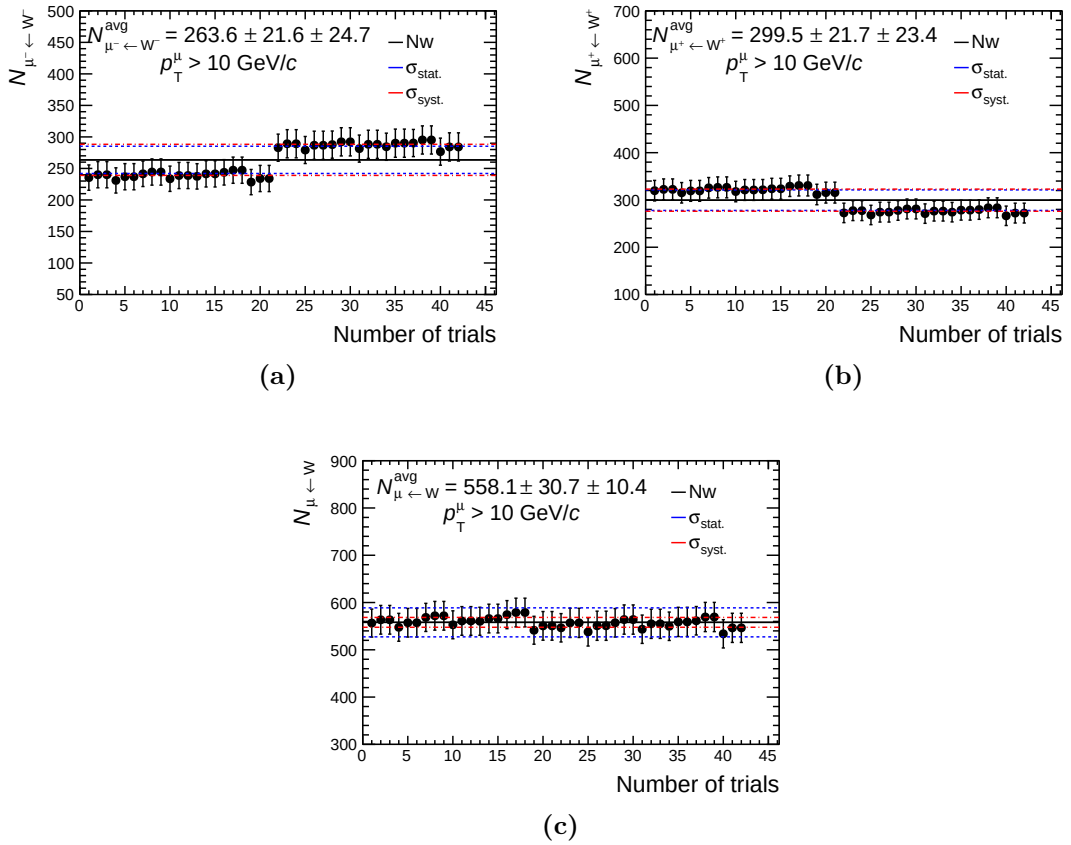

Figure 4.12: N_{W} extracted per trial for negative (top left), positive (top right) and total (bottom) muons. $N^{\mathrm{avg}}_{\mu^{\pm}\leftarrow \mathrm{W}^{\pm}}$, $\sigma_{\mathrm{stat.}}$ and $\sigma_{\mathrm{syst.}}$ are the average number of W-boson, statistical uncertainty and systematic uncertainty, respectively. The line in black represents $N^{\mathrm{avg}}_{\mu^{\pm}\leftarrow \mathrm{W}^{\pm}}$ whereas the statistical and systematic uncertainties are shown by the blue and red lines.

period (LHC13d). The trials which are systematically high and low are from fits based on the data-driven MC templates for positive and negative muons, respectively. This follows from the fact that the polarity of the dipole magnet in this data taking period is the same as in the LHC13d period. It is shows that the alignment of the tracking chamber varies with polarity (negative) of the dipole.

$N_{\mu^-\leftarrow \mathrm{W}^-}$	$N_{\mu^+\leftarrow \mathrm{W}^+}$	$N_{\mu^\pm\leftarrow \mathrm{W}^\pm}$	$N_{\mu\leftarrow \mathrm{W}}$
263.6±21.6±24.7	299.5±21.7±23.4	563.1±30.6±34.0	588.1±30.7±10.4

Table 4.3: Shown here are the weighted averages of the number of W-boson decay muons averaged over the trials with statistical (second number) and systematic uncertainty (third number), respectively. $N_{\mu^\pm\leftarrow \mathrm{W}^\pm}$ is the sum of $N_{\mu^+\leftarrow \mathrm{W}^+}$ and $N_{\mu^-\leftarrow \mathrm{W}^-}$ with their uncertainties summed in quadrature. $N_{\mu\leftarrow \mathrm{W}}$ is the fit to the inclusive p_{T} distribution without selecting a sign.

4.3.3 Normalization to minimum-bias (MB)

The integrated luminosity ($\mathcal{L}_{\mathrm{int}}$) in this analysis has been calculated from the normalisation factor (F_{norm}) obtained using the offline method, the number of MSH events and the vdM cross section (σ_{vdM}) of the V0 luminometer. Thus, the luminosity of given run is expressed as

$$\mathcal{L}_{\mathrm{int}} = \frac{N_{\mathrm{MSH}} \cdot F_{\mathrm{norm}}}{\sigma_{\mathrm{vdM}}} \tag{4.1}$$

where N_{MSH} represents the number of high-p_{T} triggered single-muon triggers used in the analysis. The normalisation factor is computed as follows

$$F_{\mathrm{norm}} = F_{\text{pile-up}} \cdot \frac{N_{\mathrm{MB}}}{N_{\mathrm{MB\&0MSL}}} \times \frac{N_{\mathrm{MSL}}}{N_{\mathrm{MSL\&0MSH}}} \tag{4.2}$$

$$F_{\mathrm{norm}} = F_{\text{pile-up}} \cdot \frac{N_{\mathrm{MB}}}{N_{\mathrm{MB\&0MSH}}} \tag{4.3}$$

where $F_{\text{pile-up}}$, N_{MB}, $N_{\mathrm{MB\&0MSL}}$, N_{MSL}, $N_{\mathrm{MSL\&0MSH}}$ and $N_{\mathrm{MB\&0MSH}}$ is the pile-up factor, number of minimum-bias events, number of minimum-bias events with low-p_{T} single muon trigger input, number of low-p_{T} single muon triggered events, number of low-p_{T} single muon triggered events with high-p_{T} single muon trigger input and finally the number of minimum-bias event with high-p_{T} single muon trigger input, respectively. Equation 4.2 and 4.3 are referred to as Offline (1) and Offline (2). The distribution of the normalisation factor fitted with a Gaussian function (left) and the normalisation factor as a function of run number (right) are shown in Figure 4.13. The Offline(2) method is statistically limited compared to the Offline(1) method because of $N_{\mathrm{MB\&0MSH}}$. The statistical limitation is shown by the large RMS. The normalisation factor used to obtain the luminosity is from the Offline(1) method and the systematic uncertainty is the difference of the two methods. The normalisation factor is 2238 ± 242.49(stat) ± 22(syst). The number of high-p_{T} triggered single muon events which passes the physics selection is 14.469M. The vdM cross section (σ_{vdM}) from the V0 luminometer was found to be 53.83 ± 0.03 (stat) ± 1.08 (syst) mb. These three ingredients are used to compute the integrated luminosity as shown in Equation 4.1 and found to be 588.76 ± 63.79 (stat) ± 11.81 (syst) nb.

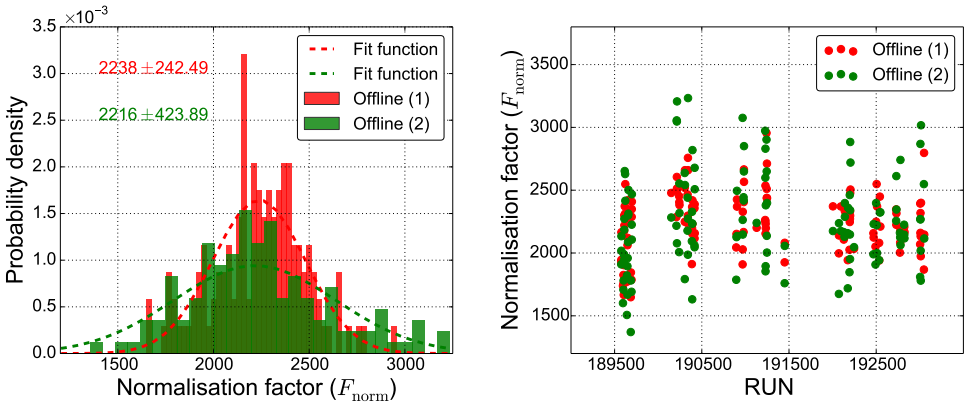

Figure 4.13: The distribution of the normalisation factor (left) and the normalisation factor as a function of run number as obtained by the offline method.

4.4 Systematic uncertainty

The systematic uncertainties are described below and summarized in Figure 4.15. The methods used to determine these uncertainties are analogous to the ones used in p-Pb collisions.

Tracking and trigger efficiency

The tracking systematic uncertainty is based on the method described in Chapter 3 which assigns the difference between tracking efficiency in data and MC as systematic. This difference amounts to 3%. An additional systematic based on a visual account of the dead area of the detector during data taking periods amount to 0.5%. Since these two uncertainties are not connected the total tracking uncertainty is obtained by adding the two values. The uncertainty from trigger efficiency comes from the determination of the efficiency of each trigger chamber from data. This uncertainty was found to be 2%. The same method used in the p-Pb case was used to determine the uncertainty due to the matching of the tracks in the tracking and trigger chambers which resulted in a 0.5% uncertainty.

Alignment

The systematic uncertainty which comes from the alignment of the tracking chambers is assessed as the difference between the misalignment obtained from the data and the data-driven Monte Carlo described in Section 3.3.1. The difference between these methods is found to be 1.4% and 0.8% for positive and negative muons, respectively.

Signal extraction

The following was performed to test whether the extracted number of W bosons follows the Gaussian distribution. This was done by generating several p_{T} distributions using the distribution from real data as input to the Poissonian (Poisson equation). The original bin content and statistical uncertainties are used as the mean and standard deviation of the Poissonian to generate the new bin content. These pseudo-data distribution were then fitted following the same procedure used to obtain plots shown in Figure 4.14. Clearly, the distribution of W bosons is a convolution of two Gaussian distribution, therefore the RMS is a suitable choice of systematics.

FONLL templates have limited statistics at high p_{T} but this does not affect the

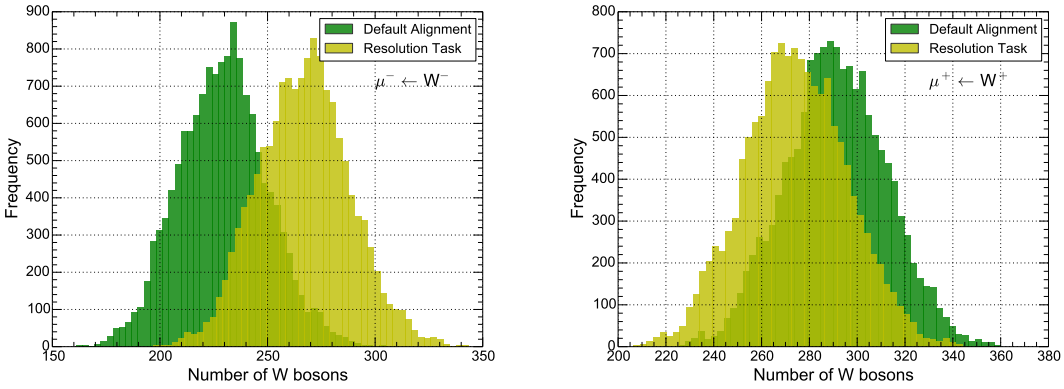

(a) **(b)**

Figure 4.14: The distribution of the number of W bosons extracted per trial of p_{T} for data generated according to Poisson statistics with uncertainties. On the left and right is the distribution of negative and positive muons, respectively.

uncertainty in the weighted average. This was tested by resampling the FONLL template (default parameter) within uncertainties using the Poissonian and then using the resulting template to extract the signal. The mean of these trials is within one percent of the number of W-boson extracted with the original FONLL (default parameter or central prediction) template.

Normalisation

The systematic uncertainty on the normalisation or luminosity determination is regarded as the systematic uncertainty propagation on the σ_{vdM} and F_{norm}. This amounts to 2%.

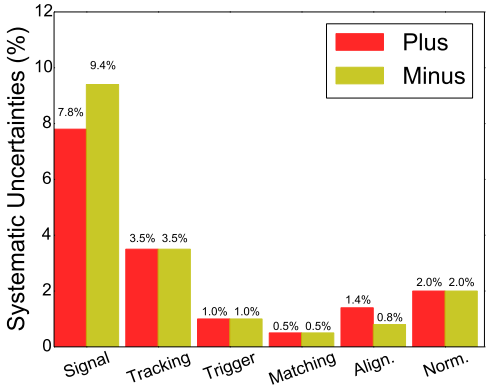

Figure 4.15: The systematic uncertainties from the sources described above are summarized in this figure. Signal, Align. and Norm. represents the uncertainty from signal extraction, alignment and normalisation, respectively. Tracking, Trigger and Matching represents the uncertainties from tracking, trigger and trigger-tracker matching, respectively.

4.5 Results

The results obtained from the analysis strategies are described. These are, the cross-section, charge ratio and asymmetry.

4.5.1 Cross section

The cross-section of W-boson decay muons is computed the same way as in the proton-lead analysis according to equation 3.14. The cross-section of muons from W^+ and W^- boson decays with $p_T > 10$ GeV/c measured at forward rapidity are shown in Figure 4.16. The systematic uncertainty on the cross-section is a quadrature sum of the uncertainties on signal extraction (includes RMS of the trials, tracking, triggering and trigger-track matching), alignment and normalisation. The systematic uncertainty on pile-up is not included since it is corrected for and is also <0.8 %, therefore negligible.

In Figures 4.16 - 4.17, the brown and green vertical bands represent the statistical and systematic uncertainties centred at the central value (red line), respectively. The values for the cross section and charge asymmetries for the experimental measurements and theoretical predictions are summarised in Table 4.4.

The small value of the production cross-section of negative ($\mu^- \leftarrow W^-$) relative to positive ($\mu^+ \leftarrow W^+$) muon is due to several combinations of effects: parity violation of weak interaction which couples left-handed fermions with right-handed anti-fermions, the helicity conservation of the semi-leptonic decay and the isospin effects. These effects favor the negatively charged muon since W^- prefers to emit μ^- in the same direction

Cross section (nb)	$\mu^+ \leftarrow W^+$	$\mu^- \leftarrow W^-$	$\mu \leftarrow W$
Experimental	657.29±47.67±53.05	578.48±47.42±55.39	1230.98±67.70± 33.67
POWHEG+CT10	714.63	598.176	1312.80
FEWZ+CT10	699.85±3.51	589.22±5.35	1289.07±6.39
FEWZ+MSTW2008	720.381±23.36	608.66±21.55	1329.04±31.78
FEWZ+NNPDF21	732.128±17.71	635.35±14.27	1367.48±22.74

Asymmetries	R_W	$\mathcal{A}_W$
Experimental	1.12±0.12±0.19	0.17±0.09±0.07
POWHEG+CT10	1.22	0.10
FEWZ+CT10	1.19±0.012	0.086±0.0051
FEWZ+MSTW2008	1.15±0.038	0.071±0.016
FEWZ+NNPDF21	1.22±0.038	0.099±.015

Table 4.4: The cross sections (top) and charge asymmetries (bottom) of muons from W-boson decay. Shown here are the measurements and corresponding theoretical predictions. The CT10 is NLO whereas MSTW2008 and NNPDF21 are NNLO PDFs.

of its momentum whereas W^+ emits μ^+ in opposite direction to its momentum. The isospin content of proton favors the production of W^+. The measured cross-section shown in Figure 4.16 are compared with Next-to-Leading Order POsitive Weight Hardest Emission Generator (NLO POWHEG) [ANOR08] and Next-to-Next-To-Leding-Order Fully Exclusive W and Z (NNLO FEWZ) [GLPQ11] theoretical predictions with CT10 [NLC+08] (NLO), MSTW2008 [MRST00] (NNLO) and NNPDF [BBC+13] (NNLO) parton distribution functions.

In Figure 4.17 the $\sigma_{\mu\leftarrow W}$ is compared to cross sections obtained from POWHEG and FEWZ calculations.

The statistical limitations due to low luminosity is a contributing factor to the large statistical uncertainties in Figure 4.16 and 4.17 making it impossible to constrain PDFs. The measurement agrees with all theoretical calculations within one sigma.

4.5.2 Charge ratio and asymmetry

The charge ratio (R_W) and asymmetry ($\mathcal{A}_W$) are computed as mentioned in the previous section. The charge asymmetries are used to reduce correlated systematic uncertainties inherent in the cross section. The systematic uncertainties which enters in the charge asymmetries are $A \times \varepsilon$, alignment and signal extraction. Also some theoretical uncertainties cancel out in these quotients. The charge ratio and asymmetry are compared to theoretical calculations used to describe the cross section. As established previously, the charge ratio gives direct access to the up and down quark PDF ratio. The results obtained for these observables are shown in Figure 4.18. A similar conclusion as

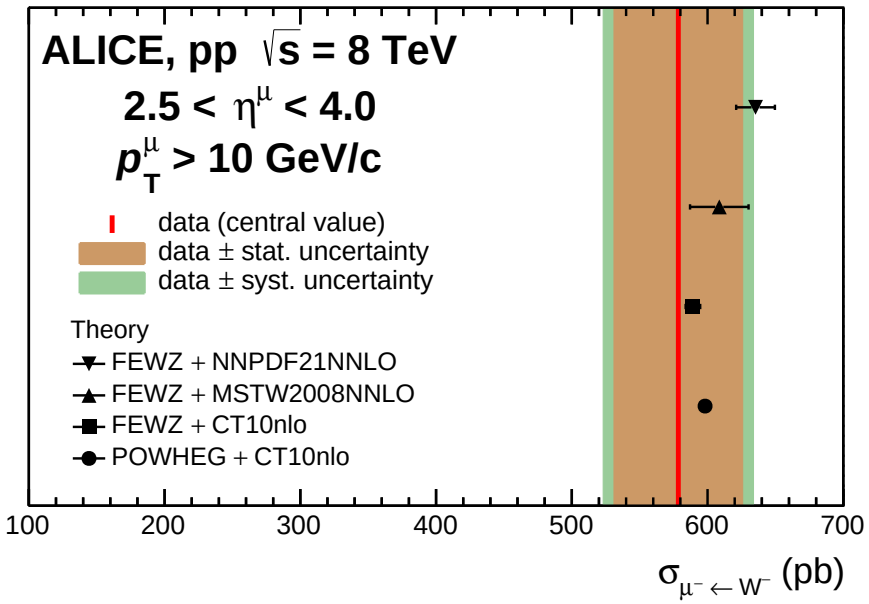

(a)

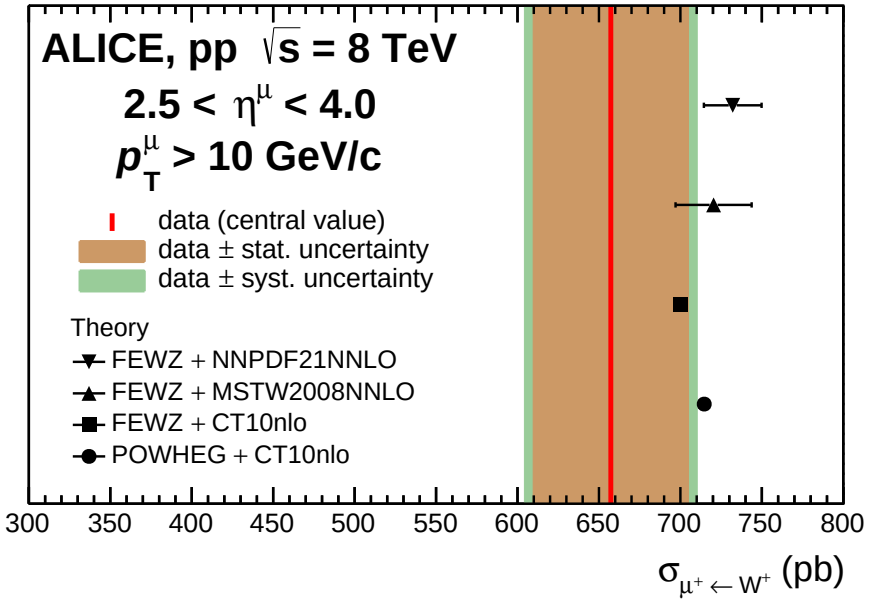

(b)

Figure 4.16: Cross sections of muons from W-boson decays compared to theoretical predictions. The top and bottom plot shows both negative and positive muons. The yellow and green band represent the statistical and systematic uncertainty, respectively. The red line represent the central value of the cross section. The theoretical predictions are based on next-to-leading (NLO) order Monte-Carlo generators with NLO parton distribution functions.

in the case of the cross section is reached, within one sigma the theoretical calculations and the measurements are in agreement.

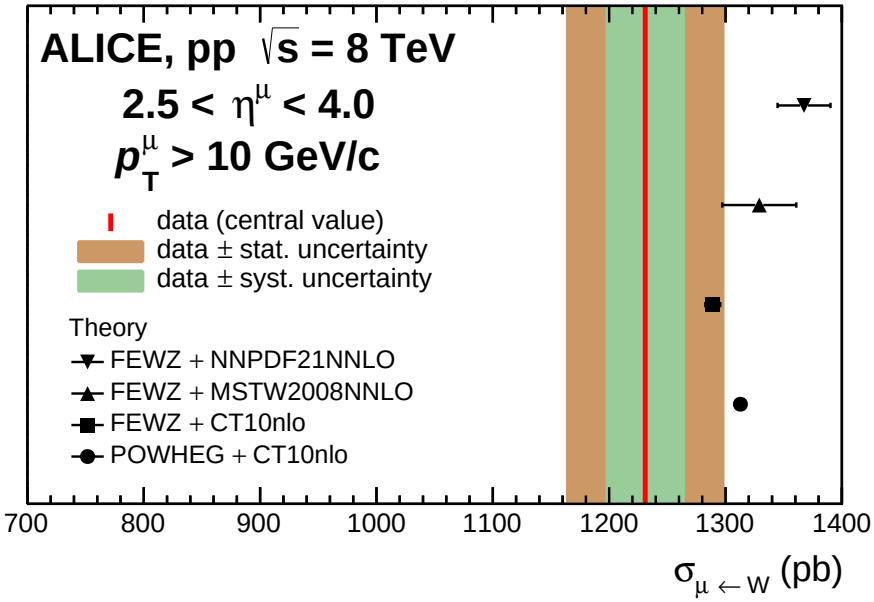

Figure 4.17: Cross section of $\mu^{\pm}$ from $W^{\pm}$ compared with theoretical predictions. The yellow and green bands represent the statistical and systematic uncertainty, respectively. The red line represent the central value of the cross section. The theoretical predictions are based on next-to-leading (NLO) order Monte-Carlo generators with NLO parton distribution functions.

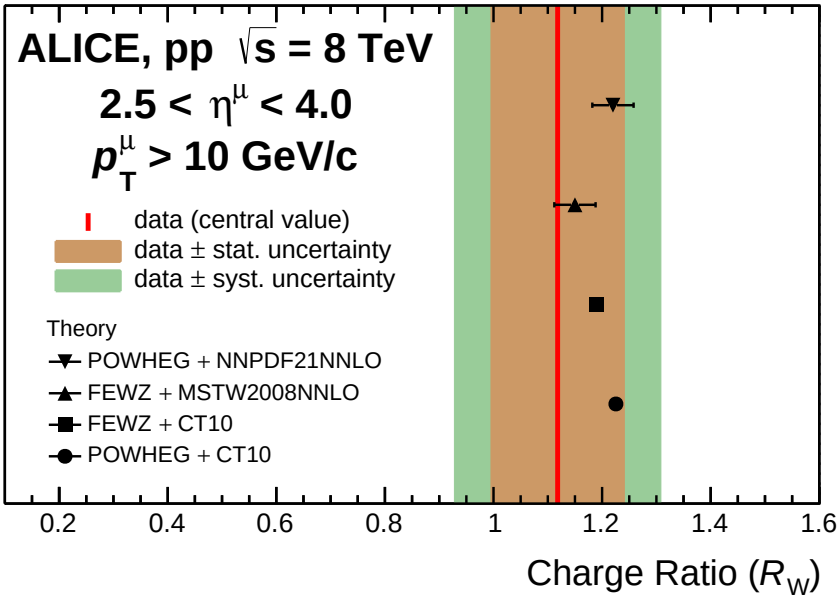

(a)

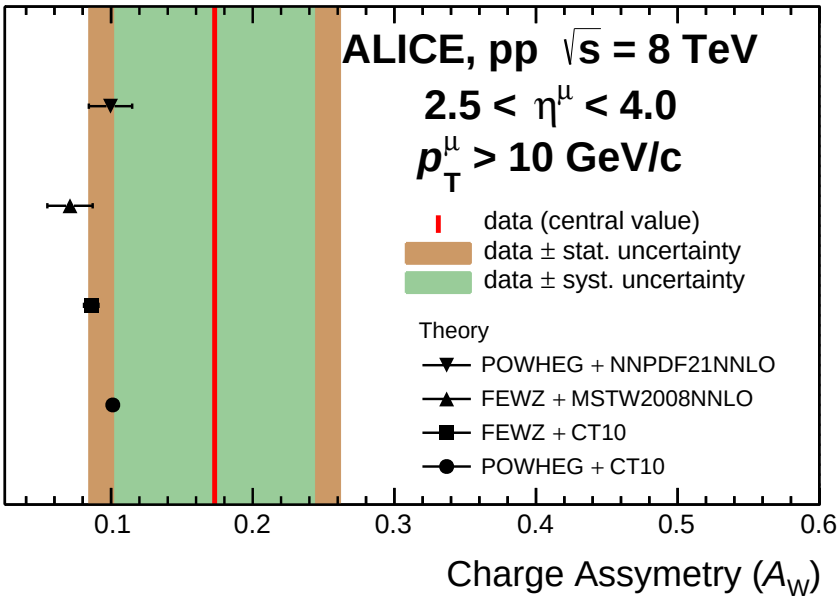

(b)

Figure 4.18: The charge ratio (top) and asymmetry (bottom) of muons from W bosons compared to different theoretical predictions. The yellow and green bands represent the statistical and systematic uncertainty, respectively. The red line represent the central value of the cross section. The theoretical predictions are based on next-to-leading (NLO) order Monte-Carlo generators with NLO parton distribution functions.

"All models are wrong, but some are useful."

George E. P. Box

5

Feasibility: W-boson in PbPb collisions

In this chapter the analysis strategy will be described in detail as a prologue for the Chapter presenting the results.

Contents

5.1 Data taking configuration

The heavy-ion data taking campaign started in 2010 with the LHC accelerating Pb ions to collide at $\sqrt{s_{\mathrm{NN}}} = 2.76$ TeV centre-of-mass energy. The number of colliding bunches as a function of run number is shown in Figure 5.1 (left). This RUN I data taking period span 203 hours delivering an integrated luminosity of 146 $\mu\mathrm{b}^{-1}$ at the ALICE IP. The RUN II lead-lead collisions at $\sqrt{s_{\mathrm{NN}}} = 5.02$ TeV centre-of-mass energy took place in November – December 2015. The number of bunches were increased until the maximum of 444 bunches were reached (see Figure 5.1 right). The trend of delivered instantaneous luminosity as a function of the fill is shown in Figure 5.2 for the two periods. The achieved luminosity for the RUN II data taking period is 432 $\mu\mathrm{b}^{-1}$ at the ALICE IP.

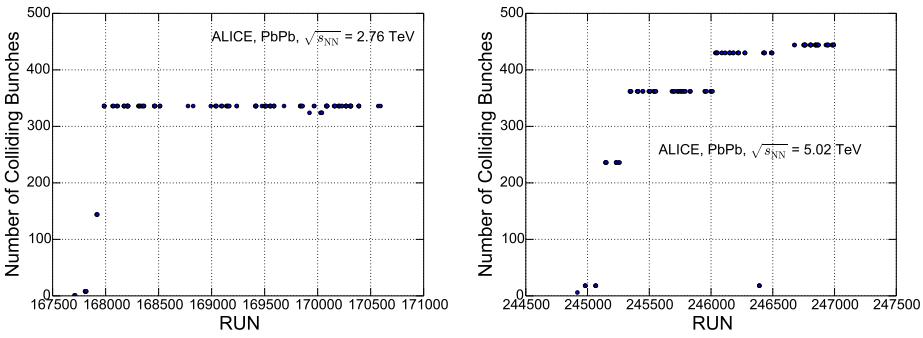

Figure 5.1: Number of colliding bunches as a function of run number for Pb-Pb collisions where the figure on the left shows Run I and right shows Run II data taking periods.

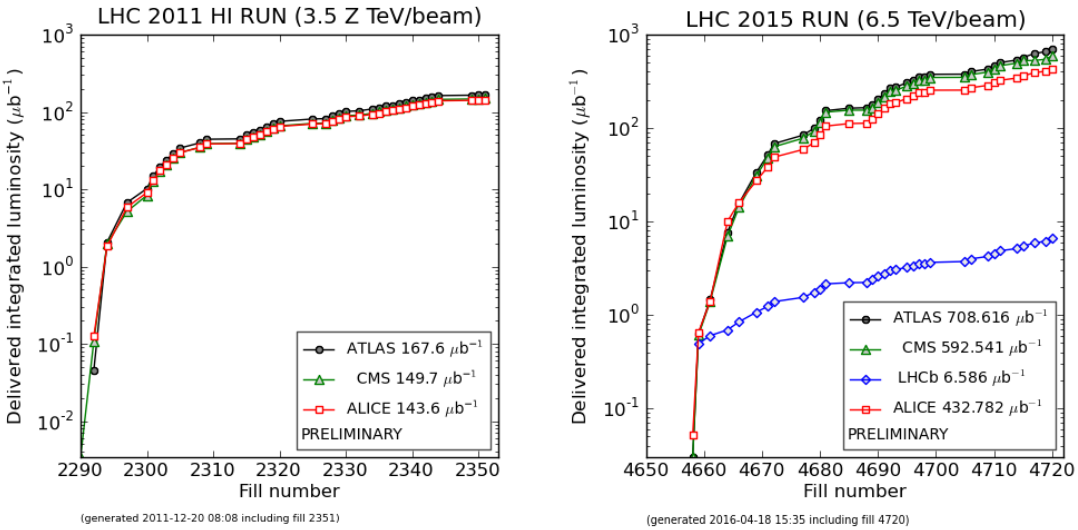

Figure 5.2: The delivered integrated luminosity as a function of the fill in the RUN II lead-lead data taking period [Coo09].

5.2 Data analysis

The data sample consists of AODs from 137 quality-assured runs each from Pb-Pb collisions of Run I (LHC11h) and Run II (LHC15o). The data sample corresponds to an integrated luminosity of 63.5 and 225 μb for Run I and Run II, respectively.

5.2.1 Event selection

The event selection has been described in Chapter 3 in section 3.2.1. The analysed data samples contains **MSH-triggered** (as described in sub-section 2.4.1) events. MSH (CMSH7-B-NOPF-MUFAST [1] and CPBI1MSH-B-NOPF-MUON [2]) correspond to muons with high p_{T} trigger threshold set at around 4.2 GeV/c. The number of events passing each selection criteria are shown in Table 5.1.

	Muon interaction	Trigger Selection	Physics Selection	Good Vertex
LHC11h	22M	21.28M	18.33M	18.33M
LHC15o	105.716M	105.381M	105.043M	105.040M

Table 5.1: Summary of the trigger-selected statistics after applying various event cuts: physics selection and primary vertex reconstruction. See text for details.

Event characterization: centrality

"The multiplicity of produced particles is an important property of the collisions and is related to the geometry, the initial parton densities and the energy density produced" [A$^+$16a]. Since the impact parameter of the collision cannot be measured directly it is inferred from the multiplicity of a collisions through the help of models like Glauber [MRSS07]. Nuclei are extended objects and thus their collisions can be classified according to the impact parameter or number of average participating neuclons ($\langle N_{\mathrm{part}} \rangle$), number of binary collisions ($\langle N_{\mathrm{coll}} \rangle$), the overlap function ($\langle T_{\mathrm{AA}} \rangle$) and $\langle N_{\mathrm{coll}} \rangle_{\langle N_{\mathrm{part}} \rangle}$ shown in Table 5.2, which are related to the overlap area of the nuclei.

[1] CMSH7-B-NOPF-MUFAST is the name of the triggers used, 7 means that the muon trigger is in coincidence with MB using corresponding to V0, B reflects that main bunches from both side were colliding and NOPF indicates NO Past-Future protection. This trigger was used for the Run I data

[2] CPBI1MSH-B-NOPF-MUON is the name of the triggers used, PBI1MSH is the high-p_{T} muon trigger in the Pb-Pb interactions, B reflects that main bunches from both side were colliding and NOPF indicates NO Past-Future protection. This trigger was used for the Run I data

Centrality (%)	$\langle N_{\mathrm{part}} \rangle$	$\langle N_{\mathrm{coll}} \rangle$	$\langle T_{\mathrm{AA}} \rangle$ (mb^{-1})	$\langle N_{\mathrm{coll}} \rangle_{\langle N_{\mathrm{part}} \rangle}$
0-20	311.0±3.3	1318±130	18.8±0.61	322.5
20-40	159.6±2.6	472.8±41	6.75±0.22	159.5
40-90	38.70±0.8	67.05±4.7	0.958±0.043	38.69
0-90	126.1±1.8	435.3±4.1	6.22±0.2	263

Table 5.2: Summary of the geometric property ($\langle N_{\mathrm{coll}} \rangle$ and $\langle N_{\mathrm{part}} \rangle$) of Pb-Pb collisions for different centrality classes. The values and their associated uncertainties are obtained with a Glauber MC calculation [MRSS07]. These numbers are for Pb-Pb collisions at 5.02 TeV centre-of-mass energy.

5.2.2 Offline muon selection

In the offline physics selection only MSH-triggered events with a good reconstructed primary vertex from the SPD were considered (details in 3.2.1). Furthermore, the data sample is refined at track level using the selection criteria detailed in section 3.2.2. The number of tracks after different cuts are shown in Table 5.3.

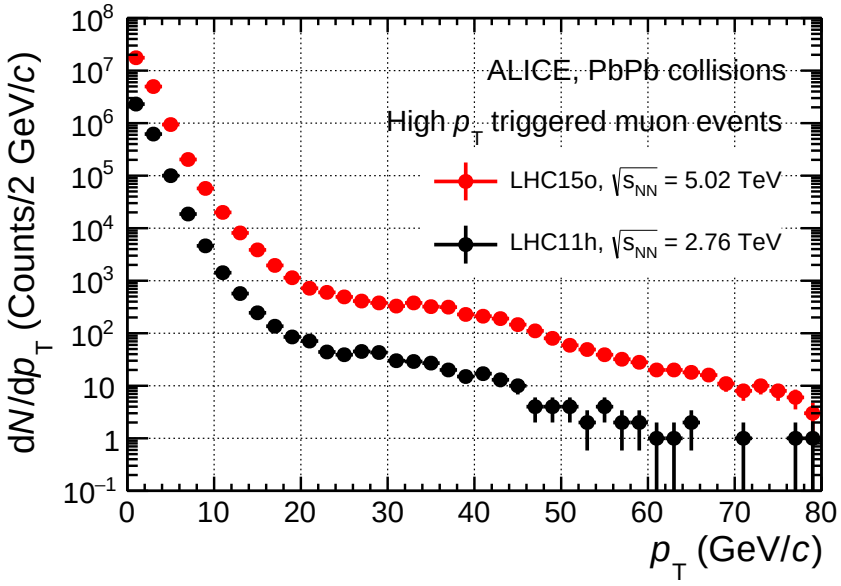

Figure 5.3: Shown in black and red are p_{T} distributions of muons after all event and track selection in Pb-Pb collisions at 2.76 and 5.02 TeV centre-of-mass energy, respectively.

The resultant inclusive single muon p_{T} distributions in different centrality bins are shown on in Figure 5.4. These plots are then used for signal extraction. In Figure 5.3 is the comparison of the p_{T} distributions from RUN I (black, LHC11h) and II (red, LHC15o) for the centrality integrated events. The comparison of the two plots shows that the statistics in RUN II is one order of magnitude higher than in RUN I. The analysis is thus performed on the RUN II data.

	Number of tracks
Event cuts	1491M
η	950M
θ_{abs}	920M
p×DCA	823M
Trigger/tracker matching	28.58M

Table 5.3: Summary of trigger-selected statistics after applying various selection cuts at event and track level: physics selection, primary vertex reconstruction and track cuts. These statistics is from the RUN II.

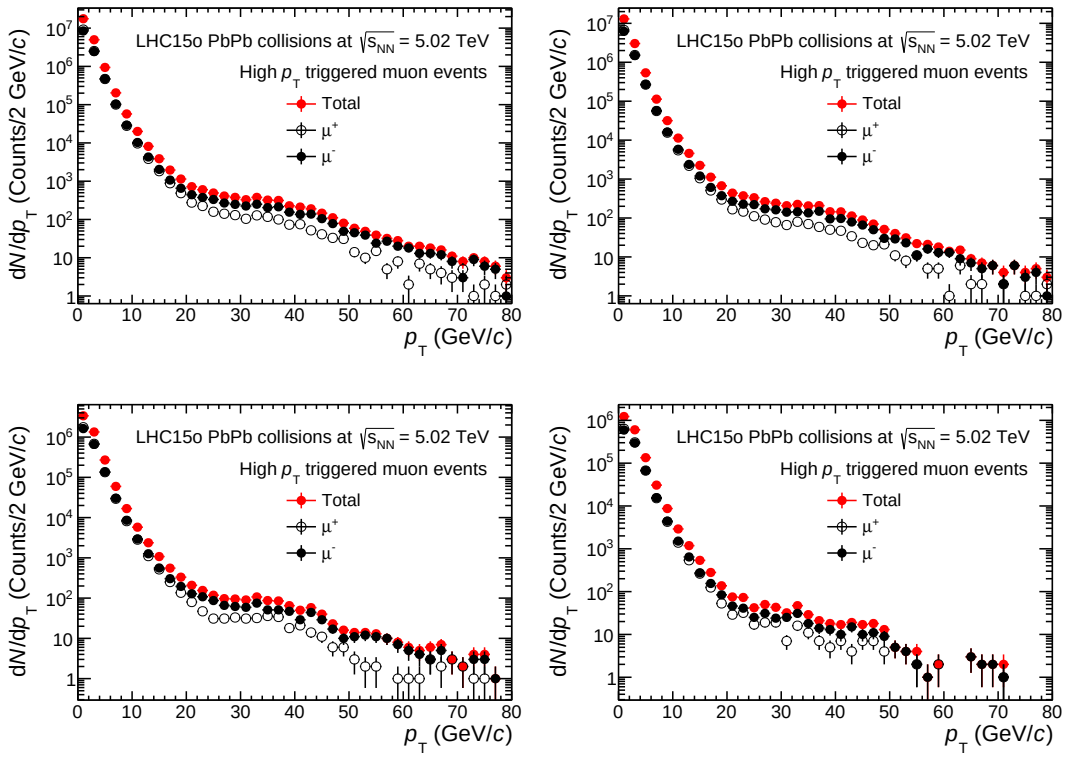

Figure 5.4: The plot show the transverse momentum distributions of muons obtained by selecting different event centrality. The V0M centrality estimator was used. Clockwise from top left is the integrated, 0_20%, 20_40% and 40_100% centrality bin.

5.3 The analysis strategy

In the following, the preliminary analysis strategy used to extract the W-boson from the p_{T} distributions shown in Figure 5.4 is described. The first step is describing the Monte-Carlo simulations (templates and $A \times \varepsilon$), then the signal extraction procedure. Finally, the normalisation procedure is outlined.

5.3.1 Monte Carlo templates and efficiency correction

The W- and Z-boson templates are based on the PYTHIA6.425 [SMS06] Leading Order (LO) event generator with CT10 [NLC+08] NLO PDF. The EPS09 [EPS09] parametrization is also used to take into account the nuclear modification of PDFs. The muons from the decay of W and Z bosons are then propagated through the absorption material using GEANT3 [BCG94] to take into account the detector effects. The simulation is based on the configuration of the detector in one run. These configurations are saved per run in an Offline Condition DataBase[3] (OCDB).

In order to take into account the isospin dependent nature of W- and Z-boson templates are simulated separately for pp, nn, np and pn collisions and combined according to Equation 5.1 below:

$$\frac{\mathrm{d}\sigma_{\mathrm{PbPb}}}{\mathrm{d}p_{\mathrm{T}}} = \frac{Z^2}{A^2} \cdot \frac{\mathrm{d}\sigma_{\mathrm{pp}}}{\mathrm{d}p_{\mathrm{T}}} + \frac{(A-Z)^2}{A^2} \cdot \frac{\mathrm{d}\sigma_{\mathrm{nn}}}{\mathrm{d}p_{\mathrm{T}}} + \frac{Z(A-Z)}{A^2} \cdot \left(\frac{\mathrm{d}\sigma_{\mathrm{pn}}}{\mathrm{d}p_{\mathrm{T}}} + \frac{\mathrm{d}\sigma_{\mathrm{np}}}{\mathrm{d}p_{\mathrm{T}}}\right) \tag{5.1}$$

where, where $A = 208$ and $Z = 82$ are the mass and atomic number of a lead ion, and $\frac{\mathrm{d}\sigma_{\mathrm{pp}}}{\mathrm{d}p_{\mathrm{T}}}$, $\frac{\mathrm{d}\sigma_{\mathrm{nn}}}{\mathrm{d}p_{\mathrm{T}}}$, $\frac{\mathrm{d}\sigma_{\mathrm{pn}}}{\mathrm{d}p_{\mathrm{T}}}$ and $\frac{\mathrm{d}\sigma_{\mathrm{np}}}{\mathrm{d}p_{\mathrm{T}}}$ are the p_{T}-differential cross sections of pp, nn, pn and np, respectively.

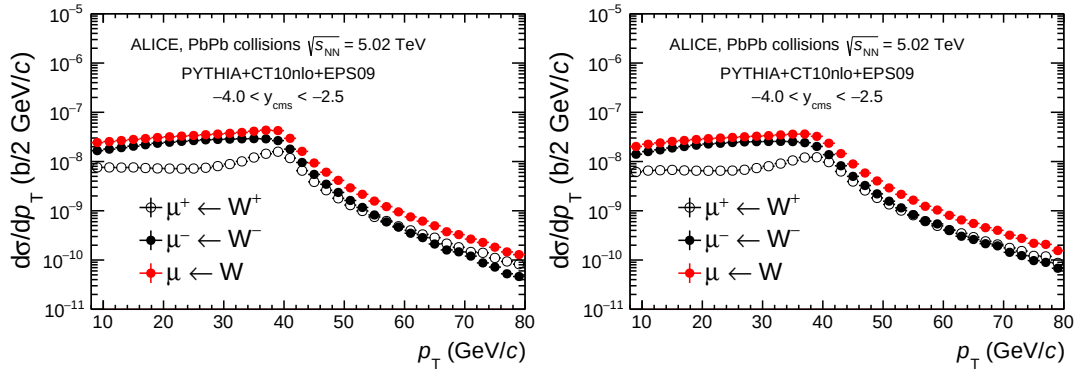

Figure 5.5: Generation (a) and reconstruction (b) level templates for PbPb collisions at 5.02 TeV using PYTHIA and CT10 (NLO) with EPS09 PDFs.

The MC templates of W-boson at generation level are shown in Figure 5.5a whereas the reconstruction level templates are shown in Figure 5.5b. The acceptance times efficiency for muons from W-boson decay with $10 < p_{\mathrm{T}} < 80$ GeV/c is 88.82±0.12% and 89.11±0.18% for negative and positive muons, respectively. The $A \times \varepsilon$ distribution as a function of p_{T} for W-boson decay muons are shown in Figure 5.6.

[3]Offline Condition DataBase (OCDB) is a catalog of files containing the calibration and alignment data. These are read-only run dependent ROOT objects stored on AliEn.

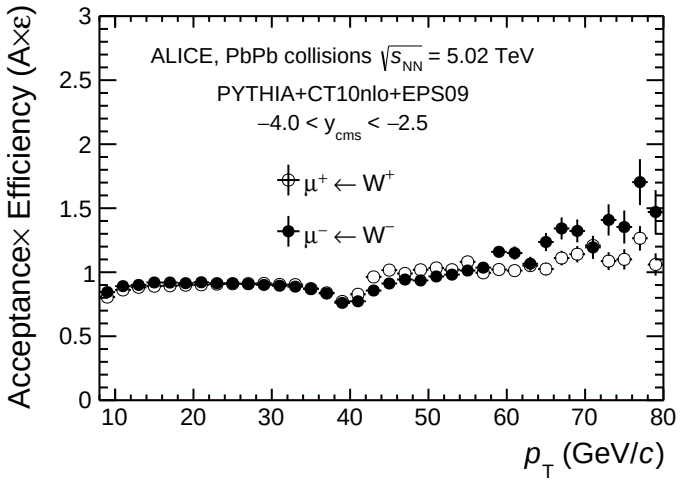

Figure 5.6: Acceptance times efficiency as a function of transverse momentum for PbPb collisions at 5.02 TeV based on the templates shown in Figure 5.5.

The heavy-flavour decay muon background template is rather tricky to obtain since FONLL simulation cannot take into account the energy loss of heavy quarks as they traverse the medium formed in heavy-ion collisions. In order to obtain the templates the R_{AA} of heavy flavour decay muons in each centrality was used to weight the FONLL central predictions. The R_{AA} [Zha17] is shown in Figure 5.7.

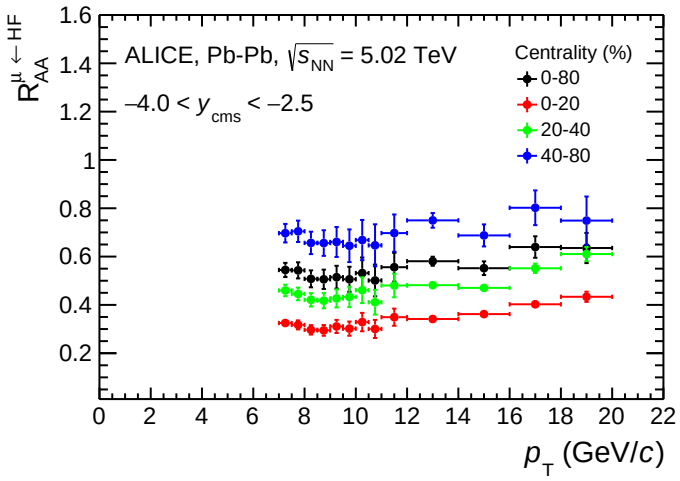

Figure 5.7: R_{AA} of muons from heavy-flavour hadron decays in various centrality classes Pb–Pb collisions at $\sqrt{s_{\mathrm{NN}}} = 5.02$ TeV. Vertical bars are the statistical uncertainties [Zha17].

The templates obtained using the R_{AA} as weights and the weights obtained by fitting the R_{AA} with a second order polynomial are shown in Figure 5.8. Additionally, shown in Figure 5.9 are the ratios of the templates in differential centrality bins relative to the 0-80% centrality.

The statistical limitation on the heavy-flavour decay muon is visible at p_{T} greater than

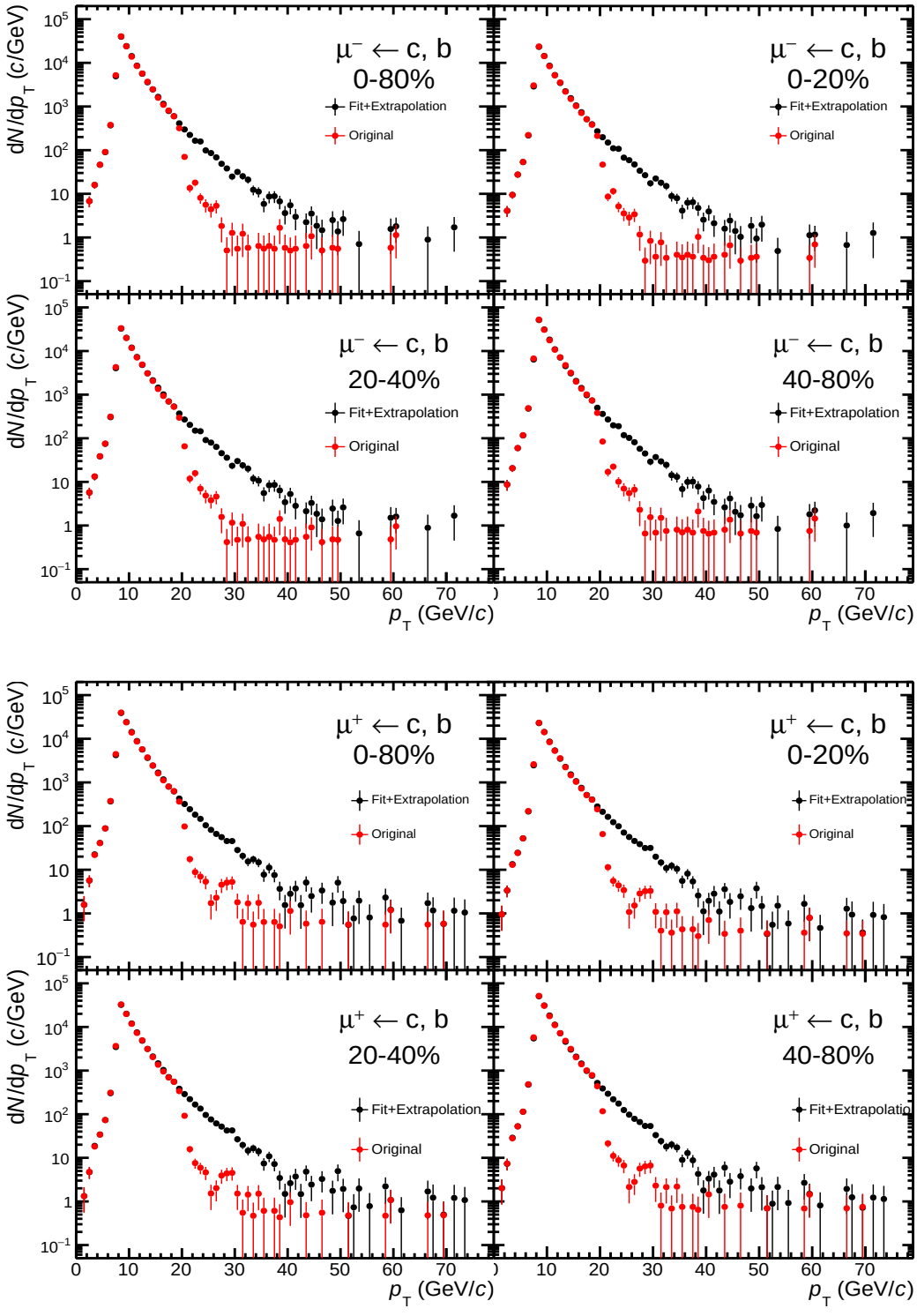

Figure 5.8: The comparison of the p_{T}-distribution of heavy-flavour decay muon templates weighted with the original R_{AA} as a function of p_{T} (red) and the ones weighted with the extrapolated fit to the R_{AA} (black).

40 GeV/c. Since this is a feasibility study, the associated systematic uncertainty is not yet taken into account.

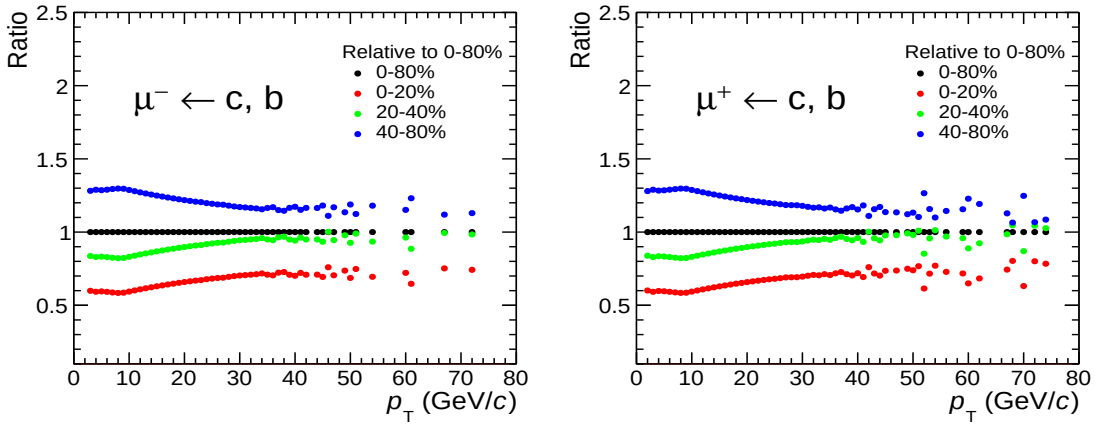

Figure 5.9: The ratio of heavy-flavour decay muons templates in each centrality bins relative to the 0-80% centrality bin. The left and right plots are for the negative and positive heavy-flavour decay muons, respectively.

5.3.2 Signal extraction

The signal extraction is based on the binned `RooFit` fits with the same selection criteria as proton-proton and proton-lead collisions. The lower fit range is set to p_{T} = 10 GeV/c where the statistics is enough to have control over the fit components, especially the heavy-flavour decay muon background. The upper limit of the lower fit range is set to p_{T} = 20 GeV/c whereas the upper fit range is varied from 50 to 80 GeV/c with steps of 5 GeV/c. The examples of the fits are shown in Figure 5.10. Considering that the W and Z boson templates are based on a simulation anchored on only one run, the fits do not describe the data well, although the fit to the negative muons is better. This effect of alignment is clearly visible in the p_{T} > 20 GeV/c. In the further studies, with all systematics taken into account, the resolution task will be used to take into account this effect. Also, a full account of alignment based on full simulations with different alignment files will be used.

The final number of muons from W-boson decays is the weighted average of the tests (trial) shown in Figure 5.11, defined as:

$$\langle N_{\mu\leftarrow\mathrm{W}}\rangle = \frac{\sum_{i=1}^{n} w_i N_{\mu\leftarrow\mathrm{W,i}}}{\sum_{i=1}^{n} w_i} \tag{5.2}$$

where i runs over the number of n tests performed and $N_{\mu\leftarrow\mathrm{W},i}$ is the number of muons from W-boson decays extracted in each test. i is the variation of p_{T} fit range. The statistical and systematic errors are computed the same way as in proton-proton and proton-lead collisions. The asymmetry of the muons is due to the isospin dependent nature of W-boson production. The quark content of Pb dictates that more W^- boson

will be formed than W^+ boson due to the abundance of the d quarks.

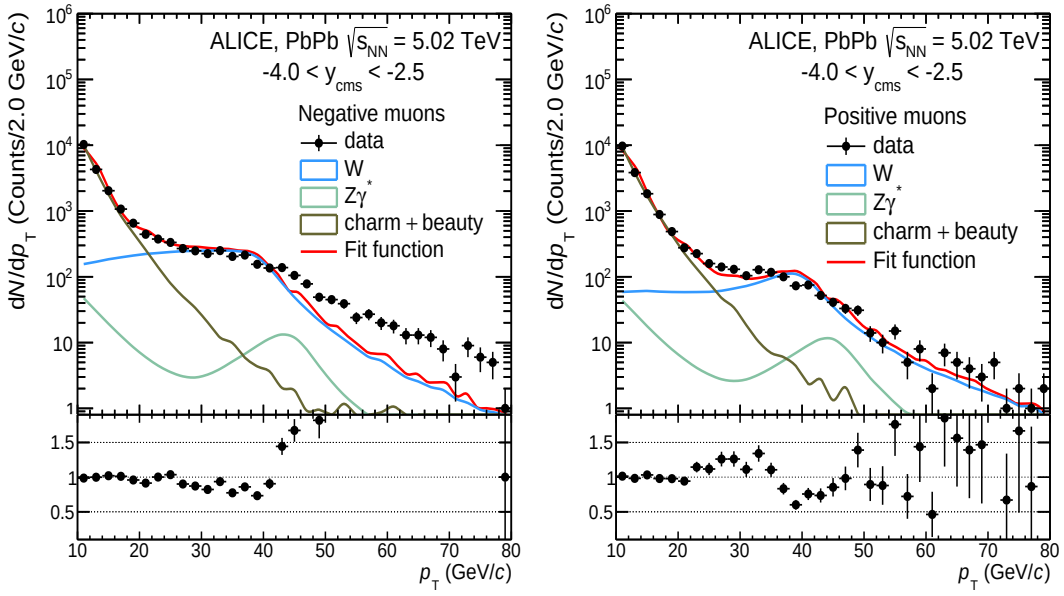

Figure 5.10: The results of the MC template fit to the inclusive distribution of negatively (left) and positively (right) charged muon candidates measured in the Pb-Pb data taking periods. In this case, the central value of the FONLL calculations weighted with the nuclear modification factor is used for the heavy-flavour background description while PYTHIA with the CT10 PDF set paired with EPS09NLO is used for W and Z boson production. Bottom panels: ratio of data and the extrapolated fit results in the range $10 < p_{\mathrm{T}} < 80$ GeV/c.

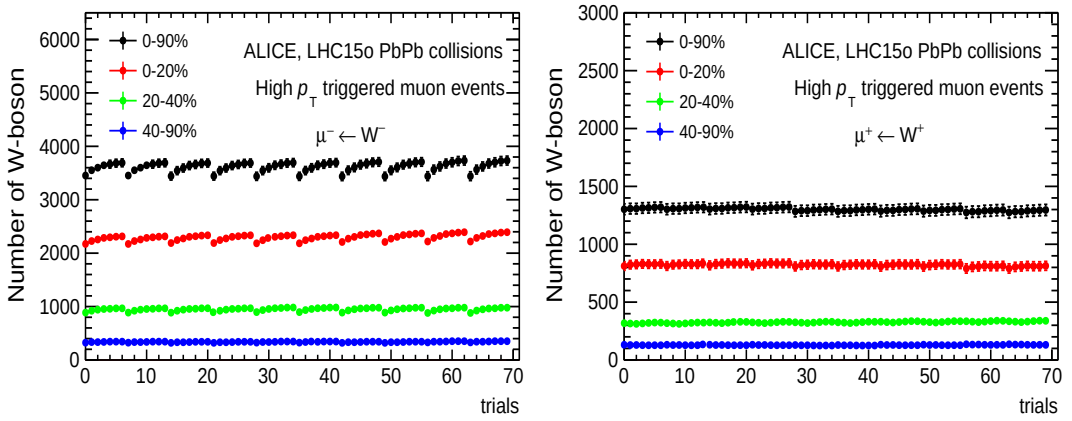

Figure 5.11: N_{W} extracted per trial (p_{T}-based trials, no alignment) for Pb-Pb data taking period in the integrated event activity bin for negative (left) and positive (right) muons. $N^{\mathrm{avg}}_{\mu^{\pm}\leftarrow \mathrm{W}^{\pm}}$, $\sigma_{\mathrm{stat.}}$ and $\sigma_{\mathrm{syst.}}$ is the average number of W-boson, statistical uncertainty and systematic uncertainty, respectively. The line in black represents $N^{\mathrm{avg}}_{\mu^{\pm}\leftarrow \mathrm{W}^{\pm}}$, and the bounds of statistical and systematic uncertainties are in blue and red.

5.3.3 Normalization to minimum-bias (MB)

The normalisation factor is computed the same way as in the p–Pb analysis (see section 3.3). The idea, as explained before, is to make sure that the results obtained with the high-p_{T} muon trigger events are normalized to the number of equivalent MB events. This is achieved using the normalisation factor (F_{norm}) which was using the offline and online methods. The offline method is the same as the one used for p–Pb, whereas the online method requires an additional correction due to the contamination of L0b scalers by V0 after pulses. So, instead of the usual CINT7-B-NOPF-MUFAST trigger the semi-central trigger C0V0M-B-NOPF-CENTNOTRD[4] is therefore used. This trigger covers the centrality range 0-60%. The normalisation factor is computed per run as:

$$F_{\mathrm{norm}}^{\mathrm{online}} = \frac{\mathrm{L0b_{C0V0M}} \times \mathrm{purity_{C0V0M}} \times F_{\mathrm{pile-up}}}{\mathrm{L0b_{MSH}} \times PS_{\mathrm{MSH}}} \tag{5.3}$$

where $\mathrm{L0b_{C0V0M}}$ and $\mathrm{L0b_{MSH}}$ are scaler values (trigger rates) for the semi-central and high-p_{T} muon triggers, $F_{\mathrm{pile-up}}$ is the pile-up correction factor and $\mathrm{purity_{C0V0M}}$ is the ratio of events events before and after the offline physics selection. The quantity $\mathrm{PS_{MSH}}$ is the ratio of events after physics selection to before physics selection. The L0b rate of both MB and MSH triggers are shown in Figure 5.12 as a function of run number.

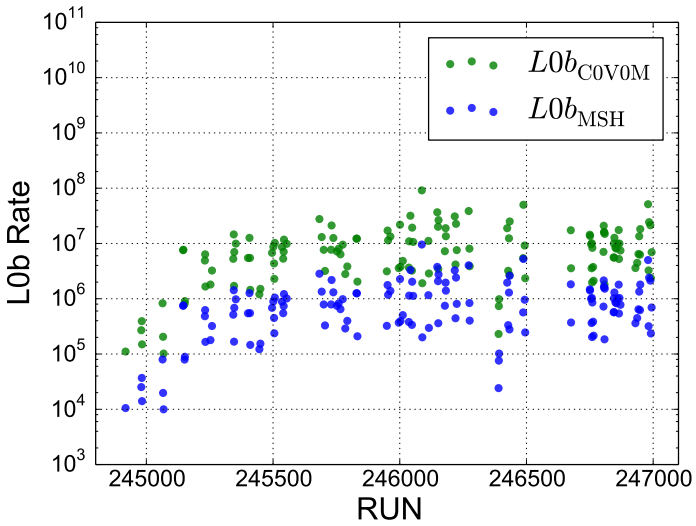

Figure 5.12: The plot shows the L0b rates of the minimum bias (C0V0M, green) and high-p_{T} muon triggers (MSH, blue) as a function of run number.

Furthermore, a correction is needed to take into account the fact that at there is 60% centrality cut for C0V0M, which is not sharp due to the V0-detector aging as seen in Figure 5.13. R is the ratio of the number of events in the 60-70% to the number

[4] C0V0M-B-NOPF-CENTNOTRD is a multiplicity based trigger which combines the V0A and V0C amplitude.

of events in the 0-70% centrality as a function of run number. The ratio decreases with increasing run number as seen in Figure 5.13. The corrected normalisation factor obtained with the online method in the centrality interval 0-90% is obtained as:

$$F_{\mathrm{norm}}(\mathrm{MSH})\ |_{0-90\%} = F_{\mathrm{norm}}^{\mathrm{online}}(\mathrm{MSH})\ \cdot\ \frac{9(1-\mathrm{R})}{6}, \tag{5.4}$$

where $F_{\mathrm{norm}}^{\mathrm{online}}(\mathrm{MSH})$ is the normalisation factor in the 0-60% centrality interval and R is the correction factor from Figure 5.13.

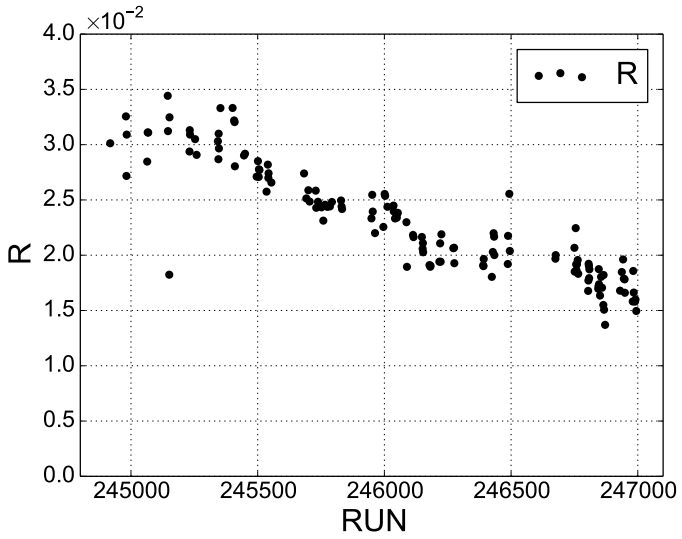

Figure 5.13: The ratio of the number of events in the 60-70% centrality bin to the number of events in the 0-70% centrality bin as a function of run number.

In Figure 5.14 are other correction factors used in computing the normalisation factor online. The $F_{\mathrm{pile-up}}$ is also used in the offline method.

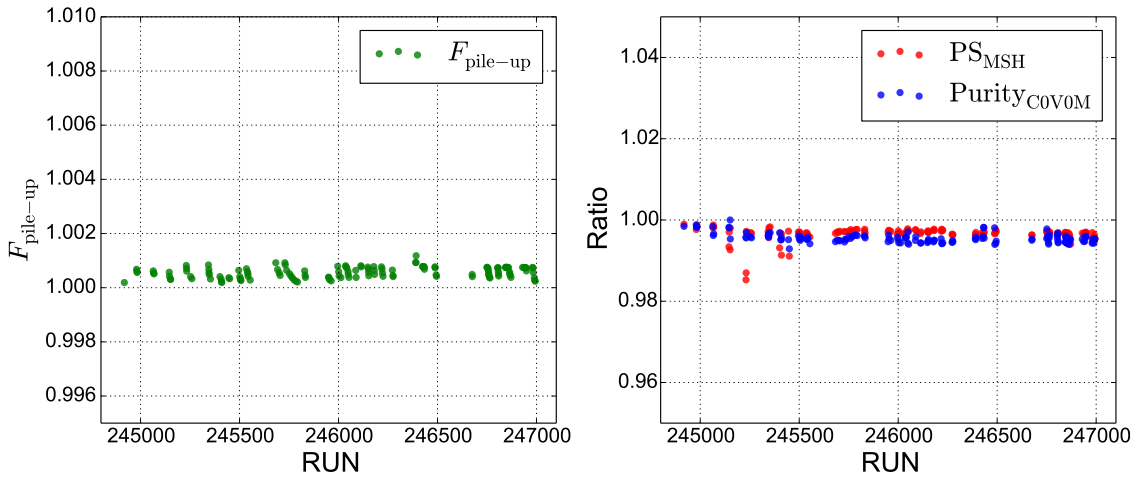

Figure 5.14: The plots show the $F_{\mathrm{pile-up}}$ (left) and ratios $\mathrm{PS_{MSH}}$ and $\mathrm{Purity_{C0V0M}}$ (right) as a function of run number.

In Figure 5.15 are distributions of the normalisation factor (left) and the normalisation factor as a function of run number (right). The mean of the fits are 14.40 and 14.36 whereas the RMS are 0.38 and 0.36 for offline and online method, respectively. Finally, the normalisation factor used to compute the MB equivalent of MSH events (see Equation 5.5) is the average of the two methods and the difference between the two is taken as a systematic uncertainty, resulting in $F_{\mathrm{norm}}\,|_{0-90\%} = 14.37 \pm 0.04$. The normalisation factor obtained as a function of centrality is shown in Figure 5.16. The MSH equivalent number of MB events as a function of centrality can be obtained in two ways according to equations 5.7 and 5.8.

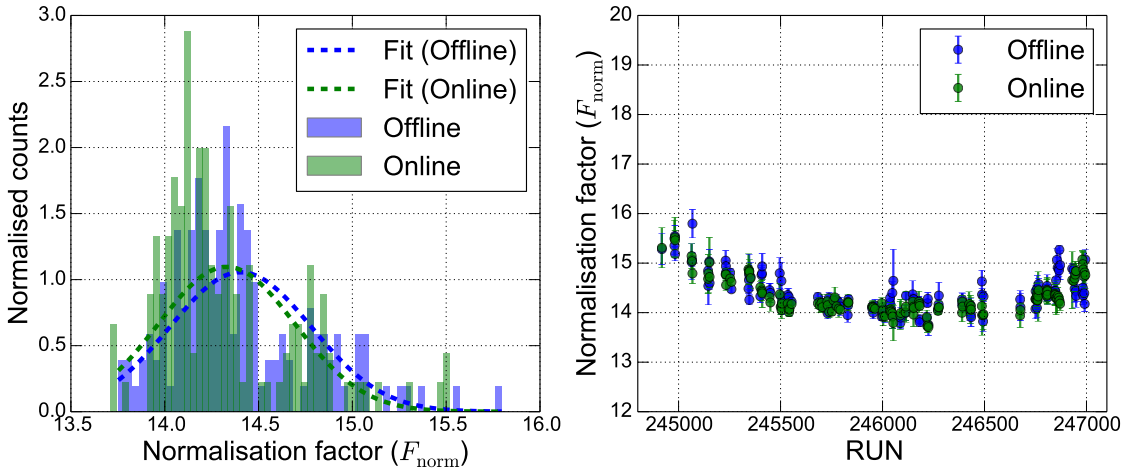

Figure 5.15: The plots show the distribution of the normalisation factor overlayed with the Gaussian distributions describing each histogram (left) and the normalisation factor as a function of run number (right).

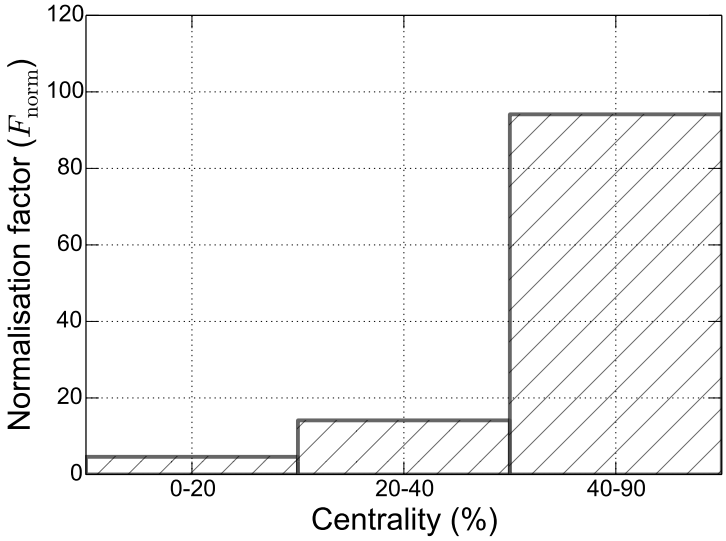

Figure 5.16: The plot shows the normalisation factor as a function of centrality.

$$N_{\mathrm{MB}}\,|_{0-90\%} = N_{\mathrm{MSH}} \cdot F_{\mathrm{norm}}\,|_{0-90\%} \tag{5.5}$$

The luminosity (shown in Table 5.4) is thus computed as:

$$\mathcal{L}_{\text{int}} = \frac{N_{\text{MSH}} \cdot F_{\text{norm}} \,|_{0-90\%}}{\sigma_{\text{MB}}} \tag{5.6}$$

where σ_{MB} is the inelastic Pb-Pb cross section which is found to be $7.7 \pm 0.1^{+0.5}_{-0.6}$ b.

In equation 5.7, N^c_{MB} is the number of MB events in centrality bin c and f_c is the scaling factor which amounts to 20/90 for centrality bins 0-20% and 20-40% and 40/90 for the 40-90% centrality bin. Alternatively, as shown in Equation 5.8, N^c_{MB} can be obtained by multiplying the normalisation factor in each centrality bin (F^c_{norm}) with the number of MSH events in each bin (N^c_{MSH}).

$$N^c_{\text{MB}} = N_{\text{MSH}} \cdot f_c \cdot F_{\text{norm}} \,|_{0-90\%} \tag{5.7}$$

$$N^c_{\text{MB}} = N^c_{\text{MSH}} \cdot F^c_{\text{norm}} \tag{5.8}$$

Centrality (%)	N_{MSH}	F_{norm}	$\mathcal{L}_{\text{integrated}}$ (μb)
0-20	72.50M	4.61±0.004	43.40
20-40	23.59M	14.14±0.018	43.31
40-90	8.88M	94.13±0.165	108.55
0-90	104.9M	14.3±0.01	195.76

Table 5.4: Summary of MSH events, normalisation factor and equivalent luminosity.

5.4 Systematic uncertainty

The signal extraction, tracking and trigger efficiency as well as the tracker-trigger matching are estimated as in the proton-lead collisions. The summary of the systematic uncertainties are shown in Table 5.5.

5.5 Results

Since the W-boson production cross section is expected to scale with the number of binary nucleon-nucleon collisions, the production of muons from W-boson decay is studied as a function of centrality. For this observable the number of μ^+ and μ^- are extracted separately and then summed in order to gain on statistics. The resulting cross sections are then normalised to the average number of binary collisions or the nuclear overlap function [A$^+$16a]. The vertical lines and open boxes represent the statistical and systematic uncertainties, respectively. Only uncorrelated systematics

Signal extraction*	0.89 - 3.4%
Tracking efficiency	1.5% (c)
Trigger efficiency	1.8% (c)
Tracker/trigger matching	0.25% (c)
F_{norm}	0.28% (c)
Inelastic cross section	6.5 - 7.8% (c)
$\langle T_{\text{AA}} \rangle$	<3.2%
Pile-up	<0.5%

Table 5.5: Summary of systematic uncertainties for W-boson analysis. The uncertainties that are correlated between measurements in different centrality bins are indicated with (c). The asterisk refer to preliminary systematic uncertainties, this is as a function of centrality.

uncertainties (these are uncertainties on $\langle N_{\text{coll}} \rangle$ and signal extraction) are included in the open boxes. The pile-up systematic uncertainty is not included, neither is it corrected since it is negligible. The global uncertainty is a quadrature sum of tracking, trigger and tracker/trigger matching efficiencies as well as the normalisation (normalisation factor and inelastic cross-section). Shown in Figure 5.17 is the $\langle N_{\text{coll}} \rangle$-normalised cross section as a function of centrality and as can be seen the results show a flat trend within uncertainties. This implies that the production of W-boson is compatible with geometric expectation of the production of hard probes, that is, W-boson production scales with the number of binary nucleon-nucleon collisions. The

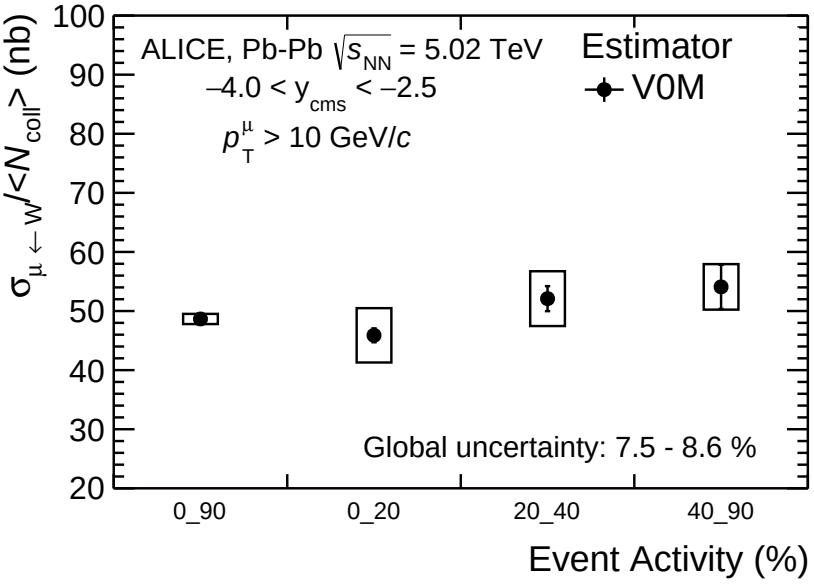

Figure 5.17: $\langle N_{\text{coll}} \rangle$-normalized cross sections of $\mu^{\pm}$ from $W^{\pm}$ as a function of centrality is shown. The vertical bars and open boxes represent statistical and systematic uncertainties, respectively. The correlated global uncertainties include the inelastic cross section, normalisation and tracking and trigger systematics.

yield of W-boson normalised to the nuclear overlap function ($\langle T_{\text{AA}} \rangle$) is plotted as a

function of $\langle N_{\mathrm{part}} \rangle$ weighted with $\langle N_{\mathrm{coll}} \rangle$ as shown in Figure 5.18. $\langle N_{\mathrm{part}} \rangle_{N_{\mathrm{coll}}}$ provides a better estimation of centrality for hard processes, since it is expected that the production of W-boson scales with the average number of colliding nucleons. The measurement in the 0-90% centrality bin is compared with two theoretical calculations: proton-proton and lead-lead cross sections are estimated using FEWZ with MSTW2008 and Pythia 6.4 with CT10 including nPDFs, respectively. The measurement and the theoretical calculations are compatible within uncertainties. The Pythia 6.4 theoretical calculation is computed by integrating the W-boson template between $10 < p_{\mathrm{T}} < 80$ GeV/c. These theoretical calculations are only compared with the measurement in the 0-90% (MB) since they can only provide MB calculations. The trend shows a decreasing yield as a function of $\langle N_{\mathrm{part}} \rangle_{N_{\mathrm{coll}}}$, although within uncertainties there is a compatibility with flatness. Furthermore, as expected the cross section of W-boson in Pb-Pb collisions is greater than the one in pp collisions as observed in the theoretical calculations.

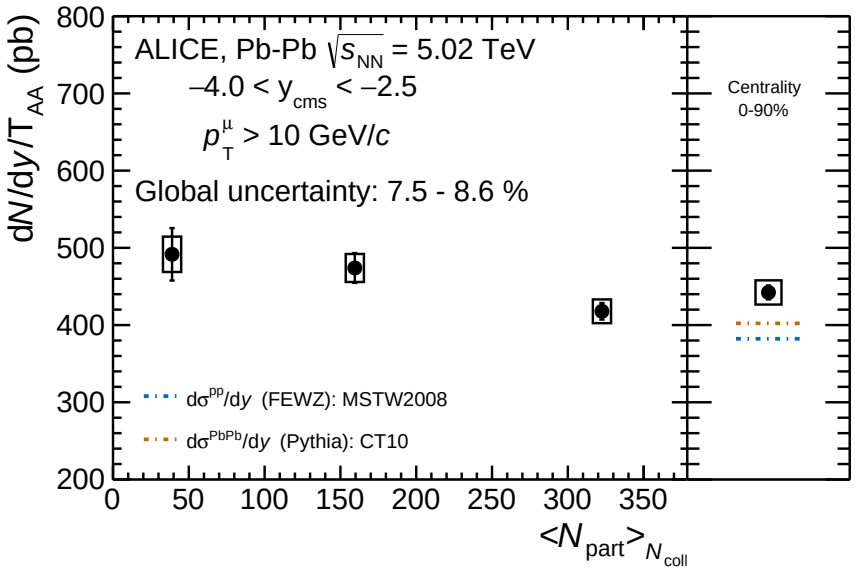

Figure 5.18: $\langle T_{\mathrm{AA}} \rangle$-normalized cross sections of $\mu^{\pm}$ from $\mathrm{W}^{\pm}$ as a function of $\langle N_{\mathrm{coll}} \rangle$-weighted $\langle N_{\mathrm{part}} \rangle$. The vertical bars and open boxes represent statistical and systematic uncertainties, respectively. The correlated global uncertainties include the inelastic cross section, normalisation and tracking and trigger systematics. The 0-90% result is compared with theoretical cross section from Pythia with CT10 including EPS09 nuclear PDF parametrization and FEWZ with CT10. The theoretical calculations only provide MB calculations and thus are only compared to the measurement in 0-90% centrality bin.

Part IV

Conclusions and Outlook

"All men by nature desire knowledge."

Aristotle

6

Summary, conclusions and outlook

This chapter concludes and summarises the results obtained in this work, and provides recommendations about future measurements and/or studies.

Contents

6.1 Summary and Conclusions

In this thesis we have studied W-boson production in pp, p-Pb and Pb-Pb collisions at LHC energies. W-boson production occurs in hard scattering processes at the initial stage of the collision, and it is expected to scale with the number of binary nucleon-nucleon collisions. The centrality-dependent yield can therefore be used as a test bench for the centrality estimation at the LHC. The focus of this report was W boson production via the muonic decay channel as measured in ALICE at forward rapidity.

In the first chapter, a brief account of the history of physics which led to the state-of-the-art particle accelerators like the LHC were presented. The chapter also touched on the history of heavy-ion experiments preceding ALICE at the LHC and the physics pertaining to the QGP in the context of QCD. In addition, it was mentioned how the QGP is studied experimentally in nucleus-nucleus collisions and how heavy-ion collisions evolve with time. The motivations to study electroweak boson production in heavy-ion collisions were also discussed in Chapter 1. Chapter 2 was mainly devoted to the experimental aspects. This included the description of the ALICE detector at the LHC, focusing on the Forward Muon Spectrometer as well as on other detectors relevant in the data analysis, and the ALICE online and offline frameworks. The data analysis and results obtained in the study were described in Chapter 3, 4 and 5 for p–Pb, pp and Pb-Pb collisions, respectively.

In order to understand the effects of cold nuclear matter effects (in this case, isospin effect and shadowing/anti-shadowing) on the muons produced from W-boson decays, their production cross sections were measured in p–Pb collisions with the ALICE Forward Muon Spectrometer. These measurements were done at forward (p-going) and backward (Pb-going) rapidity. The results presented in Chapter 3 show that the measured and theoretical cross section of muons from W-boson decays are in agreement within uncertainties. The smaller cross section of W^+ boson at backward rapidity is due to the W-boson forward/backward production asymmetry arising from the isospin effect, as well as to the combined effect of the parity violation of the weak interaction, which only couples left-handed fermions with right-handed anti-fermions, and of the helicity conservation in the leptonic decay. These results are consistent with observations by the CMS collaboration, whose measurements were done at mid-rapidity with different cuts and higher luminosity. In this context the cross sections of W bosons obtained in this study were divided by theoretical calculations and compared with the same ratio from the measurements by the CMS collaboration. Both results exhibit the same trend and are in agreement within uncertainties. The comparison of measured data with theoretical calculations show that the inclusion of a parameterisation of the nuclear modification of the PDF in the calculations results in a slightly lower value of the cross section, especially at forward rapidity, with a variation of the same order as

the uncertainties in the theoretical calculations, thereby limiting the discriminating power of the cross section alone. The asymmetry in the production of the W^+ and W^- bosons can be used to gain sensitivity in the study of the nuclear modification of the PDFs. The results obtained for charge asymmetries have reduced uncertainties, thus have a better sensitivity to the nPDFs. The results of the forward-to-backward ratio (a traditional way to quantify cold nuclear matter effects) agree with those of the cross section and charge asymmetries with current uncertainties. The measurements agree with theoretical calculations with and without accounting for nuclear modifications of the free proton PDFs. The results of the measurement of W-boson production cross section normalised by the number of binary nucleon-nucleon collisions as a function of centrality at forward and backward rapidity showed that the cross section of muons from W-boson decay scale with the average number of colliding nucleons $\langle N_{\rm coll}\rangle$. Due to limited statistics this observable could not be used to distinguish between biased and unbiased centrality estimation. Measurements of W-boson cross sections as a function of centrality, published by the CMS collaboration show a similar trend as our results. Further measurements with better precision are needed to provide more stringent constraints on the nPDFs and on the binary scaling.

Measurements in pp collisions provide information on quark PDF at high Q^2 and serves as a reference for measurements in p-Pb and Pb-Pb collisions. The cross section, charge asymmetry and charge ratio measurements show a good agreement with different theoretical calculations (FEWZ and POWHEG with different PDFs) within uncertainties. The lack of statistics limits the constraining power of these measurements to the quark PDF. The measurement by the LHCb collaboration at forward rapidity and a complimentary measurement by the CMS collaboration at mid-rapidity also show an agreement with same theoretical calculations within uncertainties. Our measurements of the cross section is higher than that of the LHCb, although the agreement between the two is within 1.5 sigma.

W-boson measurements in Pb-Pb collisions are essential to test the scaling of hard processes with binary nucleon-nucleon collisions. With these measurements, the aim is to check our understanding of collision geometry (e.g. Glauber), factorisation and provide a standard candle for colour-charge interactions in a QCD medium. In this context, we have measured W-boson production as a function of centrality in Pb-Pb collisions using RUN II data collected at centre-of-mass energy of 5.02 TeV. Indeed, the statistics in the Run II data is approximately $\sim$4.5 times higher than the statistics of Run I data at 2.76 TeV centre-of-mass energy. Therefore, there is enough statistics to conduct a centrality-differential study of W-boson cross section using RUN II data. In this preliminary study, we have measured the yield and cross section of muons from W-boson decays, normalized to the average number of binary collisions and nuclear overlap function and plotted as a function of centrality($\langle N_{\rm coll}\rangle$ and $N_{\rm coll}$-weighted $\langle N_{\rm part}\rangle$). The cross section results show a flat trend, which indicates that W-boson production scales with the average binary nucleon-nucleon collisions.

The same conclusions have been reached by the CMS and ATLAS collaboration in their measurements of W-boson production in Pb-Pb at 2.76 TeV at mid-rapidity.

To conclude, our results from p-Pb analysis at 5.02 TeV are consistent with those published by the CMS collaboration at mid-rapidity and are described by NLO pQCD calculations as well as NNLO calculations using FEWZ theoretical calculations. However, the uncertainties on the measurement cannot constrain the nuclear modification of the PDFs. Similarly in pp collisions, our results are well described by NLO pQCD calculations and NNLO calculations using FEWZ theoretical calculation. This data could be used to constrain quark PDFs. In Pb-Pb collisions at 5.02 TeV we have enough statistics to conduct differential studies and compare results with theoretical calculations as well as with measurements from other LHC experiments.

6.2 Outlook

There is an opportunity to further study the production of W-boson in different colliding systems at even higher luminosities and energies at the LHC. The measurement of W-boson production in Pb-Pb collisions using LHC Run II data has shown that enough statistics is available to perform a differential measurements, for example, centrality and rapidity studies. Currently, the full Monte-Carlo simulation, better estimation of the acceptance and efficiency ($A \times \varepsilon$), alignment and improved heavy-flavour description are the remaining ingredients to finalise the study. In 2016 the ALICE detector collected p–Pb data at 5.02 and 8.16 TeV center-of-mass energies. This data could be used to further increase the statistics, which will hopefully help to fulfill the ultimate goal of constraining the nuclear PDFs. In addition, since the start of data taking in 2009 the ALICE Collaboration has collected just more than 10 petabytes of raw data. With this data, ALICE has become the leading heavy-ion experiment in the world, quickly expanding the knowledge gathered in previous experiments all over the world. Based on results obtained thus far the collaboration has identified key measurements to further our understanding of the hot and dense matter created in these collisions, and devised a strategy to facilitate these measurements. Many of the proposed observables, the study of single muons and dimuons from W/Z bosons require a shift in the data taking strategy, moving away from triggering a small subset of events to the online processing and recording of all collisions delivered by the LHC. To achieve these goals, ALICE is rolling out a major upgrade envisaged to commence during the Long Shutdown 2 (LS2) which, at present, is foreseen to start at the end of 2018 and will last until the beginning of 2020. The upgrade entails replacement of some detectors while most other detectors, including the Muon Spectrometer (Tracking and Trigger systems) will receive new front-end and readout electronics, allowing all detectors to be read out at or near the expected interaction rate of up to 50 000 Pb-Pb collisions per second. With these data we could expand to include studies such as

double parton scattering (DPS), for example, the production of W- and Z-boson + minijets, W+W or W+Z.

"The scientists of today think deeply instead of clearly. One must be sane to think clearly, but one can think deeply and be quite insane"
- Nikola Tesla

Bibliography

[A+83a] G. Arnison et al. Experimental Observation of Isolated Large Transverse Energy Electrons with Associated Missing Energy at s**(1/2) = 540-GeV. *Phys.Lett.*, B122:103–116, 1983. (Cited on page 19)

[A+83b] G. Arnison et al. Experimental Observation of Lepton Pairs of Invariant Mass Around 95-GeV/c**2 at the CERN SPS Collider. *Phys.Lett.*, B126:398–410, 1983. (Cited on page 19)

[A+85] G.J. Alner et al. Multiplicity distributions in different pseudorapidity intervals at a CMS energy of 540 GeV. *Physics Letters B*, 160(1):193 – 198, 1985. (Cited on page 45)

[A+01] T. Affolder et al. Measurement of the W boson mass with the Collider Detector at Fermilab. *Phys. Rev.*, D64:052001, 2001. (Cited on page 19)

[A+06] J. Alcaraz et al. A Combination of preliminary electroweak measurements and constraints on the standard model. *CERN-PH-EP-2006-042, LEPEWWG-2006-01, ALEPH-2006-001-PHYSICS-2006-001, DELPHI-2006-014-PHYS-948, L3-NOTE-2833, OPAL-PR-419*, 2006. (Cited on page 19)

[A+08a] G. Aad et al. The ATLAS Experiment at the CERN Large Hadron Collider. *JINST*, 3:S08003, 2008. (Cited on page 41)

[A+08b] K. Aamodt et al. The ALICE experiment at the CERN LHC. *JINST*, 3:S08002, 2008. (Cited on page 13, 41, 42, 44, 45)

[A+08c] Jr. Alves, A. Augusto et al. The LHCb Detector at the LHC. *JINST*, 3:S08005, 2008. (Cited on page 41)

[A+11a] Georges Aad et al. Measurement of the Muon Charge Asymmetry from W Bosons Produced in pp Collisions at $\sqrt{s} = 7$ TeV with the ATLAS detector. *Phys.Lett.*, B701:31–49, 2011. (Cited on page xvi, 33)

[A+11b] K. Aamodt et al. Rapidity and transverse momentum dependence of inclusive J/ψ production in *pp* collisions at $\sqrt{s} = 7$ TeV. *Phys. Lett.*, B704:442–455, 2011. [Erratum: Phys. Lett.B718,692(2012)]. (Cited on page 95)

[A+11c] M.M. Aggarwal et al. Measurement of the parity-violating longitudinal single-spin asymmetry for $W^{\pm}$ boson production in polarized proton-proton collisions at $\sqrt{s} = 500 - GeV$. *Phys.Rev.Lett.*, 106:062002, 2011. (Cited on page 23)

[A+12a] G. Aad et al. Measurement of the inclusive $W^{\pm}$ and $Z/\gamma*$ cross sections in the e and μ decay channels in *pp* collisions at $\sqrt{s} = 7$ TeV with the atlas detector. *Phys. Rev. D*, 85:072004, Apr 2012. (Cited on page 33)

[A+12b] Georges Aad et al. Observation of a new particle in the search for the Standard Model Higgs boson with the ATLAS detector at the LHC. *Phys. Lett.*, B716:1–29, 2012. (Cited on page 6)

[A+12c] T. Aaltonen et al. Precise measurement of the W-boson mass with the CDF II detector. *Phys. Rev. Lett.*, 108:151803, 2012. (Cited on page 19)

[A+13a] Georges Aad et al. Measurement of Z boson Production in Pb+Pb Collisions at $\sqrt{s_{NN}} =$ 2.76 TeV with the ATLAS Detector. *Phys. Rev. Lett.*, 110(2):022301, 2013. (Cited on page 33)

[A+13b] E. Abbas et al. Performance of the ALICE VZERO system. *JINST*, 8:P10016, 2013. (Cited on page xvii, xviii, 46, 70)

[A+13c] Betty Abelev et al. Centrality determination of Pb-Pb collisions at $\sqrt{s_{NN}} = 2.76$ TeV with ALICE. *Phys. Rev.*, C88(4):044909, 2013. (Cited on page 72, 117)

[A+13d] Betty Abelev et al. Pseudorapidity density of charged particles in p + Pb collisions at $\sqrt{s_{NN}} = 5.02$ TeV. *Phys. Rev. Lett.*, 110(3):032301, 2013. (Cited on page 70, 73)

[A+14a] R. Aaij et al. Observation of Z production in proton-lead collisions at LHCb. *JHEP*, 09:030, 2014. (Cited on page 33)

[A+14b] Betty Bezverkhny Abelev et al. J/ψ production and nuclear effects in p-Pb collisions at $\sqrt{S_{NN}} = 5.02$ TeV. *JHEP*, 02:073, 2014. (Cited on page 95)

[A+14c] Betty Bezverkhny Abelev et al. Measurement of visible cross sections in proton-lead collisions at $\sqrt{s_{\rm NN}} = 5.02$ TeV in van der Meer scans with the ALICE detector. *JINST*, 9(11):P11003, 2014. (Cited on page 46, 94, 96)

[A+14d] Betty Bezverkhny Abelev et al. Performance of the ALICE Experiment at the CERN LHC. *Int.J.Mod.Phys.*, A29:1430044, 2014. (Cited on page xi, xvii, xviii, 42, 43, 44, 71, 116)

[A+15a] Georges Aad et al. Measurement of the production and lepton charge asymmetry of W bosons in Pb+Pb collisions at $\sqrt{\mathbf{s_{NN}}} = 2.76$ **TeV** with the ATLAS detector. *Eur. Phys. J.*, C75(1):23, 2015. (Cited on page xvii, 33, 34, 35)

[A+15b] Georges Aad et al. Z boson production in p+Pb collisions at $\sqrt{s_{NN}} = 5.02$ TeV measured with the ATLAS detector. *Phys. Rev.*, C92(4):044915, 2015. (Cited on page 33)

[A+15c] Roel Aaij et al. Observation of $J/\psi p$ Resonances Consistent with Pentaquark States in $\Lambda_b^0 \to J/\psi K^- p$ Decays. *Phys. Rev. Lett.*, 115:072001, 2015. (Cited on page 6)

[A+15d] Jaroslav Adam et al. Centrality dependence of inclusive J/ψ production in p-Pb collisions at $\sqrt{s_{\rm NN}} = 5.02$ TeV. *JHEP*, 11:127, 2015. (Cited on page 77)

[A+15e] Jaroslav Adam et al. Centrality dependence of particle production in p-Pb collisions at $\sqrt{s_{\rm NN}}$= 5.02 TeV. *Phys. Rev.*, C91(6):064905, 2015. (Cited on page xvii, 45, 47, 48, 49, 73, 96, 98, 111)

[A+16a] Jaroslav Adam et al. Centrality dependence of the charged-particle multiplicity density at midrapidity in Pb-Pb collisions at $\sqrt{s_{\rm NN}} = 5.02$ TeV. *Phys. Rev. Lett.*, 116(22):222302, 2016. (Cited on page 135, 146)

[A+16b] Jaroslav Adam et al. Inclusive quarkonium production at forward rapidity in pp collisions at $\sqrt{s} = 8$ TeV. *Eur. Phys. J.*, C76(4):184, 2016. (Cited on page 117, 124)

[A+17a] Shreyasi Acharya et al. Production of muons from heavy-flavour hadron decays in p-Pb collisions at $\sqrt{\mathbf{s_{NN}}} = 5.02$ TeV. *Phys. Lett.*, B770:459–472, 2017. (Cited on page 84)

[A+17b] Jaroslav Adam et al. J/ψ suppression at forward rapidity in Pb-Pb collisions at $\sqrt{\mathbf{s}_{\rm NN}} = 5.02$ TeV. *Phys. Lett.*, B766:212–224, 2017. (Cited on page 25)

[A+17c] Jaroslav Adam et al. W and Z boson production in p-Pb collisions at $\sqrt{s_{\rm NN}} = 5.02$ TeV. *JHEP*, 02:077, 2017. (Cited on page 74, 111)

[AA+12] G. Aad, T. Abajyan, et al. Observation of a new particle in the search for the standard model higgs boson with the {ATLAS} detector at the {LHC}. *Physics Letters B*, 716(1):1 – 29, 2012. (Cited on page 6)

[AAA+89] G.S. Abrams, Chris Adolphsen, D. Averill, Joseph Ballam, Barry C. Barish, et al. Measurements of Z Boson Resonance Parameters in e^+e^- Annihilation. *Phys.Rev.Lett.*, 63:2173, 1989. (Cited on page 19)

[Abb98] B. Abbott. Determination of the mass of the w boson using the dØ detector at the fermilab tevatron. *Phys. Rev. D*, 58:012002, Jun 1998. (Cited on page 19)

[Abe89] F. Abe. Measurement of the mass and width of the Z^0 boson at the fermilab tevatron. *Phys. Rev. Lett.*, 63:720–723, Aug 1989. (Cited on page 19)

[Abe13] B. et. al. Abelev. Centrality dependence of π, K, and p production in Pb-Pb collisions at $\sqrt{s_{NN}} = 2.76$ TeV. *Phys. Rev. C*, 88:044910, Oct 2013. (Cited on page 15)

[Ada07] A. et. al. Adare. Scaling properties of azimuthal anisotropy in Au + Au and Cu + Cu collisions at $\sqrt{s_{\rm NN}} = 200$ GeV. *Phys. Rev. Lett.*, 98:162301, Apr 2007. (Cited on page 15)

[ADN11] Javier L. Albacete, Adrian Dumitru, and Yasushi Nara. CGC initial conditions at RHIC and LHC. *J. Phys. Conf. Ser.*, 316:012011, 2011. (Cited on page 13, 14)

[Ae12] R. Aaij and etal. Inclusive w and z production in the forward region at $\sqrt{s} = 7$ tev. *Journal of High Energy Physics*, 2012(6):58, 2012. (Cited on page 33)

[ALI08a] ALICE Collaboration. The ALICE Dimuon Spectrometer. https://twiki.cern.ch/twiki/bin/viewauth/ALICE/MuonTracking, 2008. [Online; accessed 7-March-2016]. (Cited on page xvii, 50)

[ALI08b] ALICE Collaboration. The ALICE Dimuon Spectrometer. http://aliceinfo.cern.ch/Public/en/Chapter2/Chap2_dim_spec.html, 2008. [Online; accessed 18-August-2015]. (Cited on page xvii, 52)

[ANOR08] Simone Alioli, Paolo Nason, Carlo Oleari, and Emanuele Re. NLO vector-boson production matched with shower in POWHEG. *JHEP*, 0807:060, 2008. (Cited on page xxiii, 81, 119, 123, 129)

[B+83a] P. Bagnaia et al. Evidence for $Z^0 \to e^+e^-$ at the CERN anti-p p Collider. *Phys.Lett.*, B129:130–140, 1983. (Cited on page 19)

[B+83b] M. Banner et al. Observation of Single Isolated Electrons of High Transverse Momentum in Events with Missing Transverse Energy at the CERN anti-p p Collider. *Phys.Lett.*, B122:476–485, 1983. (Cited on page 19)

[B+12] A. Bazavov et al. The chiral and deconfinement aspects of the QCD transition. *Phys. Rev.*, D85:054503, 2012. (Cited on page 11)

[Baz09] Bazavov, A. etal. Equation of state and QCD transition at finite temperature. *Phys. Rev. D*, 80:014504, Jul 2009. (Cited on page xv, 12)

[BBC+13] Richard D. Ball, Valerio Bertone, Stefano Carrazza, Christopher S. Deans, Luigi Del Debbio, et al. Parton distributions with LHC data. *Nucl.Phys.*, B867:244–289, 2013. (Cited on page xv, 22, 23, 129)

[BBK+13] Francesco Becattini, Marcus Bleicher, Thorsten Kollegger, Tim Schuster, Jan Steinheimer, and Reinhard Stock. Hadron Formation in Relativistic Nuclear Collisions and the QCD Phase Diagram. *Phys. Rev. Lett.*, 111:082302, Aug 2013. (Cited on page 11)

[BCG94] Rene Brun, Federico Carminati, and Simone Giani. GEANT Detector Description and Simulation Tool. *CERN-W-5013*, 1994. (Cited on page 81, 138)

[BCL+04] Oliver Sim Brüning, Paul Collier, P Lebrun, Stephen Myers, Ranko Ostojic, John Poole, and Paul Proudlock. *LHC Design Report*. CERN, Geneva, 2004. (Cited on page 40)

[BDMP09] E Bruna, A Dainese, M Masera, and F Prino. Vertex reconstruction for proton-proton collisions in ALICE. *ARDA-Note-2009-002*, Nov 2009. (Cited on page 72)

[BL58] R. A. Beth and C. Lasky. The Brookhaven Alternating Gradient Synchrotron. *Science*, 128(3336):1393–1401, 1958. (Cited on page 13)

[Blo06] V. Blobel. Software alignment for tracking detectors. *Nuclear Instruments and Methods in Physics Research Section A: Accelerators, Spectrometers, Detectors and Associated Equipment*, 566(1):5 – 13, 2006. {TIME} 2005 Proceedings of the 1st Workshop on Tracking in High Multiplicity Environments1st Workshop on Tracking in High Multiplicity Environments. (Cited on page 54)

[BMM06] Sophie Baron and A. Monera Martinez. Status of the TTC upgrade. In *Proceedings, 12th Workshop on Electronics for LHC and Future Experiments, Valencia, Spain, 25-29 September 2006*, pages 236–240, 2006. (Cited on page 58)

[BNV10] Debasish Banerjee, Jajati K. Nayak, and Raju Venugopalan. Two introductory lectures on high energy QCD and heavy ion collisions. *Lect. Notes Phys.*, 785:105–137, 2010. (Cited on page xv, 14)

[BR97] R. Brun and F. Rademakers. ROOT: An object oriented data analysis framework. *Nucl. Instrum. Meth.*, A389:81–86, 1997. (Cited on page 62)

[BRS92] Jean-Louis Boyard, Pierre Radvanyi, and Madeleine Soyeur. SATURNE: A versatile hadron facility. *Nuclear Physics News*, 2(4):15–20, 1992. (Cited on page 13)

[C+08] S. Chatrchyan et al. The CMS experiment at the CERN LHC. *JINST*, 3:S08004, 2008. (Cited on page 41)

[C+11] S. Chatrchyan et al. Measurement of the inclusive W and Z production cross sections in pp collisions at $\sqrt{s} = 7$ TeV with the CMS experiment. *JHEP*, 2011(10):132, 2011. (Cited on page 33)

[C+12a] S. Chatrchyan et al. Measurement of the Electron Charge Asymmetry in Inclusive W Production in pp Collisions at $\sqrt{s} = 7$ TeV. *Phys. Rev. Lett.*, 109:111806, Sep 2012. (Cited on page xvi, 25, 33)

[C+12b] Serguei Chatrchyan et al. Study of W boson production in PbPb and pp collisions at $\sqrt{s_{NN}} = 2.76$ TeV. *Phys. Lett.*, B715:66–87, 2012. (Cited on page xvii, 33, 34, 35)

[C+13] Serguei Chatrchyan et al. Observation of a new boson with mass near 125 GeV in pp collisions at $\sqrt{s} = 7$ and 8 TeV. *JHEP*, 06:081, 2013. (Cited on page 6)

[C+15] Serguei Chatrchyan et al. Study of Z production in PbPb and pp collisions at $\sqrt{s_{\mathrm{NN}}} = 2.76$ TeV in the dimuon and dielectron decay channels. *JHEP*, 03:022, 2015. (Cited on page 33)

[CDV07] Zaida Conesa Del Valle. *Performance of the ALICE muon spectrometer. Weak boson production and measurement in heavy-ion collisions at LHC.* Theses, Université de Nantes ; Universitat Autónoma de Barcelona, July 2007. (Cited on page xvi, 32)

[CdV09] Zaida Conesa del Valle. Vector bosons in heavy-ion collisions at the LHC. *Eur.Phys.J.*, C61:729–733, 2009. (Cited on page xix, 19, 81)

[Ce12] S. Chatrchyan and V. Khachatryan etal. Study of w boson production in pbpb and pp collisions at $sqrts_{NN}$ = 2.76 tev. *Physics Letters B*, 715(1–3):66 – 87, 2012. (Cited on page 33)

[CFH+12] Matteo Cacciari, Stefano Frixione, Nicolas Houdeau, Michelangelo L. Mangano, Paolo Nason, et al. Theoretical predictions for charm and bottom production at the LHC. *JHEP*, 1210:137, 2012. http://www.lpthe.jussieu.fr/~cacciari/fonll/fonllform.html. (Cited on page xxii, 84, 121)

[CH14] Serguei Chatrchyan and Helen F Heath. Evidence for the direct decay of the 125 gev higgs boson to fermions. *Nature Physics*, 10, 2014. (Cited on page 6)

[Cha04] Michel Chanel. Leir: the low energy ion ring at {CERN}. *Nuclear Instruments and Methods in Physics Research Section A: Accelerators, Spectrometers, Detectors and Associated Equipment*, 532(1–2):137 – 143, 2004. International Workshop on Beam Cooling and Related Topics. (Cited on page 41)

[Cha14] A. K. Chaudhuri. *A short course on Relativistic Heavy Ion Collisions*. IOPP, 2014. (Cited on page 15)

[CKe15] S. Chatrchyan, V. Khachatryan, and etal. Study of z production in pbpb and pp collisions at $\sqrt{s_{NN}}$ = 2.76 tev in the dimuon and dielectron decay channels. *Journal of High Energy Physics*, 2015(3):22, 2015. (Cited on page 33)

[Col94] ATLAS Collaboration. *ATLAS: technical proposal for a general-purpose pp experiment at the Large Hadron Collider at CERN*. LHC Tech. Proposal. CERN, Geneva, 1994. (Cited on page 41)

[Col95] ALICE Collaboration. *ALICE: Technical proposal for a Large Ion collider Experiment at the CERN LHC*. LHC Tech. Proposal. CERN, Geneva, 1995. (Cited on page xvii, xviii, 41, 46, 48, 54, 57, 58, 59, 64)

[Col97] CMS Collaboration. *The CMS muon project: Technical Design Report*. Technical Design Report CMS. CERN, Geneva, 1997. (Cited on page 41)

[Col98] LHCb Collaboration. *LHCb : Technical Proposal*. Tech. Proposal. CERN, Geneva, 1998. (Cited on page 41)

[col13] NICA collaboration. NICA. http://nica.jinr.ru/tech.html, 2013. [Online; accessed 20-March-2017]. (Cited on page 13)

[Coo09] LHC Programme Coordination. LHC Programme Coordination Home Page. https://lpc.web.cern.ch/lpc/, 2009. [Online; accessed 16-November-2015]. (Cited on page xviii, xxii, xxiv, 71, 117, 134)

[Cor15] G Herrera Corral. Diffractive Physics with ALICE at the LHC: the control of quantum collisions. *Journal of Physics: Conference Series*, 624(1):012008, 2015. (Cited on page 116)

[CORW06] J. Cleymans, H. Oeschler, K. Redlich, and S. Wheaton. Comparison of chemical freeze-out criteria in heavy-ion collisions. *Phys. Rev.*, C73:034905, 2006. (Cited on page 15)

[dFSZS12] Daniel de Florian, Rodolfo Sassot, Pia Zurita, and Marco Stratmann. Global Analysis of Nuclear Parton Distributions. *Phys.Rev.*, D85:074028, 2012. (Cited on page xvi, 26, 30)

[dFV10] Daniel de Florian and Werner Vogelsang. Helicity Parton Distributions from Spin Asymmetries in W-Boson Production at RHIC. *Phys.Rev.*, D81:094020, 2010. (Cited on page 23)

[DM16] Cinzia De Melis. The CERN accelerator complex. Complexe des accélérateurs du CERN. Jul 2016. General Photo. (Cited on page xvii, 40)

[DMD15] Marie Laure Delignette-Muller and Christophe Dutang. fitdistrplus: An R package for fitting distributions. *Journal of Statistical Software*, 64(4):1–34, 2015. (Cited on page 96, 176)

[ea76] R. Force et al. Bevatron/bevalac. *LBL–5370*, 1976. (Cited on page 12)

[ea80] A. M. Baldin et al. *The Synchrophasotron: An Accelerator of Relativistic Nuclei*, pages 229–231. Birkhäuser Basel, Basel, 1980. (Cited on page 12)

[ea14] K.A. Olive et al. Review of particle physics. *Chin. Phys. C*, 38:090001, 2014. (Cited on page xv, 10, 19, 21, 22)

[EB08] Lyndon Evans and Philip Bryant. LHC Machine. *JINST*, 3:S08001, 2008. (Cited on page 6, 40)

[Ell14] John Ellis. The Discovery of the Gluon. *Int. J. Mod. Phys.*, A29(31):1430072, 2014. ,189 (2015). (Cited on page 10)

[EPS09] K. J. Eskola, H. Paukkunen, and C. A. Salgado. EPS09: A New Generation of NLO and LO Nuclear Parton Distribution Functions. *JHEP*, 04:065, 2009. (Cited on page xii, xxi, 26, 28, 81, 110, 138)

[FJL+04] Christian Wolfgang Fabjan, L Jirdén, V Lindestruth, Lodovico Riccati, D Rorich, Pierre Van de Vyvre, O Villalobos Baillie, and Hans de Groot. *ALICE trigger, data-acquisition, high-level trigger and control system: Technical Design Report*. Technical Design Report ALICE. CERN, Geneva, 2004. (Cited on page xviii, 57, 58, 59)

[Fuk08] Kenji Fukushima. Chiral Symmetry and Heavy-Ion Collisions. *J.Phys.*, G35:104020, 2008. (Cited on page 11)

[FW13] Stefano Forte and Graeme Watt. Progress in the Determination of the Partonic Structure of the Proton. *Ann. Rev. Nucl. Part. Sci.*, 63:291–328, 2013. (Cited on page 22, 24, 25, 108)

[Gai82] J. Gaiser. *Charmonium Spectroscopy From Radiative Decays of the J/ψ and ψ'*. PhD thesis, SLAC, 1982. (Cited on page 83)

[Gil87] F.J. Gilman. Phenomenology of heavy quark systems. *SLAC-PUB–*, 4253, 1987. (Cited on page 10)

[GLPQ11] Ryan Gavin, Ye Li, Frank Petriello, and Seth Quackenbush. FEWZ 2.0: A code for hadronic Z production at next-to-next-to-leading order. *Comput. Phys. Commun.*, 182:2388–2403, 2011. (Cited on page xx, xxi, 99, 101, 102, 103, 104, 105, 106, 129)

[GPP98] B Genolini, J Pouthas, and J Peyré. A Full-Scale Prototype for the Tracking Chambers of the ALICE Muon Spectrometer. Part I: Mechanics, Anode and Cathode Plane Design, Assembly and Construction. Technical Report ALICE-INT-1998-28. CERN-ALICE-INT-1998-28, CERN, Geneva, 1998. (Cited on page 53)

[Gri08] D. Griffiths. *Introduction to Elementary Particles*. Physics textbook. Wiley, 2008. (Cited on page 8, 9)

[Gro09] Tevatron Electroweak Working Group. Updated Combination of CDF and D0 Results for the Mass of the W Boson. *TEVEWWG-WZ-2009-01, FERMILAB-TM-2439-E, CDF-NOTE-9859, D0-NOTE-5965*, 2009. (Cited on page 19)

[Har15] John W Harris. Introduction to hard scattering processes and recent results from hard probes at rhic and lhc. *Journal of Physics: Conference Series*, 630(1):012052, 2015. (Cited on page xvi, 26)

[Heu09] Johann M. Heuser. The Compressed Baryonic Matter Experiment at FAIR: Progress with feasibility studies and detector developments. *Nucl. Phys.*, A830:563C–566C, 2009. (Cited on page 13)

[HM08] F. Halzen and A.D. Martin. *QUARK & LEPTONS: AN INTRODUCTORY COURSE IN MODERN PARTICLE PHYSICS*. Wiley India Pvt. Limited, 2008. (Cited on page 8)

[Ian14] Edmond Iancu. QCD in heavy ion collisions. In *Proceedings, 2011 European School of High-Energy Physics (ESHEP 2011): Cheile Gradistei, Romania, September 7-20, 2011*, pages 197–266, 2014. (Cited on page xv, 11, 14)

[JAB+12] A Jeff, M Andersen, A Boccardi, S Bozyigit, E Bravin, T Lefevre, A Rabiller, F Roncarolo, C P Welsch, and A S Fisher. Measurement of Satellite Bunches at the LHC. *Conf. Proc.*, C1205201(CERN-ATS-2012-088):MOEPPB010. 3 p, May 2012. (Cited on page 116)

[Joh75] K. Johnson. The mit bag model. *Acta Physica Polonica Series B*, 6(6):865–892, 1975. (Cited on page 11)

[JRR04] François Jouve, P. Rosnet, and L. Royer. Front-End Electronics of the ALICE dimuon trigger. Technical report, 2004. (Cited on page 55)

[K+15] Vardan Khachatryan et al. Study of W boson production in pPb collisions at $\sqrt{s_{\mathrm{NN}}} = 5.02$ TeV. *Phys. Lett.*, B750:565–586, 2015. (Cited on page xxi, 33, 100, 107)

[K+16] Vardan Khachatryan et al. Study of Z boson production in pPb collisions at $\sqrt{sNN}$=5.02TeV. *Phys. Lett.*, B759:36–57, 2016. (Cited on page 33)

[Kie88] Paul Kienle. *SIS/ESR: A Heavy Ion Synchrotron and Coolre Facility at GSI*, pages 373–391. Springer US, Boston, MA, 1988. (Cited on page 13)

[KL99] Frithjof Karsch and Martin Lutgemeier. Deconfinement and chiral symmetry restoration in an SU(3) gauge theory with adjoint fermions. *Nucl.Phys.*, B550:449–464, 1999. (Cited on page 11)

[Koc95] Volker Koch. Introduction to chiral symmetry. In *3rd TAPS Workshop on Electromagnetic and Mesonic Probes of Nuclear Matter Bosen, Germany, September 10-15, 1995*, 1995. (Cited on page 11)

[Kra87] K.S. Krane. *Introductory Nuclear Physics*. Wiley, 1987. (Cited on page 5)

[Kry14] E. Kryshen. Analysis Tutorial, 2014. [Online; accessed 09-March-2017]. (Cited on page xviii, 72)

[Las98] C. Lasseur. POSITIONING STRATEGY, METROLOGY AND SURVEY IN ALICE. Technical Report ALICE-INT-2008-018. CERN-ALICE-INT-1998-28, CERN, Geneva, 1998. (Cited on page 54)

[Ley12] Michael Leyton. Minimum Bias and Underlying Event Measurements with ATLAS. In *Proceedings, 3rd International Workshop on Multiple Partonic Interactions at the LHC (MPI@LHC 2011): Hamburg, Germany, 21-25 Nov 2011*, pages 11–19, 2012. (Cited on page 45)

[Lip03] L. N. Lipatov. Dglap and bfkl equations now. *International Journal of Modern Physics A*, 18(supp01):68–90, 2003. (Cited on page 14)

[Lof56] E. J. Lofgren. *Experiences with the Bevatron.* Apr 1956. (Cited on page 12)

[Mar08] Alan D. Martin. Proton structure, Partons, QCD, DGLAP and beyond. *Acta Phys. Polon.*, B39:2025–2062, 2008. (Cited on page 25)

[Mre07] Stephen Mrenna. Pile-up events. http://home.fnal.gov/~mrenna/lutp0613man2/node189.html, 2007. [Online; accessed 13-March-2017]. (Cited on page 75)

[MRSS07] Michael L. Miller, Klaus Reygers, Stephen J. Sanders, and Peter Steinberg. Glauber modeling in high energy nuclear collisions. *Ann.Rev.Nucl.Part.Sci.*, 57:205–243, 2007. (Cited on page xii, xv, 15, 16, 17, 19, 45, 135, 136)

[MRST00] Alan D. Martin, R.G. Roberts, W. James Stirling, and R.S. Thorne. Parton distributions and the LHC: W and Z production. *Eur.Phys.J.*, C14:133–145, 2000. (Cited on page xv, 20, 21, 25, 99, 129)

[MSTW09] A.D. Martin, W.J. Stirling, R.S. Thorne, and G. Watt. Parton distributions for the LHC. *Eur.Phys.J.*, C63:189–285, 2009. (Cited on page 22)

[NLC+08] Pavel M. Nadolsky, Hung-Liang Lai, Qing-Hong Cao, Joey Huston, Jon Pumplin, Daniel Stump, Wu-Ki Tung, and C. P. Yuan. Implications of CTEQ global analysis for collider observables. *Phys. Rev.*, D78:013004, 2008. (Cited on page xii, xxi, xxiii, 81, 84, 99, 110, 119, 123, 129, 138)

[oJ15] University of Jyväskylä. T0 detector in ALICE experiment at CERN, 2015. [Online; accessed 21-April-2015]. (Cited on page xvii, 46, 47, 48)

[oNP05] SAHA Institute of Nuclear Physics. Large Area Cathode Pad Chambers, 2005. [Online; accessed 09-March-2017]. (Cited on page xvii, 53)

[Pil14] P. Pillot. Private communication, 2014. (Cited on page 83)

[PS11] Hannu Paukkunen and Carlos A. Salgado. Constraints for the nuclear parton distributions from Z and W production at the LHC. *JHEP*, 1103:071, 2011. (Cited on page xi, xii, xvi, xx, xxi, 27, 29, 30, 31, 32, 99, 100, 101, 102, 103, 104, 105, 106, 108, 110)

[R C16] R Core Team. *R: A Language and Environment for Statistical Computing.* R Foundation for Statistical Computing, Vienna, Austria, 2016. (Cited on page 96, 176)

[RZC+15] Peng Ru, Ben-Wei Zhang, Luan Cheng, Enke Wang, and Wei-Ning Zhang. Production of Z^0 and W^+/W^- in relativistic heavy-ion collisions at the LHC. *J. Phys.*, G42(8):085104, 2015. (Cited on page xvi, 24, 26, 27, 28, 30)

[Sat10] Helmut Satz. The Thermodynamics of Quarks and Gluons. *Lect.Notes Phys.*, 785:1–21, 2010. (Cited on page xv, 11)

[Sat11] Helmut Satz. The Quark-Gluon Plasma: A Short Introduction. *Nucl.Phys.*, A862-863:4–12, 2011. (Cited on page xv, 11)

[Ser15] Nicola Serra. Standard model. http://www.physik.uzh.ch/groups/serra/StandardModel.html, 2015. [Online; accessed 31-January-2015]. (Cited on page xv, 7)

[SKNM13] Ranbir Singh, Lokesh Kumar, Pawan Kumar Netrakanti, and Bedangadas Mohanty. Selected Experimental Results from Heavy Ion Collisions at LHC. *Adv. High Energy Phys.*, 2013:761474, 2013. (Cited on page 12)

[SMS06] Torbjorn Sjostrand, Stephen Mrenna, and Peter Z. Skands. PYTHIA 6.4 Physics and Manual. *JHEP*, 05:026, 2006. (Cited on page 81, 138)

[Sne06] Raimond Snellings. Heavy-Ion Physics at the LHC with Alice. In *Proceedings, 34th SLAC Summer Institute on Particle Physics: The Next Frontier: Exploring with the LHC (SSI 2006): Menlo Park, California, July 17-28, 2006*, 2006. (Cited on page 11, 12)

[Tay02] B. G. Taylor. Timing distribution at the LHC. In *8th Workshop on Electronics for LHC Experiments Colmar, France, September 9-13, 2002*, pages 63–74, 2002. (Cited on page 58)

[V. 09a] V. Blobel. Millepede: Linear Least Squares Fits with a Large Number of Parameters. http://www.desy.de/~blobel/, 2009. [Online; accessed 28-August-2015]. (Cited on page 54)

[V. 09b] V. Blobel. "MILLEPEDE program description and code". http://www.desy.de/~blobel/, 2009. [Online; accessed 28-August-2015]. (Cited on page 54, 83)

[V.15] Khachatryan V. Study of W boson production in pPb collisions at $\sqrt{s_{\mathrm{NN}}} = 5.02$ TeV. *Physics Letters B*, 750:565 – 586, 2015. (Cited on page 31)

[VM16] Xabier Cid Vidal and Ramon Cid Manzano. Lhc trigger. http://www.lhc-closer.es/taking_a_closer_look_at_lhc/0.lhc_trigger, 2016. [Online; accessed 21-October-2016]. (Cited on page 93)

[Vog01] R. Vogt. Shadowing effects on vector boson production. *Phys.Rev.*, C64:044901, 2001. (Cited on page 25, 27)

[Zha17] Z. Zhang. Private communication, 2017. (Cited on page xxiv, 139)

A

Appendix

Contents:

A.1 W and Z boson weights

Figure A.1 shows the distribution used to weight the POWHEG and CT10 with EPS09 simulations in order to take into account the systematic due to input PDFs in the signal extraction. These distributions were used to re-weights the LHC13de production.

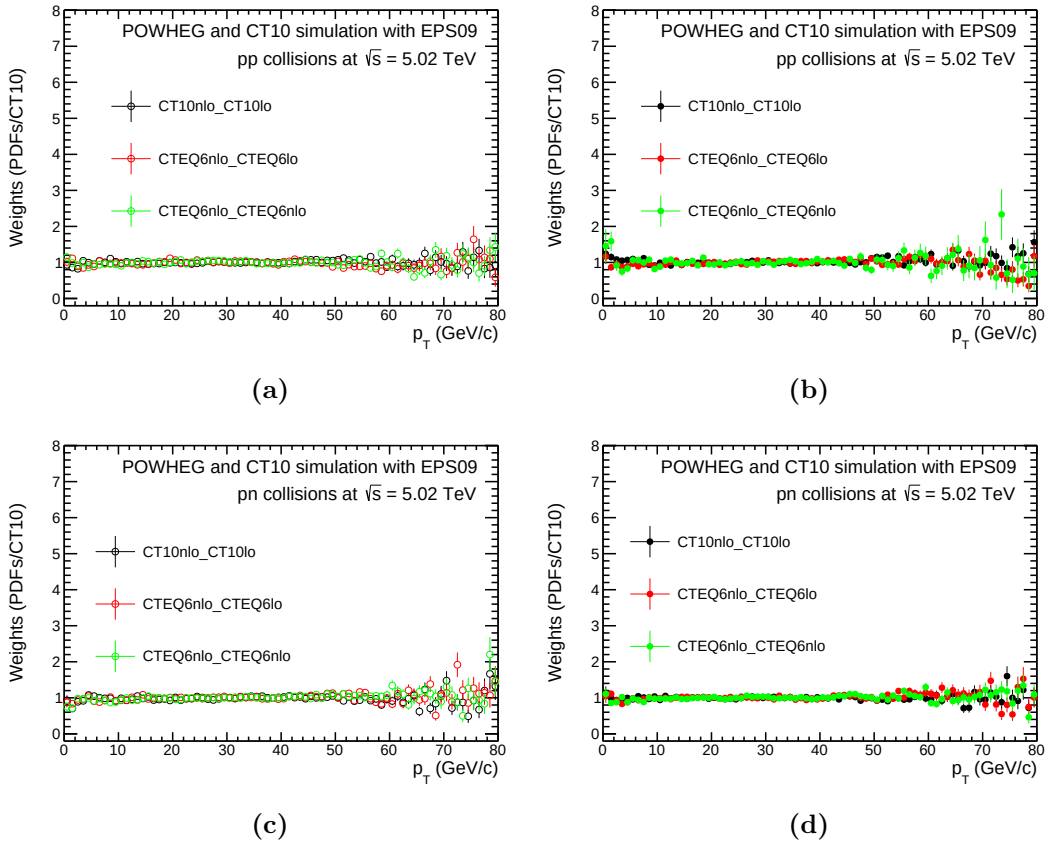

Figure A.1: Shown here are distributions used to weight the POWHEG and CT10 with EPS09 simulations (p-going) in order to take into account the systematic due to input PDFs.

Figure A.2 shows the distribution used to weight the POWHEG and CT10 with EPS09 simulations in order to take into account the systematic due to input PDFs in the signal extraction. These distributions were used to re-weights the LHC13f production.

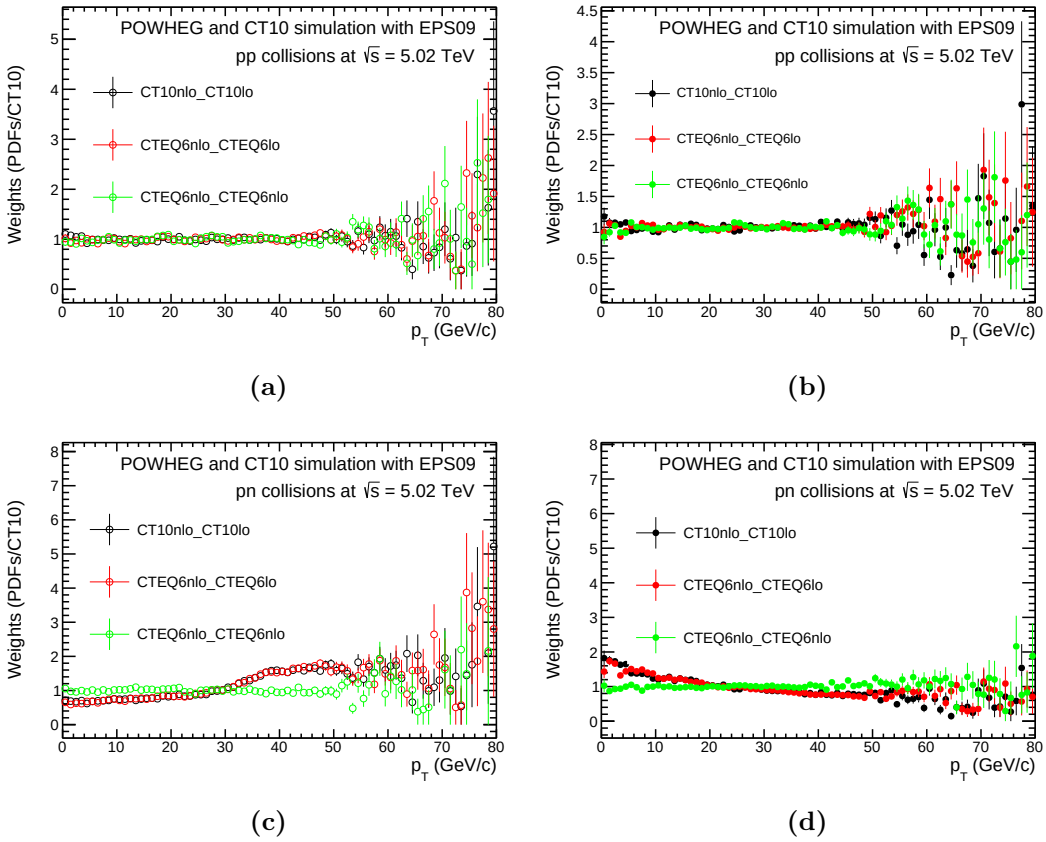

Figure A.2: Shown here are distributions used to weight the POWHEG and CT10 with EPS09 simulations (Pb-going) in order to take into account the systematic due to input PDFs.

A.2 Acceptance × Efficiency

In Figures A.3 and A.4 are the Monte-Carlo templates and the $A \times \varepsilon$ for the p-going and Pb-going period, respectively.

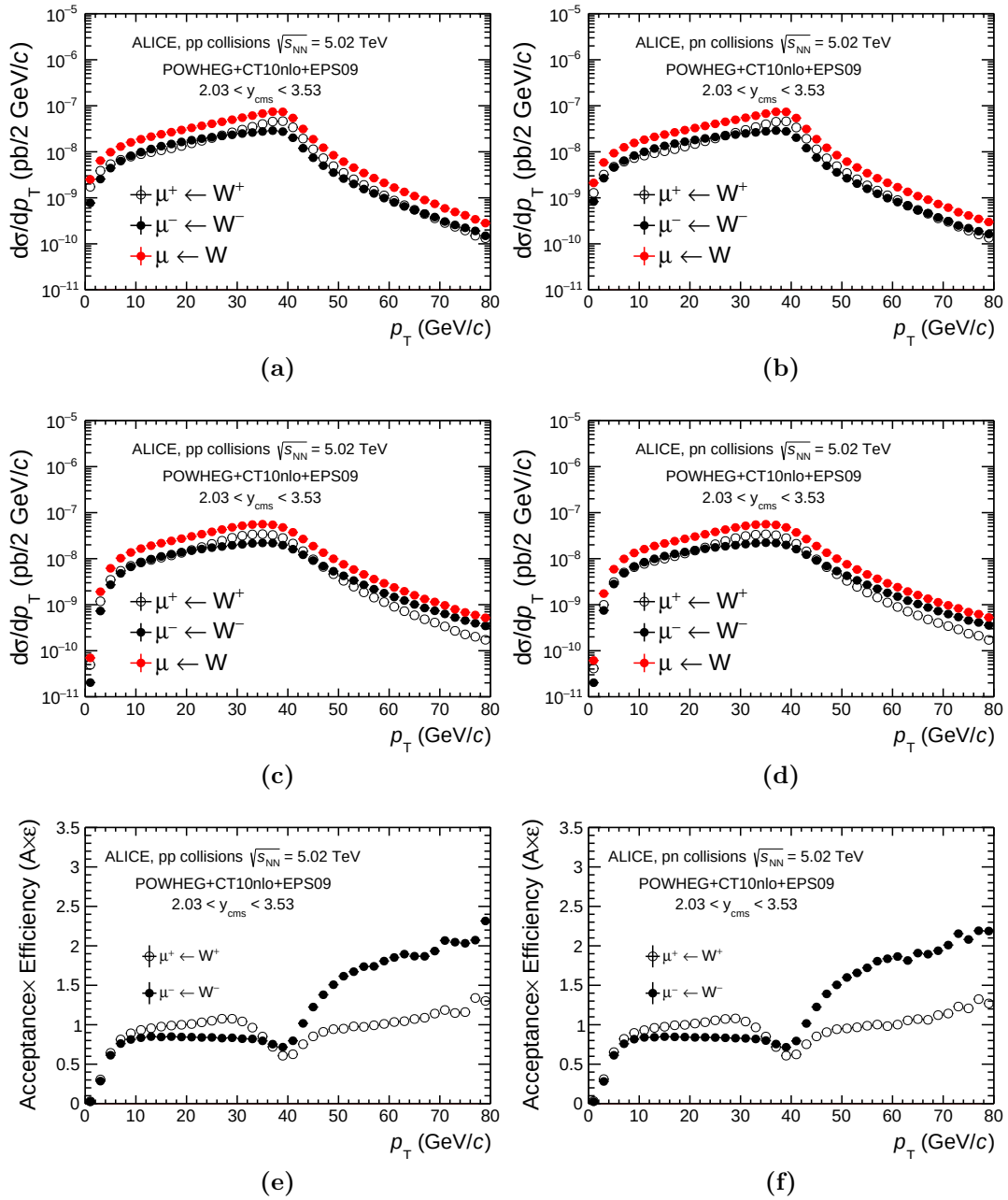

Figure A.3: Generation level templates for pp (a) and pn (b) collisions at 5.02 TeV using POWHEG and CT10 with EPS09 PDFs for LHC13e. Reconstruction level templates for pp (c) and pn (d) collisions at 5.02 TeV using POWHEG and CT10 with EPS09 PDFs for LHC13e. Acceptance times efficiency for pp (e) and pn (f) as function of transverse momentum for LHC13e period.

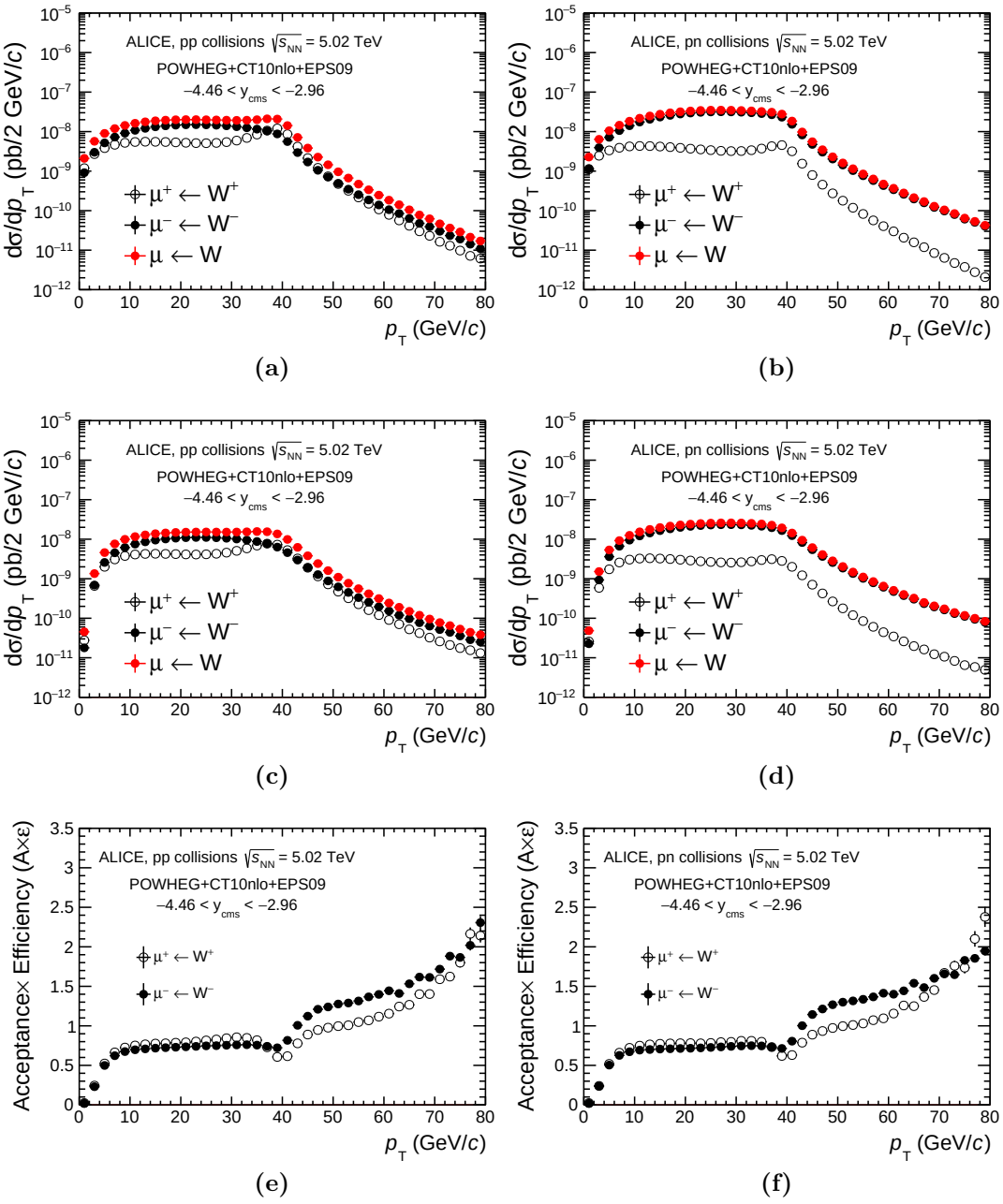

Figure A.4: Generation level templates for pp (a) and pn (b) collisions at 5.02 TeV using POWHEG and CT10 with EPS09 PDFs for LHC13f. Reconstruction level templates for pp (c) and pn (d) collisions at 5.02 TeV using POWHEG and CT10 with EPS09 PDFs for LHC13f. Acceptance times efficiency for pp (e) and pn (f) as function of transverse momentum for LHC13f period.

B

Appendix

Contents:

B.1 Normalization factor: p-Pb collisions

Shown in Figure B.1 are the L0B rates used to compute the normalisation factor. In Figure B.3 is the normalisation factor as a function of centrality for the three data taking periods. Shown in Figure B.2 is the purity of MB events and the fraction of physics selected MSH events for both forward (left) and backward (right) rapidity.

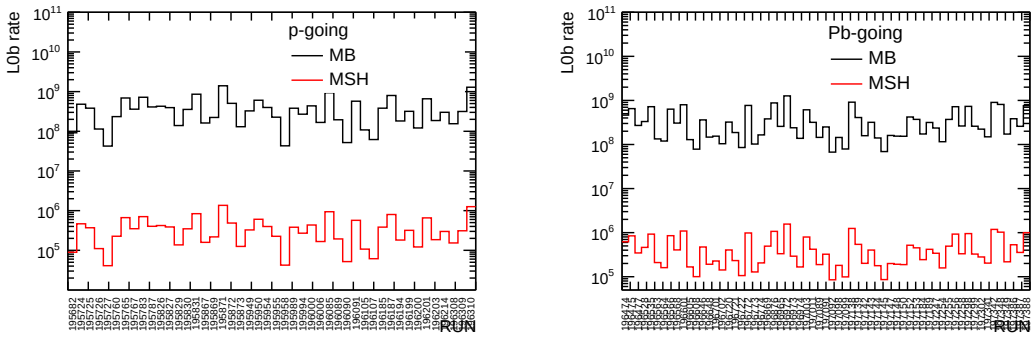

Figure B.1: L0b rate for the minimum-bias (MB) and high-p_{T} muon triggered (MSH) events for the p-going period (left) and Pb-going (right).

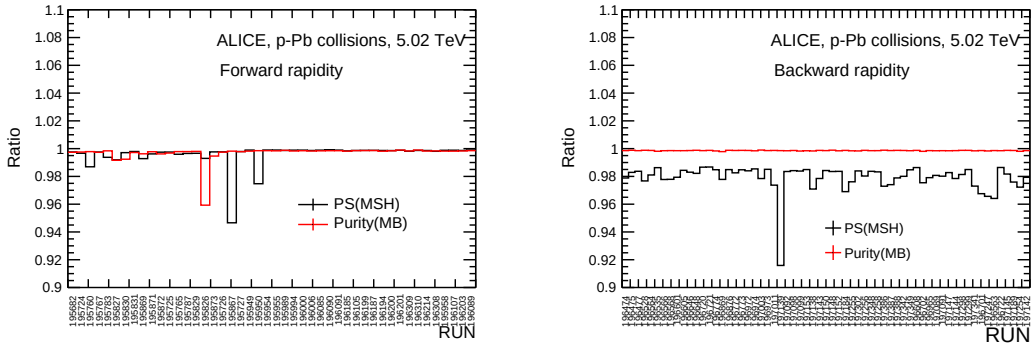

Figure B.2: On the left is the purity of minimum-bias (MB) in red and the fraction of physics selected MSH events in black for the forward rapidity period. On the right is the purity of minimum-bias (MB) in red and the fraction of physics selected MSH events in black for the backward rapidity period.

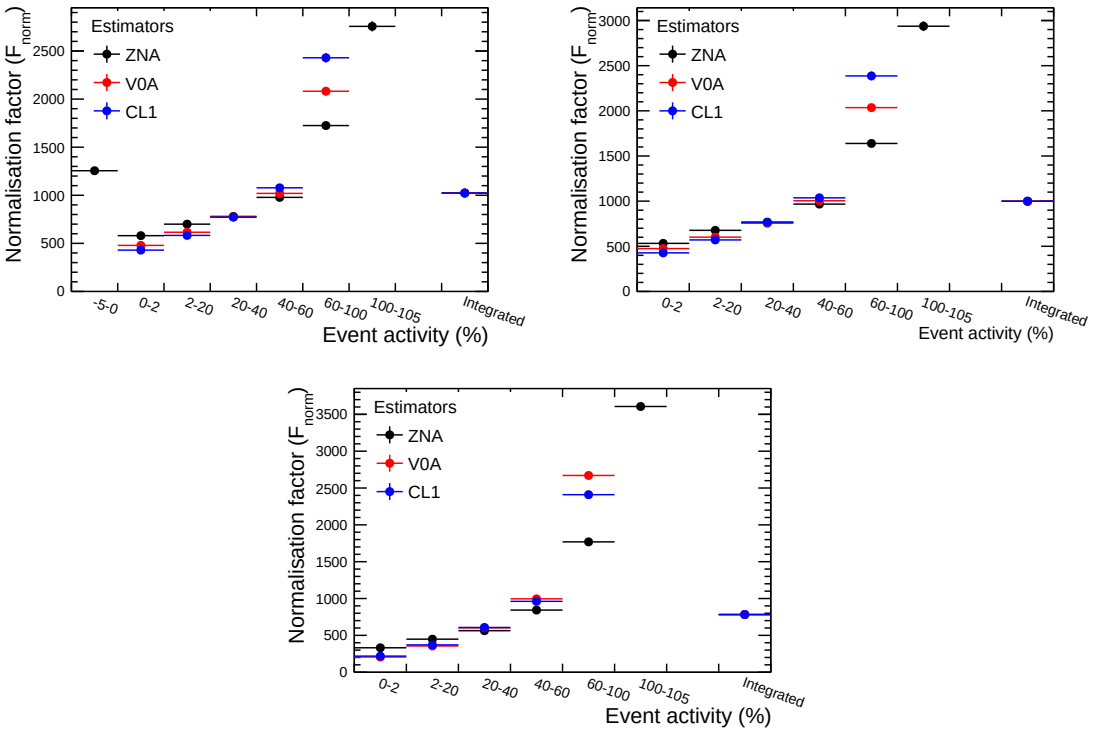

Figure B.3: Normalization factor (offline method) as function of event activity for the LHC13d (top), LHC13e (top) and LHC13f (bottom) without the pile-up correction.

B.2 Systematic uncertainty study: p–Pb collisions

The distributions of the number of W-boson in the p-going (LHC13e) and Pb-going (LHC13f) periods compared with theoretical functions from the R statistical package [R C16, DMD15]. It is clear that the number of W-boson are normally (Gaussian) distributed and thus the RMS is thus a suitable systematic uncertainty also in these cases.

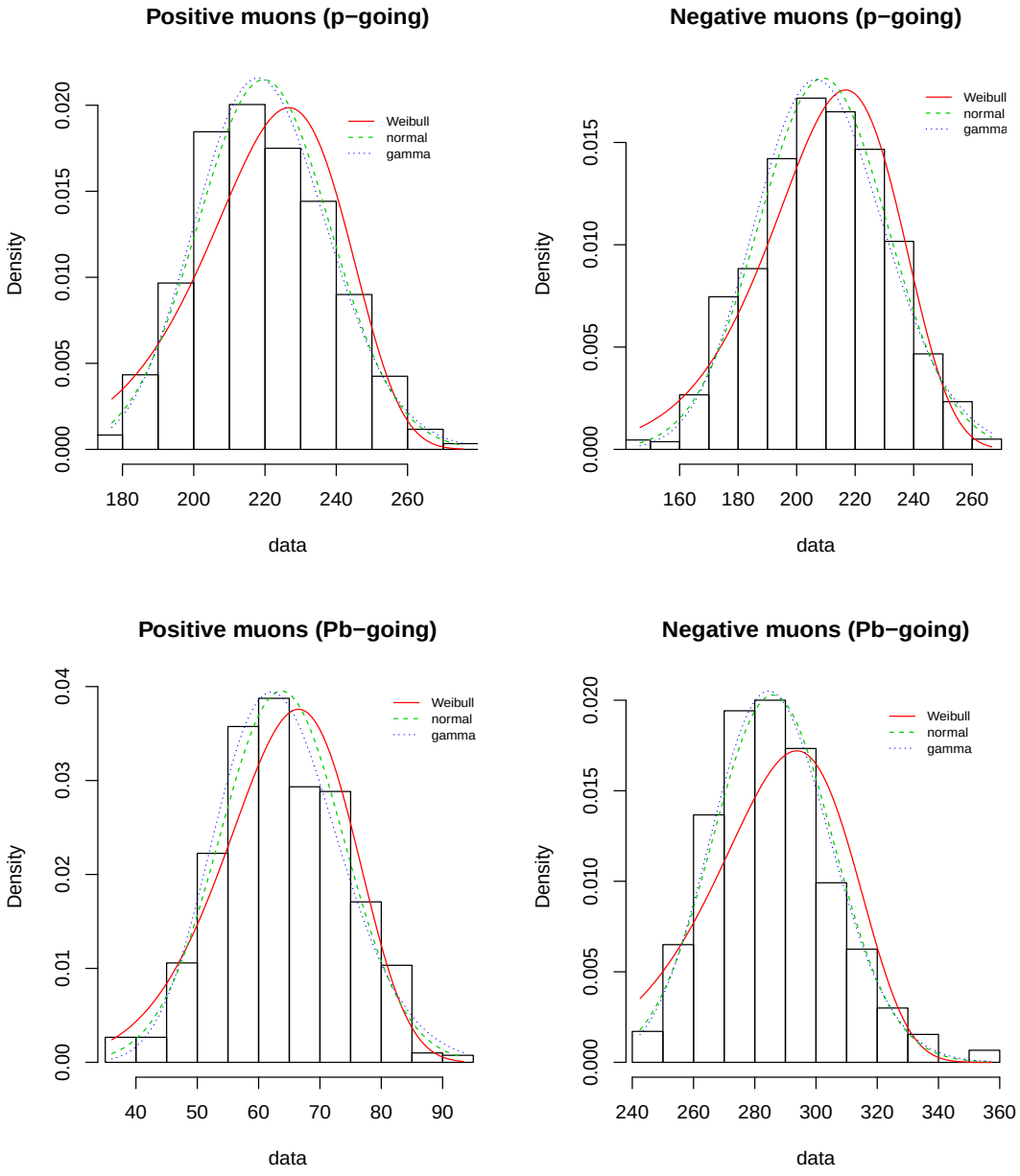

Figure B.4: The distribution of W-boson in the p-going direction period LHC13e (top) and LHC13f (bottom), the colored lines represents different theoretical distributions.

B.3 Systematic uncertainty study: pp collisions

In Figures B.5 and B.6 are the distributions of the number of negative and positive muons from W-bosons decays compared with theoretical distributions, respectively.

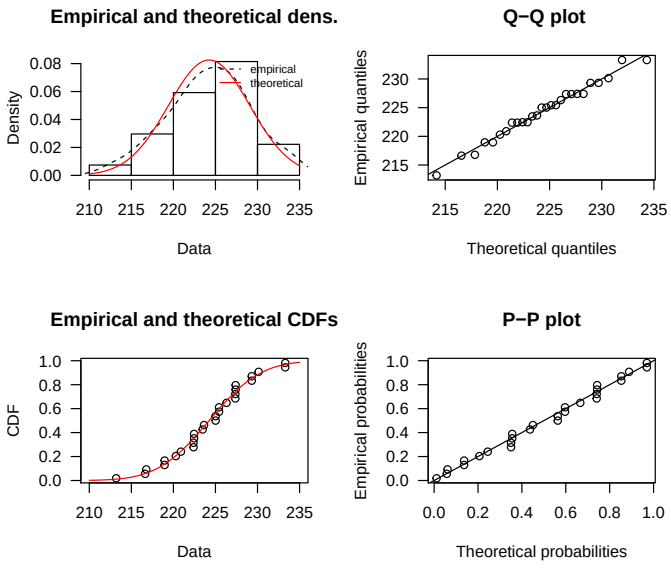

(a)

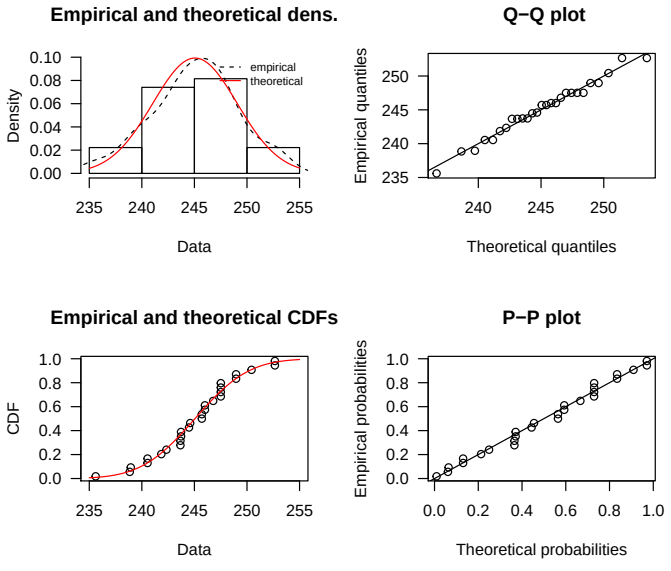

(b)

Figure B.5: The test of normality of number of W bosons using different methods, comparison of the histogram overlayed with probability density functions of a normal distribution (top left), Q-Q plot (top right), cumulative distribution function (bottom left) and finally P-P plot (bottom). Figure B.5a and B.5b for default alignment and resolution task for negative muons, respectively.

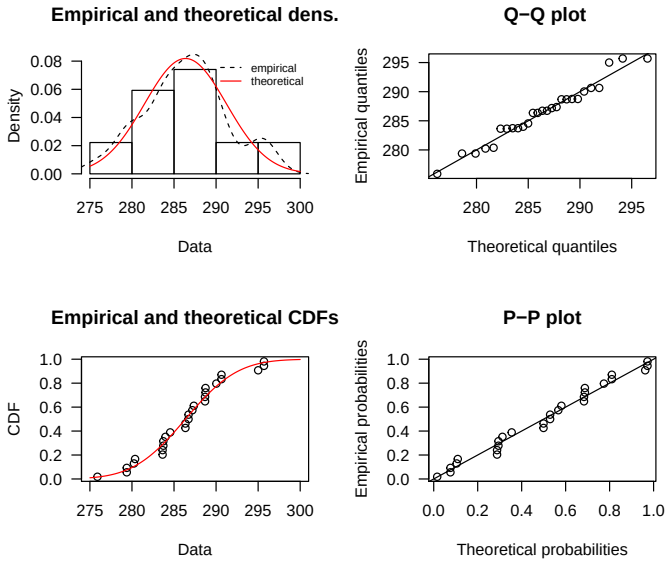

(a)

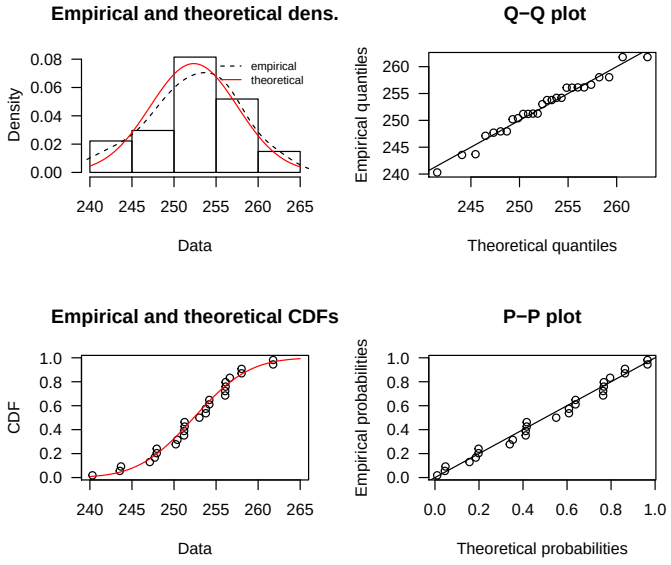

(b)

Figure B.6: The test of normality of number of W bosons using different methods, comparison of the histogram overlayed with probability density functions of a normal distribution (top left), Q-Q plot (top right), cumulative distribution function (bottom left) and finally P-P plot (bottom). Figure B.5a and B.5b for default alignment and resolution task for positive muons, respectively.

Glossary

Symbols

$A \times \varepsilon$

is the ratio of reconstructed to generated tracks in a particular acceptance region. This is known as acceptance times efficiency. viii, 70, 81, 82

I

Integrated luminosity

is the integral over instantaneous (delivered) luminosity per second. $\mathcal{L}_{\text{int}} = \int_0^T L(t)\mathrm{d}t$. 95

J

jets

are collimated stream of particle (mostly hadrons) which comes from the hadronisation of a high energy partons. 14

L

luminosity

is a quantity that measures the ability of a particle accelerator to produce the required number of interactions. Or, the number of collisions that can be produced in a detector per cm^2 and per second. 30

S

sea quarks

are quarks that come from the kinetic energy of a colliding system. 23

T

trigger

is a criterion used to select interesting events, useful in an environment of high background. 46

V

valence quarks

are quarks that determine the quantum numbers of hadrons. 30

vector bosons

also refers to massive electroweak bosons (W and Z boson) in this thesis. 6

Index